An electrochemical and physical study of chlorine electrocatalysis on commercial RuO2/TiO2 anodes

Shingleton, Anthony

Award date:
1996

Awarding institution:
University of Bath

An Electrochemical and Physical study of Chlorine Electrocatalysis on Commercial RuO_2/TiO_2 Anodes

Submitted by Anthony Shingleton

For the degree of PhD

of the University of Bath

1996

ProQuest LLC
789 East Eisenhower Parkway
P.O. Box 1346
Ann Arbor, MI 48106-1346

This thesis is dedicated

to

my father and mother

Abstract

A complete characterisation of chlorine electrocatalysis on a commercial RuO_2/TiO_2 catalyst has been carried out under industrially relevant conditions, by controlling temperature, pH, electrolyte concentration, convection and current. The aim was to determine the reaction mechanism and the factors responsible for the loss of catalytic performance. This has been achieved by using physical techniques such as XPS, XRF, SEM, as well as electrochemical methods, including cyclic voltammetry, steady state current-voltage measurements, Tafel plots, impedance spectroscopy and open potential circuit decay (OCPD). Work was carried out in a classical three compartment cell and various types of channel flow cells.

This work has established that chlorine evolution on a commercial RuO_2/TiO_2 anode takes place via the following two steps : adsorption of chlorine at the surface, i.e. $Cl^- + M \rightarrow Cl_{ads}\text{-}M + e^-$, followed by *electrochemical* desorption to give a chlorine molecule, i.e. $Cl_{ads}\text{-}M + Cl^- \rightarrow Cl_2 + M + e^-$. The use of an accelerated wear test has also established that the loss of electrocatalytic performance is not due to a loss of catalytic activity of the RuO_2/TiO_2 coating but due to the growth of a resistive layer of TiO_{2-x} at the boundary of the RuO_2/TiO_2 coating and the titanium substrate.

Acknowledgements

First of all, I would to thank a number of people on a professional level. I am especially grateful to my academic supervisor, Professor Peter, who has significantly acted on my behalf in order to offer me a PhD project, for his supervision and support throughout the hard times. I am also very grateful to my industrial supervisor, Dave Hodgson (soon to be Dr. Hodgson), for his support and role in making this project a true collaboration between academia and industry. I appreciate this has been a very complicated task and I would to thank him for having allowed me the freedom and the opportunity to work at ICI facilities at my convenience. In particular, I would like to acknowledge the various colleagues in his group who have helped me, Neil Malone for the time he has spent performing and fitting XPS measurements on my behalf and Helen for her involvement in performing XRF measurements.

Special thanks are given to Dr. Mike Bailes for his infinite patience and the significant contribution he has made to this project.

On a financial level, I would like to thank ICI Chemicals & Polymers Ltd for fully sponsoring this project, sending me on various conferences and giving me the opportunity to gain a PhD. I would also like to thank my beloved parents and brother for their charity towards me. They have been of great support in these times of intellectual wealth and financial poverty.

I would now like to acknowledge various people on a social level. Again, I would like to thank Laurie for the great times I have had while working in his research group. I will never forget the most excellent parties at his home (special thanks to Renata for her marvellous cooking and most delicious deserts !) and his unsuccessful attempts to get me to be truly English by being a bitter and not a lager drinker. I would like to thank him for the people he has put me touch with, some of which have now become close friends. In this respect, I would like to thank Dave for being more than an industrial supervisor (no innuendo intended) and hope that we will have many more of his 'beer-talking' sessions in the future. I am especially thankful to him for making me appear as a 'wino' after picking up all the food bills and letting me pay all the alcohol bills during our conference in Ferrara. Visiting Venice with one's industrial

supervisor is not quite the same as doing it with one's girlfriend. Who knows, if this happens again, I would be curious to find out what Rachel thinks of this... I can think of many moments that I cherish and would like to thank him for the good memories.

I would also like to pay a special tribute to people such as Mr Beano (alias Roger), Phil Mitchell (alias Pete), Mr Sunglasses (alias Andy), The ambassador of Lager and most tasteful shirts (alias Mark) and Mr Two-Face (alias Rob) for being good friends and not just lab-mates throughout my time as a PhD student. We have had great times together and hope there will be many more in the future, no matter where we all end up. Furthermore, I would liketo extend this tribute to Shayesta. I would also like to thank Kieran Molloy for being a good mentor and helping me stay in relatively good physical shape (Once again, no innuendo intended). May his leap forward in technological matters have mercy on his soul and his capability to appreciate such quantities of wine that made it allegedly impossible to play squash during the week. It also goes without say that I would like to thank most of the people who have worked in Laurie's group throughout my stay. In this respect, I would like to thank Dave for having tried to give us culture and being an example of a virtuous person ; Siva for his many samosas, excellent cooking, punctuality and craziness ; Greg and Eric for the many rounds of beer they have paid for ; Gunter for his tea ; last and not least (in many respects), Nicki & John for reminding all of us what a PhD is all about...

I would like to make a special tribute to His & Hers, my two red gold fish, for having kept me company during my writing up period and all the conversations we had that allowed me to feel alive and remain sane.....

Finally, I would like to thank Sarah for her patience, support throughout the hard times, loving care during the latter part of my PhD and making sure my belly was always being looked after (I hope the food bit will continue once my PhD project is over....).

Table of content

Chapter One : introduction

Chapter Two : experimental

Chapter Three : flow cell and reference electrodes

Chapter Four : cyclic voltammetry and impedance spectroscopy

Chapter Five : steady state techniques

Chapter Six : interrupt techniques

Chapter Seven : physical techniques

Chapter Eight : correlation of physical and electrochemical techniques

Chapter Nine : conclusions and future work

Appendix

Chapter One
Introduction

Electrochemistry has had a great impact on industry. Of historical importance are the electrolytic production of aluminium (1886), chlorine (1890) and adiponitrile (1930's). Today, the applications of industrial electrochemistry have diversified in terms of both scale of operation and nature of the electrode reaction involved. Five areas of electrochemical technology applications can now be distinguished :

Electrosynthesis : i.e. inorganic & organic chemicals, metals & alloys, semiconductors, conductive polymers and composites.

Material processing : i.e. electrochemical machining, etching of metals & semiconductors, electrophoretic painting, electroplating & anodising and corrosion protection.

Electrical power conversion : i.e. fuels cells, storage batteries, redox batteries, solar cells.

Environmental protection : i.e. sensors, metal ion removal, inorganic and organic decontamination, water purification, recycling and salt splitting.

Biomedical applications : i.e. *in-vivo* sensors & monitors, *in-vivo* diagnostics and slow-release drug delivery devices.

1.1 Historical background

Chlorine was first prepared in 1774 by K. W. Scheele from hydrochloric acid and manganese, i.e.

$$MnO_2 + 4\ HCl \longrightarrow Cl_2 + MnCl_2 + 2\ H_2O \qquad (1.1)$$

Only one third of the hydrochloric acid produced chlorine and the process was hindered by corrosive substances. This meant that the process was difficult as well as expensive. As a result, this reaction mechanism was replaced in 1868 by the Deacon process in which chlorine was made by the reaction of hydrogen chloride gas and atmospheric oxygen :

$$4\,HCl + O_2 \longrightarrow 2\,Cl_2 + 2\,H_2O \qquad (1.2)$$

As for the Weldon process, this reaction mechanism was reversible and incomplete. Although 70 % of the hydrogen chloride reacted to produce chlorine, this process was abandoned as electrolytic methods became widely used and also because the hydrogen chloride used in this process was a by-product of the Le Blanc soda process that became obsolete.

Electrolytic chlorine was first produced successfully on a commercial scale about 1890 and became the major source of chlorine by the early 1960s. Although the process has remained the same since it was first used, technological improvements have greatly improved its efficiency. Of importance are the various cell technologies and the different catalytic materials that have been developed. A brief description of them will be given later.

1.2 Overview of electrolytic processes

Traditionally, electrolytic processes have been used on a large scale for the manufacture of chlorine and caustic soda, for the extraction of aluminium from its ores and for the production of adiponitrile, all of which still represent the core uses of electrochemistry in industry.

Before going any further, it is important to consider the principles of an electrolytic cell: the simplest cell is made of two electrodes submerged in a conducting electrolyte and connected externally to a power supply. As a whole, the cell is electrically neutral and the total rate of electron gain at the cathode is equal to the rate of electron loss at the anode. Electrical conduction takes place via transport of cations and anions in the electrolyte and the movement of electrons in the external circuit. Current is driven through the circuit by the external power supply.

Expressions for the important parameters of reactor duty, cell voltage and space time yield can be summarised as follows :

The overall rate of an electrochemical reaction can be expressed in terms of the current I. If the reaction is under complete mass transport control, the maximum production rate of a reactor can be expressed via the limiting current I_l, i.e.

$$I_l = k_m AzFc \qquad (1.3)$$

where k_m is the averaged value of mass transport coefficient, A is the electrode area, z the number of electrons involved in the reaction, F is the Faraday constant and c is the bulk concentration of the reactant. For a fixed concentration, it is important to have a high value of both electrode area and mass transport in order to achieve a high production rate in a compact reactor design.

As for the electrolytic power consumption, it depends on the cell voltage which, in turn, depends on several components, i.e.

$$E_{cell} = E_{rev} + \sum|\eta| + \sum IR \qquad (1.4)$$

where E_{rev} is the reversible cell potential determined from thermodynamics (Nernst equation), $\sum|\eta|$ is the sum of overpotentials at the electrodes and $\sum IR$ the ohmic potential drops in the electrical circuit (including electrolyte and membrane).

The space time yield of an electrochemical reactor, i.e. the number of moles of product per unit reactor volume per unit time is defined as follows:

$$\rho_{st} = \frac{1}{V_R}\frac{dn}{dt} = \frac{I}{zFV_R} \qquad (1.5)$$

where V_R is the overall reactor volume, n is the number of moles of material, dn/dt is the rate of production of the material and t is the time. In order to increase the space time yield it is therefore important to achieve a high current efficiency and to operate at high current densities.

1.3 Electrocatalysis

To minimise power consumption it is important to minimise each loss component by choosing a suitable reaction, electrocatalytic electrodes, conductive cell components, small inter-electrode gap and an adequate membrane, i.e. one that fulfils permeability requirements and makes a small ohmic contribution.

As mentioned in section 1.1, the basic method for chlorine production has not changed since the late 1890s. However, major improvements in efficiency were obtained by improving the design of electrolytic reactors and their individual components.

Consider a two step reaction with adsorbed intermediate, i.e. electrocatalysis of hydrogen, oxygen or chlorine. It was discovered that the nature of the electrode material had a great influence on the efficiency of electrocatalysis. In the case of chlorine electrocatalysis, while a variation of anode material to increase the free energy of adsorption will favour the formation of the chlorine intermediate, it will have the opposite effect for the desorption step if one considers the overall reaction. It is therefore expected that the maximum rate of chlorine production will occur at intermediate values of the Gibbs free energy of adsorption. The dependence of adsorption on electrode material is illustrated for the case of hydrogen in figure 1.1 below where the exchange current is plotted as a function of the adsorbate/surface bond energy for different materials.

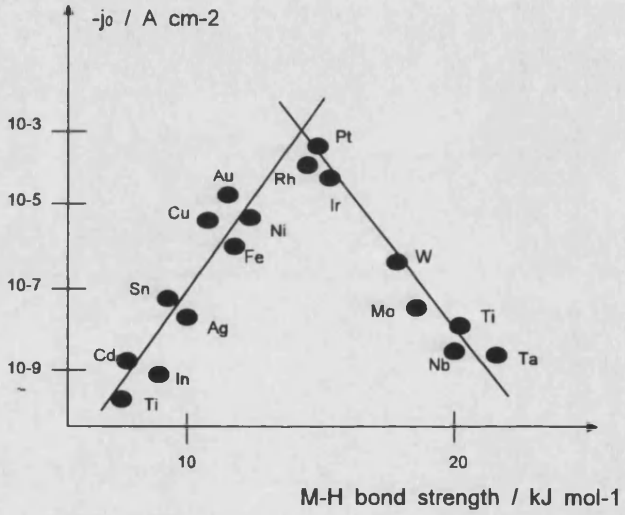

Figure 1.1 : Dependence of the exchange current density for the hydrogen reaction on the strength of the metal-hydrogen bond.

Figure 1.1 indicates that materials such as platinum, iridium and ruthenium would be ideal as catalytic materials for the hydrogen evolution reaction (HER). Although platinum seems to be the best material it is too expensive to be used for large area electrocatalysis. As a result, other cheaper materials have been selected as catalytic materials for hydrogen production.

Compared to the electrocatalysis of hydrogen, chlorine production occurs under strongly oxidising conditions. As a result, stability of the metal with respect to oxidation, i.e. corrosion, becomes an influential factor in the choice for a catalyst

material. Most of the metals in figure 1.1 would not be suitable for chlorine evolution because of this. As a result, the anode must either be a noble metal or have a material which has a very stable oxide which still permits electron transfer. Mechanistic studies have revealed that mixed oxides of ruthenium and titanium, i.e. RuO_2/TiO_2 materials, are good catalysts for the production of chlorine as they exhibit very good electrocatalytic performance, good resistance to corrosion and are cheap to manufacture. It must noted that the choice of materials investigated has been semi-empirical as the role of each component is still not well understood (explaining the role and importance of each component was of one the aims of this project).

Presently, industrially active electrocatalysts are mainly based on mixed oxides of RuO_2 and IrO_2 but preliminary research has shown that spinels of Co_3O_4, $NiCo_2O_4$[1] and MnO_2[2] could be used to replace the precious metals for the electrocatalysis of chlorine or oxygen. Although this field of research is of general interest, most of it is sponsored by industry and, as result, it is very hard to know what efforts and discoveries have been made. It is also important to remember that this is a very competitive area and since the focus has always been a financial one, i.e. the return on investments, technology is still mainly based on mixed oxides of RuO_2 and IrO_2.

Because of the nonideality of these mixed oxide materials, most theoretical information has been obtained from studies performed on platinum and mixed oxide electrodes prepared in the laboratory which are simpler to study : platinum offers the advantages of having well defined crystallographic planes, homogeneous composition and a smooth surface. On the contrary, it has been well established that mixed oxides are multiphase materials[3,4], highly heterogeneous and have roughness coefficients in the order of hundreds[5,6].

An impressive range of physical techniques has been used to characterise mixed oxide electrodes. Summarised below is a list of techniques used to investigate various aspects of these materials:

Thermal decomposition	TGA, DTA
Lattice structure Crystallinity Crystallite size	X-ray diffraction

Surface area	BET, ion adsorption
Electronic structure	Electrical conductivity
Chemical composition (bulk, surface, profile)	RBS, AES, XPS, SIMS, TDS
	Tritium exchange
Hydration	Immersion heat
	Nuclear techniques
Acid-base properties	Potentiometric titration
Point of zero charge	Electrophoretic mobility
Surface charge	

Likewise, a broad spectrum of electrochemical techniques has been used to study the kinetics and electrocatalytic performance of these materials. These include cyclic voltammetry[7,8,9,10,11,12,13], Tafel plot measurements[5,14,15,16,17,18,19,20,21], a.c. impedance spectroscopy[13,1422,23,24,25,26], rotating disk experiments[7,8], chronocoulometry and open circuit potential decay[5,14,22,23,24,25,27,28,29,30,31]. Unfortunately, spectroscopic techniques such as FTIR, IR, UV-UHV cannot be used since these surfaces are either non-transparent or too rough for external reflectance measurements to be carried out.

With such an extensive study of the properties of catalytic surfaces and the electrochemistry taking place at their interface, one would expect this area of chemistry to be well understood. This is not the case. The main reason for this is that most work published in literature concentrates either on material characterisation or interfacial studies. In order to get a complete picture of electrocatalysis, one must correlate surface properties to interfacial chemistry and reaction kinetics. Once again, it is the industrial nature of this area of chemistry that has inhibited this approach so far. Commercial interests and confidentiality reasons limit the information disseminated.

Another major reason for the lack of theoretical understanding of chlorine generation is the fact that most of the work published has been carried out in

conditions irrelevant to industrial operating conditions. Mechanistic information has been mostly obtained on ideal surfaces such as platinum [13,14,37] at low current densities (i.e. in the region of 0-20 mA cm^{-2}).

Problems such as surface roughness, heterogeneous composition, oxidation states of mixed oxides, bubble nucleation, electrolyte composition and pH, extremely high current densities (up to 1 A cm^{-2}), current and potential distribution along the catalyst electrode surfaces have not been studied in great detail. This clearly represents a major challenge in terms of reproducing industrial conditions in the laboratory and the published literature seems to reflect an unwillingness to study the formation of chlorine under these conditions.

There is an inadequate understanding of the processes responsible for the loss of electrocatalytic activity of commercial electrodes. Work has been carried out on freshly prepared electrodes and fully worn electrodes. Although the state of fully 'worn' electrodes is well established and significantly characterised, the problem is that these electrodes can no longer be considered as catalyst electrodes. This is because the composition and morphology of these electrodes have changed dramatically. Since, in practice, loss of electrocatalytic performance is a gradual process, it is not known what factors are responsible for the early stages of the degradation process.

1.4 Reactor design

According to equation 1.4, the total cell voltage can also be optimised if the sum of the ohmic contributions is minimised. This area was an important field of research that has lead to the development of different cell geometries and technologies. Since this has been covered in detail elsewhere[32], only a brief description of some of the important factors will be given in this sections.

Of all the types of electrochemical reactor designs, the parallel plate geometry is the most common choice for laboratory and industrial applications as it is the most straightforward design. The following figure shows a typical design of such a parallel plate electrochemical reactor :

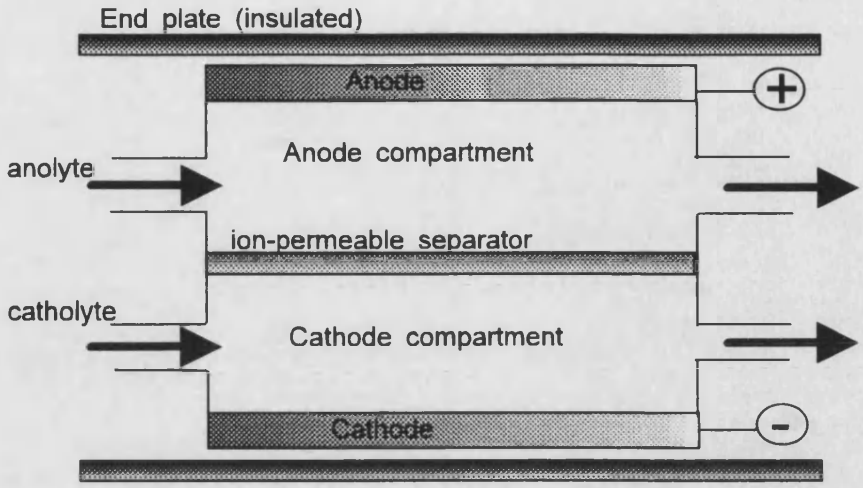

Figure 1.2 : typical parallel plate cell design

The advantages of this design are as follows[33]:

- Ease of construction, assembly and disassembly
- Wide choice of electrodes and membrane materials
- Uniform current and potential distribution over 90 % of electrode surfaces
- Mass transport rates may be well controlled and enhanced by turbulence promoters
- Scale-up is straightforward

Over the years, different variants of the same design have been developed depending on the intended use of the reactor.

The anodes used in this project are derived from the FM21 electrolytic cell developed by ICI and launched in the chlor-alkali market in 1981. These cell have a monopolar design with a nominal single electrode area of 21 dm^2. A series of anode and cathode sub-assemblies, interspersed when necessary with ion exchange membrane is supported on two slide rails and compressed by six tie-rods. The electrode assemblies are sandwiched between two polymer-lined steel end plates, one fixed and the other floating. The reactor is sealed by a moulded gasket system which is an integral part of each electrode and the electrolyte is internally manifolded. A number of electrode configurations is possible, including flat plates, lantern blades and expanded meshes. As for material selection, this depends very much on process conditions. Electrode materials include titanium, copper, lead, nickel, niobium, zirconium, stainless

steels and speciality alloys. Anode coatings of precious metals, or their oxides, on titanium are commonly used.

1.5 Energy and environmental considerations

A few facts and figures help to put the chlor-alkali industry into perspective with respect to the chemical industry. The overall reaction, i.e.

$$2\ NaCl + 2\ H_2O \longrightarrow Cl_2 + 2\ NaOH + H_2 \qquad (1.6)$$

produces both chlorine and sodium hydroxide. Depending upon the economy at the time, it is either the chlorine which is in demand and the caustic soda considered as the by-product or vice-versa, i.e. chlorine and caustic soda are defined as by-products of the material which is in most demand and therefore most expensive. This is illustrated in the figure 1.3 below :

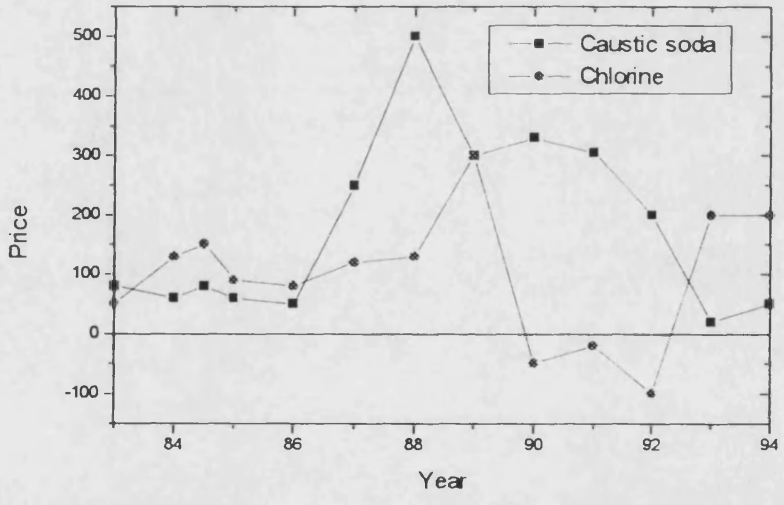

Figure 1.3 : variation of the price of chlorine and caustic soda from 1984 to 1994. A negative price means that the product is considered as waste and is unwanted at the time.

In terms of importance, this is an industry that employs 500 000 people world-wide and that is relied upon by 50 % of the chemical industry[34]. This is because of the very high usage of chlorine or chlorine derivatives in areas such as pharmaceuticals, plastics, disinfectants and for many intermediates. Furthermore, it is considered that 80 % of infectious diseases are waterborne and that 25000 people die every day from non

disinfected water. So the chlorine industry is vital to our society as well as our economy. In spite of this, production of chlorine has decreased steadily since the early eighties because of economical and, increasingly, environmental issues. Nevertheless, in 1994 the total production of chlorine was still 45 million tonnes.

Various technologies have been developed throughout the years. Basically, there are three technologies based on mercury, diaphragm and membrane cells.

In a mercury cell, the electrode reactions are

$$2\,Cl^- - 2\,e^- \longrightarrow Cl_2 \qquad (1.7)$$

$$Na^+ + Hg + e^- \longrightarrow NaHg \qquad (1.8)$$

and the sodium amalgam is hydrolysed :

$$2\,NaHg + 2\,H_2O \longrightarrow H_2 + 2\,Na^+ + 2\,OH^- + 2\,Hg \qquad (1.9)$$

in the presence of a catalyst in a separator know as the denuder.

A diaphragm cell has a separator based on asbestos with various polymers added to improve its performance. The advantage of this technology is that chlorine and sodium hydroxide are produced directly, i.e.

$$2\,Cl^- - 2\,e^- \longrightarrow Cl_2 \qquad (1.10)$$

$$2\,H_2O + 2\,e^- \longrightarrow H_2 + 2\,OH^- \qquad (1.11)$$

However, the use of an asbestos has several problems associated with it :

1. it is a purely physical barrier, i.e. all ions can travel across it and this leads to contamination of the chlorine and sodium hydroxide concentration limitations.
2. it produces a significant iR drop contribution. Furthermore, this increases in time due the deposition of calcium and magnesium hydroxides in the pores. The only way to minimise this effect is to use ultra-pure brine which leads to significant operating costs
3. the asbestos does not last indefinitely, i.e. the diaphragm must be replaced every few months and the cell design must permit washing-off of old asbestos and replacement.

The difference between diaphragm and membrane technology is that the separator used in membrane cells is cation-permeable. This improvement only dates from the 1970s when it was realised that perfluorinated polymer membranes also had properties essential to the chemistry of a chlor-alkali cell. The main advantage is that the iR drop contribution is very low in comparison with the asbestos separator. It also allows the inter-electrode gap to be much smaller.

At present, 35 % of chlorine is produced via the old mercury cell process, 43 % by diaphragm cells and 20 % by ion-selective membrane technology. The remaining 2 % are produced via HCl electrolysis. Since the membrane technology consumes less energy overall, more and more chlorine is produced this way and the two other technologies are gradually being phased out.

Environmental considerations are becoming increasingly important. Not only is the technology used to produce chlorine being questioned but so is the use of chlorinated products. The lack of public understanding of the chlor-alkali industry and the change in its public image present new challenges. Environmental pollution is branded as a strong argument against the production of chlorine. Mercury emissions, pulp bleaching, CFCs and PVC products are all being attacked as strong environmental pollutants. The high energy consumption is also important in view of the high usage for chlorine production. For instance, ICI's production of chlorine is responsible for 1% of the total electricity consumption in England. In view of these challenges and the competition of new products as in the case for CFCs, there is renewed interest in this field and a moderate effort in the design of new manufacturing processes or improvements of existing technologies (another aim of this project). The next figure shows a comparison in between the energy consumption of all the different cell technologies :

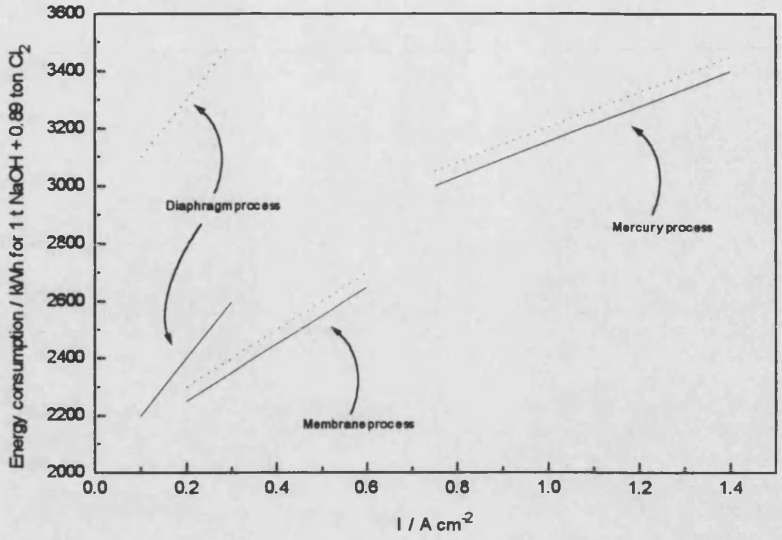

Figure 1.4 : comparison of the energy of consumption for the mercury, diaphragm and membrane technologies. The full lines represent electrolysis only; the broken lines, total energy consumption, including evaporation and heating of electrolyte.

Figure 1.4 clearly shows that the energy saving when improving the technology from the mercury cells to the two other types is significant. It also shows that although the energy efficiency for the diaphragm process is good, the current density range is much lower than for the membrane process. If one is interested in rate of production as well as efficiency, the membrane process is therefore better than the diaphragm one. This clearly demonstrates the importance of the factors that determine the *total* cell voltage and power consumption.

1.6 The mechanism of chlorine generation

The development of the more refined membrane cell technology has led to renewed interest in the field of chlorine electrocatalysis. Much of the research has been carried out in industry and results are generally not accessible. In terms of reaction mechanism, there is still some controversy about the individual reaction steps responsible for the production of chlorine. The generally accepted mechanism is that chlorine production takes place by the same mechanism as the hydrogen electrode

reaction[35,36,37]: i.e. firstly a chlorine ion is discharged at the surface then formation of chlorine occurs either by electrochemical recombination or via reaction with another chlorine ion in solution:

$$Cl^- + M \rightleftharpoons Cl_{ads}\text{-}M + e^- \qquad \text{step 1} \qquad (1.12)$$

$$Cl_{ads}\text{-}M + Cl^- \rightleftharpoons Cl_2 + M + e^- \qquad \text{step 2} \qquad (1.13)$$

OR

$$2\ Cl_{ads}\text{-}M \rightleftharpoons Cl_2 + 2\ M \qquad \text{step 3} \qquad (1.14)$$

Other reaction steps have been suggested for step 2, such as that proposed by Krishtalik[38]:

$$M\text{-}Cl_{ads} \longrightarrow M\text{-}Cl^+ + e^- \qquad (1.15)$$

followed by a rapid step

$$M\text{-}Cl^+ + Cl^- \longrightarrow Cl_2 + M \qquad (1.16)$$

This mechanism is based on the assumption that the chloronium ion, Cl^+, could as an adsorption species. However, the oxidation of a very electronegative element to an onium-type ion is highly unlikely[39]. Instead, one could consider that OCl^- would be the intermediate from adsorption of Cl^- ,i.e.

$$Cl_{ads} + H_2O \longrightarrow OCl^- + 2\ H^+ + e^- \qquad (1.17)$$

from which Cl_2 can be formed.

Nevertheless, step 2 and 3 appear to be the most likely and are considered in the majority of mechanistic studies on ideal electrodes or from studies at low current densities. At present, it is believed that the reaction mechanism depends on the nature of the electrocatalytic surface as well as the method used to produce it. For instance, it is reported that there is no unique mechanism established for the production of chlorine at mixed oxide electrodes such as RuO_2/TiO_2; the preparation method determines whether step 2 or 3 is involved[40].

1.7 Aim of the project

The aim of this project was to tackle mechanistic and ageing issues using a commercial mixed oxide coating of RuO_2/TiO_2 on a titanium substrate. The generation of chlorine was reproduced under industrially relevant conditions in an attempt to derive a reaction mechanism that is relevant to the industrial process. Once this was achieved, the ageing of electrodes was studied using an 'accelerated wear test' in order to determine the factor(s) responsible for the loss of electrocatalytic performance of commercial chlorine catalyst electrodes. The experimental apparatus was constructed and subsequently modified to be able to cope with the following conditions :

- Operating temperature of 60°C
- High rate of chlorine evolution
- Current densities up to 1.5 A cm^{-2}

In order to study the ageing process of commercial anodes, electrodes were degraded artificially according to a procedure developed by ICI and improved upon in our laboratory in order to obtain greater control of degradation conditions.

An important aspect of this project was to establish a true collaboration with industry so that a better picture of chlorine evolution and loss of electrocatalytic performance could be obtained under industrially relevant conditions. This was achieved by correlating the physical and interfacial properties of the same electrodes. It appears that such a comprehensive approach has never been carried out before.

1 V.V. Shalaginov, D.M. Shub, N.V. Kozlova, V.N Lomova, *Elektrokhimiya*, 19, 537, 1989

2 E.A. Kalinovskii, E.M. Shembel, V.V. Stender, *Elektrokhimiya*, 8, 810-815, 1972

3 S. Trasatti, J.F.C. Boodts, *J. Electrochem. Soc.*, 137(12), 3784-3789, 1990

4 S. Trasatti, Lj. Atanasoska, R. Atanasoski, *Vacuum*, 40(1-2), 91-94, 1990

5 B.E. Conway, L. Bai, L. Gao, *J.Chem. Faraday Trans.*, 89(2), 235-242, 1993

6 B.E. Conway, L. Bai, L. Gao, *J.Chem. Faraday Trans.*, 89(2), 243-249, 1993

7 B.E. Conway, D.M. Novak, *J. Electroanal. Chem.*, 99, 133-256, 1979

8 B.E. Conway, D.M. Novak, *J. Chem. Soc. Faraday Trans.*, 1(77), 2431-2359, 1981

9 B.E. Conway, J. Mozota, *J. Electrochem. Soc.*, 128(10), 2142-2149, 1981

10 S. Trasatti, C. Angelinetta, Lj. D. Atanasoska, Z.S. Minevski, R.T. Atanasoski, *Mater. Chem. And Phys.*, 22, 231-247, 1989

11 S. Ardizzone, M. Falciola, S. Trasatti, *J. Electrochem. Soc.*, 136(5), 1545-4, 1989

12 S. Ardizzone, G. Fregonara, S. Trasatti, *Electrochimica Acta*, 35(1), 263-267, 1990

13 H. Vogt, *Electrochim. Acta*, 39(13), 1981-1983, 1994

14 L.J. Janssen , G.J. Vissier, E. Barendrecht, *Electrochimica Acta*, 22, 1093-7, 1977

15 B.V.Tilak, B.E. Conway, *Electrochimica Acta*, 21, 745-752, 1976

16 B.V.Tilak, B.E. Conway, *Electrochimica Acta*, 22, 1167-1178, 1977

17 B.E. Conway, L. Bai, D.F. Tessier, *J. Electroanal. Chem.*, 161, 39-49, 1984

18 B.E. Conway, A. Damjanovic, D.B. Sepa, *Ber. Bunsenges. Phys. Chem.*, 93, 510-513, 1989

19 B.E. Conway, G. Ping, *J. Chem. Soc. Faraday Trans.*, 86(6), 923-930, 1990

20 B.V. Tilak, B.E. Conway, *Electrochimica Acta*, 37(1), 51-61, 1992

21 B.V. Tilak, *J. Electrochem. Soc.*, 136(7), 1977-1982, 1989

22 B.E. Conway, G. Ping, *J. Chem. Faraday Trans*, 87(17), 2705-2714, 1991

23 B.E. Conway, L. Bai, *J. Electrochem. Soc.*, 138(10), 2897-2907, 1991

[24] R. De Levie, *Advances in Electrochemistry and Electrochemical Engineering*, ed. P. Delahay, Interscience, New York, 1964, vol. 6

[25] A.S. Viner, P.S Fedkiw, *J. Electrochem. Soc.*, 137(5), 1435-1444, 1990

[26] J. Jacquelin, *Electrochimica Acta*, 39(18), 2673-2684, 1994

[27] G.H. Kelsall, *Techniques in Electrochemistry, Corrosion and Metal Finishing- A Handbook*, ed. A.T. Kuhn, Wiley & Sons ltd., 7594, 1987

[28] L.J.J. Janssen, *Electrochimica Acta*, 25, 641-649, 1980

[29] B.E. Conway, P.L. Bourgault, *Can. J. Chem.*, 37, 292-307, 1959

[30] B.E. Conway, S. Hadzi-Jordanov, *J. Electroanal. Chem.*, 326, 177-195, 1992

[31] B.E. Conway, P. Gu, L. Bai, L. Gao, R. Brousseau, *Electrochimica Acta*, 37(12), 2145-2154, 1992

[32] D. Pletcher, F. Walsh, *Industrial electrochemistry*- 2nd ed., Blackie A&P, 1993

[33] F. Walsh, D. Robinson, *Chemical Technology*, 2(3), 16-23,1995

[34] D.M. Nott, *Modern Chlor-Alakli Technology*, 6, 13-20,1994

[35] B.E. Conway, L. Bai, D.F. Tessier, *J. Electroanal. Chem.*, 161, 39-49, 1984

[36] D.A. Harrington, B.E. Conway, *J. Electroanal. Chem.*, 221, 1-21,1987

[37] T. Yokoyama, M. Enyo, *Electrochimica Acta*, 24, 997-1004, 1979

[38] L. Krishtalik, G.E. Titova, *Elektrohimiya*, 4, 285-290, 1968

[39] B.E. Conway, G. Ping, A. De Battisti, A. Barbieri, G. Battaglin, *J. Mater. Chem.*, 1(5), 725-734, 1991

[40] S. Trasatti, *Electrochimica Acta*, 36(2), 225-241,1991

CHAPTER TWO

Chapter Two

Experimental Conditions

This section covers all experimental aspects apart from the flow cells and reference electrodes that were used in this project. The latter will be discussed in a separate chapter as they constitute a major part of the work carried out during this project.

2.1 Electrolyte preparation

Two types of electrolytes were used throughout this project, one for the accelerated degradation of anodes and one for the electrochemical characterisation.

As mentioned in chapter 1, the aim of the project was to study the evolution of chlorine in industrially relevant conditions. This section covers preparation procedures for the characterisation and degradation electrolyte.

Initially a 5 mol dm^{-3} NaCl solution was used for electrochemical characterisation. This was made up from analytical grade sodium chloride (Aldrich) and ultrapure water (Millipore). 1461 g of NaCl were dissolved in 5 litres of millipore water. However, the pH of the electrolyte was found to change appreciably over the duration of experiments, especially when using the flow cell.

During current flow, hydrogen is evolved at the cathode. This removes protons and makes the solution more basic. However, the chlorine evolved also reacts with solution species to form hydrochloric acid and water :

$$2\,H_2O + 2\,e^- \longrightarrow H_2 + 2\,OH^- \qquad (a) \qquad (2.1)$$

$$H_2O + Cl_2 \rightleftharpoons HOCl + HCl \qquad (b) \qquad (2.2)$$

Reaction (a) causes the pH to increase but (b) minimises the effect of (a) on the pH by preventing it from being solely dominated by hydrogen evolution. However the buffering effect of (b) is insufficient to prevent an increase in electrolyte pH during prolonged operation of the cell. Hydrochloric acid was therefore added to the solution in order to minimise changes brought about by hydrogen evolution at the cathode. This

approach set a lower initial pH and was preferred to using a buffer which would have introduced other species into the solution. 1461 g of NaCl were dissolved in 5 litres of millipore water. 2.162 ml of analytical grade conc. HCl (11.3 mol dm^{-3}, Aldrich) were then added in order to bring the pH down to a value of 2. Solution of this composition was used for the remainder of the project.

The alkali wear test used to simulate anode lifetime involved accelerating the degradation of anodes in a strong alkali environment. The electrolyte composition was also chosen to eliminate chlorine evolution and promote oxygen evolution. Two alkali wear test electrolytes were used during this project. Initially, a 20% NaCl-20% NaOH in water (by percentage weight per volume of water) solution was used. However, it proved impossible to dissolve all the sodium hydroxide at room temperature. Heating would have introduced too many safety and experimental difficulties so that another composition that allowed solution preparation at room temperature was used. The amount of sodium hydroxide was reduced and a 20% NaCl-15% NaOH was used instead. 1000 g of NaCl and 750 g of NaOH were dissolved in 5 litres of millipore water. The solution was stirred for 2 hours in order to ensure complete dissolution.

2.2 Electrode preparation

Two types of electrode masking were developed during the course of this project. In both cases titanium rods, nuts and clamps were provided by ICI as anode holders. The rods were 20 cm long and 0.6 cm wide. In the case of the degradation experiment the only major concern was to protect the titanium holders from dissolution in the alkali solution. PTFE tape was wrapped around the holders and the clamped area of the anode.

After much development work, Apiezon N-100® wax was chosen as a masking agent for the electrochemical characterisation experiments. The anodes were first mounted and clamped onto the titanium holders. A soldering iron with a conventional tip was then heated up to operating temperature in order to carefully melt wax in small amounts onto the anodes. The side with no engraved number was always completely covered using this procedure as it was decided to restrict characterisation to the engraved side. A square area (typically 0.8 cm^2) towards the end opposite to the engraved number was carefully left non-masked on the engraved side. This was the

working area. All other parts of the anodes were waxed, and special care was taken to mask the edges. The top part of the anode (where the electrode was clamped) was completely covered with wax in order to prevent leakage.

2.3 The alkali wear control system

Under normal industrial operating conditions, anodes are used to produce chlorine for long periods of time. Since loss of performance is extremely slow under these conditions, an alkali wear test has been designed in order to artificially accelerate the degradation of anodes.

The alkali wear control setup was designed at Southampton University following a detailed analysis of safety aspects. Since it was intended to study the loss of electrode activity over a wide range of degradation times, the system was built to provide great control of operating conditions. During degradation, the critical factors were solution temperature, running potential, current density and solution composition.

Since previous work has suggested that the increase in running potential was the predominant factor in electrode performance, a control unit was built in order to monitor changes in total cell voltage and stop degradation once a set running potential limit was reached.

The operating conditions for the alkali wear test were as follows :

Temperature : A PTFE coated heater was utilised to heat the alkali solution up to 65°C. A platinum resistance thermometer was glued inside a hollow titanium rod and immersed in the solution in order to control the temperature. A sensor based on a negative temperature coefficient thermistor was added as a safety overridefeature to trigger shutdown in case the temperature control system failed.

Current density : A current density of 1 A cm^{-2} per electrode was used. Initially, four electrodes were degraded simultaneously. A current divider was

provided by ICI in order to set accurately the required current density for each electrode. Finally, only one electrode was degraded at a time at 2 A cm^{-2}.

Electrolyte : Evaporation was a problem when running the alkali wear test at 65°C. In order to minimise solution composition changes due to evaporation, a liquid level sensor was mounted in the wear pot. As soon as the level dropped below a certain level, the control unit started a peristaltic pump which added millipore water to adjust the water level.

Potential : The potential difference between one electrode and the nickel cathode was measured continuously in the setup. A voltage sensor was used to set a maximum limit so that the control unit 'tripped' and stopped degradation once that limit was reached.

A Rustrak data logger was used to record the variation of potential of all electrodes with time in order to obtain a degradation 'fingerprint' of each anode. It allowed simultaneous recording of up to 4 channels over a period of up to 100 days. Its voltage range was modified to read from 0 to 20 volts, giving a resolution of 10 mV. Usually it was set to record for up to 5 days in order to get maximum time resolution as it recorded data as a logarithmic function of time : this ensured full use of the maximum 70 Kilobytes of memory space as well as recording short and long times with great precision. Once an experiment was finished, the data was transferred to PC using a serial data transfer cable. Data analysis of length of degradation, maximum/minimum determination and charge integration was carried using a software package called PRONTO®. Further analysis was performed by importing the ASCII files into SIGMA PLOT®.

In terms of equipment the alkali wear pot consisted of :

- a 4 x 2 amp/channel current divider (provided by ICI)
- a power supply : 70 Volts-10 Amps (Farnell TSV70 MK.2)
- a PTFE coated heater :110 Volts - 160 W
- a 240 Volt - 110 Volt transformer

- a PT100 platinum resistance thermometer (RS) : -50 to 150°C
- a regulatory temperature coefficient thermistor
- 3 liquid level switches (RS)
- a 12 V dc peristaltic pump (RS)
- a 'Whisper 500' fish tank air pump (5 l/min maximum flow)
- a 'Whisper 800' fish tank pump (8 l/min maximum flow)
- 1 Model 100 air Flo-sensor (McMillan)
- a Home built control unit
- a 'Rustrack' Data logger
- a 4 litre polypropylene pot
- a 'Perspex' cover
- 3 litre glass beaker
- 3 water cooled condensers
- 1 liquid flow detector (Aldrich)
- 200 ml round bottom flask
- 2 dreschel bottles
- 5 metres of silicone rubber tubing

Titanium rods (20 cm x 0.6 cm diameter), covered with PTFE tape, were used as anode holders and a nickel mesh (15 cm diameter) was used as a cathode.

2.4 Safety analysis of alkali wear system

A detailed safety analysis was made of the alkali wear test system. Not only does this system contain highly basic electrolyte at 65°C but the reaction taking place can produce an explosive mixture of oxygen and hydrogen in the head space. In order to prevent the build-up of an explosive mixture, two air pumps were used to flush the head space with air.

At a current of 12 A, the number of moles of hydrogen produced per minute is $N(H_2) = 60*(12/2*F)$. At 65°C, V_M = 25.5 l that means that 9.52 10^{-2} l/min are produced.

It was decided that a dilution factor of 100/1 would be adequate in order to prevent an explosion. As a result, 2 fish tank air pumps with a theoretical total flow of 13 l/min were used. The high flow rate was chosen in case leaks reduced the flow rate.

A flow sensor was connected to the gas output in order to monitor the flow rate. If the flow rate decreased below a critical limit (5 l/min) either because of leakage or pump malfunction, then the control unit shut down the degradation and triggered an audio-visual alarm.

Loss of the basic electrolyte as spray was also identified as a safety problem. Analysis of condensed vapour revealed a pH greater than 11. In order to minimise this effect, 3 water cooled condensers were used to condense the evacuation gases. Two condensers were placed on top of the alkali wear pot cover so that condensed vapour was returned to solution. A third condenser connected to a round bottom flask was used on the exit in order to trap vapour that passed the other condensers.

This arrangement was found to be very satisfactory and over a ten day running period only 150 - 200 ml of condensate was collected in the flask. Analysis of the gas output revealed that there was still a small amount of vapour and spray coming through. A pH paper placed at the output revealed a pH = 11 mixture coming through. A glass bottle filled with glass beads and concentrated hydrochloric acid was connected to the exhaust in order to neutralise the traces of basic spray. This method of prevention was found to be effective.

As mentioned previously, a liquid level switch was used to keep the electrolyte level constant. As an additional safety feature, a liquid level switch was placed inside the millipore water reservoir to detect loss of liquid. Under these conditions the control unit was designed to shut down the degradation experiment.

Spillage was also considered, and two safety measure were taken to deal with such a hazard. Firstly, the alkali wear pot was placed inside a plastic safety bucket (usually used to carry winchesters of organic solution). Secondly, the bucket was placed in a plastic tray. Finally, the whole setup was placed inside a metal box to restrict access and to prevent splashes in case of rupture of the wear pot.

The fail-safe electronic control unit was designed in order to monitor and check for safe running of the degradation experiment, especially since it was intended to

operate for periods of up to 80 hours without supervision. In summary, 5 conditions were programmed to trigger experiment shutdown :

1. Water reservoir low level
2. Low level of electrolyte inside pot
3. Voltage excess
4. Air flow malfunction
5. Excess temperature

The experimental set up for the alkali wear test is shown in the following diagram.

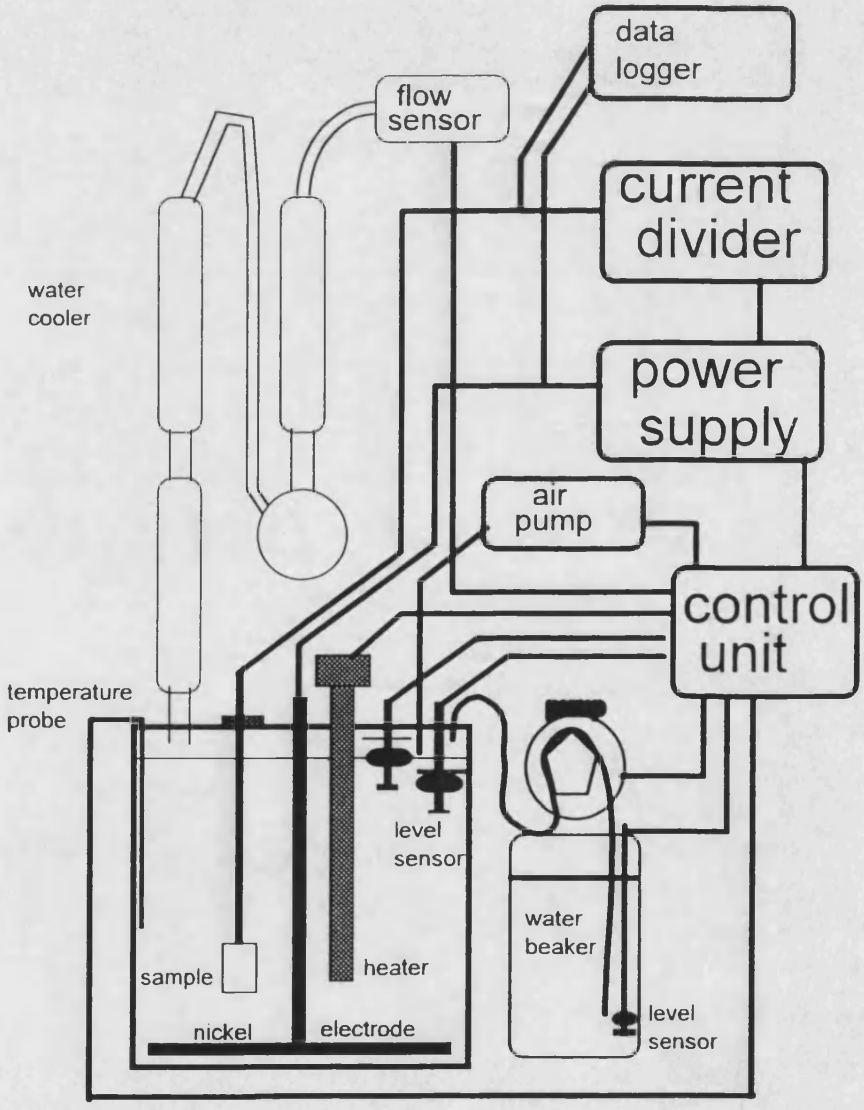

Figure 2.1 : diagram of alkali wear pot setup.

2.5 Characterisation techniques

2.5.1 Cyclic voltammetry

Cyclic voltammetry was used for two purposes. The first was to check whether the anodes were properly masked and that no leakage took place underneath the masking. Secondly, it was employed to calculate the value of the double layer capacitance by recording voltammograms in the 'double layer' region.

The experimental setup consisted of a home-built potentiostat, a waveform generator (Hi-Tek PPR1), a storage oscilloscope (ITT instrument, OX 7520) and an X-Y plotter (HP 7475A). The reference electrode was a saturated calomel electrode (SCE), the counter electrode consisted of 4 RuO_2/TiO_2 electrodes and the 5 mol dm^{-3} NaCl in 10^{-2} mol dm^{-3} HCl was used as electrolyte. The sweep rate used was 100 mV/s and the potential was swept from 0 to 350 mV.

2.5.2 Impedance spectroscopy

A frequency response analyser (Solartron 1250) and a potentiostat (Solartron 1286 electrochemical interface) were used in combination with a software package (ZPLOT and ZVIEW) in order to carry out impedance spectroscopy. Experiments were performed both in the double layer and chlorine evolution regions.

Double layer region

Counter electrode :	4 Strips of RuO_2/TiO_2 (120 cm^2 approximately)
Reference electrode:	saturated calomel electrode
Electrolyte :	5 mol dm^{-3} NaCl in 10^{-2} mol dm^{-3} HCl
Settings :	Potentiostatic control
	DC potential = 0 V
	10 mV AC amplitude
	Frequency range 10 mHz - 10 kHz
	Integration time : 3 cycles
	3 Electrode mode

Chlorine evolution region

Counter electrode :	4 Strips of RuO_2/TiO_2
Reference electrode:	Platinum gauze (0.8 cm^2 geometric area) bubbled with chlorine
Electrolyte :	Chlorine saturated 5 mol dm^{-3} NaCl in 10^{-2} mol dm^{-3} HCl
Settings :	Galvanostatic control Current 10 mA cm^{-2} - 900 mA cm^{-2} 10 - 40 mA AC amplitude Frequency range 10 mHz - 2 kHz Integration time : 3 cycles 3 Electrode mode

2.5.3 Current interrupt techniques

This section covers experimental details for Tafel, open circuit potential decay (OCPD) and close circuit potential rise (CCPR) setups. The instrumentation required was identical for all three types of experiments and, after some development work, was as follows:

- a Thurlby 30 Volts - 1 Amp power supply (RS) modified to be computer controlled
- a home-built unit containing a mercury wetted switch (RS, SPNO form A)
- a very fast OP Amp voltage follower (home-built)
- a storage oscilloscope (OX 7050 ITT instruments)
- a computer fitted with an Analogue to Digital Converter (RISC Archimedes 410/1)
- Acquisition software (written in RISC BASIC and compiled using RiscBasic compiler Version 3)
- a home-built current divider (CCPR experiment only)

Printouts of all the programs as well as technical details about OP Amp and home built equipment can be found in the appendix.

In all experiments, the electrolyte utilised was chlorine saturated 5 mol dm^{-3} NaCl+10^{-2} mol dm^{-3} HCl and a platinum gauze bubbled with chlorine was used as

reference electrode. The power supply was set to operate in constant current mode. In constant potential mode, it was found to be difficult to establish a set current as there were significant fluctuations due to chlorine bubble generation.

The following diagram shows the arrangement for the current interrupt experiments.

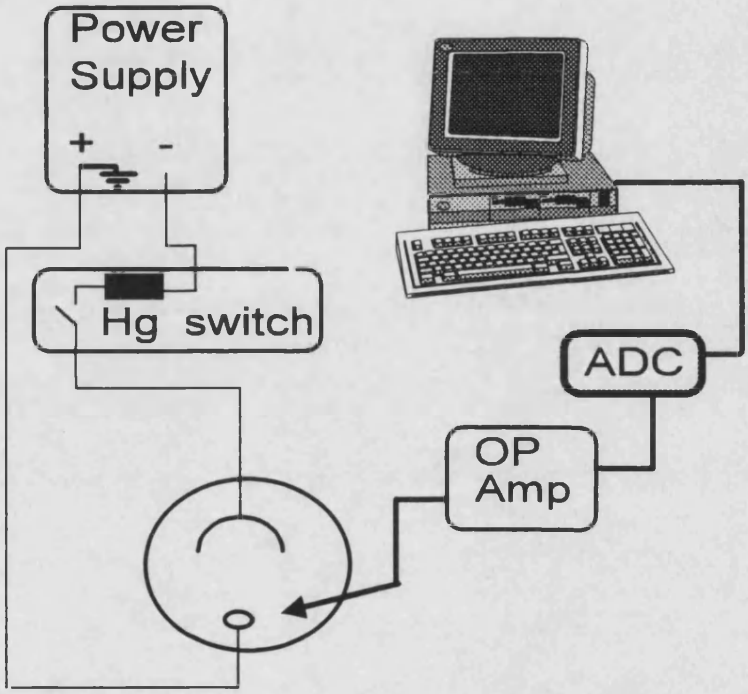

Figure 2.2 : Electronic circuitry for interrupt techniques.

The working electrode is connected to ground to allow a single ended amplifier to be used to monitor the overpotential.

2.5.4 Potential-time or 'Noise' measurements

Noise measurements were carried out in order to obtain information about bubble generation. They were also utilised as a way of obtaining steady state plots of reference vs working electrode potential : the ASCII files were imported into SIGMA PLOT and a routine was created to calculate the average value of the overpotential at each current density measured.

The instrument used and experimental setup were identical to the Tafel and OCPD experiments. A program was written to acquire 4096 points so that a frequency spectrum could be calculated by performing a Fast Fourier Transform on the data.

Measurements of the potential fluctuations were carried for currents ranging from 5 mA to 1100 mA.

2.5.5 Scanning Electron Microscopy (SEM)

No special preparation was required to obtain SEM pictures of RuO_2/TiO_2 anodes as they were excellent conductors. All samples were either studied using the SEM instrument at ICI's Winnington laboratory or at Bath university.

2.5.6 X-ray Fluorescence (XRF)

This technique was used to obtain a total ruthenium loading map of each anode before and after a degradation session. The instrument used was made by Fischerscope. The Fischerscope was calibrated prior each session using a ruthenium standard. Each sample was analysed according to the following procedure :

- 2 strips perpendicular to each other were placed on the Fischerscope platform.
- the anode was placed with engraved side placed upwards on the platform using the strips to maintain the position constant.
- 7 points were used to scan along the width (X-axis) and 14 measurements were used to scan the length (Y-axis) of the anode.
- The first point was always chosen to be at the bottom left hand side of the anode and the last at the top right hand side of the anode.
- measurements were carried using a 5 seconds sampling time.

After each scan, the data was saved to disk and printed out on paper. To measure another sample, the only requirement was to place the pointer at the bottom left hand side of the anode for the first measurement and press the 'XY Offset' option.

2.5.7 X-ray Photon Spectroscopy (XPS)

These measurements were performed by Neil Malone at the ICI research centre at the Heath (Runcorn). The aim was to obtain information about the composition of the anode surface, and in particular the variation of the Ti/Ru ratio.

In order to prepare the samples for these measurements they were rinsed in distilled water and dried in air. No cleaning in solvent was carried out as there was

concern that such a treatment might change the surface and composition of the anodes after degradation.

2.6 Computer hardware and software

2.6.1 Acorn Archimedes and ADC

For most experiments apart from impedance spectroscopy, a RISC type coprocessor based computer was used. Its main use was for recording and storing data. The main advantage of using a computer fitted with an Analogue to Digital Converter over a storage oscilloscope is that it is far more versatile. Apart from being a multitasking instrument, the amount of storage space is far greater than most oscilloscopes. This allows sampling of up to 30 seconds at 140 kHz in one scan without changing the sampling frequency. An alternative approach to the acquisition of data from the microsecond to the second scale has been described by Conway[1] who used two storage oscilloscopes recording a transient on different time scales. Such an approach was rejected on the grounds of cost and versatility in the present work

In order to control current interrupt experiments such as Tafel and OCPD, a 12 bit Analogue to Digital Converter (ADC) and 8 control lines were fitted to the Archimedes 410/1. The ADC had a resolution of 2.54 mV and could sample at 160 kHz. The highest sampling rate used was 142 kHz. The control lines were of the CMOS (0 - 5 Volts) type.

2.6.2 Software

A program was written in RiscBasic and developed for each of the current interrupt experiments. This section summarises the function and operation of each program.

Tafel experiment :

variable measured:	overpotential as function of current
current range:	5 to 1100 mA
sampling rate :	142 kHz
number of points recorded:	290

number of measurements/average:	variable (typically 20)
overpotential determination :	linear back extrapolation to time t=0
	from 130 to 280 μsec (20 points)
	after interruption. (y = a*x + b)

OCPD :

variable measured:	overpotential as a function of time
current range:	5 to 1100 mA
time range :	μsecs to 30 secs
sampling rate :	100 kHz from 0 to 1 sec
	30 Hz from 1 to 28 secs
number of points recorded:	537
number of measurements/average:	variable (typically 5)

One control line was used to open/close the mercury switch. Once the switch was closed, the program waited until steady state was reached, then instructed the switch to open and the ADC to record the overpotential. After trying different ways of determining the overpotential at t=0, it was decided that the difference between one overpotential and the next one was the best, most accurate and reproducible method of determining the point of interruption.

In the case of Tafel experiments, the program determined the first point after the iR drop and calculated the overpotential at t=0 using a linear back regression routine.

Although the OCPD program sampled at 100 kHz for the first second and 30 Hz for the next 27 seconds, it only recorded 537 points to file. A routine was utilised so that 100 points per decade were saved to disk from 10^{-4} to 10 secs and 40 points from 10 to 30 secs. This approach resulted from analysis of the shape of the OCPDs and was designed to have the most efficient data files in terms curve fitting requirements as well as minimising usage of hard disk space

Time range / Secs	Number of points
10^{-5}- 10^{-4}	10
10^{-4} - 10^{-3}	100

10^{-3} - 10^{-2}	100
10^{-2} - 10^{-1}	100
10^{-1} - 10^{0}	100
10^{0} - 10^{1}	100
10^{1} - 27	27

Two sampling frequencies were used for the recording of the decay of potential. In order to accurately record the first second of the decay, a high sampling rate of 140 kHz was necessary. There were two reasons why a single frequency was not used. Firstly, there was not enough memory space to record 30 seconds of decay at 140 kHz (this would mean 4,200,000 points). Secondly, there was no need to have such an accuracy after the first second since most of the electrochemical information to be obtained from OCPDs was in the 0 to 1 second range. The second sampling frequency was set at 30 Hz. The use of two sampling frequencies meant that the recording of the potential trace was not continuous. A command line was required in order to change the sampling frequency during the decay. This introduced a time delay which depended on the speed of execution of the program. This complication was tackled by calibrating and measuring the actual speed of execution of the Archimedes. The time delay was evaluated at 3.99 10^{-5} seconds and added to the routine that associated a time value for each recorded potential value.

The noise measurement program involved a simple routine to measure 4096 points and save them to disk. The frequency of sampling was variable but was mostly set below 100 Hz as previous work done in the ICI laboratories indicated that frequencies associated with bubble generation were in the mHz - Hz range.

2.6.3 IBM compatible

A 386 DX fitted with an IEEE interface was used to control the 1286 electrochemical interface/1250 FRA for impedance spectroscopy. Data analysis was carried out either on a 386DX, 486DX or 486DX2.

After trying out some data analysis packages it was decided that SIGMA PLOT (Jandel Scientific) would be chosen as spreadsheet software package.

An IBM compatible software package called "The Student edition of Micro Cap IV" was purchased for equivalent circuit simulations. Its purpose was to study the

influence of porosity and other possible effects such as uneven current distribution along the anode surfaces on the shape of OCPDs.

2.7 Problems encountered during development work

2.7.1 Electrode masking

This section covers the problems encountered due to the extreme operating conditions that result from working under relevant industrial conditions of chlorine generation. At the start of the project, a major requirement was that the electrodes should not be permanently masked as they were to undergo various types of analysis, some of which would be hindered by masking agents. The aim was to be able to study various parts of an anode and since many electrodes were to be used, as little time as possible should be wasted trying to remove masking reagents.

Initially PTFE tape was tried as a masking agent in order to have constant working area. However it quickly became apparent that this was not a good material. Because the anodes were very rough, substantial leakage occurred. Also, the combination of heat and bubble evolution often led to detachment of the tape during experiments.

From this initial trial it was concluded that a good masking material should not only be resistant to chlorine but also completely mask the anodes during the whole length of analysis. In order to fulfil the masking requirement, a liquid sealing agent was considered to be more suitable as it would penetrate into the pores, blocking them before solidifying. For this reason tests were conducted with epoxy resin (RS). Three different types of resin were used : quick set (RS), standard epoxy (RS) and bubble-free epoxy resin (RS). Although some success was achieved with the bubble-free epoxy, it was concluded that this was not a convenient masking reagent. One problem was that this type of epoxy resin needed to be heated up in order to remove all bubbles from it. However, by increasing the temperature the resin became too fluid to handle, hard to apply carefully and precisely onto the anode. Furthermore, it was found that epoxy resin was not very resistant to chlorine attack and portions of the resin coating were lost during chlorine evolution. Silicone rubber was also tested and found to be unsuitable. A combination of a solid PTFE holder and PTFE tape was then tried. The

idea was to place the anode inside a PTFE trough in order to cover the edges and rear of the electrode. PTFE tape was wrapped tightly around the cover in order to mask the front side. Leakage to the rear of the electrode was reduced, but still took place over a longer time period. As for the front side, the same problem as simply using PTFE tape was encountered again.

In view of the failure to find an adequate masking agent, a different approach was taken. Instead of trying to find a material to mask part of the anode when dipping it in electrolyte, a new cell that only exposed a fixed area of the electrode was designed. In total, 4 cells were designed on this basis. These will be discussed in a later section.

Finally, once the idea of flow cells was abandoned, Apiezon wax N-100© (BDH) was tried as a masking agent and found to be successful.

In order to determine the working area as accurately as possible the following procedure was followed. Once the electrodes were masked, they were laid flat on a scanner (HP scan jet IIp) and scanned to disk. The picture was then optimised to contrast the masked area from the exposed area using a software package (Photofinish). It was then magnified to fit an A4 page and printed on paper. Knowing the dimensions of the whole electrode and the magnification factor it was then possible to digitise the working area more accurately than just assuming it was rectangular.

Although it was not possible to get an accurate value of the error margin associated with the scanner and digitisation software this was not a problem as it was a systematic effect.

The following figure shows an example of a digitised RuO_2/TiO_2 sample attached to its titanium holder and waxed. A ruler was placed by its side to allow to get a feel for the dimension of the sample and its active area. Although the waxing did not permit a rectangular area to be marked out this picture shows that the working area is nearly rectangular. More importantly in terms of current density over the active surface area, it shows that the thickness of the wax means that the electrode is not flush with the insulating material and therefore will probably cause edge effects and an uneven current density distribution.

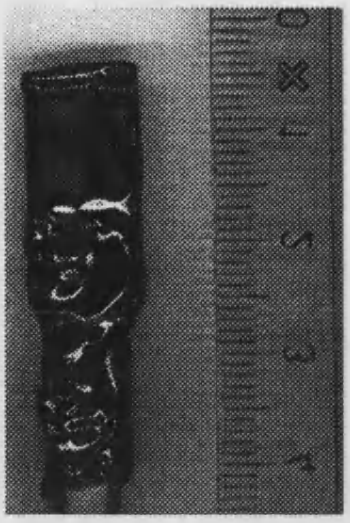

Figure 2.3: photo of a RuO_2/TiO_2 electrode mounted on a titanium holder and waxed.

2.7.2 Current interrupt instrumentation

In order to obtain error-free reliable results from the Tafel and OCPD techniques, a significant amount of work in optimising and tuning the experimental setup was performed. This section summarises electronic as well as instrumental problems that were tackled and solved.

Initially, the experimental setup consisted of a potentiostat (Hitek DT2101 100 Volts-1 Amps) and a waveform generator (PPR1). The working and reference inputs of the potentiostat were connected together with a 5 Ohm resistor, turning the potentiostat into a galvanostat. The PPR1 was used as a voltage source which was converted into a constant current by the potentiostat. A home-built differential amplifier and the ITT scope were used to record the open circuit potential decays. The negative end of the differential amplifier was connected to the counter electrode input and the positive to the reference input on the potentiostat (see diagram below).

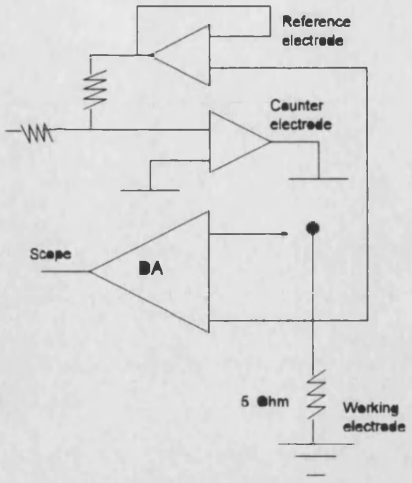

Figure 2.4 : Electronic circuit diagram for the OCPD setup using a potentiostat as a galvanostat.

The Archimedes computer was then used to trigger the PPR1 and record the OCPD to file. Since the solution resistance was in the order of 2-3 ohms the cell voltage was dominated by the iR contribution. This also caused problems as a gain of 10 was being used to get reasonable accuracy in the recording of the OCPD and the ADC sampling potential range was limited to -5 to +5 volts.

The differential amplifier was modified so that the iR drop could be compensated using a bridge circuit and, also, to offset the cell potential in order to make full use of the ADC's potential sampling range. Since the pulse used for iR compensation was the same as the one used to produce the current pulse, it was possible to synchronise it so that it was switched off as the current pulse was ended. This was achieved by using three identical differential amplifiers. The first one recorded the true cell voltage and was connected to the positive input of the third differential amplifier. The second fed the compensating pulse into the negative input of the third differential amplifier (see below).

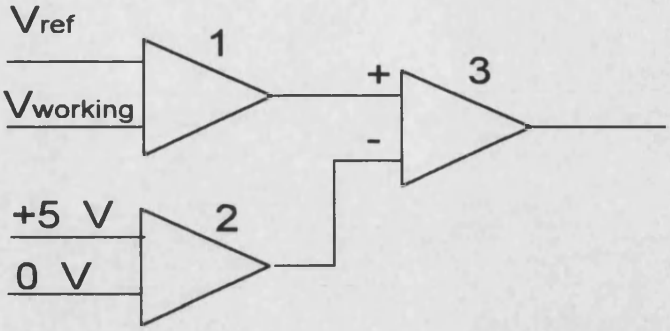

Figure 2.5 : circuit diagram for the differential amplifier required to measure the potential difference between anode and reference electrode.

By varying the subtracting pulse it was possible to adjust the pulse so that the iR drop was completely compensated. Knowing both the current and pulse amplitude it was possible to calculate the solution resistance. In fact, the compensating facility was used as a vital part for the determination of the overpotential : instead of just compensating the iR drop, the pulse was chosen to significantly overcompensate the running potential. This meant that the potential during current flow was lower than the one measured when the circuit had been opened since compensation was only applied during current flow. In principle, this gave an excellent way of determining the overpotential at time t=0 as the maximum amplitude recorded in the OCPD signal. It is much easier to design a program that detect a maximum situated on a spike rather than located on a plateau as in the case where the iR drop was not overcompensated.

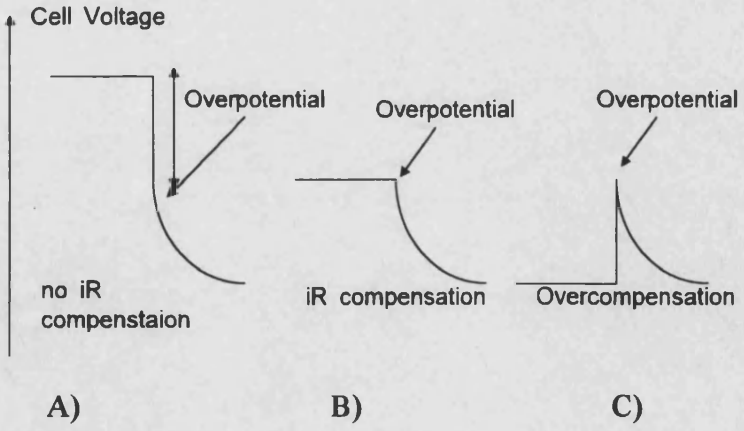

Figure 2.6 : Effect of using compensating pulse on the potential trace before and after interruption of the current. A)- no compensation B)- 100 % compensation and C)- overcompensation.

However the synchronous subtraction of the pulse from the cell voltage turned out be a non-trivial matter and more of a problem than an advantage. Although the compensating and current pulse originated from the same PPR1 pulse, the compensating pulse had to pass through electronic components which created a delay in the microsecond scale. This delay was sufficient to create a reproducible voltage spike when the compensating pulse was subtracted from the cell voltage. The OCPD signal could therefore not be recorded reliably in the 6- 15 microsecond scale (see above). Since this effect was reproducible this meant that the overpotential could not be recorded accurately using this procedure.

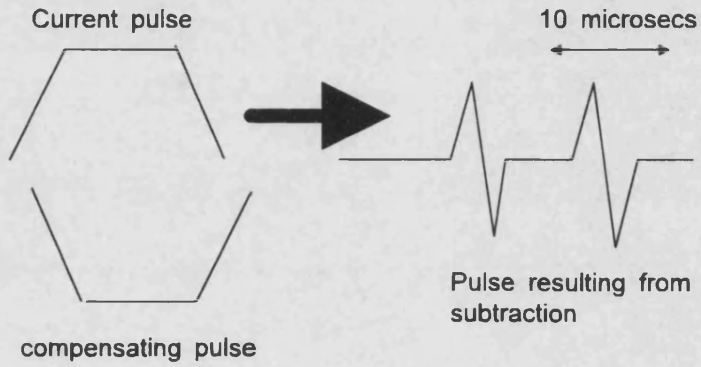

Figure 2.7 : illustration of synchronisation problem when using a compensating pulse only during current flow.

A second PPR1 was added to the setup in order to calibrate the length of the compensating pulse so that subtraction would be synchronous. Although this was achieved, this added too many complications in the control and simultaneous operation of two PPR1s. This also meant that two expensive pieces of apparatus were used for the sole purpose of triggering which was not acceptable. Other problems also arose from the performance of the potentiostat. Oscillations of the 100 V potentiostat frequently occurred, leading to damage of the differential amplifier.

In view of these electronic problems it was decided to simplify the experimental setup by purchasing a power supply and building a switching device (hence freeing up 1 potentiostat and 2 PPR1s). The idea was to use the power supply as a current source and a mercury wetted relay as a spike free switch in order to open and close the circuit. The mercury switch was built into a box so that it could be controlled by computer using CMOS control lines. A 5 Volt maximum iR compensation source was also built.

In addition, the power supply was modified so that the current could be computer controlled hence automating the experiment. The same overcompensating procedure for determining the current interrupt point was tried with the new circuitry but was abandoned due to problems with synchronisation.

During the course of this work, problems with earth loops became apparent. The problem was traced to the fact that the computer, the power supply, the differential amplifier and the mercury switch had different earth connections. This was also found to be a source of acquisition and experimental problems. After inspection of the circuitry and various earth sources it was discovered that the power supply of the differential amplifier was not properly earthed. This was a battery powered supply using two PP9 9V rechargeable batteries. Instead of earthing the amplifier to ground, a virtual earth had been created using balanced resistors. However, this meant that the whole device drifted with respect to the ground which was used for all other devices. This problem was corrected by earthing the supply common to ground. After modifications, each individual set of equipment was checked, calibrated and the setup tested for proper behaviour using a dummy cell.

Since the overcompensating procedure was found to be unsatisfactory a different amplifier was used to measure the overpotential. This was a fast single ended voltage follower based on an operational amplifier with a line driver to drive a coaxial cable.

2.7.3 The alkali wear test

Initially 4 anodes were degraded simultaneously in the alkali wear test. The potential of one anode was monitored during degradation and experiments were stopped once its potential had reached the set voltage limit. Experiments were carried out this way because it was thought that all electrodes cut from a same strip would exhibit similar behaviour. However, this was not the case. Furthermore, since total voltage was the parameter monitored, the voltage depended on the individual iR drop contributions from each electrode. It quickly became apparent that electrodes did not behave in the same way and that it was not possible to place the electrodes in the pot so that they had equal iR contributions. In addition, it was not possible to apply 2 A cm^{-2} per channel as that would have meant using a total current of 16 A : each of

the electrodes had roughly 2 cm^2 exposed to solution (i.e. two sides of 1 cm^2 each, not counting the edges). Because the power supply used could only deliver a total 10 amps it was decided to apply 1 Amp/cm^2 per channel instead. It was believed this would only lengthen the degradation process, which was seen as a possible advantage in the continuous study of electrode performance throughout its lifetime: the experimental results showed that halving the current amplitude did not double the length of degradation as it would be expected if the length of degradation was linearly dependent of current intensity. In fact, degradation lasted up to 3-4 times longer when using half the current density.

Another requirement was to remove electrodes from the pot, characterise them and put them back for further degradation. It was intended to repeat this procedure until all electrodes were fully degraded in order to study loss of activity. In order to stop the experiment once one of the four electrodes reached the set potential limit, the control unit was modified to monitor the potential of all four electrodes as opposed to just electrode 1. Since the composition and topography of electrodes was not identical and neither was the electrode distance w.r.t. the cathode it was not possible to use this method. Using one voltage limit for four electrodes did not reflect degradation as each electrode had a different starting potential and iR contribution. Only one set of four electrode was degraded this way.

Apart from the limitations discussed above, it was found that the control unit was extremely sensitive to switching equipment on and off in the laboratory. In particular, switching of fume cupboard lights or power supplies for photocurrent setups generated voltage spikes through the mains as well as radio interference. By moving the alkali wear test mains input plugboard away from the fume cupboard and power supplies the interference was eliminated. However this did not prevent radio frequency spikes from triggering the control unit, stopping the degradation experiment prematurely. It proved impossible to stop this effect from interfering with the operation of the control unit. However, damping of the control unit's response using extra RC filters significantly reduced the frequency of premature shutdown.

In view of safety considerations, initial measurements were carried out only during working hours. Since it took one hour to heat the pot up to 65°C this meant that the system was running for up to 10-11 hours maximum per day. With total

degradation times of up to 250 hours, 25 working days (approximately) were required to finish one set of 4 electrodes. Since no work could be carried out until a set was degraded (i.e. electrode masking limitations) this was not satisfactory as this resulted in too much 'dead' time.

In view of electrode masking requirements and the problems discussed above it was decided to change the entire procedure for degradation and characterisation of electrodes. Instead of degrading four electrodes simultaneously only one electrode was degraded at time. In order to follow the degradation process, subsequent electrodes were degraded to an increasingly higher final differences between the starting and final running potentials. Typically, the settings were as following :

Electrode	Voltage difference/increase	Comments
1	not degraded	to be used as standard
2	1 hour	Investigation of 'activation'
3	200 mV	
4	400 mV	
5	600 mV	
6	800 mV	
7	1000 mV	
8	1200 mV	

Since every strip was cut into similar electrodes, this procedure allowed comparison of performance as a function of voltage increase. The advantages over the previous method were the following :

- ***Shorter degradation time*** : since one electrode was degraded it was possible to use 2 A cm^{-2} per channel. Two of the current divider outputs were modified to allow a maximum 4 A per channel. The maximum degradation time dropped from 250 hours (approx.) to 80 hours (approx.). Also, once the experiment had proved to be safe, degradation runs were carried overnight until the set voltage limit was reached.
- ***Better control of degradation*** : once the system was set up and the solution was heated up to 65°C, the experiment was switched on. Apart for electrode 2 which was only degraded for 1 hour, the voltage limit was set w.r.t. the

running potential after one hour of degradation time. That was because it took approximately 1 hour for the system to reach an equilibrium running potential.

- ***Reduction of 'dead' time*** : electrochemical characterisation could be carried out in parallel with degradation experiments.
- ***Electrode masking problems minimised*** : once the electrode was degraded, it was waxed and characterised by cyclic voltammetry. The electrode was then sent for XRF and XPS measurements.
- ***Very few undesired interruptions*** : as the experiments were carried out continuously, this removed the possibility that electrodes could 'recover' from the degradation experiment. During certain experiments where the control unit was overloaded by a spike and the experiment shut down, it was possible to restart the experiment within minutes. After the experiment was restarted, the running potential returned to the value measured for a short time. This was a source of concern in the previous method, since the electrodes were allowed to 'rest' overnight. After having modified the control unit to protect it from interference, few degradation runs were interrupted before their voltage set limit was reached.
- ***Fewer data logger files*** : previously there were up to 25 data logger files for the degradation of a single electrode. Instead, only one file was required for the complete running potential vs. time 'fingerprint'. Typically, the data logger was set to record either for 2 hours (for electrode 2) or 80 hours (for all other electrodes).

By varying the initial voltage increase limit, ranges from 200 mV up to 4 V were studied. In total, 3 sets of 8 electrodes were degraded this way.

2.7.4 Chlorine

Throughout the latter part of this project, chlorine gas from cylinders was used to saturate the various types of cell with chlorine. Tubing and connections for the cylinders was found to be a source of problems. Conventional tubing used in the laboratory such as rubber tubing or PVC tubing were found to be very poorly resistant

to passage of chlorine. Various types of tubing were tried and silicone rubber was found to be the most convenient, relatively cheap and easy to use. PTFE tubing coated PVC tubing ('Chemflex' from Aldrich) was also tried but found to be too rigid.

Simple brass needle valve taps were used for control the flow of gas from the cylinders because proper chlorine cylinder taps were found to be prohibitively expensive. Although it was satisfactory to use brass taps, passage of chlorine caused significant corrosion and resulted in the introduction of impurities in solution. The only way to prevent too much solution contamination was to rinse the taps with water after each day of experimentation.

2.7.5 Different cell and reference electrodes types

In total, 8 different flow cells and nearly as many reference electrodes were tried throughout this three year project. A separate chapter will be dedicated to these issues since they constituted the bulk of experimental development work.

2.8 Calibrations

This section summarises the calibration procedure for each of the instruments that required such attention. The same calibrated voltmeter (ISO-TECH IDM 203) was used for all calibrations :

PPR1 waveform generator : The LED display of the PPR1 was checked against its BNC output and the display was accurate within ±1 mV.

Oscilloscope : once the PPR1 was calibrated, it was connected to the storage oscilloscope. Both digital and analogue modes were checked for accuracy. The oscilloscope was found to be correct within the manufacturers specified ± 2% calibration. This value was set against the full voltage range of the specified voltage sensitivity : at 2 Volts/division the scope displayed a maximum of 10 divisions. The measured values were therefore within a 200 mV range, since full scale corresponded to 20 V.

Analogue to Digital Converter : calibrations were performed both in steady state and transient conditions. The PPR1 output was connected to all ADC lines in order to check for differences in potential as a function of ADC line

used. The ADC was found to have an accuracy corresponding to its smallest resolution of 2.55 mV on all its lines. Since it was far more accurate, it was decided that recorded values should be taken from it as opposed to the oscilloscope.

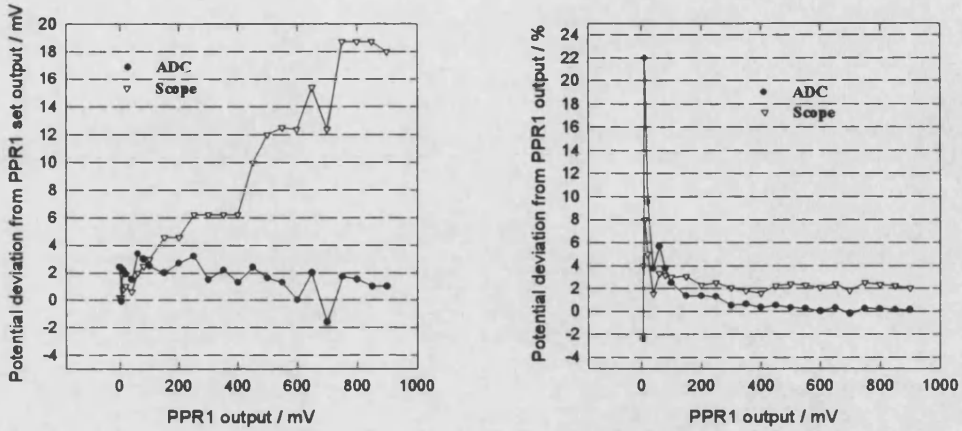

Figure 2.8 : Calibration plots for ADC and oscilloscope.

Differential amplifier and operational amplifier: the output of the PPR1 was fed through the differential amplifier, the scope and ADC via a T piece. It was also checked in steady state and transient mode. The same procedure was used for the fast voltage follower amplifier. Both amplifiers were tested for leakage current at regular intervals : this procedure was necessary in view of the harsh experimental conditions used. Results showed that both amplifiers operated properly on gain 1 and 10. Another test was also used to checked whether the amplifiers drew any significant leakage current. This test was carried out using a 1 MΩ resistor in order to check whether voltage spikes had damaged the amplifiers. This test resulted in changing amplifiers twice over the length of the project.

Data logger and control unit : the PPR1 was used to produce a voltage signal which was fed through the logger and control unit. Although the data logger measured the input signal with an accuracy better than 2 %, the control unit was found to be less accurate. Analysis showed that the accuracy was only of 6 %. However, this was not a problem since the purpose of the control unit was to monitor a voltage increase.

Calomel and chlorine reference electrodes : In order to check the proper functioning of the calomel electrode, it was compared to a new calomel electrode in a beaker containing dilute sulphuric acid. Since the voltage difference was less than 5 mV, the calomel electrode used was judged to be working satisfactorily. For the chlorine reference electrode, the calibrated voltmeter was utilised and two tests were carried out to check for proper functioning. One involved comparing the potential of the chlorine electrode with a calomel electrode in chlorine saturated 5 mol dm^{-3} NaCl + 10^{-2} mol dm^{-3} HCl solution. The second test involved was measuring the potential difference between the RuO_2/TiO_2 reference and RuO_2/TiO_2 working electrode in chlorine saturated 5 mol dm^{-3} NaCl + 10^{-2} mol dm^{-3} HCl solution and checking for zero voltage difference.

---

1 B.E. Conway, L. Bai, D.F. Tessier, *J. Electroanal. Chem.*, 161, 1984, 39-49

CHAPTER THREE

Chapter Three

Cells and

Reference Electrodes

3.1 Introduction

A major source of experimental challenges was due to problems arising from the extremely high rate of chlorine evolution, mainly unwanted bubble layer effects. Working in chlorine saturated environment also meant that few reference electrodes could be used. This section details the work carried out in order to optimise the electrochemical cell.

This chapter concentrates on the challenges encountered when trying to resolve problems related to high current densities, bubbles and reference electrodes. The different cells tried will be described and problems due to local current density variations, bipolarity, forced convection, varying reference potential, flow cell design will also be discussed.

3.2 Why are these problems so acute ?

Most theoretical studies usually involve using small working area electrodes, current ranges that are not industrially relevant, low pH electrolytes to minimise chlorine evolution and so on. However, as mentioned before, the aim of this project was to reproduce industrial conditions and study chlorine evolution under these restrictions. As a result, large electrodes were used, the pH was kept close to that of industrial conditions, a highly conducting brine solution was used as electrolyte and currents ranging from 5 up to 1500 mA cm^{-2} were utilised.

Working under such conditions highlighted five main challenges. They were the following :

1. ***Dimensions*** : instead of using small working area electrodes, electrodes based on commercial chlorine catalyst material were used. Initially, the coated titanium strips were 20 cm long and 0.6 cm wide. Finally, they were 20 cm long and 1 cm wide as it was found to be more convenient to handle. Each strip was cut into 2x1 cm samples . These electrodes were not ideal, they were very rough and therefore very hard to mask. Other areas where dimensions were important were those of cell design and reference/cathode electrode size.
2. ***Flow rates*** required to remove the bubble layer.
3. ***Sampling speeds*** required for interrupt measurements.
4. ***Current range*** : to reproduce industrial conditions, current densities of up to 1500 mA cm^{-2} were required. Since the working areas were in the range of 0.8-1 cm^2, this required specific instrumentation : electrochemical experiments often involve smaller currents, typically milliamps or less. In this case, the currents involved were such that potentiostats and waveform generators could not be used for anything else than cyclic voltammetry. As it became clear later, in order to obtain such high current densities, significant voltages were required. The later resulted in bipolarity problems with the reference electrode. The current range used also meant that care had to be given to the geometry of the various cells used. Restrictions on current flow lines, current density variations along working, cathode and reference electrodes were all found to be critical.
5. ***Bubbles and convection*** : in most laboratory studies, electrolytes designed to minimise bubble formation and high chlorine activity have been used. The 5 mol dm^{-3} NaCl+10^{-2} mol dm^{-3} HCl used was highly conducting. The high current densities resulted in significant bubble generation. The necessity to remove the bubble layer was recognised at a very early stage and forced convection as a means of tackling this problem became an intensive area of development work that culminated in the use of various types of flow cells. This is because the bubble layer was expected to modify the total cell resistance and hence the iR contribution[1].

3.3 Electrode materials

This section summarises the development work that was associated with the choice of electrode and cell materials.

3.3.1 Problems of contamination

Working in the presence of chlorine meant that corrosion and resulting solution contamination were a source of experimental problems. The biggest challenge was to find a material that combined the following qualities :

- Resistance to alkali, acid and, especially, chlorine environment
- Chemically inert
- Optically transparent
- Heat resistant up to 70°C
- Easily machinable in the workshop

Initially, glass cells were tried. Although all the above conditions were fulfilled, it was not possible to resolve the electrode masking and convection requirements. Two glass cells were tried out. The first one was a classical three way electrochemical cell. The working electrode was sealed with epoxy resin and placed in the middle of the main body. The second was constructed from glass, PTFE, Viton® and Polypropylene. The materials that were not glass were part of the masking and clamping of the working electrode.

As the bubble layer problem persisted, it was decided to design a cell that used forced convection to minimise or tackle this effect. Initially, a wall jet electrode was considered but the engineering requirements in terms of design and instrumentation were found to be too complex. It was decided to build a flow cell instead. Glass was no longer used because the flow cell involved many plates clamped together in a sandwich and also because its design was too complicated to make out of glass. The following polymer materials were considered in view of the requirements described above:

- E-CTFE (Ethylene-chloro-trifluoro-ethylene)
- Viton® (Hexafluoro-propylene-vinyldene-fluoride)

- ABS (Polycrylo-nitrile-butadiene-styrene)
- Polyamide Nylons (11, 46, 6, 612 and 66)
- Torlon® (Polyamide imide)
- Kevlar® (Polyaramid)
- PMMA or 'Perspex' (Poly-methyl-methacrylate)
- Polypropylene
- PTFE (Poly-tetrafluoro-ethylene)

PMMA was chosen because of its overall properties and low cost. Although it was not strongly resistant to all types of chemical environments, it was the only material that was moderately resistant to all of them. Other materials had excellent resistance to some type of chemical attack but not all of them.

The body of the first cell was made of PMMA. It cell consisted of 4 PMMA plates, 3 Viton® sheets (1 mm thick), a Nafion® membrane (provided by ICI), a steel counter electrode, 16 brass bolts, 32 brass nuts and washers. Unfortunately there were leakage problems and the chlorine saturated solution attacked the brass components. The resulting corrosion caused severe contamination of the electrolyte.

In the next two flow cells utilised, no corrodable materials that would be in contact with solution were utilised. The cells only consisted of PMMA, aluminium and steel. The metal parts were required to clamp the cells in a sandwich.

3.3.2 Preventing and minimising hydrogen formation

In industrial cells, the cathodes are separated from the anodes using a membrane. There are two reasons for this : firstly, to prevent the hydroxide produced at the cathode from reacting with chlorine to form hypochlorite compounds and secondly, to prevent the buildup of an explosive mixture of hydrogen and oxygen. There is also the possibility of the hydrogen formed at the cathode interfering with the anode reaction since hydrogen can be reduced at the anode.

In order to completely separate catholyte and anolyte one would require two pumps and an elaborate experimental setup. In view of the cost of such a setup and the time constraints, it was decided to adopt a simpler approach by only using one pump. A Nafion® membrane was used, but only to act as a separator : two holes were

pierced at each end of the flow cell channel. The idea was to prevent the hydrogen produced from reaching the anode over the length of the flow cell.

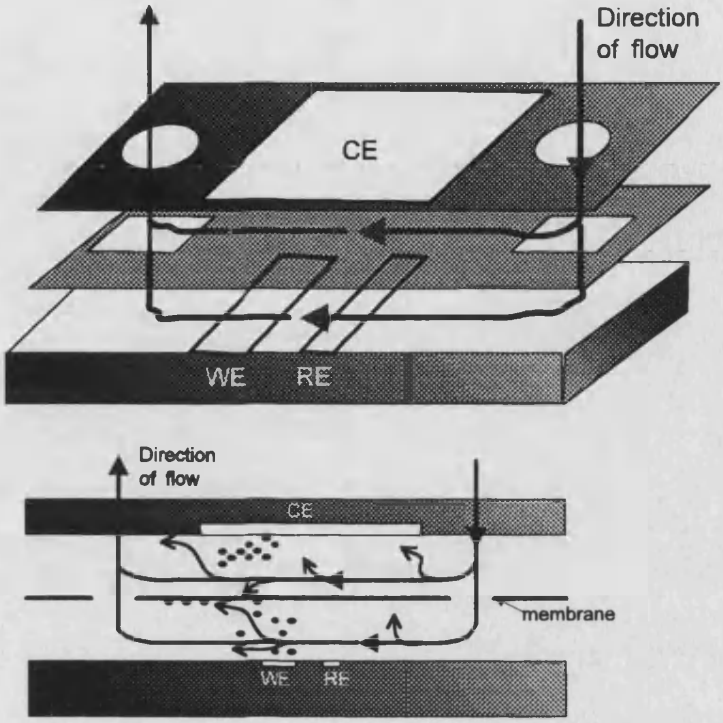

Figure 3.1 : use of membrane to prevent chlorine produced at the anode from reacting at cathode and hydrogen produced at cathode from reacting with the anode.

In later cells, the membrane was abandoned because it was not possible to eliminate leakage that resulted from having it as part of the cell. Instead, the flow cell channel height and flow rate were increased. The assumption was that hydrogen produced at the cathode could not reach the anode if the interelectrode gap was sufficiently great. The horizontal flow would flush the gas away before it would have time to reach the anode.

Inspection of the anode during chlorine evolution showed that a cloudy area above the anode and near the counter electrode only extended to half of the cell height. Since this cloudy area only appeared above a critical current density, this was attributed to the cathode switching to hydrogen production. The presence of this cloudy area also confirmed that the flow was turbulent.

3.3.3 Identical electrode materials

In the last two flow cells, all electrodes were made from RuO_2/TiO_2 material provided by ICI. The formation of hydrogen was minimised by making the counter electrode much bigger than the working electrode. Platinum would have been prohibitively expensive. Using steel led to contamination and, since it was not possible to make a counter electrode of adequate size out of graphite (far too fragile), another material had to be found. A RuO_2/TiO_2 electrode was finally used as a cathode material. Likewise, the reference electrode was also made from RuO_2/TiO_2 because of its high selectivity towards chlorine. Using the same material for all electrode had the major advantage of eliminating possible sources of contamination that could result from corrosion. Minor leakage was no longer a problem as it had no other effect than loss of electrolyte.

3.3.4 Cl_2/Pt reference electrode

It was previously mentioned that RuO_2/TiO_2 was ideal as a reference electrode material since it is used as a chlorine catalyst. That is why it was used as reference electrode in the flow cell. Attempts were made to use it in the final cell but titanium and glass have such different heat expansion coefficients so that it is not possible to seal titanium into glass. A platinum gauze was used instead.

3.3.5 Flow regime

Ideally, one would want to work in a laminar flow regime. This is because the hydrodynamics have been well studied and also because this allows kinetic information to be obtained. A literature survey was carried out in order to find out the necessary requirements for laminar flow to be obtained[1]. It quickly became evident that it would be impossible to work in such a regime in view of the convection requirements to remove the problems associated with the bubble layer. In order to have a Reynolds number in the range that corresponds to laminar flow it would have been necessary to have a flow cell channel width of the order of meters. This results from the fact that the channel height was of 2.5 cm. Most flow cell experiments under laminar flow are carried out in very small flow cell. The channel height is usually in the order of a few

millimetres, the width in the same order and the length in the 0.5-2.0 centimetre range. In our case the height was of 2.5 cm, the width of a 1 cm and the length of 15 cm.

Since convection was required only to minimise problems associated with the bubble layer, laminar flow was not considered as necessary. In fact, turbulent flow was considered to be more appropriate since it is the flow regime in industry. The flow of electrolyte and turbulence areas inside the flow cell channel could easily be seen when passing a high current. Hydrogen produced was trapped inside an area close to the channel input. As hydrogen was removed one could follow the flow of electrolyte by looking at the hydrogen being flushed away.

3.4 Cell designs

In total, 9 different arrangements with 6 cells were tried out. This section describes the evolution of cells used throughout this project. It will also outline the advantages and problems associated with each of the cell.

3.4.1 Cell 1

The first setup used was a classical three compartment electrochemical glass cell. No chlorine saturation was used and the electrodes were masked using quick set epoxy resin. The counter electrode was made of a platinum gauze (0.8 cm^2 geometric area) and a SCE was used as reference electrode.

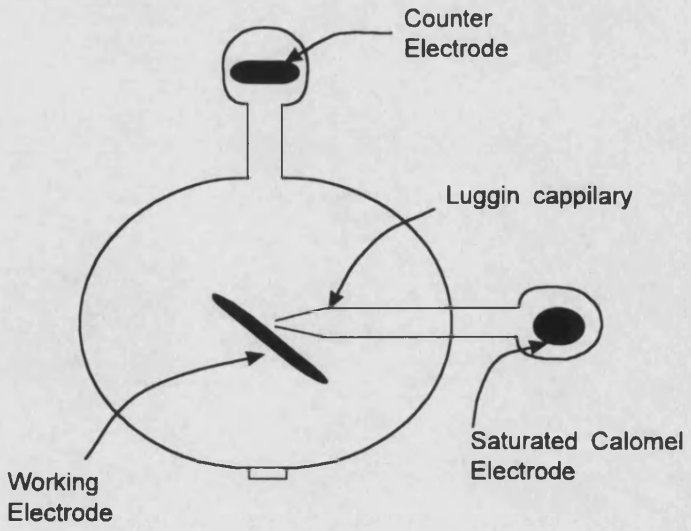

Figure 3.2: classical three compartment cell used as Cell 1.

This cell suffered from two major drawbacks. Not only was the design such that experiments could not be carried out a high temperatures but, also, a good masking agent for the working electrode could not be found. Leakage underneath the masking agents was a significant problem.

A SCE was used as reference electrode in this experimental setup and this gave large values of potential which restricted the sensitivity of measurements. The overpotentials measured were in the order of 0 to 200 mV (approx) and the difference in standard potential was of 1200 mV (approx), i.e.

Reaction	Potential, V vs NHE at 25 ° C
$Cl_2(g) + 2e^- = 2\ Cl^-$	1.3583
$Hg_2Cl_2 + 2e^- = 2\ Hg + 2\ Cl^-$ (sat'd KCl)	0.2415

Since it was not possible to find an adequate masking agent, a new cell was designed. It was also decided to make a chlorine reference electrode as it was not possible to use a SCE in a chlorine saturated environment for long periods of time. It was also concluded that forced convection was required to clear the working electrode surface from bubbles.

3.4.2 Cell 2

Since it was not possible to modify the previous cell to fulfil the improvements required, another glass cell was built. The idea was to use a chemically inert material and to punch a hole in it in order to use it to define the working electrode area. The electrode would then be mounted under the hole on the outside of the cell so that only the area above the hole would be exposed to solution. In this way, one could perform measurements anywhere along the anode strip. The position of the anode was given careful consideration. It was decided to place the anode horizontally. Had it been placed vertical then bubbles produced at the bottom of the plate would have an effect on the upper area of the anode. One could assume that the area placed in the upper region of the working electrode to be more obstructed by bubbles. By placing it horizontally, all bubbles left the surface without travelling along it.

A platinum wire was used in order to make a chlorine reference electrode. It was sealed into the glass and placed above the working area. The assumption was that

if it was placed above the anode then the chlorine produced from passing current would be sufficient to keep the platinum wire at the chlorine potential.

The cell consisted of 2 glass side arms (one with glass frit), 1 main glass body, a glass holder for the working electrode, 2 Viton® sheets (1 mm thick), 1 polypropelene cylindrical base (0.8 cm thick, 3 cm diameter), a stainless steel disk (0.5 cm thick, 3 cm diameter), 2 clamps and a platinum gauze (0.8 cm^2 geometric area) as counter electrode. The total cell volume was in the order of 400 ml. Figure 3.3 shows the base of the glass cell with the electrode mounting.

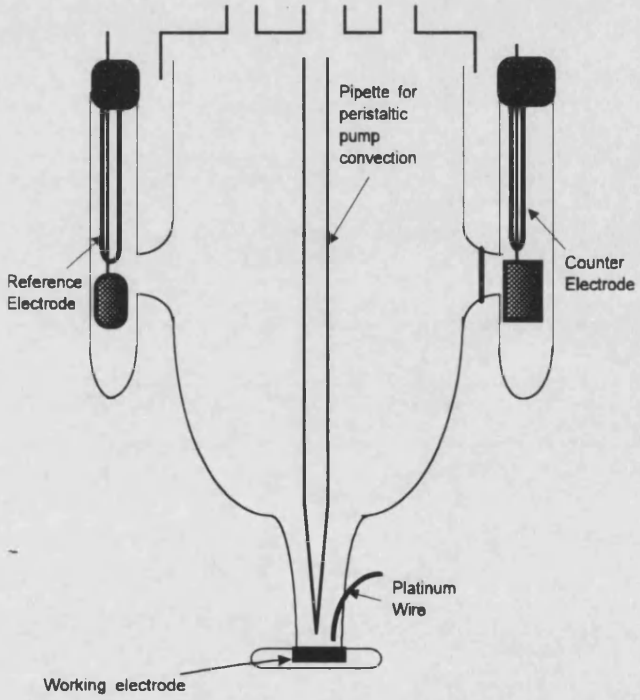

Figure 3.3 : side view of Cell 2.

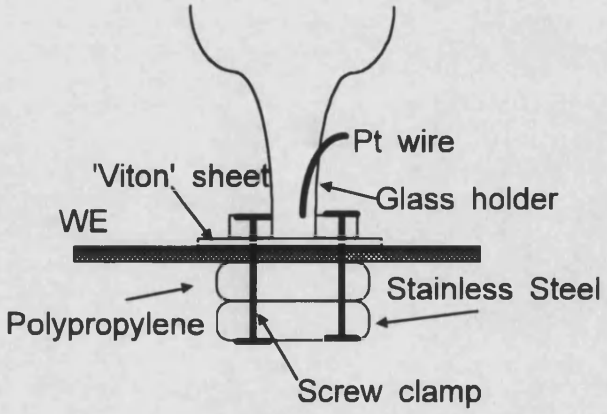

Figure 3.4 : detailed diagram of the working electrode clamping arrangement for Cell 2.

Initially, the new masking procedure seemed to be successful and the cell used a chlorine reference electrode without a Luggin tip in order to avoid the shielding problems that often arise when using a Luggin capillary close to an electrode surface. This was always a source of worries since the current used were so big. Shielding can seriously affect the local current density of the working electrode and a non uniform current density distribution would clearly complicate interpretation of results.

The clamping procedure was found to be inconvenient and hard to use. In order to mask the electrode, the pierced Viton® sheet had to be placed between the glass and the electrode. The electrode had then to be fitted into a polypropylene holder which, in turn, was positioned on top of a stainless steel disk. The latter was required so that the whole arrangement could securely be clamped using two screw clamps. In cases where the clamping was not done properly, leakage problems reoccurred (the high roughness of the electrodes meant it was impossible to eliminate leakage entirely). As for the reference electrode, the assumption that the chlorine produced by current flow would be sufficient to keep the platinum tip at chlorine potential was found to be incorrect. By comparing its potential with respect to a SCE it was found that its potential varied as a function of current density. Because of the position of the platinum wire with respect to the anode-cathode geometry it was suspected that it only measured an average potential. Since it was placed vertically above the working electrode but not equidistant from it, the potential measured was expected to be complicated by bipolar effects.

Cork bores were used to pierce holes in the Viton® sheets, and this procedure led to problems because of the roughness of the edges. Bubbles became trapped, obstructing part of the working electrode. Since the size of the working electrode was small (3-10 mm diameter), there was a significant 'bubble layer' between the reference electrode and the working electrode. At high current densities, the trapped bubble layer grew so large that the working area became partially isolated from the electrolyte.

Having identified all the drawbacks with this arrangement, it seemed that minor changes to the design could possibly yield an operational electrochemical cell. A platinum tip would eliminate problems of chlorine reference electrode and a peristaltic pump could be used to remove the bubble layer. It would also allow experiments to be carried out at high temperature.

3.4.3 Cell 2b

Thin PTFE rings (1 mm thick) of different internal diameters (2- 10 mm) were machined out of a block. The idea was to cut a thin groove on the top side of the ring so that a platinum wire could be mounted inside the ring exposing only a tip. Sticky PTFE tape was used to cover the ring and to fix the new reference electrode 'ring' together (PTFE is very chemically inert and it was difficult to fix the platinum to it). Each ring was cut so that the top inside diameter is greater than the lower one. This was to prevent bubbles form becoming trapped since the angle between the ring and the surface was greater than 90°.

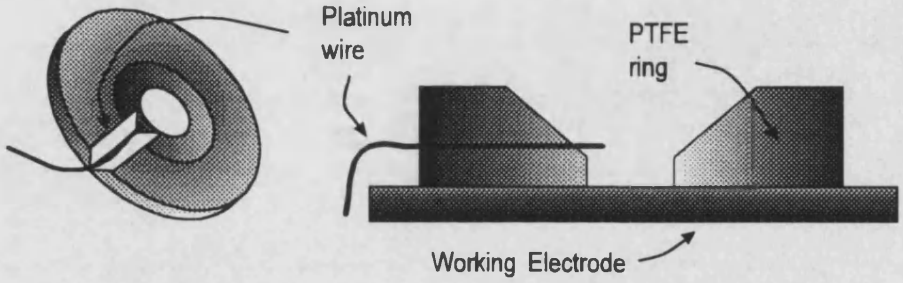

Top view Cross section

Figure 3.5 : top view and cross section of platinum reference electrode arrangement.

A peristaltic pump was purchased in order to recirculate electrolyte and squirt it onto the working electrode. Initially the pump was only used as a source of convection in order to clear the working electrode from trapped bubbles and remove the bubble layer. Later, a hot plate was used to preheat the electrolyte so that measurements could be done at high temperatures. The pump was then used to recirculate the electrolyte to keep the solution at constant temperature.

Attempts to keep the working electrode surface clear of trapped bubbles were unsuccessful. Furthermore, although the reference electrode was placed closer to the working electrode, its potential was still found to vary with current density. Bringing it closer only introduced further problems since bubbles became trapped underneath its tip. The forced convection created by the use of the peristaltic pump was not constant (inherent to the design of such devices) and, therefore, did not reproducibly remove trapped bubbles. The introduction of the PTFE ring as a further piece in the clamping

of the working electrode finally became too complicated to use, especially since very little advantage was gained from this non permanent masking of the working electrode.

Since the platinum tip reference electrode did not work satisfactorily, a chlorine reference electrode based on a platinised platinum wire mounted inside a glass syringe was built. Once the platinum was platinised, the electrode was cleaned and filled with the same electrolyte as the one used for experiments. Chlorine was then generated electrochemically by placing the electrode inside beaker filled with 5 mol dm^{-3} NaCl + 10^{-2} mol dm^{-3} HCl and passing current via a platinum counter electrode. Since the chlorine gas was trapped inside the glass, the platinum took the chlorine potential. Attempts to connect this electrode via a thin glass capillary tube placed close to the working electrode were relatively successful. However this arrangement suffered from two major drawbacks. The first one was that bubbles got stuck inside the glass tube and the second was that, since the solution was not chlorine saturated, the reference electrode quickly lost its chlorine gas bubble via diffusion into solution.

In summary, the design of cell 2x did not solve the problems it was aiming to. No satisfactory chlorine reference electrode arrangement was found. No sustained measurements at high temperature were feasible and problems due to the high chlorine activity were not tackled. If success was to be achieved, the next experimental setup should have an in-built heating system, high convection rates and an operational reference electrode. Building a wall-jet electrode was considered as this would eliminate bubble layer problems. A literature survey was carried out, but the conclusion was that it seemed far too complex and time costly (especially in view of the amount of time spent on such a relatively simple setup) to build such a cell. Instead, it was decided to build a flow cell.

3.4.4 Cell 3

The flow cell apparatus consisted of:

- a 3 litre conical flask modified to act as electrolyte reservoir
- a pump (EMP 40/6 from Toton Pumps)
- a quartz tube heater (BDH)
- Nafion® membrane
- a flow meter made out of U-PVC (Platon flow bits)

- 3 taps made out of U-PVC
- a flow cell (see details)
- 1-2 meters of polyethene (1.5 cm diameter)
- some clamping equipment such as stands and clamps

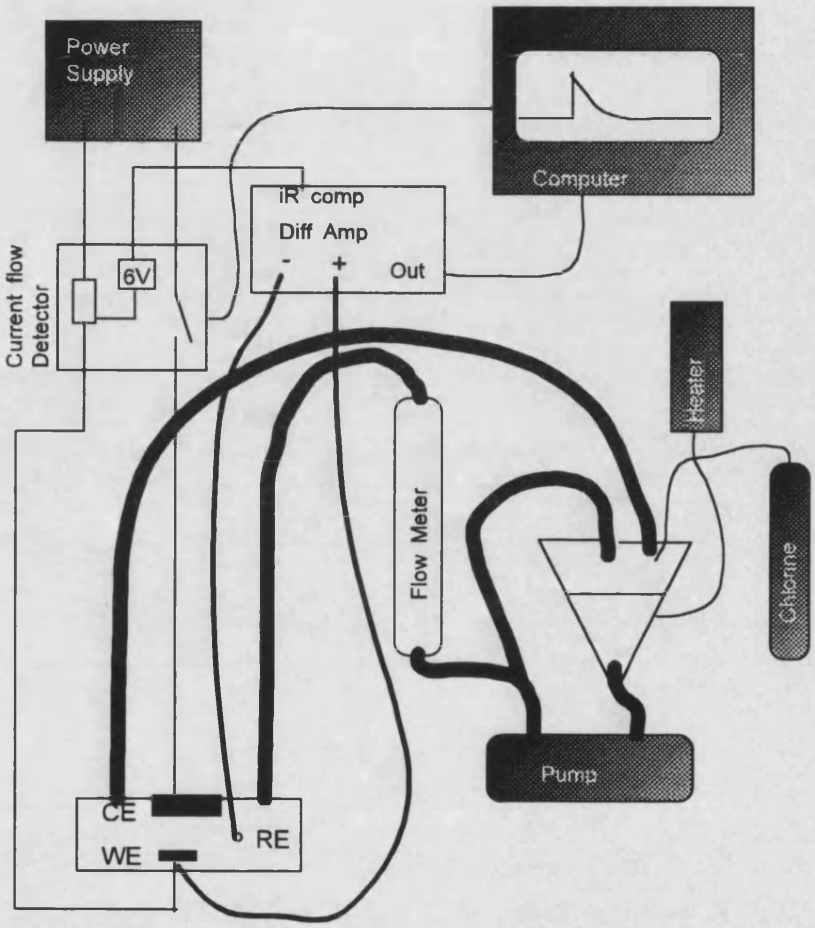

Figure 3.6 : electronic and electrochemical setup used for Cell 3 .

Cell 3 consisted of 4 PMMA plates (3 cm wide, 20 cm length and 1 cm thick), 4 Viton® sheets (1 mm thick) and a sheet of Nafion® membrane (less than 1 mm thick). 9 holes on each side of the PMMA plates were drilled in order to assemble all the pieces together and clamp the cell. A total of 16 brass bolts and 32 nuts/washers were required.

Initially, the platinised platinum wire enclosed in glass was tried out as a reference electrode. The PMMA bottom plate was drilled and pierced sideways in the direction of the flow so that bubbles would not be trapped. The hole was placed above the middle of working electrode groove, as shown in figure 3.7.

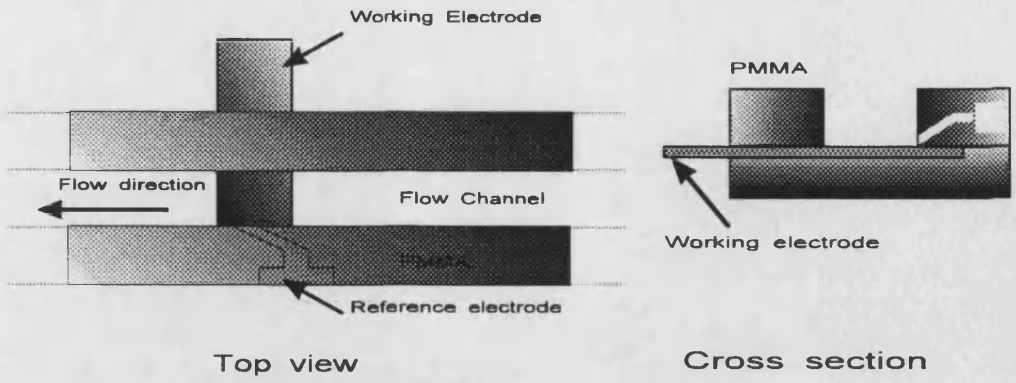

Figure 3.7 : reference electrode arrangement with respect to working electrode for Cell 3.

The flow rate produced (300 l/h) resulted in an horizontal electrolyte velocity sufficiently powerful to sweep the bubble layer away. Since the flow was constant and one could always see the working electrode, it seemed that the effects of the bubble layer had been minimised. Although the bubble layer did not disappear the effect of the flow was to make its effects independent of current density. This meant the bubble layer was no longer a variable. Chlorine was bubbled in the main body and experiments could now be carried out at 60°C over long periods of time. It looked as if all the initial aims had finally been achieved.

Initially, it was assumed that the chlorine reference electrode was at 1 atmosphere pressure. That was only true in the case of cell 2x. The internal pressure resulting from the flow of electrolyte did, however, cause problems with the reference electrode. Various methods of clamping the reference electrodes were tried to prevent it from popping out of its holder. When it was used in conjunction with the flow cell, the internal pressure was greater than 1 atm. This could easily be seen when switching the pump on : the chlorine gas trapped inside the glass electrode was compressed and the level of meniscus moved up, as shown in figure 3.8.

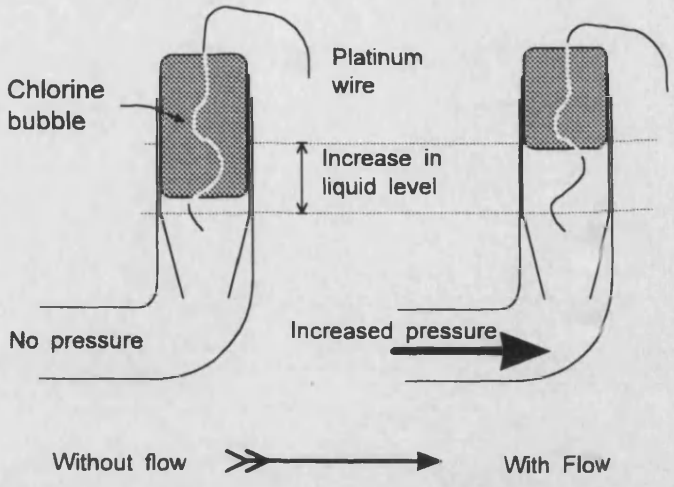

Figure 3.8 : effect of pressure on chlorine gas trapped inside reference electrode.

Furthermore, after making some calculations of the amount of chlorine required to saturate the electrolyte, it was realised that bubbling of chlorine in the main cell had not taken place for long enough. The combination of lack of chlorine saturated electrolyte and high pressure resulted in the problem encountered earlier, i.e. degeneration of the chlorine reference electrode via diffusion of chlorine gas into solution reoccurred. The fact that the high pressure also caused the reference electrode to pop out of its side arm led to the conclusion that it was not an adequate electrode arrangement.

Having explored many ways of using an external reference electrode, it was then decided to use an ICI electrode not only as cathode (in order to eliminate contamination) but also as reference electrode. Since RuO_2/TiO_2 is a good catalyst for the chlorine reaction, one would expect it to adopt the chlorine potential. A groove (6 mm wide, 1 mm deep) was made in the base of the flow cell in order to minimise turbulence by making the reference electrode flush with the surface.

The width of the flow channel was used to define the working area. No elaborate masking of the electrode was required. There was, however, one major problem with this cell; too many nuts and bolts were required for its assembly. Not only did this cause problems with the fragile plates, but it led to significant leakage of electrolyte. This is because it was impossible to apply equal pressure over the PMMA plates and prevent electrolyte from creeping through the membrane and Viton® sheets.

The leakage of chlorinated electrolyte caused corrosion of the brass components which, in turn, resulted in solution contamination. Protecting the bolts with heat shrink material and/or PTFE tape did not prevent contamination from occurring.

At this early stage of flow cell development work it was thought that the reference electrode used was working properly. Although the solution was not saturated, it was the first time reproducible results were achieved over a series of samples. It was discovered subsequently that the reference electrode was actually behaving as a bipolar electrode. This is discussed in section 3.4.3.

The conclusion of this work was that another cell that avoided metal components should be built and that the Nafion membrane should no longer be used. The new cell also increased the interelectrode gap so as to ensure no hydrogen produced reached the anode.

3.4.5 Cell 4

Another flow cell was built along the same design as cell 3. Instead of piercing the plates and using nuts and bolts to hold the cell together, two aluminium plates with two bolts at each end were made up. The cell was built so that it would stack up between the two bolts and be clamped by tightening the two plates together in a sandwich. It was also designed to solve the problem of solution contamination since it did not have any corrodable components directly in contact with the solution. The working electrode was 1 cm wide and a reference electrode (0.6 cm wide) was placed 0.3 cm away upstream as shown in figure 3.9 below.

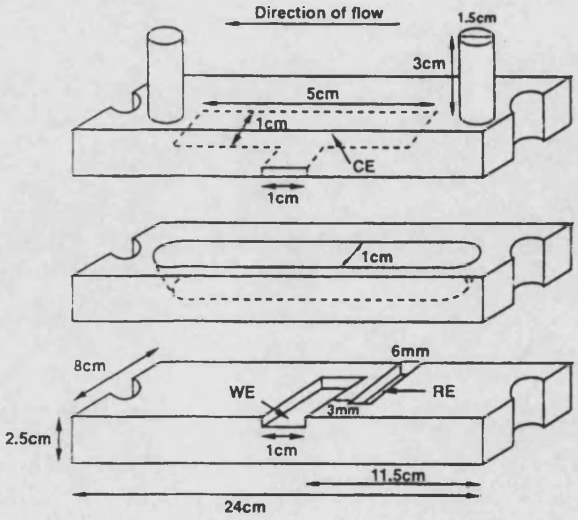

Figure 3.9 : diagram of Cell 4.

Cell 4 was far more convenient to use since only two nuts were required. Only 3 plates were required as opposed to 4 in cell 3. By removing the membrane, only one plate was required to define the flow channel height. In cell 3, the channel was 2 cm high whereas in cell 4 the height was increased to 2.5 cm. This was to compensate for not using the membrane.

In order to prevent leakage, two Viton® rings were made up and placed inside two grooves, one on either side of the middle plate. Although it was never possible to eliminate leakage, it was reduced even further by using two extra PTFE sheets as seals.

The flow cell seemed to work properly and was easy to use. Reproducibility was achieved and measurements could not only be carried out at different temperatures but they could also be done at different flow rates.

Eventually, it was realised that problems of constant electrolyte composition and pH had been overlooked. The flow cell required 4 litres of electrolyte (approximately) per electrode. Not only was this too costly and inefficient but it also introduced uncertainties concerning the reproducibility of experimental conditions. pH variations as well as electrolyte concentration were a source of concern. Since it was intended that electrodes should to be compared with each other, it was decided to build a cell that could take 4 electrodes at a time. This way, cost was tackled and reproducibility was thought to have been improved.

3.4.6 Cell 5

Cell 5 was built using PMMA plates and aluminium following a similar design as cell 4. The height was the same but the length was increased from 24 to 27.5 cm to give space for 4 working electrodes and 4 reference electrodes slots. The distance between the each reference electrode and the respective working electrode was kept at 0.3 cm, i.e. as shown in figure 3.10.

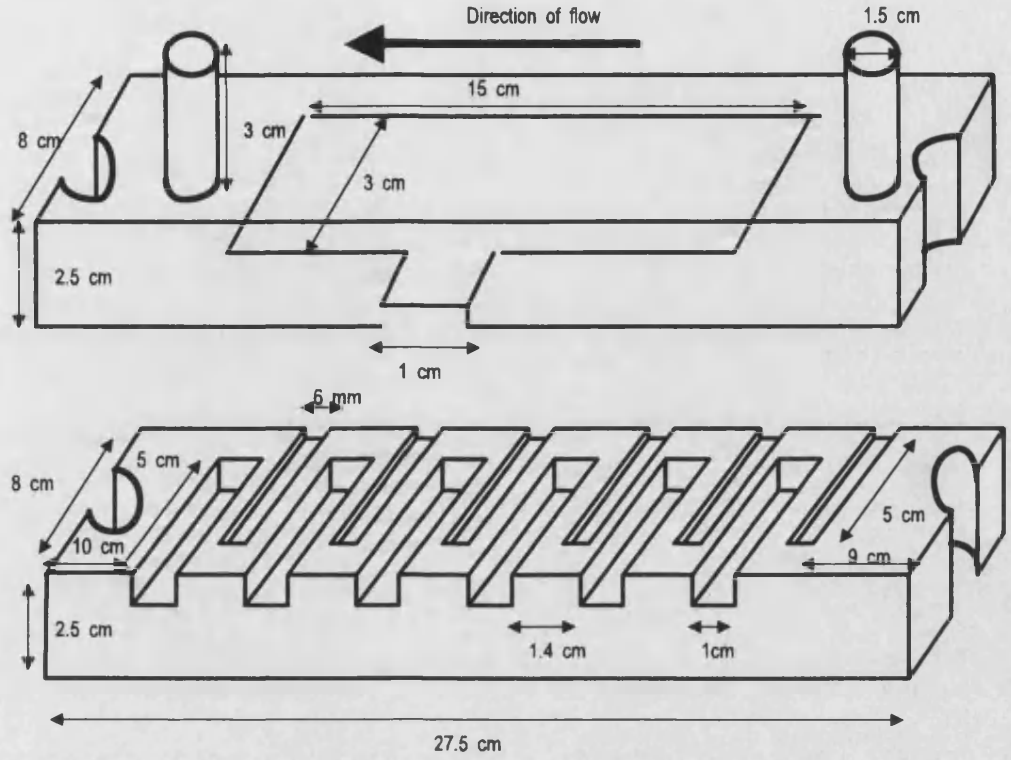

Figure 3.10 : diagram of Cell 5.

Because the cell was a little bigger, the number of bolts was increased to six. This was to ensure equal pressure over all the length. Once the cell was built no apparent problems became evident, and measurements were carried for a series of electrodes. Reproducibility was finally achieved over the study of 4 electrodes. The addition of 4 reference electrodes as well as 4 working electrodes introduced slightly more leakage problems but the consequences were minimal. The counter electrode area was increased to 15 cm^2 as there was concern about the cathode switching from chlorine reduction to hydrogen evolution at high current densities. When the cell was running at high current, a small area of the cathode was evolving gas. Since this area was placed above the anode, it indicated that the current flow lines were concentrated over the area of the anode. It also meant that it had not been possible to prevent the cathode from switching to hydrogen evolution.

The idea of using a flow cell was finally discarded because it was eventually discovered that the reference electrodes became bipolar. It would have taken too much time and development work to obtain an error-free reference electrode system in the

flow cell, and, as a result, it was concluded that another approach should be considered.

3.4.7 Cell 6

The final cell used was a classical three arm electrochemical cell that was designed originally for rotating disk electrode measurements. In the first arrangement, only the main cell was jacketed so that measurements could also be carried out at various temperatures. This was achieved by using a heating bath with a recirculating pump. The working electrodes were masked using Apiezon® wax. The counter electrode was made of 4 strips of RuO_2/TiO_2 material, and the reference electrode used in the side arm was a platinum gauze bubbled with chlorine gas. A magnetic stirrer was used in order to minimise the bubble layer problems. Although convection was not as powerful as the flow produced in the flow cell, it was great enough to ensure reproducibility. The main cell was covered with a PTFE lid in which three holes were pierced, one for the working electrode, one for the counter electrode and one for a thermometer. Chlorine was bubbled in the main body and reference electrode side arm using a cylinder and silicone rubber tubing via a polypropylene T piece. The PTFE cover ensured that the head space (less than a 1 cm high) was filled with chlorine and that the solution was easily chlorine saturated without using too much chlorine gas. A bubbler was used in the side arm to regulate the flow of chlorine to approximately 1 bubble/second.

The total volume of electrolyte used was approximately 200 ml. This was found to be far more convenient than the flow cell which required around 5 litres at a time. It also meant less chlorine gas being used. This was a significant improvement not only in terms of safety but also in terms of cost (chlorine gas cylinders cost 70 pounds for 500 grams). A piece of silicone tubing was connected to the cell so that chlorine could be scrubbed out with water in the fume cupboard. Using such a smaller volume meant that chlorine saturation was definitely achieved and that both reference and working electrode were operating satisfactorily.

The cell was modified once more by making a jacketed side arm (cell 6b). This was because the temperature difference between the side arm at room temperature and the working electrode at 65°C was such that even under chlorine saturation, the

potential difference was not equal to zero at equilibrium. At open circuit, the potential difference was in the order of 30 mV. It decreased to 0-4 mV once the reference and working electrode were at the same temperature.

The temperature dependence of the equilibrium potential difference between reference and working electrode can be explained using the Nernst[2] equation and the temperature coefficient change of standard e.m.f:

$Cl_{2(aq)} + 2\ e^- \rightarrow 2\ Cl^-_{(aq)}$ $E^\phi = 1.396$ V vs NHE (a)

$Cl_{2(g)} + 2\ e^- \rightarrow 2\ Cl^-_{(aq)}$ (b)

The temperature coefficient change of standard e.m.f for (a) is $dE^\phi/dT = -0.716$ mV K^{-1} and $dE^\phi/dT = -1.244$ mV K^{-1} for (b). The difference in coefficient values comes from the difference in solubility between chlorine dissolved in aqueous solution and chlorine gas.

Since the main body was at 60°C and the side arm was at 25°C, this led to a difference in the chlorine reaction potential, i.e. according to the Nernst equation

$$[\Delta E]_{60-25} = \Delta E^\phi * \Delta T + \Delta T * \left(\frac{R}{nF}\right) \ln\left(\frac{a_{ox}}{a_{red}}\right) \quad (3.1)$$

$$\therefore \quad [\Delta E]_{60-25} = -0.025 * 35 + 25 * \ln\left(\frac{a_{ox}}{a_{red}}\right) \text{ if } dE^\phi/dT = -0.716 \text{ mV K}^{-1} \quad (3.2)$$

or

$$[\Delta E]_{60-25} = -0.043 * 35 + 25 * \ln\left(\frac{a_{ox}}{a_{red}}\right) \text{ if } dE^\phi/dT = -1.244 \text{ mV K}^{-1} \quad (3.3)$$

Equation 3.2 and 3.3 show that the temperature difference between the side arm and main cell can produce a potential difference between the RuO_2/TiO_2 reference electrode and RuO_2/TiO_2 working electrode at equilibrium. This is only an approximation because the dE^ϕ/dT values used in this derivation only apply for studies performed in HCl. However, the order of magnitude of the potential difference is in agreement with the observed equilibrium potential difference of -25 mV when the side arm was not at the same temperature as the main body.

Figure 3.11 shows the experimental setup for cell 6b.

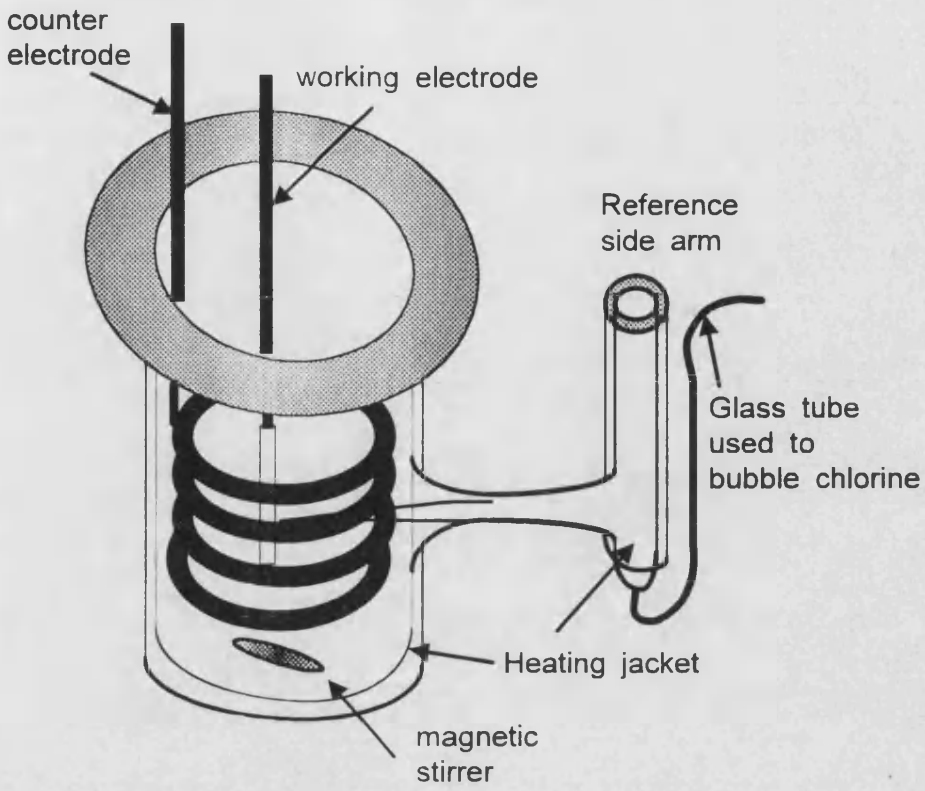

Figure 3.11 : diagram of Cell 6b, i.e. main cell and side arm heated.

3.5 Reference electrodes

Over the course of this project, 6 types of reference electrodes were tried out. This section covers each of them in detail, summarising their main advantages and problems.

3.5.1 Saturated calomel electrode

Working with chlorine was one of the reason why it was not possible to use a saturated calomel electrode (SCE) over long periods of time without causing damage to it. Chlorine reacts with the mercury inside the SCE to form a solid, i.e.

$$2\ Hg_2Cl_2 + Cl_2 \rightarrow 2\ HgCl \qquad (3.4)$$

The reaction prevents the reference electrode from operating satisfactorily over long periods of time and, since the reaction is irreversible, it damages the reference electrode. This is why it was only used for short measurements such as calibrations or experimental tests during development work.

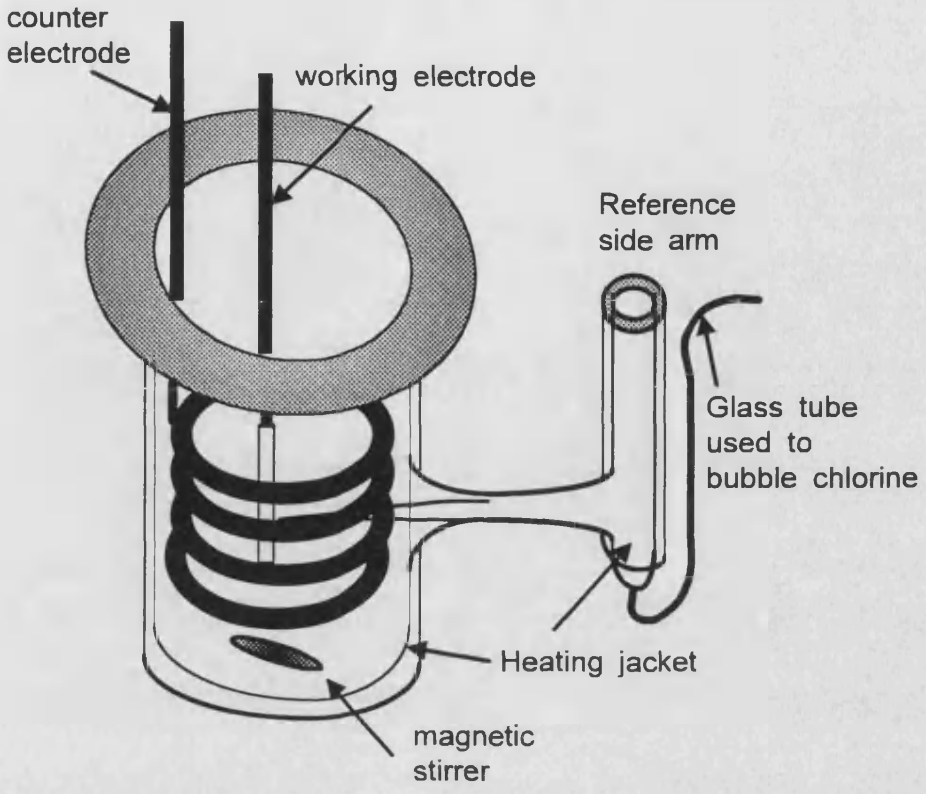

Figure 3.11 : diagram of Cell 6b, i.e. main cell and side arm heated.

3.5 Reference electrodes

Over the course of this project, 6 types of reference electrodes were tried out. This section covers each of them in detail, summarising their main advantages and problems.

3.5.1 Saturated calomel electrode

Working with chlorine was one of the reason why it was not possible to use a saturated calomel electrode (SCE) over long periods of time without causing damage to it. Chlorine reacts with the mercury inside the SCE to form a solid, i.e.

$$2\ Hg_2Cl_2 + Cl_2 \rightarrow 2\ HgCl \qquad (3.4)$$

The reaction prevents the reference electrode from operating satisfactorily over long periods of time and, since the reaction is irreversible, it damages the reference electrode. This is why it was only used for short measurements such as calibrations or experimental tests during development work.

Another reason why a SCE was not convenient reference electrode to study chlorine evolution originates from the large potential difference between the standard potential for the chlorine reaction and the calomel reaction. This gave problems with the large voltage range needed for measurements of the overpotential (typically 1.4 V), i.e. the loss of sensitivity was judged to be unacceptable.

3.5.2 Platinum reference electrodes

In order to use platinum as a reference electrode material for the study of chlorine evolution, a chlorine saturated environment was a prerequisite. The first arrangement used was in cell 2 where 1 cm of a 1 mm diameter platinum wire was exposed to solution. Apart from chlorine saturation problems, the geometric arrangement of the cell caused problems of non-uniform potential distribution along the exposed length of the platinum wire. Since the electrode was normal to the working electrode, the definition of the iR drop was problematic. The same concept applies to the measurement of overpotential. The current density distribution and current flow lines were such that the platinum wire was not measuring an equipotential line over the whole length of wire exposed. This is illustrated in figure 3.12 below :

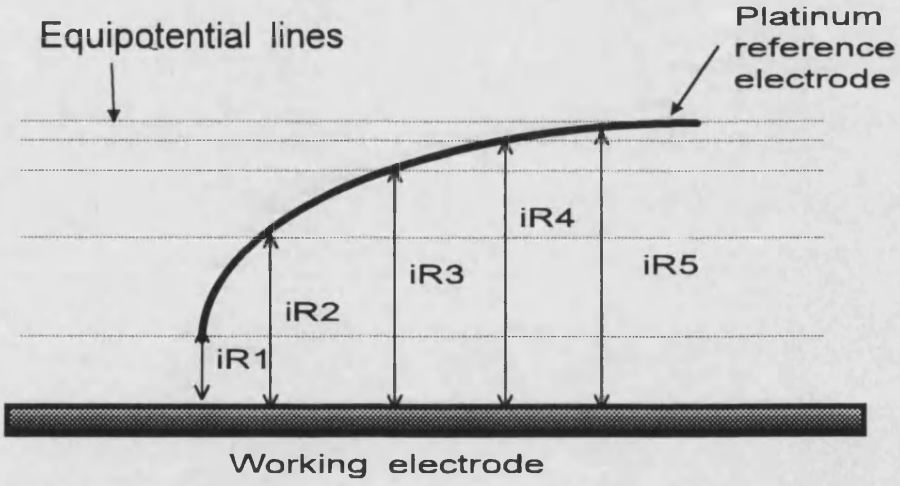

Figure 3.12 : problems with the platinum wire used as a reference electrode.

Instead of exposing a length of wire, cell 2 was modified to use a small platinum tip placed 2 mm above the working electrode as a reference electrode. The idea was that if a tip was used then there would be no problem with distance from the working electrode nor would there be any average potential value. Since no Luggin

was used, shielding was expected to be minimal. The small uncompensated resistance (less than 1 Ohm) meant that the 5 V voltage range of the ADC could be used without having to offset the baseline. However, the tip collected chlorine bubbles so that the it was no longer in contact with the solution. This problem was partly solved by using a peristaltic pump to remove trapped bubbles.

The use of a platinum reference electrode without an independent source of chlorine saturation proved to be unsatisfactory. The potential of the reference electrode was found to vary with current density. As soon as the current was interrupted, the potential of the platinum reference electrode drifted away from its initial value. At low current density the platinum electrode was not well poised at the chlorine potential, and measurements below 100 mA cm^{-2} were impossible to interpret. This preliminary study showed that the platinum tip electrode was not suitable for kinetic measurements.

Instead of relying on an external source of chlorine to produce a chlorine saturation environment, a glass encapsulated platinum wire electrode was built. In order to increase the surface area, the platinum wire was platinised[3] using the following procedure. The electrode was cleaned with conc. sulphuric acid and aqua regia, then with ultrapure water. A solution made of H_2PtCl_6 and 0.02 % lead acetate was used to platinise the electrode electrochemically for 10 minutes at 50 mA cm^{-2}. Lead acetate was added at it promotes deposition dramatically. The electrode was then rinsed with ultrapure water. The 5 mol dm^{-3} NaCl+10^{-2} mol dm^{-3} HCl was then injected into the cell and chlorine was evolved electrochemically, forming a trapped bubble as shown in figure 3.13 below. The volume of electrolyte required to fill the glass electrode was 5 ml. Once the chlorine was produced, the electrode was placed inside a small conical flask in order to minimise diffusion effects.

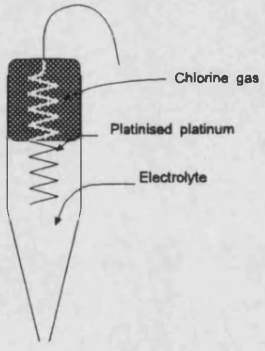

Figure 3.13 : description of the platinised platinum reference electrode.

The potential of the electrode was measured vs. SCE in dilute sulphuric acid overnight. Apart from an initial rise, the potential of the reference platinum electrode stabilised at 1380 mV. The electrode was replatinised every three weeks using the procedure described above (aqua regia was also used to clean the platinised platinum off the electrode). So long as chlorine gas was present in the electrode it kept the chlorine potential.

This electrode was used mainly with the first of the flow cells (cell 3). Unfortunately, diffusion of chlorine into the flowing unsaturated electrolyte caused the electrode to fail as a reference electrode. Since development work continued in flow cell design, this electrode was abandoned.

3.5.3 RuO_2/TiO_2 reference electrodes

It was concluded that a flow cell would require an internal reference electrode. It was also decided to use the same RuO_2/TiO_2 material for all electrodes. This was an ideal material because of its high surface area and specificity towards chlorine evolution. The reference electrodes were 6 mm wide, 1 cm long and placed upstream so that chlorine bubbles produced by the working electrodes would not block the surface area of the reference electrode. As mentioned previously, chlorine saturation was a prerequisite for stable reference electrode operation. In view of the quantity of electrolyte used, it proved impossible to saturate the solution with chlorine. However, it failed to act as a reference electrode for a more important reason. The dimensions of the flow cell and magnitude of potential required to pass up to 1100 mA were such that the reference electrodes became bipolar.

During current flow, the potential distribution along the length of the flow channel was such that a significant potential difference was induced between one edge of the reference electrode and the other. The magnitude was sufficient enough to cause the reference electrode strip to act as a bipolar electrode, i.e. one side of the reference electrode behaved as an anode and the other as a cathode. Although no current passed through the external circuit, internal currents flowed from one edge of the reference electrode to the other in order to maintain overall zero current. The consequence of this was the potential of the reference electrode drifted negative of the chlorine potential.

The reference electrode only acted as a bipolar electrode when the current was flowing through the external circuit. Once the current flow was interrupted, the potential distribution along the reference electrode became uniform. The reference electrode potential started to relax back to its initial value prior current flow through the external circuit. The bipolar behaviour meant that the reference electrode was not working properly. It was therefore impossible to measure the decay of the anode overpotential as a function of time during interrupt measurements.

Newman[4] has treated the potential distribution along the length of insulating material in a parallel plate flow cell. In this model, the length of the anode and cathode are identical. The aim of this analysis was to study the dependence of the potential variation across the reference electrode as a function of distance from the working electrode. The assumptions are that the anode and cathode have the same kinetic behaviour and that concentrations variations are negligible.

The only difference between this model and the flow cells used in this project is that the length of the cathode is 15 times bigger than that of the anode. The effects of this will be discussed later.

The following calculations are used to highlight the problem of bipolarity of the reference electrode. The following diagram show the cell geometry assumed in Newman's case.

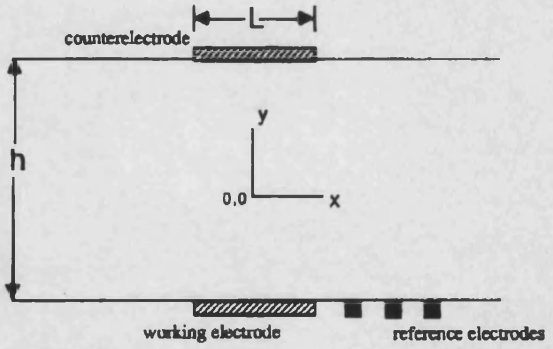

Fig. 1. Cell geometry, showing the two characteristic lengths, the co-ordinate system, and possible reference electrode placements.

Figure 3.14 : parallel plate cell geometry used in Newman's analysis.

The next plot shows the calculated potential variation along the length of the insulating material during current flow through the external circuit. The potential as

well as the distance along the x-axis have been normalised so that results do not depend on the chosen dimensions.

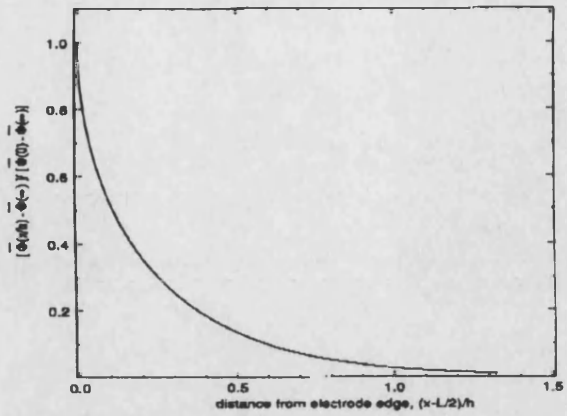

Fig. 2. Primary potential distribution along the insulator, measured from the edge of the electrode, for h/L = 0, h/L = 0.5, and h/L = 1.0.

Figure 3.15 : potential variation along the x-axis during current flow.

In this project, the interelectrode gap (h) was of 2.5 cm, the length of the anode was 1cm and the length of the cathode was of 15 cm. The electrode width was of 0.6 cm. Therefore h/L= 0.16. Let X_n be the edge of the reference electrode nearest to the working electrode and X_f be the edge furthest away from the anode.

Since the reference electrode was placed 3 mm away from the working electrode this corresponds to X_n = 0.8 cm and X_f = 1.4 cm in Newman's model, i.e. there is a 47 % difference between the potential at the edge of the reference electrode nearest to the anode and the potential at the edge furthest away from it.

Approximately 4 V were required to produce 1 A cm^{-2}. Based on Newman's model, the reference electrode potential would have been of 1.88 V at the edge closest to the anode and 0.88 V and the edge furthest away. As a result, there would be a 1 V potential drop along the width of the reference electrode. This is significant enough to make the reference electrode act as a bipolar electrode. In order for the potential drop along the reference electrode to be less than 1% in this project, its width would have had to be 0.02 cm. This would have meant using thin wires as opposed to strips. However, it would have been impossible to machine such dimensions out of PMMA accurately to prevent significant leakage from taking place.

Further experiments were carried out in order to confirm that the reference electrode was acting as a bipolar electrode. The geometry of the flow cell was

reproduced in a three way electrochemical cell. A 6 mm wide strip was placed parallel to the working electrode and sticky PTFE tape was used to gradually narrow the width of the reference electrode. The potential variation of the reference electrode was measured with respect to a SCE for each configuration during interrupt measurements. Figure 3.16 shows the different configurations :

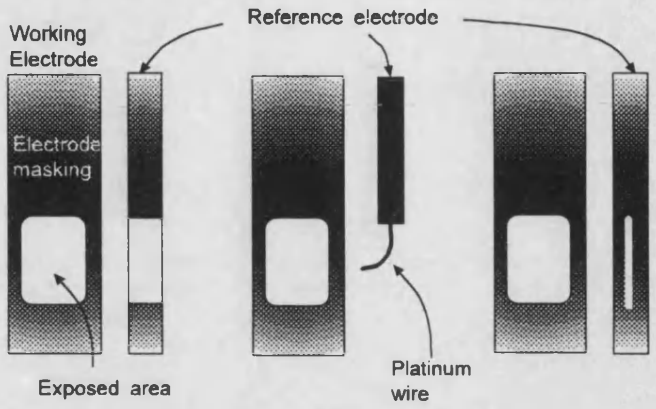

Figure 3.16 : different reference electrode/working electrode geometries tried to investigate bipolar effect.

Ideally, the potential of the reference electrode is constant. What one measures is usually the potential difference between the working and reference electrode, i.e. E + iR where E is the potential difference and iR is the ohmic contribution coming from the solution resistance between the working and reference electrode. On interruption of the current, one expects the iR term to disappear 'instantaneously'. One can then measure the decay of potential E with time. However, this analysis assumes that the potential of the reference electrode remains constant. This only applies if there are no currents flowing through the reference electrode and concentration of potential dependent species, i.e. Cl^- and Cl_2, are constant.

As mentioned above, the iR contribution between the working and reference electrode disappears 'instantaneously' when the current is interrupted. The potential difference between the working and reference electrode can therefore be measured. Since the potential of the reference electrode is constant then one can measure the decay of the working electrode potential. This was not the case when the width of the RuO_2/TiO_2 strip used as reference electrode was left unmasked. Instead of the potential decaying exponentially to the chlorine potential after interruption, it jumped

to a more negative value than the chlorine potential. The whole decay back to the value of chlorine potential lasted approximately 70 ms.

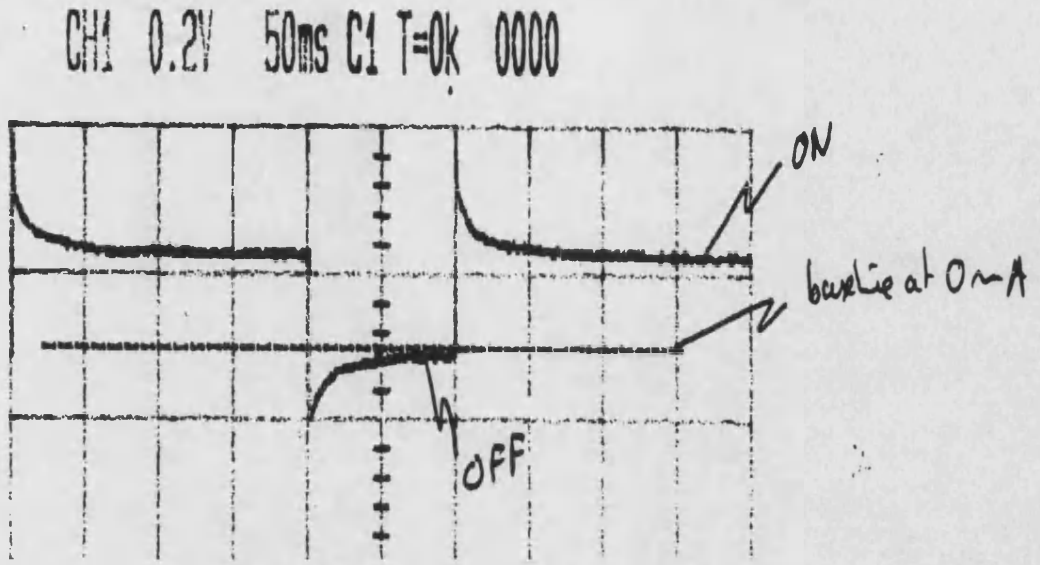

Figure 3.17 : Shape of the potential difference between working and reference electrode before and after interruption of the external current when the reference electrode width was significant.

Figure 3.17 shows that the potential of the 'bipolar' electrode goes cathodic of the reference electrode potential. This behaviour disappeared when the width of the reference electrode was narrowed down to a thin strip using sticky PTFE, as shown in figure 3.18 below

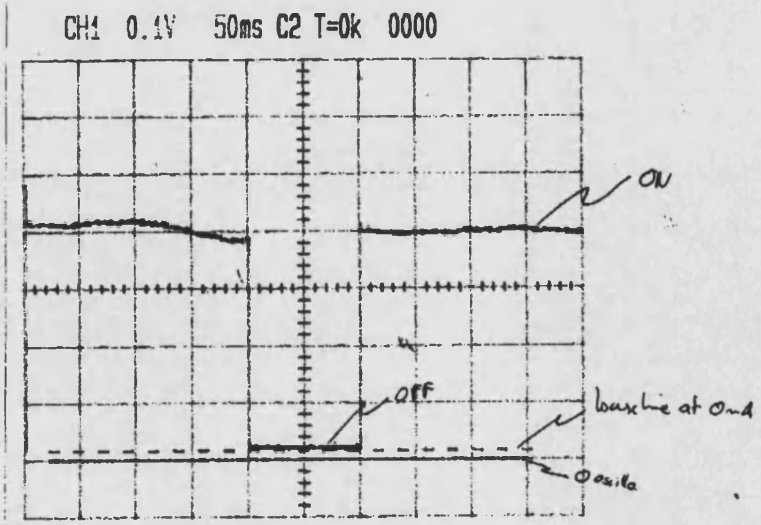

Figure 3.18 : potential difference between working and reference electrode when the width of the reference electrode is small.

A further experiment was carried out using a platinum 1 mm diameter platinum wire. A small exponential decay that lasted 10 ms was observed. Although no decay should have been observed this was attributed to the fact that the wire was not equidistant from the working electrode as in the case where sticky PTFE was used. This also confirmed that the platinum wire used as a reference electrode in the cell was operating satisfactorily.

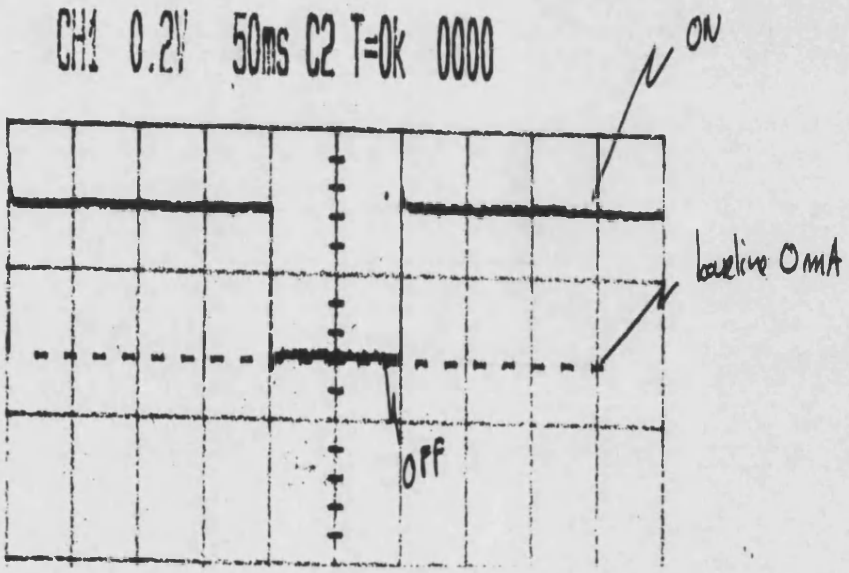

Figure 3.19 : potential difference between working and reference electrode when using a platinum wire as reference electrode that is not equidistant from the working electrode.

In summary, these experiments showed that the cathodic shift of the potential difference between working and reference electrode with respect to the chlorine potential was a function of current density. Since the OCPD measurements and Tafel plots were measured with respect to the reference electrode strip, this explains why the overpotentials were initially surprisingly high. This is because the reference electrode potential was not constant and because the greater the current density was the more cathodic the potential difference was with respect to the chlorine potential just after interruption. The effect of bipolarity on Tafel plots is shown in fig 3.20 below :

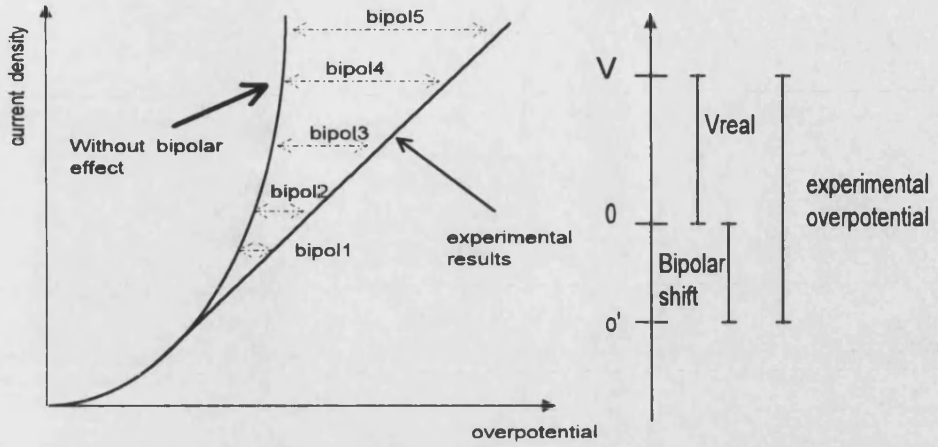

Figure 3.20 : effect of reference electrode bipolar behaviour on Tafel plots.

The conclusions of this work was that the RuO_2/TiO_2 strips used as reference electrodes acted as bipolar electrodes because the width of the reference electrode exposed to solution was sufficiently big that the reference electrode could not be considered as equidistant from the working electrode and because the voltages required to pass currents up to 1 A cm^{-2} generated a potential difference across the width of the reference electrode that allowed internal currents to flow in it. This is why the use of flow cells was finally abandoned. Too much work had already been spent and there was no more time to carry on in this direction.

1 D. Pletcher, F.C. Walsh, *Industrial Electrochemistry* - 2nd ed, Blackie A&P, New York, 1993

2 E.B. Smith, *Basic chemical thermodynamics* - 3rd ed.,Oxford chemistry series, 1987

3 D.J.G. Ives, *Reference Electrodes*, 1961,106-111

4 J. Newman, A.C. West, *J. Electrochem. Soc.*, 138(6), 1991

CHAPTER FOUR

Chapter Four
Cyclic Voltammetry
and Impedance Spectroscopy

This chapter describes results obtained from cyclic voltammetry (CV) and impedance spectroscopy experiments. The results from both techniques have been grouped together because they yield information about the double layer capacitance and porous behaviour of electrodes.

4.1 Cyclic Voltammetry

Cyclic voltammetry is a very versatile and powerful electrochemical technique. The purpose of using it in this project was to determine the double layer capacitance value and estimate whether there was a link between degradation and porous electrode behaviour. It was also used as a crude method to determine whether the electrodes were properly masked : by running a CV before and after a complete series of experiments, it was possible to determine whether leakage of electrolyte had taken place.

4.1.1 Theory

Since the theory of cyclic voltammetry is discussed in detail elsewhere[1,2], only aspects relevant to this project will be derived in this section.

Previous work[3] has suggested that the double layer capacitance in commercial RuO_2/TiO_2 electrodes is a function of their ruthenium concentration. Trasatti et al[4,5,6,7] have also established that the double layer capacitance of RuO_2/TiO_2 electrodes is a function of the initial ruthenium concentration. However, the interpretation of the double layer capacitance is controversial in the case of RuO_2/TiO_2 electrodes. It is not clear whether the electrode should be treated as a 'porous metal' or as a redox active surface with properties analogous to those of redox polymers, for example.

If ruthenium leaches steadily with during degradation in the alkali wear pot, cyclic voltammetry should, in principle, detect it. The double layer capacitance can be calculated from a cyclic voltammogram measured in the 'charging region', where the only process taking place is charging/discharging of the double layer.

The current density measured by cyclic voltammetry can be derived by noting that

$$C_{dl} = \frac{dQ}{dE} \tag{4.1}$$

where C_{dl} is the double layer capacitance. It follows that

$$j = \frac{dQ}{dt} = \frac{dQ}{dE} * \frac{dE}{dt} = C_{dl} * \nu \tag{4.2}$$

where $\nu = dE/dt$ is the sweep rate. It follows that the double layer capacitance is given by

$$C_{dl} = \frac{j}{\nu} \tag{4.3}$$

In an ideal case where the electrode is flat, non porous and Cdl is potential independent, the CVs are box shaped. This is illustrated in the figure below :

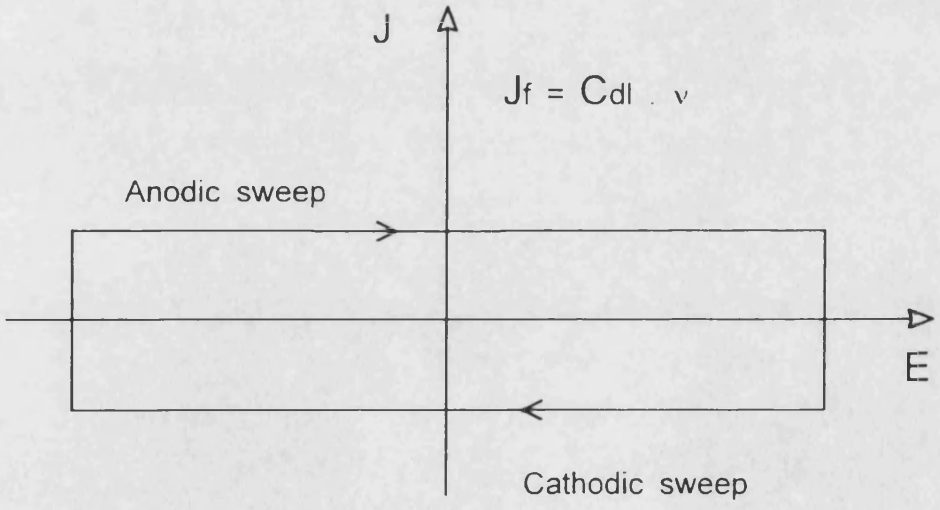

Figure 4.1 : cyclic voltammogram for an ideal electrode in the charging region where C_{dl} is independent of potential.

It is not expected that commercial RuO_2/TiO_2 electrodes will behave ideally since their surface roughness factor is of the order of hundreds as measured by BET[8]. Porosity or surface roughness can influence the shape of CVs in the charging region. Instead of being box-like, the CVs exhibits a slow transition on sweep reversal. This can be attributed to the RC time constant of the electrode which is very large for porous electrodes with high C_{dl} values. An example of this shown in the figure below.

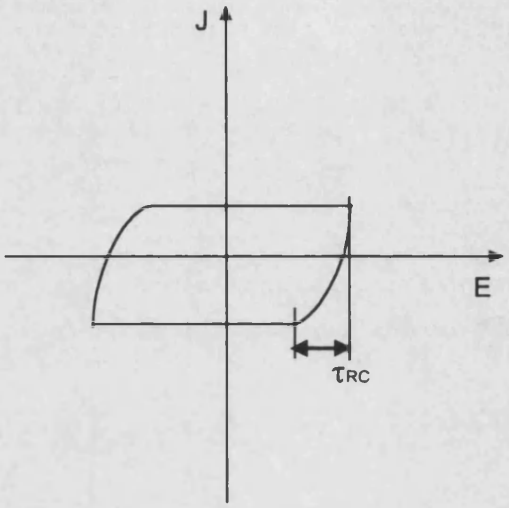

Figure 4.2 : typical shape of a porous electrode cyclic voltammogram. τ_{RC} is the RC time constant.

In practice, the experimental cyclic voltammogram deviated from the shape illustrated in figure 4.2. An example is given in figure 4.3.

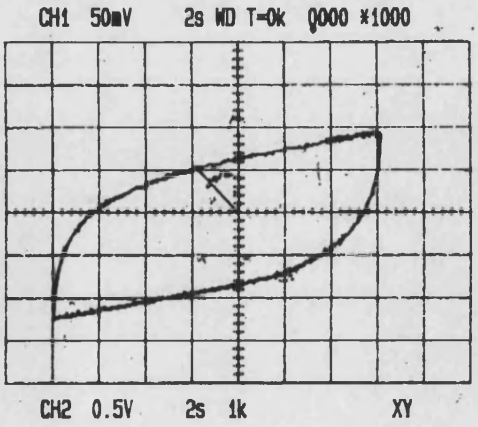

Figure 4.3 : cyclic voltammogram for degraded sample M58 at 100 mV s^{-1} and 60°C.

It can be seen that the CV is 'tilted up'. This is attributed to the fact that some leakage of electrolyte occurs under the insulating wax because the electrode is porous and hydrophobic. The time constant associated with the leakage path is sufficiently high that on the time-scale of the CV, the charging current contribution obeys Ohm's law, i.e.

$$i = \frac{V}{R_{leakage}} \tag{4.4}$$

where $R_{leakage}$ is the resistance associated with a thin film of electrolyte that creeps under the insulating wax. This effect is unavoidable, but does not affect substantially the value of C_{dl} determined this way : C_{dl} was determined from the difference between the currents on the forward and reverse scan, so that the influence of leakage contribution is eliminated. In cases where the leakage contribution changed with time, it was concluded that the masking agent was not satisfactory (e.g. PTFE tape). By contrast, the Apiezon® wax generally gave CVs which varied little with time, indicating that it was a satisfactory masking agent.

4.1.2 Results and Discussion

Analysis of cyclic voltammetry data showed that all samples exhibited the same type of cyclic voltammogram as sample M58 shown in figure 4.3. As a result, one can conclude that the RuO_2/TiO_2 samples exhibited porous type behaviour as well as being subject to leakage. However, since the shape of the CV was found to be independent of time, this meant that variation of the active surface area as a function of time was not going to be a problem. This also meant that an adequate masking agent had finally been found.

The analysis of the shape of the CVs for each series revealed that the RC time constant increased as a function of degradation. Since the magnitude of the charging current did not increase significantly, this implies that the resistance component must have increased. Since the RC time constant is too high to be attributed to the solution resistance in series with C_{dl} (the solution resistance is less than 1 Ω), this increase in resistance component must be due to an increase in electrode porosity.

The following tables summarise results obtained for the 3 series of 8 electrodes, i.e. M3x, M4x and M5x (where $1 \leq x \leq 8$). Each electrode was degraded to a pre-set increase of the alkali wear test running potential ($\Delta V_{running}$) (See chapter 2).

Strip	C_{dl} / mF	Area / cm^2	C_{dl} / mF cm^{-2}	ΔV / mV
M31	11	0.82	13.5 ± 0.7	0
M32	16	0.76	21.0 ± 1.1	192
M33	17	0.82	20.8 ± 1.1	250
M34	16	0.73	22.0 ± 1.1	400
M35	19	1.14	16.7 ± 0.8	580
M38	19	0.79	23.9 ± 1.2	900
M36	16	0.72	22.2 ± 1.1	950
M37	16	0.77	20.8 ± 1.1	1500

Table 4.1 : summary of double layer capacitance values calculated from cyclic voltammetry for the M3x series.

Strip	C_{dl} / mF	Area / cm^2	C_{dl} / mF cm^{-2}	ΔV / mV
M41	14	0.83	16.9 ± 0.8	1 hour
M42	15	0.70	21.4 ± 1.1	0
M43	15	0.71	21.1 ± 1.1	230
M34	14	0.75	18.6 ± 0.9	360
M45	14	0.70	20.0 ± 1.0	340
M46	19	0.85	22.3 ± 1.1	370
M47	13	0.83	15.9 ± 0.8	1470
M48	14	0.83	16.9 ± 0.8	2090

Table 4.2 : summary of double layer capacitance values calculated from cyclic voltammetry for the M4x series.

Strip	C_{dl} / mF	Area / cm^2	Cdl / mF cm^{-2}	ΔV / mV
M51	6.8	0.70	11.4 ±0.6	0
M52	12	0.72	17.1 ±0.8	120
M53	18	0.80	22.7 ±1.1	600
M55	15	0.73	21.4 ±1.1	960
M54	19	0.91	21.1 ±1.1	1000
M56	16	0.72	22.8 ±1.1	1800
M57	12	0.71	17.1 ±0.9	2460
M58	6-8*	0.73	11.4 ±0.6	4500

Table 4.3 : summary of double layer capacitance values calculated from cyclic voltammetry for the M5x series.

Analysis of tables 4.1 to 4.3 revealed two key features. The first observation is that the double layer capacitance values are very high at around 20 mF cm^{-2} and comparable to supercapacitor values. As mentioned earlier, two possible models have been used to define the double layer capacitance for RuO_2/TiO_2 anodes. The first one is that RuO_2/TiO_2 anodes can be considered as a metal, i.e. there is a large excess of free electrons. This means that the double layer capacitance value must be comparable to that of platinum, for example. In the case of hydrogen on platinum C_{dl} is equal to approximately 30 μF cm^{-2}. The apparent value of 20 mF cm^{-2} for RuO_2/TiO_2 electrodes can be explained by the fact that RuO_2/TiO_2 electrodes are rough. BET experiments carried out by ICI revealed that the RuO_2/TiO_2 coating had a surface roughness factor ranging from 300 to 1000, i.e. the anode coating is *microporous*. The apparent double layer capacitance measured by cyclic voltammetry is therefore defined as

$$C_{dl}(app) = C_{dl}(true) \times \Re \qquad (4.5)$$

where $C_{dl}(app)$ is the double layer capacitance measured by cyclic voltammetry, $C_{dl}(true)$ is the true double layer capacitance per geometric unit area and $\Re$ is the surface roughness factor as measured by BET experiments. If we assume that $\Re$ = 500 then if $C_{dl}(app)$ = 20 mF cm^{-2} then $C_{dl}(true)$ = 40 μF cm^{-2}, i.e. comparable to platinum.

It must noted that it is assumed that the BET experiments probe the same surface area as that exposed to the liquid (this is dependent on the oxide/solution interface angle).

The second model assumes that the double layer capacitance of RuO_2/TiO_2 anodes is due to surface redox processes, i.e. electrons are located on specific sites, and the double layer capacitance is dependent on the oxidation state of ruthenium, i.e.

$$Ru^{M-1} \rightleftharpoons Ru^{M} \rightleftharpoons Ru^{M+1} \text{ etc...} \qquad (4.6)$$

If each of the oxidation states was well defined then cyclic voltammetry should exhibit well defined and separate peaks for each of the oxidation states. If the charge associated with each peak was 200 μC (e.g. for redox polymers) and the half peak height was 59 mV then the associated double layer capacitance would be 40 mF cm^{-2}. The fact that cyclic voltammograms do not show well resolved peaks can be explained by the fact that the peaks corresponding to ruthenium oxidation states are not well resolved and that they are super-imposed to each other. This is illustrated in figure 4.4 below :

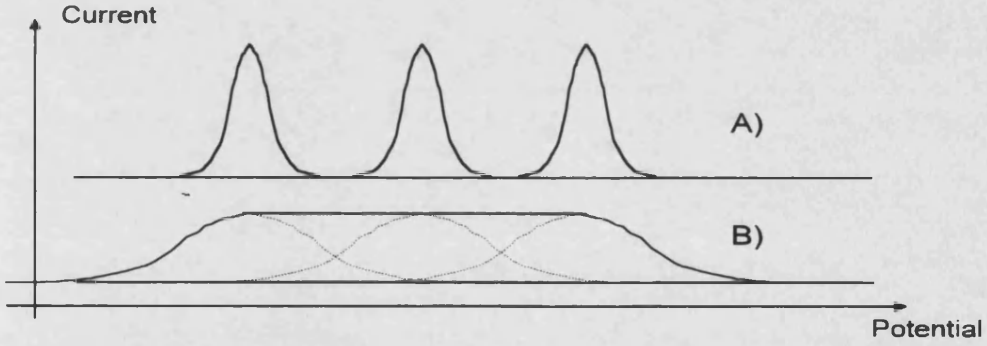

Figure 4.4 : shape of the cathodic part of a cyclic voltammogram for RuO_2/TiO_2 electrode when A) the oxidation states have well defined potentials B) the oxidation peaks are not well defined (the solid line represent the apparent shape of CV, i.e. the sum of all peaks)

Calculations reveals that this model would give double layer capacitance values of the order of 20 mF cm^{-2} for the 'squashed peaks' model shown in figure 4.4b.

In the absence of additional information, it is therefore not possible to conclude whether the RuO_2/TiO_2 electrode should be treated as a metal or a redox system..

The second key feature is the dependence of the double layer capacitance on the increase in alkali wear pot running potential. The next three figures show the dependence of the double layer capacitance on the increase in alkali wear pot running potential for series M3x, M4x and M5x :

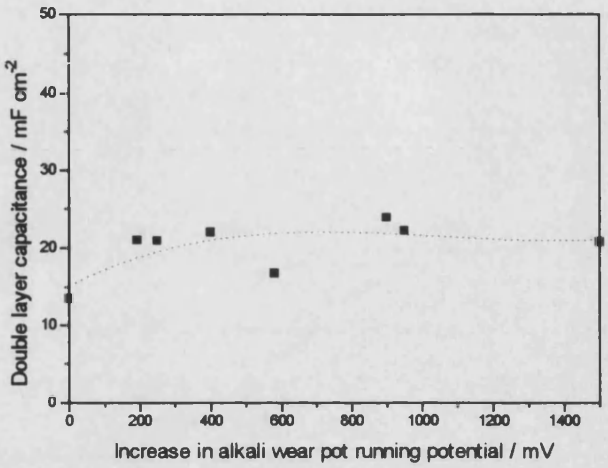

Figure 4.5 : variation of the double layer capacitance as a function of increase in alkali wear pot running potential for the M3x series.

Figure 4.5 shows that after an initial increase, the double layer capacitance seems to remains constant up to a 1500 mV increase in the alkali wear pot running potential. The average double layer capacitance value for degraded samples in this range is 20 mF cm^{-2} .

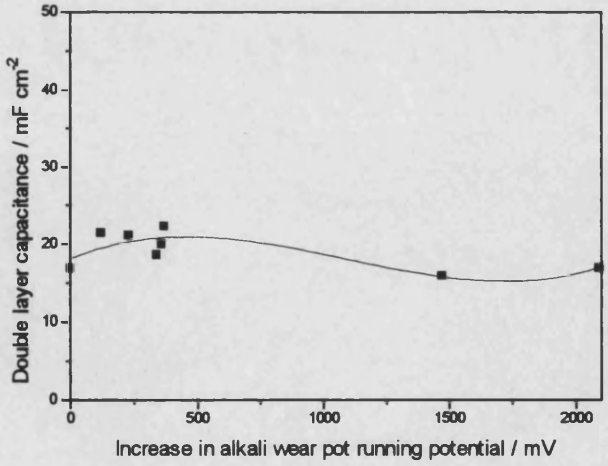

Figure 4.6 : variation of the double layer capacitance as a function of increase in alkali wear pot running potential for the M4x series.

In the case of the M4x series, the deviation from the ideal box-shaped CV increased with the extent of degradation (See CVs at the end of this section). Table 4.2 shows that the double layer capacitance values of M47 and M48 are substantially lower than those of samples M42-M46. Whereas M42 to M46 all seem to be at around 20 mF cm^{-2} (which is in agreement with results from the M3x series), samples M47 and M48 have double layer capacitance values in the order of 16 mF cm^{-2}. This is illustrated in figure 4.5 where a polynomial fit was used as a visual aid to show that the plot of the double layer capacitance as a function of increase in alkali wear pot running potential goes through a maximum.

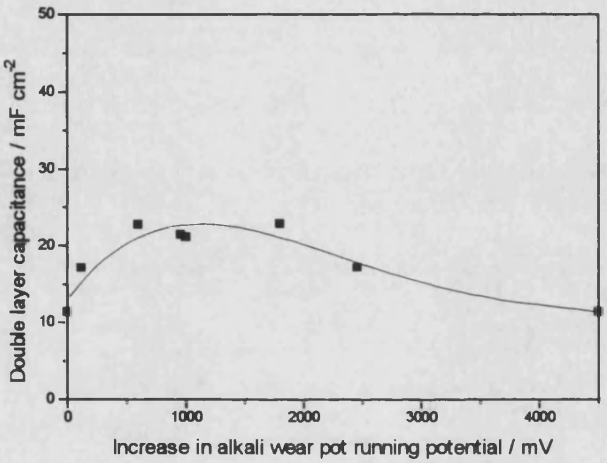

Figure 4.7 : variation of the double layer capacitance as a function of increase in alkali wear pot running potential for the M5x series.

For the M5x series, figure 4.7 seems to confirm the trend observed for series M3x and M4x. It shows more clearly than figure 4.5 and 4.6 that the double layer capacitance value passes through a maximum. The next figure shows the cumulated CV data for the variation of the double layer capacitance as a function of increase in alkali wear pot running potential.

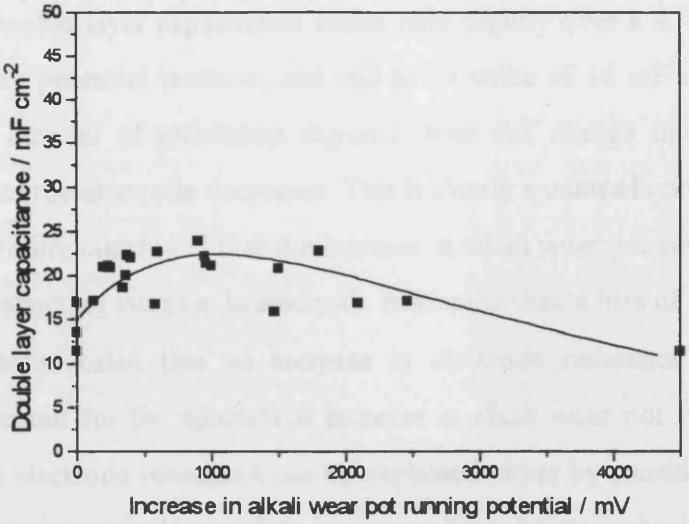

Figure 4.8 : CV cumulated data for the variation of the double layer capacitance as a function of increase in the alkali wear pot running potential for the RuO_2/TiO_2 commercial electrode.

A possible explanation of the initial increase of C_{dl} is that the electrode surfaces were initially contaminated and that evolving chlorine at high current densities cleaned the surface. Alternatively, it is possible that evolving chlorine causes some reorganisation of the electrode surface so as to expose a greater density of active ruthenium sites.

The trend in figure 4.8 is remarkable. The changes in C_{dl} are less than a factor of 2 over the entire range of degradation voltages. When the alkali wear pot running potential has increased by 4 V, the double layer capacitance is still around 16 mF cm^{-2}. Clearly, the electrode still behaves as expected for RuO_2/TiO_2 electrodes in cyclic voltammetry. It therefore seems very likely that the increased voltage in the alkali wear pot does not arise from loss of catalytic activity. The simplest explanation is that degradation increases the electrode resistance. Since the current is 2 A cm^{-2} in the alkali wear pot an additional resistance of just 1 Ω suffice to explain the increase in running potential.

4.1.3 Conclusions

Cyclic voltammetry has revealed a major surprise. The substantial increase in alkali wear pot running potential was assumed to indicate loss of catalytic activity.

However, the double layer capacitance varies only slightly over a 4 V range of alkali wear pot running potential increase, and still has a value of 16 mF cm^{-2}. This would imply that the amount of ruthenium exposed does not change much although the overall activity of the electrode decreases. This is clearly a contradiction.

It is therefore concluded that the increase in alkali wear pot running potential is more likely to reflect an increase in electrode resistance than a loss of catalytic activity. Calculations has revealed that an increase in electrode resistance of just 1 Ω is sufficient to account for the substantial increase in alkali wear pot running potential. This increase in electrode resistance can be explained either by considering an increase in electrode porosity or build-up of an insulating layer between the RuO_2/TiO_2 anode coating and the titanium substrate. Both models will be examined in chapter 8.

4.2 Impedance Spectroscopy

Impedance spectroscopy is a well-developed technique for obtaining information about parameters such as the double layer capacitance as well as the solution and charge transfer resistances. It also leads to a convenient way of modelling an electrochemical system : in order to obtain quantitative information, it is standard practice to model the electrochemical system in terms of so-called equivalent circuits consisting of resistances, capacitors and inductors. It was hoped that impedance spectroscopy would allow to determine whether the RuO_2/TiO_2 electrodes exhibited porous electrode behaviour. Impedance spectroscopy was also carried out on the RuO_2/TiO_2 system in order to check whether the mechanism of chlorine evolution on mixed oxides was the same as on platinum[9,10,11] electrodes.

4.2.1 Theory

Since the theory of impedance spectroscopy has been described in detail elsewhere[1,2,12] only aspects relevant to this project will be treated in this section.

Consider a purely sinusoidal voltage. It can be expressed as follows :

$$E = E_0 \sin(\omega t) \qquad (4.7)$$

where E_0 is the amplitude, ω is the angular frequency and E is the observed voltage at time t. Figure 4.9 shows E as a function of time :

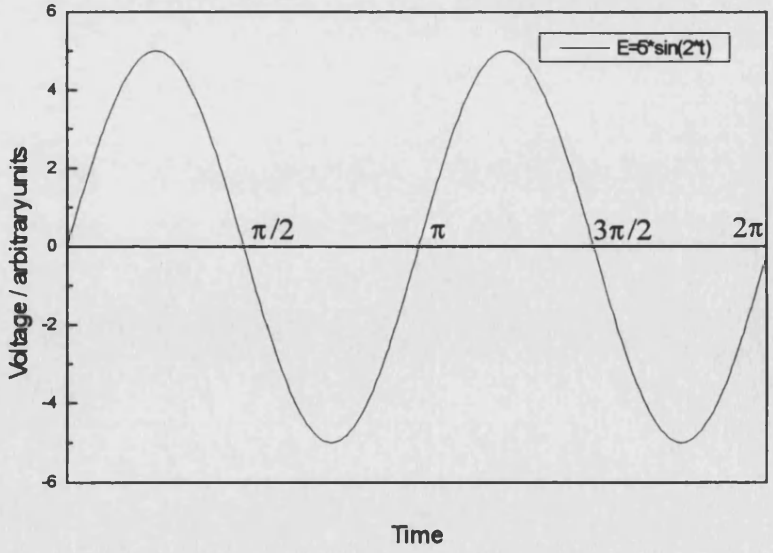

Figure 4.9: typical alternating sinusoidal voltage.

When such a voltage is applied to a circuit consisting of linear elements, the resulting current has the same frequency but its phase is different, i.e.

$$I = I_0 \sin(\omega t + \phi) \qquad (4.8)$$

where I is the current at time t, I_0 is the current magnitude and ϕ is the phase angle between I and E. The amplitudes and phases of the current and voltage are related by the following equation :

$$E = \mathbf{Z}\, I \qquad (4.9)$$

where **Z** is the impedance.

At this point, it is convenient to represent E and I using the concept of phasors. E and I are represented as vectors in a complex plane or Argand diagram : in such a plane, the voltage and current can be represented as vectors rotating around the origin at the same frequency ω and with an angle between them of ϕ, as illustrated in figure 4.10 below :

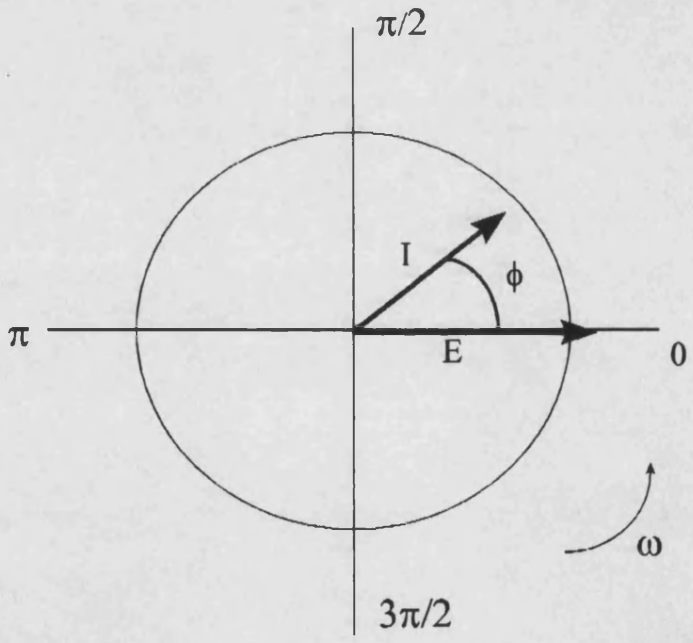

Figure 4.10 : phasor diagram representing current and voltage vectors separated by a phase angle ϕ

Since the current and voltage are rotating at the same frequency, the phase angle in between them remains constant. By convention, the voltage vector is always

aligned with the horizontal axis and the phase angle is therefore the angle in between the horizontal axis and the current vector.

In mathematical terms, the components of the current and voltage phasors can be represented in the Argand diagram with the *real* component on the abscissa axis and the *imaginary* component on the ordinate axis. The impedance Z can therefore be expressed in terms of its real and imaginary components according to the following equation :

$$\mathbf{Z} = Z' + jZ'' \qquad (4.10)$$

where the imaginary part, Z'', is multiplied by $j = \sqrt{-1}$. The next figure shows a representation of E in terms of I and the complex components of the impedance Z :

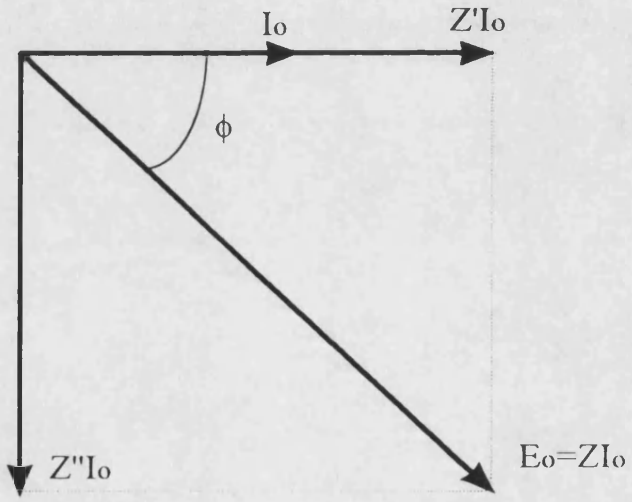

Figure 4.11 : relationship between voltage, current and impedance.

During an impedance spectroscopy measurement, the frequency of the applied voltage modulation is varied over a wide range and measurements of the real and imaginary components of the impedance are measured for each frequency. Results are then usually displayed in graphical formats. Three types of plots are usually used in impedance spectroscopy.

1. Complex plane plot : the imaginary component of the impedance is plotted as a function of its real component for a range of frequencies.
2. Bode phase angle plot : ϕ is plotted as a function of $\log(\omega)$
3. Bode impedance plot : $\log(Z)$ is plotted as a function of $\log(\omega)$

Examples of these plots and conclusions that can be obtained from them will be shown later.

Impedance of a resistor

According to Ohm's law, the voltage and current are related by

$$E_0 = RI_0 \tag{4.11}$$

where R is the value of the resistance. As a result, the impedance of a pure resistor is a single point on the real axis at Z' = R.

Impedance of a capacitor

Consider an ideal capacitor, C, that has a stored charge Q. Q is defined as follows :

$$Q = CE$$

where E is a sinusoidal voltage as described earlier, i.e. equation 4.7. The current flowing through the capacitor is

$$I = \frac{dQ}{dt} = \left(\frac{dQ}{dE}\right)\left(\frac{dE}{dt}\right) = C\frac{dE}{dt} \tag{4.12}$$

Substituting equation 4.7 into equation 4.12 gives

$$I = \omega C E_0 \cos(\omega t) \tag{4.13}$$

which can be rewritten as

$$I = \omega C E_0 \sin\left(\omega t + \frac{\pi}{2}\right) \tag{4.14}$$

As a result, comparison of equation 4.14 with equation 4.7 gives the following expression of E_0 as a function of I_0

$$E_0 = -j\frac{I_0}{\omega C} = -jZ_C I_0 \tag{4.15}$$

where $Z_C = 1/\omega C$ is the impedance of the ideal capacitor. Equation 4.15 also indicates that the current has a 90° phase angle relative to the voltage and that the magnitude of the impedance is an inverse function of the angular frequency.

Impedance of a resistor in series with a capacitor

The total voltage drop across a resistor in series with a capacitor is the sum of the voltage drops across each individual elements. Therefore

$$E_{0,\,TOTAL} = E_{0,\,RESISTOR} + E_{0,CAPACITOR} \tag{4.16}$$

which leads to

$$E_{0,\,TOTAL} = I_0(Z_R+Z_C) = I_0\left(R - j\frac{1}{\omega C}\right) = Z_{TOTAL}I_0 \tag{4.17}$$

The next three figures show the complex plane plots for circuits involving a resistor, a capacitor and a resistor in series with a capacitor :

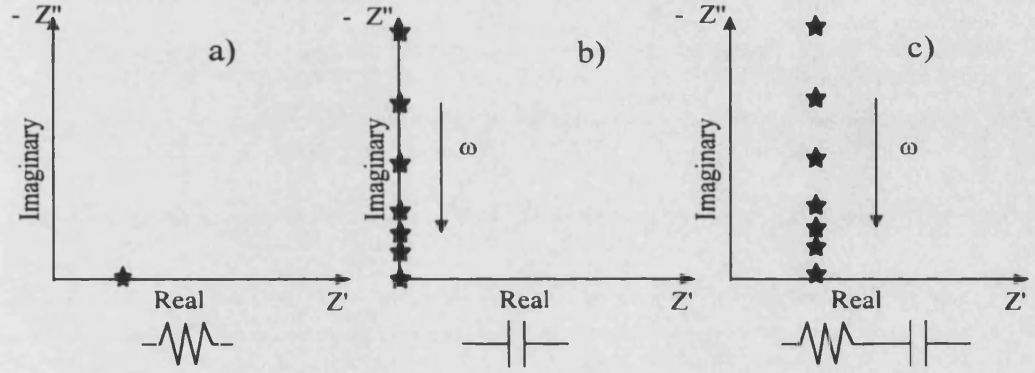

Figure 4.12 : complex plane plots for a) a resistor b) a capacitor and c) a resistor and capacitor in series.

The magnitude of the impedance obeys the same rule as that for calculating the magnitude of a vector expressed in Cartesian co-ordinates, i.e.

$$Z = \sqrt{(Z')^2 + (Z'')^2} = \sqrt{R^2 + \left(\frac{1}{\omega C}\right)^2} \tag{4.18}$$

and the phase angle can be calculated from

$$\tan\phi = \frac{Z''}{Z'} = \frac{1}{R\omega C} \tag{4.19}$$

Impedance of a resistor in parallel with a capacitor

For a circuit made of components in parallel, the inverse of the total impedance is equal to the sum of the inverses of the individual components, i.e.

$$\frac{1}{Z_{TOTAL}} = \frac{1}{Z_{RESISTOR}} + \frac{1}{Z_{CAPACITOR}} = \frac{1}{R} + \frac{\omega C}{j} \qquad (4.20)$$

which leads to

$$Z_{TOTAL} = \frac{R - jR^2\omega C}{1+(R\omega C)^2} \qquad (4.21)$$

Equation 4.21 shows that as ω is varied, the values of Z vary along a semicircle of diameter R and of origin co-ordinates (R/2,0) in the complex plane. Equation 4.21 can be rearranged as follows :

$$Z_{TOTAL} = \frac{R}{1+(R\omega C)^2} - j\frac{R^2\omega C}{1+(R\omega C)^2} \qquad (4.22)$$

Equation 4.22 shows that for small values of ω, the imaginary part tends towards to 0 and the real part towards R. The total impedance then behaves as resistor through which flows most of the current. At high values of ω, the real part tends to 0 and the imaginary towards 1/RωC. The total impedance then behaves as a capacitor. Figure 4.13 illustrates the behaviour of such a circuit :

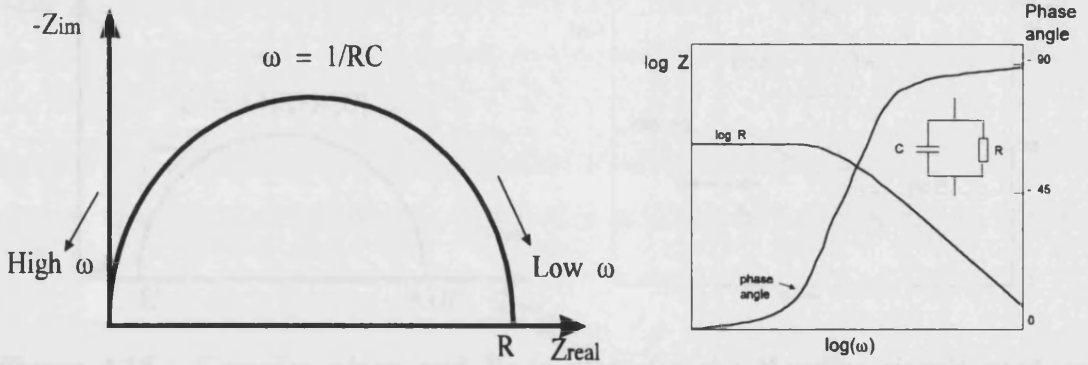

Figure 4.13 : Complex plane behaviour and bode plot of RC circuit in parallel.

Equivalent circuits

Electrochemical systems are often modelled using equivalent circuits made of resistors, capacitors and inductors. The simplest model that can be used as an approximation to the mechanism of chlorine evolution is the Randles[13] circuit which is defined for a simple electron transfer process without adsorption effects nor mass transfer control. This model has been used for chlorine evolution on platinum[14,15].

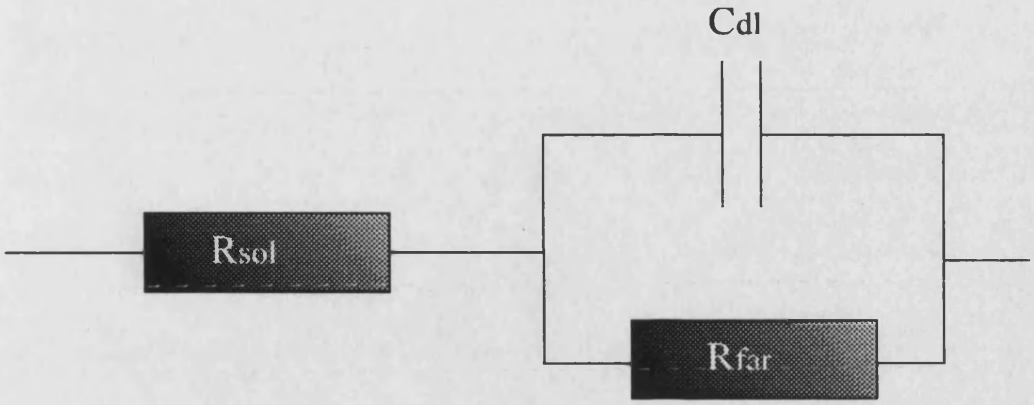

Figure 4.14 : Randles equivalent circuit where R_{sol} is the solution resistance and R_{far} is the faradaic resistance.

The model assumes that the a.c. response of the electrochemical system can be modelled using a solution resistance (R_{sol}) coupled with the double layer capacitance (C_{dl}) in parallel with a faradaic resistance (R_{far}). The complex plot is expected to show a semi-circle centred on the axis and the Bode phase plot to show only one peak. The complex plane and Bode plots of such a model are as follows :

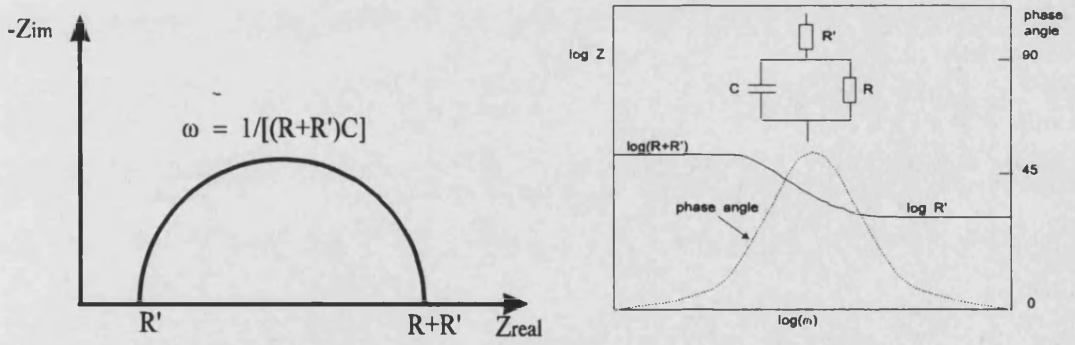

Figure 4.15 : Complex plane and Bode plots for the Randles circuit used as approximation model for chlorine evolution.

Other models used for interpreting chlorine evolution include an additional pseudocapacitance[16], C_ϕ, in parallel with a resistor, R_Φ, in order to account for the adsorption/desorption process of the chlorine adsorbate. R_Φ is defined as the resistance related to desorption of the Cl^- intermediate[15] in step 2) or 3).

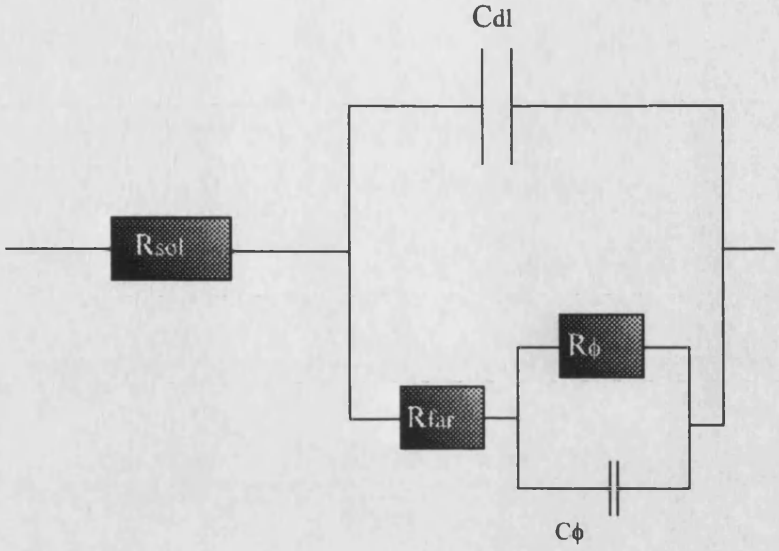

Figure 4.16 : Equivalent circuit used to model pseudocapacitive behaviour

The pseudocapacitance is defined as follows :

$$C_{\phi} = nF\Gamma_{max}\frac{d\theta}{dE} = nF\Gamma_{max}\frac{d\theta}{di} * \frac{di}{dE} \qquad (4.23)$$

where θ is the chlorine adsorbate surface coverage, i is the current flowing through the circuit at time t and Γ_{max} is the saturation coverage in mol cm^{-2}. The surface coverage depends on the nature and adsorbate concentration as well as on the electrode potential, solution pH, temperature and other adsorbing species. In order to relate the surface coverage to the adsorbate concentration and free energy of adsorption, various *isotherms* have been derived. The difference between them comes from the assumptions made about the interactions between the adsorbate and surface as well as the lateral interactions between adjacent adsorbed species.

For qualitative purposes, a Langmuir[17,18] isotherm is assumed. This model is used to describe adsorption where only one monolayer of adsorbate is possible, all sites on the surface are equivalent and where there are no interactions between neighbouring adsorbate molecules. The latter condition is equivalent to assuming that the free energy of adsorption is independent of coverage. Most isotherms are usually expressed as a function pressure as illustrated in figure 4.17 in the case of the Langmuir isotherm.

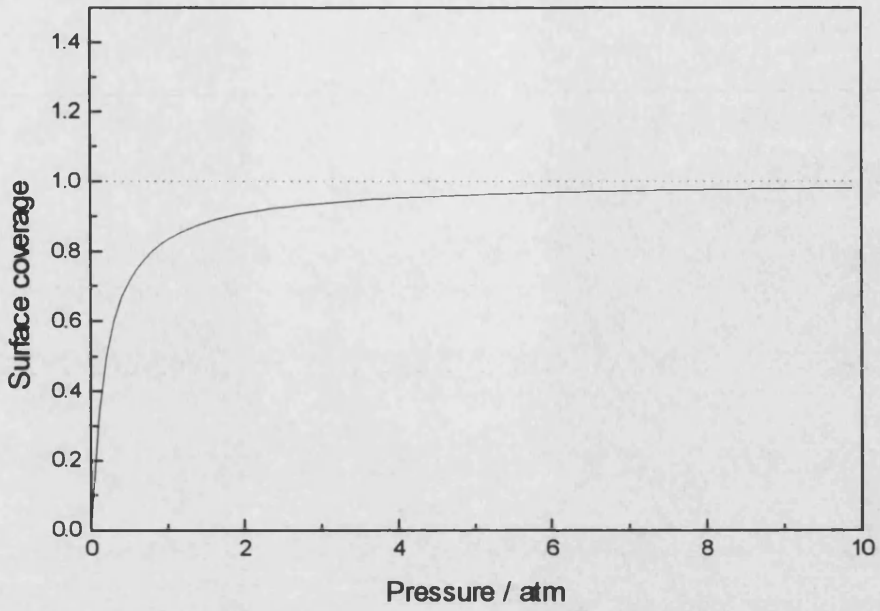

Figure 4.17 : variation of surface coverage of an adsorbate as a function of pressure for the Langmuir isotherm.

In the electrochemical case, the surface coverage is determined by the concentrations and electrochemical rate constants.

We consider the generally accepted reaction mechanism for chlorine evolution :

$Cl^- + M \rightleftharpoons Cl_{ads} + e^-$ step 1)

$2\ M\text{-}Cl_{ads} \rightleftharpoons Cl_2 + 2\ e^-$ step 2)

$Cl^- + M\text{-}Cl_{ads} \rightleftharpoons Cl_2 + e^- + M$ step 3)

and assume that the reaction takes place either via steps 1&2 (mechanism A) or via steps 1&3 (mechanism B), i.e. we do not consider the case where steps 2 and 3 are taking place simultaneously. v_1, v_2 and v_3, the rates of reaction for steps 1-3 respectively, are defined as

$$v_1 = k_1(1-\theta)\exp\left(\frac{\alpha_1 F}{RT}\eta\right) - k_{-1}\theta\exp\left(-\frac{(1-\alpha_1)F}{RT}\eta\right) \qquad (4.24)$$

$$v_2 = k_2\theta^2 - k_{-2}(1-\theta)^2 \qquad (4.25)$$

$$v_3 = k_3\theta\exp\left(\frac{\alpha_3 F}{RT}\eta\right) - k_{-3}(1-\theta)\exp\left(-\frac{(1-\alpha_3)F}{RT}\eta\right) \qquad (4.26)$$

where $k_1 \rightarrow k_3$ are the net rates of the forward and reverse reactions for steps 1 to 3. For convenience, [Cl⁻] and [Cl_2] are incorporated[19] in the rate constant $k_1 \rightarrow k_3$ and the value of the cathodic transfer coefficient for step n (α_n) is considered to be equal to 0.5.

In order to derive the Langmuir isotherm for this process we consider all the possible rate determining steps for this reaction.

I. *Step 1 is the rate determining step (RDS)*

Since this step is common to both mechanisms, it is not possible to distinguish between mechanism A and B. In this case, the rate of chlorine desorption via steps 2&3 is much faster than the rate of adsorption by step 1, and θ is therefore very small, i.e. for small values of θ, $(1-\theta) \approx 1$. Equation 4.24 can therefore be rewritten as

$$v_1 = k_1 \exp\left(\frac{F}{2RT}\eta\right) \tag{4.27}$$

The current produced by chlorine evolution is therefore

$$j = Fv_1 = Fk_1 \exp\left(\frac{F}{2RT}\eta\right) \tag{4.28}$$

Equation 4.28 can be rewritten as

$$\log_{10}(j) = \log_{10}(Fk_1) + \frac{F}{4.6RT}\eta \tag{4.29}$$

At T = 333 K (60°C) the Tafel slope ($d\log_{10}(|j|)/d\eta$) is therefore 134 mV decade^{-1}.

II. Step 2 is the RDS for mechanism A

If the rate of the reverse reaction is negligible, equation 4.25 can be approximated as

$$v_2 = 2k_2\theta^2 \tag{4.30}$$

and the current density is

$$j = 2k_2F\theta^2 \tag{4.31}$$

θ can be determined from the steady state conditions, $d\theta/dt = 0$. Note that k_2 is potential independent.

Step 1 can be considered as a pre-equilibrium if $k_2 << k_1$ and k_{-1} under all conditions. This leads to

$$k_1(1-\theta)\exp\left(\frac{F}{2RT}\eta\right) = k_{-1}\theta\exp\left(\frac{F}{2RT}\eta\right) \tag{4.32}$$

which can be rearranged to give θ :

$$\theta = \frac{K_1\exp\left(\frac{F}{2RT}\eta\right)}{1+K_1\exp\left(\frac{F}{2RT}\eta\right)} \tag{4.33}$$

where $K_1 = k_1/k_{-1}$. Combining equation 4.31 and 4.33 then gives an expression for the current density as function of the potential :

$$j = 2Fk_2K_1^2\exp\left(\frac{2F}{RT}\eta\right) \tag{4.34}$$

or

$$\log_{10}(j) = \log_{10}(2Fk_2K_1^2) + 2\log_{10}\left(\frac{2F}{2.3RT}\eta\right) \tag{4.35}$$

Equation 4.35 shows that the Tafel slope has a value of 33.5 mV decade^{-1} at 333 K.

Recombining equation 4.33 and 4.34 yields an expression of the surface coverage as a function the applied d.c. current density :

$$\theta = \frac{\left(\frac{j}{2Fk_2}\right)^{\frac{1}{2}}}{1+\left(\frac{j}{2Fk_2}\right)^{\frac{1}{2}}} \tag{4.36}$$

Equation 4.36 is of the form Y = X/(1+X), i.e. the Langmuir isotherm. The variation of surface coverage as a function of current is therefore expected to have the same shape as that the Langmuir isotherm (figure 4.17). This is illustrated in figure 4.18 :

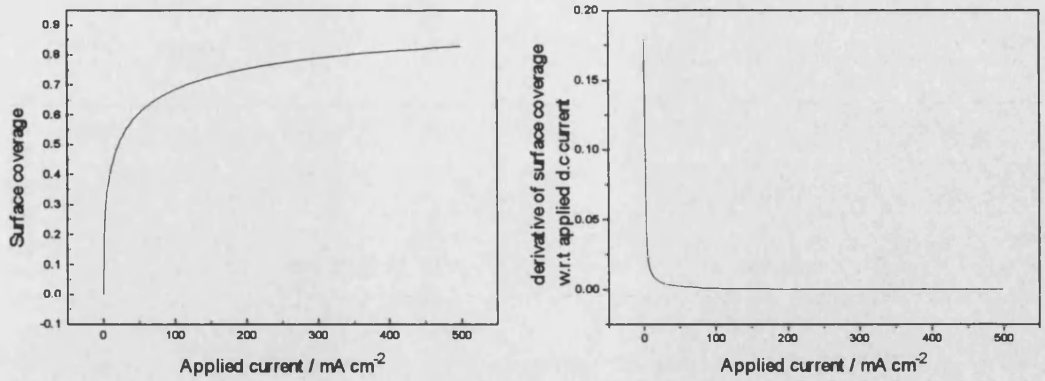

Figure 4.18 : coverage as a function of applied current density (T = 333 K and $k_2 = 10^{-6}$ mol cm^{-2} s^{-1}) calculated from equation 4.36 (Langmuir isotherm). The derivative of surface coverage dθ/di shows that the pseudocapacitance is only significant over a limited applied current, i.e. 0-50 mA cm^{-2}.

III.Step 3 is the RDS for mechanism B

As in case II, (1-θ) is very small and equation 4.26 can be approximated as

$$v_3 = k_3 \exp\left(\frac{F}{2RT}\eta\right)\theta \tag{4.37}$$

where θ can also be determined in the same way as in case II.

Equation 4.26 will result in different Tafel slopes at low and high overpotential values.

At low overpotentials (low coverage), v_1 is much greater than v_3, hence

$$j = 2Fk_3 \exp\left(\frac{F}{2RT}\eta\right) K_1 \exp\left(\frac{F}{2RT}\eta\right) \tag{4.38}$$

which leads to

$$j = 2Fk_3K_1 \exp\left(\frac{1.5F}{RT}\eta\right) \tag{4.39}$$

As a result,

$$\log_{10}(j) = \log_{10}(2Fk_3K_1) + \frac{1.5F}{RT}\eta \tag{4.40}$$

If $\alpha_3 = 0.5$, then the Tafel slope has a value of 45 mV $decade^{-1}$ at 333 K.

At high overpotentials (high coverage)

$$k_1 \exp\left(\frac{F}{2RT}\eta\right)(1-\theta) = k_3 \exp\left(\frac{F}{2RT}\eta\right)\theta \qquad (4.41)$$

and θ is independent of potential. The current density for this expression then becomes

$$j = 2Fk_3K_1 \exp\left(\frac{F}{2RT}\eta\right) \qquad (4.42)$$

which is equivalent to

$$\log_{10}(j) = \log_{10}(2Fk_3K_1) + \frac{F}{4.6RT}\eta \qquad (4.43)$$

Therefore, for high overpotentials, the Tafel slope is 134 mV decade^{-1} at 333 K.

In summary, depending on the mechanism for chlorine evolution and the RDS, different Tafel slope values may be obtained. These values are summarised in table 4.4.

Mechanism	RDS	Overpotential range	Tafel slope / mV decade^{-1}
A or B	1	All	134
A	2	Low	34
B	3	Low	45
B	3	High	134

Table 4.4 : Tafel slopes values depending on the RDS and mechanism for the chlorine evolution reaction at 333 K.

If step 1 is the RDS, the value of the Tafel slope cannot be used to conclude whether the reaction is taking place via mechanism A or B. Considering the accuracy in measuring Tafel slopes, table 4.4 also shows that, at low overpotentials, it would not be easy to distinguish between mechanism A with step 2 as the RDS and mechanism B with step 3 as the RDS.

The plot of surface coverage as a function of applied current density (figure 4.18) shows two regions. The first region is for small values of applied current density. In this case, the derivative of the surface coverage with respect to applied current density is not equal to zero. The second region corresponds to the state where the surface coverage is approaching its limiting value of 1. By contrast, dθ/dj approaches 0

in this region. As a result, according to equation 4.23, one only expects to detect the pseudocapacitance for small values of the applied current density. At higher currents, the simpler Randles circuit (figure 4.14) is applicable.

If the presence of the chlorine adsorbate produces a pseudocapacitance then impedance spectroscopy should detect it. By varying the amplitude of the d.c. current one can perform a study over the whole current-potential range. In this project, impedance experiments were carried out in galvanostatic mode in order to have greater control of operating conditions. The amplitude of the sinusoidal signal used must be small enough that the current-voltage behaviour of the electrochemical system can be considered as linear in that range. This is illustrated in figure 4.19 below :

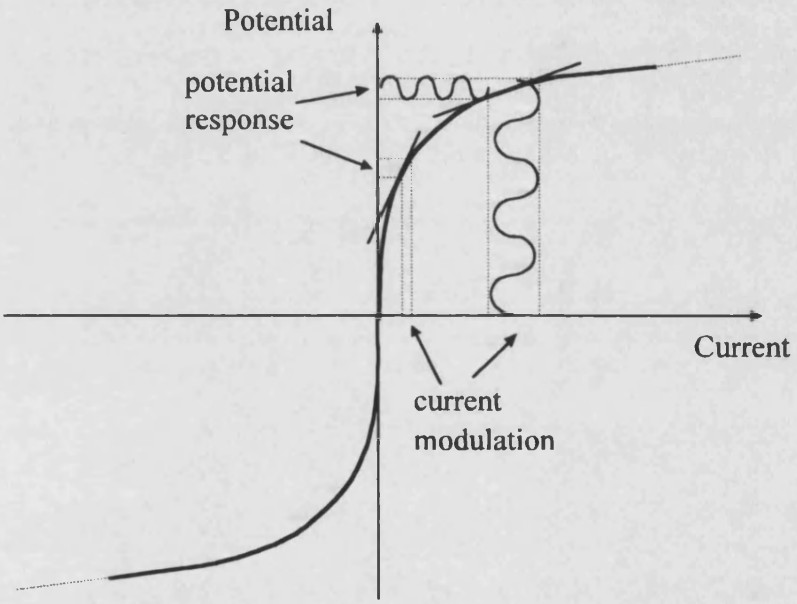

Figure 4.19 : variation of the current modulation in order to be able to linearise the current-voltage behaviour and carry out impedance spectroscopy measurements.

Non-ideal behaviour

So far, we have only considered cases where all the components behave ideally. For instance, when considering capacitances we have only looked at the cases where they are potential and frequency independent. Likewise, we have only considered cases where the resistance is ideal. When modelling real electrochemical systems, one has to account for the fact that the double layer capacitance and faradaic resistance may not

behave as ideal linear components. In the case of RuO_2/TiO_2 systems, it is known[20,21,22,23] that the surface is not ideal and has a roughness factor of the order of hundreds. This means that the RuO_2/TiO_2 anodes are expected to exhibit non-ideal behaviour. it is anticipated that the double layer capacitance will be frequency dependent and that it will therefore not be possible to represent it as a sum of a small number of resistances and capacitances. The situation is further complicated by the fact that the anode coatings are also heterogeneous in composition and that this also leads double layer capacitance frequency dependence. The combination of surface roughness and composition heterogeneity is difficult to distinguish from porous electrode[24,25,26] behaviour.

It is important to examine more closely what is meant by the concepts of roughness, electrode porosity and surface inhomogeneity.

Surface inhomogeneity refers to the spatial variation of catalytic activity associated with inhomogeneous composition of the electrode. The double layer capacitance per unit area is not constant but varies depending on factors such as the ruthenium content or oxidation state. The total impedance of the equivalent circuit is equal to a parallel sum of local impedances distributed in some way, as illustrated below

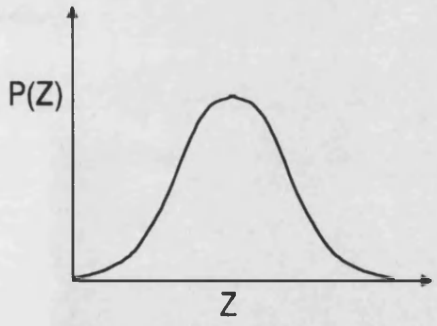

$$\frac{1}{Z_{tot}} = \frac{1}{Z_1} + \frac{1}{Z_2} + \frac{1}{Z_3} + \ldots\ldots \frac{1}{Z_n} \qquad (4.44)$$

$$\therefore \frac{1}{Z_{tot}} = \sum_{1}^{n}\left(\frac{1}{Z_n}\right) \qquad (4.45)$$

Figure 4.20: Normal distribution of impedance values and formula for total impedance calculation of an inhomogeneous electrode.

By contrast, the double layer capacitance per unit area for a rough electrode of uniform composition has the same magnitude all over the electrode. The total impedance is a parallel sum of impedances of the same magnitude and electrodes can exhibit transmission line[17] type behaviour depending on the nature of the porosity (for

semi-infinite pores, i.e. pores that behave as infinitely deep, the phase angle of the pore impedance is half of that of the interfacial impedance which would be measured if the electrodes were flat). The nature of surface roughness is reflected in the number of capacitances and resistors used for the equivalent circuit. Porous electrode behaviour is usually characterised by a flattened semi-circle in the complex plane instead of an ideal semicircle.

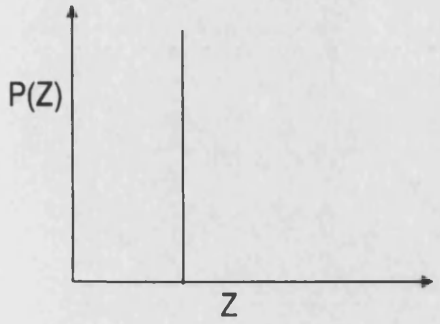

$$\frac{1}{Z_{tot}} = \sum_{1}^{n}\left(\frac{1}{Z_{local}}\right)$$

$$\therefore \frac{1}{Z_{tot}} = \frac{n}{Z_{local}}$$

Figure 4.21: distribution of impedance values and formula for the calculation of the total impedance for a porous electrode.

The difference between electrode surface roughness and heterogeneous composition can be seen in terms of equivalent circuits as illustrated in figure 4.22 below :

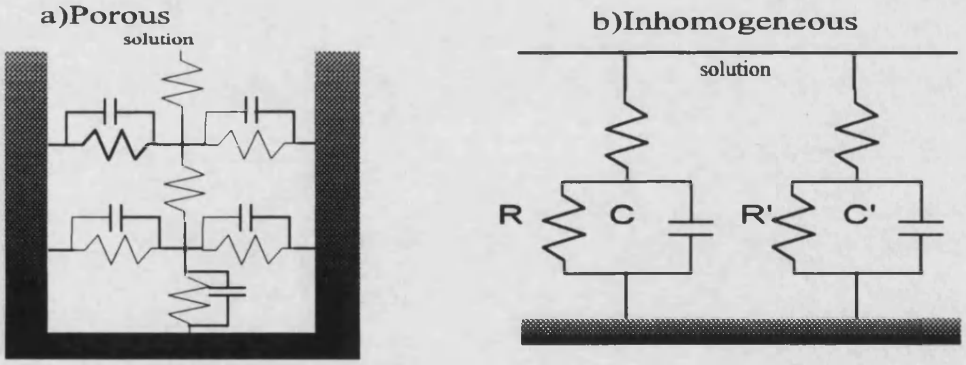

Figure 4.22 : equivalent circuits corresponding to a) a porous electrode b) an inhomogeneous electrode surface.

4.2.2 Results

Impedance measurements were carried out using a 1286 interface and a 1250 frequency response analyser (Solartron). Experiments were carried out potentiostatically in the double layer region, where the only process taking place is that of charging/discharging of the double layer, and galvanostatically in the chlorine evolution region. Measurements were carried out on new and degraded electrodes. Graphical representation of results and fitting of data was made using Zview®.

The following figure shows results obtained for undegraded electrode M31 in the chlorine evolution region for currents ranging from 20 to 140 mA (for most electrodes, the geometric area was approximately 0.75 cm^{-2}).

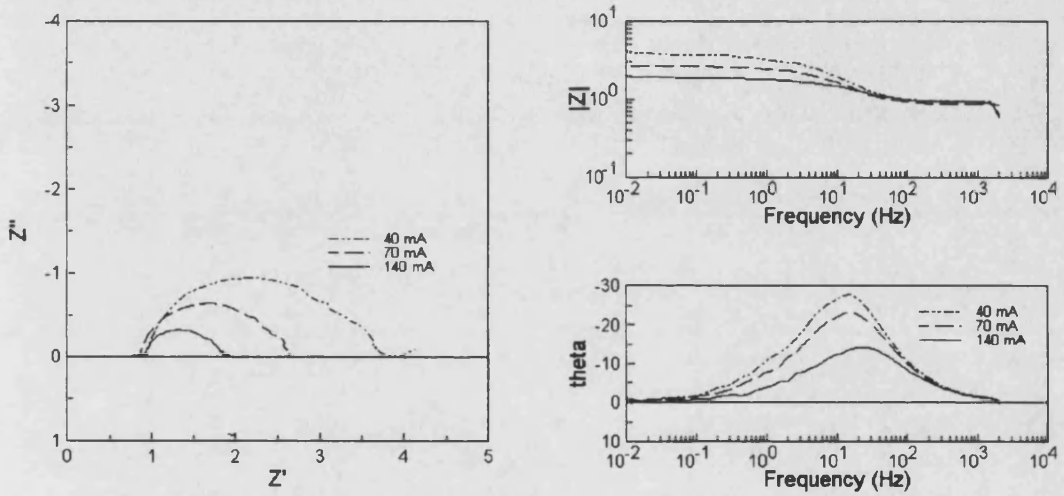

A) B)

Figure 4.23 : a.c. impedance results for sample M31 undegraded at various d.c. currents. A) Complex plane B) Bode plot.

The complex plane plots are approximately semicircular and the Bode phase angle plot shows only one peak. This seems to suggest that chlorine evolution on RuO_2/TiO_2 anodes can be modelled using the simple Randles circuit, i.e. figure 4.14. However, closer analysis of the data reveals that the complex plane plot is not an ideal semicircle. Instead, the data fall on an arc of circle which is centred below the real axis. All electrodes exhibited one depressed semi-circle in the complex plane plot and only one peak in the Bode phase angle plot.

The Bode phase angle peak is also too broad to be accounted for by a single impedance. Attempts to fit the impedance response to a semi-infinite and infinite porous model were not successful.

In view of this non-ideality experimental data were fitted to a constant phase element (CPE)[9,27,28] equivalent circuit. CPE is a concept used to model effects of surface roughness and inhomogeneity, and it has been applied to describe the behaviour of fractal surfaces. Although the microscopic link between the surface structure and the equivalent circuit corresponding to the CPE is still controversial and not well understood, CPEs have been used to explain the fact that the phase angle shift in between the modulated current and potential across the circuit element differs significantly from $\pi/2$. The ZARC-Cole CPE was chosen to replace the capacitance in the Randles circuit (figure 4.14). Excellent fits were obtained for all data using the modified Randles circuit (the root mean square percentage error was less than 2 %).

The purpose of using this model was to calculate the phase shift angle associated with the CPE and to look for variations as a function of current density and electrode wear. The double layer capacitance was replaced by a CPE and the faradaic resistance was assumed to be frequency independent. This analysis revealed no trend : the exponent of the phase angle varied randomly between 0.71 and 0.92 which is equivalent to the phase angle shift varying in between 63° and 89°.

CPEs are basically used as a mathematical tool but they have little to offer in the present work. In order to detect trends in the variation of the double layer capacitance and charge transfer resistance as a function of electrode wear and applied d.c. current, experimental data obtained from measurements at high d.c. currents were fitted to the Randles circuit model. Tables 4.7 - 4.9 summarise the values obtained for the double layer capacitance, charge transfer resistance and $\omega_{max} = 1/C_{dl}R_{ct}$ for the M3x, M4x and M5x series. In some cases, it was not possible to fit the experimental data accurately enough to obtain reliable values. Samples for which this was the case are labelled N/A (Not Available) in the tables. Tables 4.7 - 4.9 can be found at the end of this chapter.

The first variable investigated was the dependence of the charge transfer resistance (R_{ct}) on the applied d.c. current as well as the increase in alkali wear pot running potential ($\Delta V_{running}$ in tables 4.7 - 4.9). The next plot shows the behaviour of R_{ct} as a function of d.c. current for sample M35 :

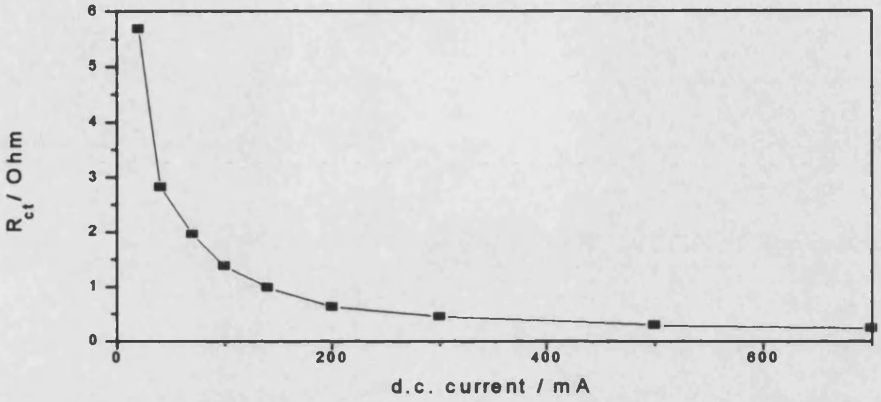

Figure 4.24 : Variation of charge transfer resistance as a function of applied d.c. current during impedance experiment on sample M35.

R_{ct} is normally expressed as a function of j_0, the exchange current density, when impedance experiments are carried out at the equilibrium potential (j_{dc} = 0). In the present work, however, experiments were carried out at d.c. current values of up to 900 mA.

In the Tafel region, the current density can be expressed as follows :

$$j + \tilde{\Delta j} = j_0 \exp\left[\frac{\alpha n F}{RT}\left(\eta + \tilde{\Delta\eta}\right)\right] \qquad (4.46)$$

which is equivalent to

$$j + \tilde{\Delta j} = j_0 \exp\left[\frac{\alpha n F}{RT}\eta\right] * \exp\left[\frac{\alpha n F}{RT}\tilde{\Delta\eta}\right] \qquad (4.47)$$

where $\tilde{\Delta j}$ and $\tilde{\Delta\eta}$ are the modulated current and potential. For small values of x, $e^x \approx 1 + x$ and equation 4.47 can therefore be rewritten as

$$j + \tilde{\Delta j} = j_0 \exp\left[\frac{\alpha n F}{RT}\eta\right]\left(1 + \frac{\alpha n F}{RT}\Delta\eta\right) = j\left(1 + \frac{\alpha n F}{RT}\tilde{\Delta\eta}\right) \qquad (4.48)$$

which leads to

$$R_{ct} = \frac{\tilde{\Delta\eta}}{\tilde{\Delta j}} = \frac{RT}{\alpha n F j} \qquad (4.49)$$

According to equation 4.49, plotting R_{ct} as a function of 1/j should yield a straight line of slope RT/αnF. Figure 4.25 shows the result of such a plot for the data shown in figure 4.24.

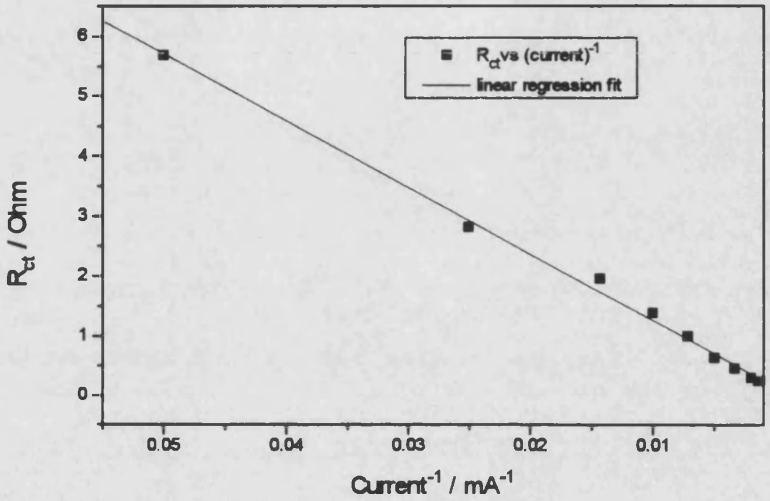

Figure 4.25 : plot of R_{ct} vs. 1/(d.c. current) for sample M35

Figure 4.25 shows that R_{ct} is proportional to the inverse of the applied d.c. current. Inspection of all experimental data confirmed that this was the case for all samples.

The value of the Tafel slope value ($d\log_{10}(i)/d\eta$) fell in the range of 207 to 299 mV decade^{-1} for all the samples, i.e. the distribution of slope values showed no trend with wear. Although measurements were carried out up to j_{dc} = 900 mA, a limiting current was never reached. As a result, comparison with theoretical values from table 4.4 leads to the conclusion that the high experimental Tafel slopes indicate a high surface coverage.

The magnitude of the charge transfer resistance at a particular applied current density was also studied for each sample. The next plot shows the variation of R_{ct} at 3 different applied current densities for all the samples in the M5x series.

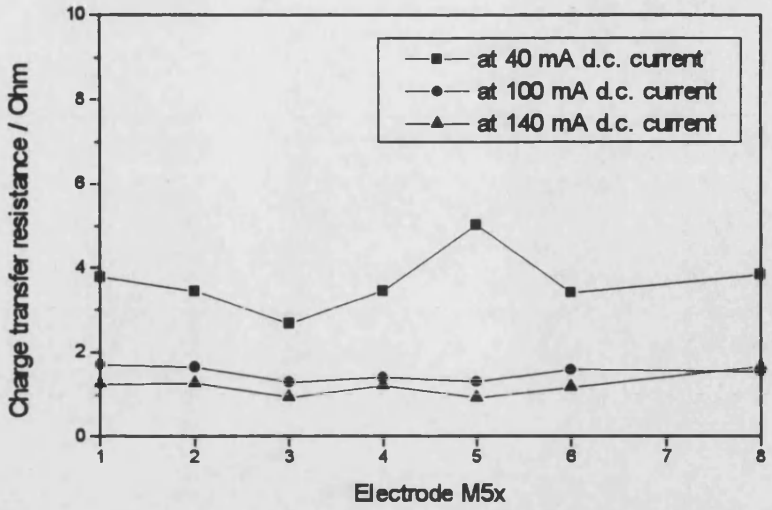

Figure 4.26 : variation of R_{ct} at different applied d.c. currents for the M5x samples M51 - M58.

Figure 4.26 shows that the magnitude of the charge transfer resistance at a particular applied current density is similar for each sample. Since the value of the slope of R_{ct} vs. 1/j is also practically the same for all samples, it can be concluded that degradation in the alkali wear pot did not affect the charge transfer resistance.

The Tafel slope is defined as follows :

$$b = \frac{d\log_{10}(j)}{d\eta} = \frac{RT}{2.3 * \alpha n F} \qquad (4.50)$$

Comparison of equation 4.49 and 4.50 shows that

$$b = \frac{1}{2.3} * R_{ct} * j \qquad (4.51)$$

As a result, the slope of R_{ct} as a function of 1/j is in fact $(2.3)^{-1}$ times the Tafel slope. Tables 4.5 - 4.7 summarise the Tafel slope values calculated from the R_{ct} vs. 1/j slope for each sample.

Sample	Increase in alkali wear running potential / mV	Tafel slope calculated from AC impedance / mV decade^{-1}
M31	0	225 ± 3.5
M32	≈100 (1 hour)	230 ± 10.7
M33	250	209 ± 2.6
M34	400	228 ± 4.7
M35	580	255 ± 2.6
M38	900	235 ± 3.2
M37	950	200 ± 3.1
M36	1500	219 ± 3.2

Table 4.5 : Tafel slope values calculated from a.c. impedance for the M3x series

Sample	Increase in alkali wear running potential / mV	Tafel slope calculated from AC impedance / mV decade^{-1}
M42	0	285 ± 12.2
M41	≈100 (1 hour)	269 ± 2.1
M43	230	329 ± 12.2
M45	340	N/A
M44	360	202 ± 5.5
M46	370	N/A
M47	1470	336 ± 2.8
M48	2090	287 ± 4.1

Table 4.6 : Tafel slope values calculated from a.c. impedance for the M4x series

Sample	Increase in alkali wear running potential / mV	Tafel slope calculated from AC impedance / mV decade^{-1}
M51	0	354 ± 5.2
M52	≈100 (1 hour)	253 ± 2.7
M53	600	212 ± 2.9
M55	930	N/A
M54	1000	230 ± 7.4
M56	1800	364 ± 3.5
M57	2460	N/A
M58	4492	301 ± 6.3

Table 4.7: Tafel slope values calculated from a.c. impedance for the M5x series

The next variable investigated was the dependence of the double layer capacitance on the applied d.c. current and increase in alkali wear pot running potential. Analysis of the values in tables 4.8 - 4.10 revealed two types of behaviour.

For increases in the alkali wear pot running potential ranging from 0 to (500-600) mV, the double layer capacitance was found to be constant and independent of the applied d.c. current. In that range, values of the double layer capacitance ranged from 24 to 40 mF cm^{-2}.

In the case of samples which had been degraded to increases in alkali wear pot running potential greater than 600 mV, the double layer capacitance was found to increase with applied d.c. current. The double layer capacitance varied from 20 ± 5 (at 20 mA cm^{-2}) to 90 ± 5 mF cm^{-2} (at 300 mA cm^{-2}). Some samples showed that the value of the double layer capacitance at 20 mA was lower than the average value for electrodes which had were degraded to increases in alkali wear pot running potential less than 600 mV. The reason for this behaviour is not clear at present but it could be related to the increase of overpotential observed for degraded electrodes (Cf. chapter 6)

Examples of samples behaving as described are shown below for both regions of increase in alkali wear pot running potential :

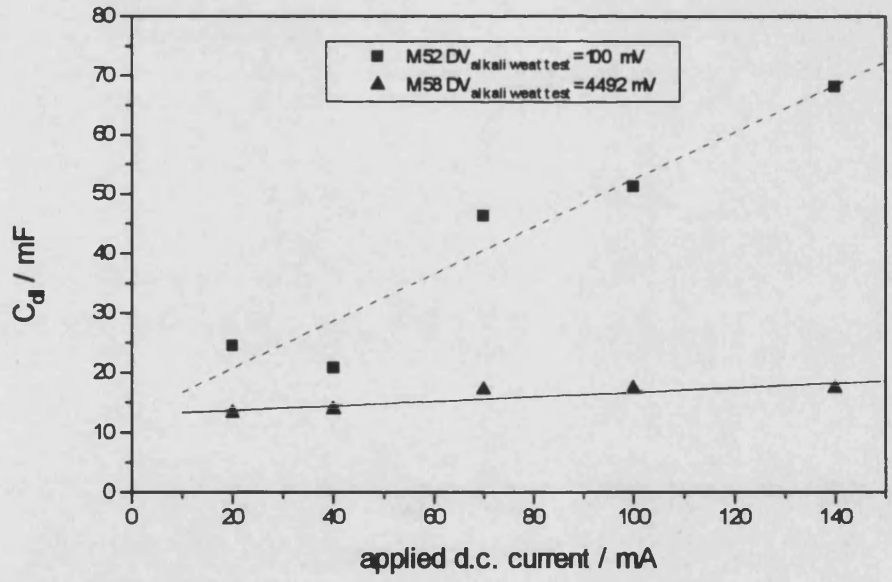

Figure 4.27 : Plot of C_{dl} as a function of applied d.c. current for both regions of increase in alkali wear pot running potential. The solid and dashed line represent the linear regression fit to data from samples M52 and M58 respectively.

Experiments were also carried out at d.c. currents lower than 20 mA. In this region, complex plane plots exhibits two semicircles. Although they are not as clearly

defined as the semicircle for d.c. currents higher than 20 mA, this kind of behaviour is an indication that there is a pseudocapacitance associated with the chlorine adsorbate. Pseudocapacitive behaviour is illustrated in the figure below in the case of sample M32:

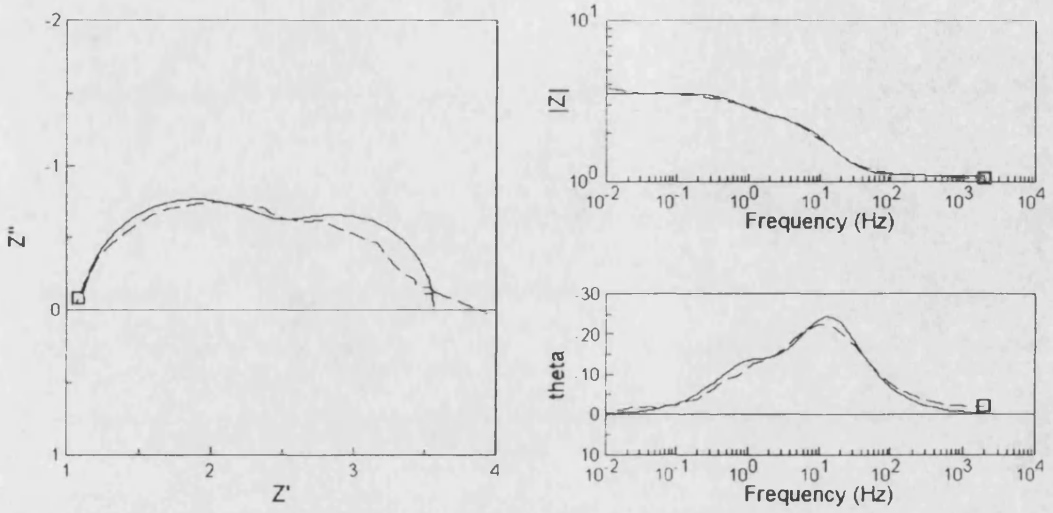

Figure 4.28 : Pseudocapacitive behaviour of sample M32 at 40 mA. The dashed line represents experimental data and the solid line represents fit according to figure 4.16).

4.2.3 Conclusions

Impedance spectroscopy has revealed that degradation does not affect the charge transfer resistance nor the double layer capacitance value. Impedance spectroscopy therefore does not indicate any loss of catalytic activity (R_{ct}) or ruthenium content (C_{dl}) with degradation in spite of the enormous increase in alkali wear pot running potential.

In general, values of the double layer capacitance are in good agreement with data from cyclic voltammetry and results from both techniques lead to the conclusion that the increase in alkali wear pot running potential is due to formation of a resistive layer. Various models can be used to account for this and will be discussed in chapter 8.

However, it was also discovered that the double layer capacitance becomes dependent on applied d.c. currents for electrodes that have degraded beyond a certain value of the increase in alkali wear pot running potential. The reasons for this are still

unclear and further work needs to be carried out in order to explain this.

Electrode	ΔVrunning / mV	dc current / mA	Cdl / mF	Rct / Ohm	ωmax / Hz
M31	0.00				
		20.00	12.28	5.01	16.23
		40.00	11.30	2.51	34.96
		70.00	13.40	1.64	45.16
		100.00	10.81	0.95	97.29
		140.00	11.55	0.89	97.29
M32	100.00				
		20.00	11.20	5.50	16.23
		40.00	14.23	2.01	34.96
		70.00	10.87	1.58	58.32
		100.00	11.90	1.44	58.32
		140.00	15.70	1.09	58.32
		200.00	13.65	0.75	97.29
M33	250.00				
		20.00	21.31	4.82	9.73
		40.00	12.58	2.27	34.96
		70.00	14.34	1.54	45.16
		100.00	18.76	1.18	45.16
		140.00	14.76	0.90	75.33
		200.00	15.95	0.64	97.29
		300.00	15.83	0.50	125.66
M34	400.00				
		20.00	19.87	5.17	9.73
		40.00	9.50	3.01	34.96
		70.00	23.31	2.05	20.96
		100.00	25.23	1.46	27.07
		140.00	27.01	1.06	34.97
		200.00	29.82	0.74	45.16
		300.00	26.15	0.51	75.33
M35	580.00				
		20.00	23.37	5.68	7.53
		40.00	16.93	2.82	20.96
		70.00	40.00	1.95	12.56
		100.00	44.74	1.38	16.23
		140.00	37.41	0.99	27.07
		200.00	58.61	0.63	27.07
		300.00	63.34	0.45	34.96
		500.00	74.41	0.30	45.16
		700.00	198.00	0.24	20.96
M38	900.00				
		20.00	19.07	5.38	9.73
		40.00	17.61	2.71	20.96
		70.00	24.74	1.93	20.96
		100.00	32.88	1.45	20.96
		140.00	36.47	1.01	27.07
		200.00	37.76	0.76	34.97
		300.00	43.35	0.51	45.16
M36	950.00				
		20.00	22.28	4.61	9.73
		40.00	12.72	2.90	27.07
		70.00	33.32	1.85	16.23
		100.00	35.25	1.35	20.96
		140.00	50.84	0.94	20.96
		200.00	36.53	0.61	45.16
		300.00	N/A	N/A	N/A
		500.00	17.37	0.21	270.74
M37	1500.00				
		20.00	15.88	5.01	12.56
		40.00	13.19	2.80	27.07
		70.00	26.39	1.81	20.96
		100.00	34.85	1.37	20.96
		140.00	36.96	1.00	27.07
		200.00	66.75	0.71	20.96
		300.00	63.06	0.45	34.96

Table 4.8 : a.c. impedance data obtained by fitting experimental results for the M3x series of RuO_2/TiO_2 samples in the chlorine evolution region at 60°C.

Electrode	ΔVrunning / mV	d.c. current / mA	Cdl / mF	Rct / Ohm	ωmax / Hz
M42	0.00				
		20.00	28.50	46.58	0.75
		40.00	19.20	3.21	16.23
		70.00	26.24	2.35	16.23
		100.00	28.05	1.70	20.96
		140.00	30.89	1.20	27.07
		200.00	35.13	0.81	34.97
		300.00	33.30	0.51	58.32
M41	100.00				
		20.00	13.24	4.65	16.23
		40.00	19.81	3.11	16.23
		70.00	24.76	1.95	20.96
		100.00	26.13	1.41	27.07
		140.00	26.20	1.09	34.97
		200.00	27.86	0.79	45.16
		300.00	22.14	0.60	75.34
		500.00	32.33	0.41	75.34
M43	230.00				
		20.00	10.62	7.49	12.56
		40.00	8.04	2.75	45.16
		70.00	20.61	2.31	20.96
		100.00	13.98	1.58	45.16
		140.00	24.49	1.16	34.96
		200.00	16.56	0.80	75.33
M45	340.00	N/A	N/A	N/A	N/A
M44	360.00				
		20.00	16.32	4.87	12.56
		40.00	12.73	2.90	27.07
		70.00	27.68	2.22	16.23
		100.00	24.18	1.52	27.07
		140.00	23.80	1.20	34.96
		200.00	24.50	0.90	45.16
		300.00	27.50	0.62	58.32
M46	370.00	N/A	N/A	N/A	N/A
M47	1470.00				
		20.00	14.89	5.34	12.56
		40.00	47.48	3.61	5.83
		70.00	67.81	1.95	7.53
		100.00	56.36	1.41	12.56
		140.00	104.94	0.97	9.73
		200.00	53.99	0.68	27.07
M48	2090.00				
		20.00	9.70	6.34	16.23
		40.00	28.90	3.55	9.72
		70.00	7.82	2.19	5.83
		100.00	51.83	1.53	12.57
		140.00	73.93	1.07	12.57
		200.00	84.40	0.72	16.23
		300.00	209.40	0.49	9.72

Table 4.9: a.c. impedance data obtained by fitting experimental results for the M4x series of RuO_2/TiO_2 samples in the chlorine evolution region at 60°C.

Electrode	ΔVrunning / mV	d.c. current / mA	Cdl / mF	Rct / Ohm	ωmax / Hz
M51	0.00				
		20.00	N/A	N/A	N/A
		40.00	21.04	3.78	12.56
		70.00	19.05	2.50	20.96
		100.00	27.70	1.71	20.96
		140.00	29.48	1.25	27.07
		200.00	31.35	0.91	34.96
		300.00	38.39	0.58	45.16
		500.00	28.89	0.36	97.29
		700.00	39.82	0.26	97.29
		900.00	24.28	0.20	209.62
M52	100.00				
		20.00	13.19	6.03	12.56
		40.00	13.80	3.45	20.96
		70.00	17.09	2.16	27.07
		100.00	17.30	1.65	34.96
		140.00	17.35	1.27	45.16
M53	600.00				
		20.00	16.40	4.84	12.56
		40.00	10.64	2.68	34.96
		70.00	21.15	1.75	27.07
		100.00	22.11	1.29	34.96
		140.00	23.57	0.94	45.16
		200.00	27.36	0.63	58.32
M55	930.00				
		20.00	N/A	N/A	N/A
		40.00	20.40	5.02	9.72
		70.00	37.78	2.11	12.56
		100.00	47.03	1.30	16.23
		140.00	51.60	0.92	20.96
		200.00	66.80	0.71	20.96
M54	1000.00				
		20.00	14.56	5.46	12.64
		40.00	29.70	3.45	9.72
		70.00	37.77	2.10	12.56
		100.00	33.35	1.40	20.96
		140.00	30.44	1.21	27.07
M56	1800.00				
		20.00	17.05	6.02	9.72
		40.00	30.01	3.41	9.72
		70.00	38.05	2.09	12.56
		100.00	64.40	1.59	9.73
		140.00	52.70	1.17	16.23
		200.00	59.91	0.80	20.96
M57	2460.00				
		200.00	29.19	0.76	45.16
		300.00	N/A	N/A	N/A
M58	4492.00				
		20.00	24.40	7.02	5.83
		40.00	20.69	3.84	12.56
		70.00	46.30	2.22	9.72
		100.00	51.30	1.54	12.56
		140.00	68.20	1.66	12.56

Table 4.10: a.c. impedance data obtained by fitting experimental results for the M5x series of RuO_2/TiO_2 samples in the chlorine evolution region at 60°C.

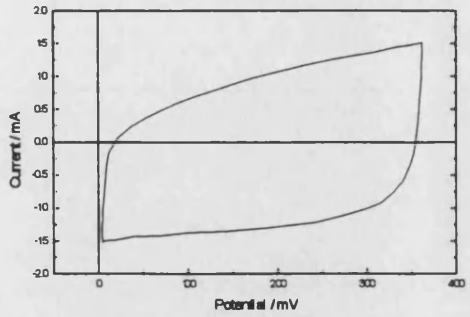

M31 (ΔV_{alkali}=0 mV)

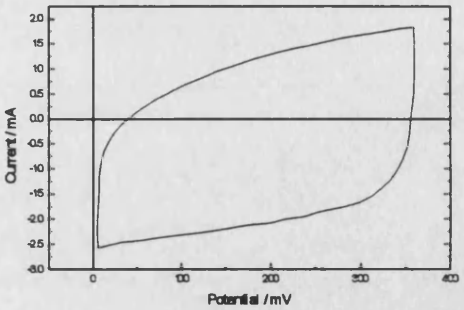

M32 (ΔV_{alkali}=100 mV)

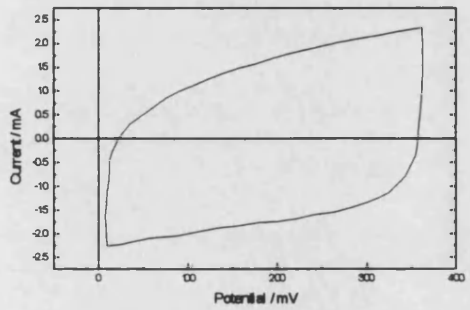

M33 (ΔV_{alkali}=250 mV)

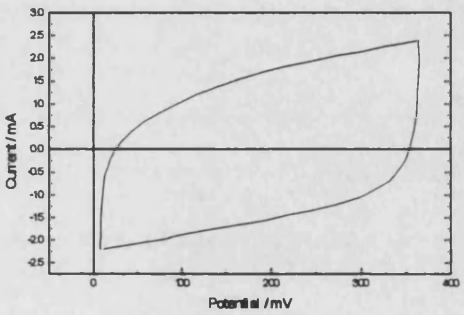

M34 (ΔV_{alkali}=400 mV)

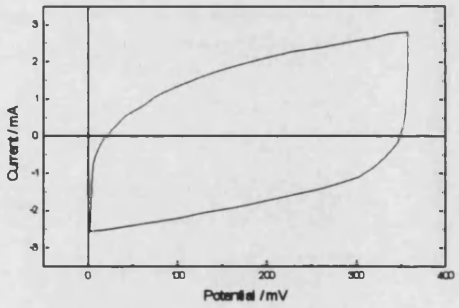

M35 (ΔV_{alkali}=580 mV)

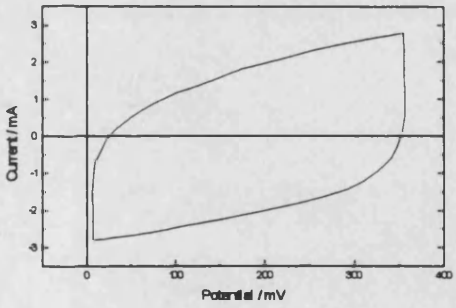

M38 (ΔV_{alkali}=900 mV)

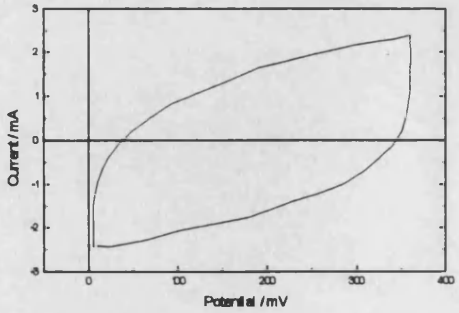

M36 (ΔV_{alkali}=950 mV)

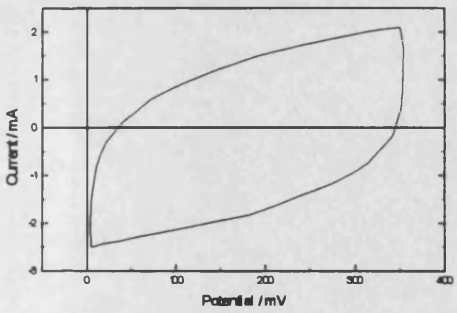

M37 (ΔV_{alkali}=1500 mV)

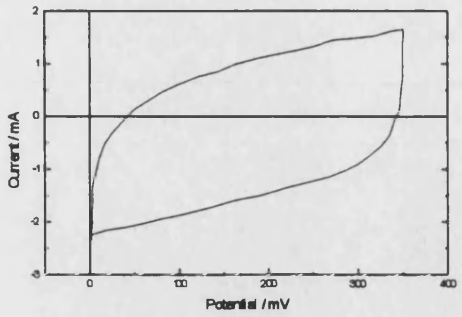

M42 (ΔV_{alkali}=0 mV)

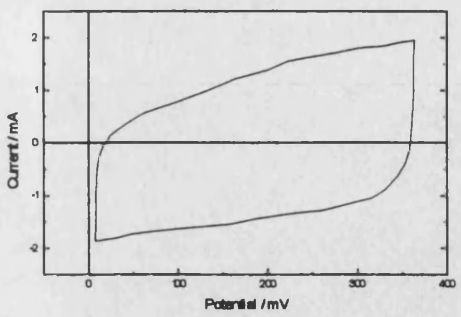

M41 (ΔV_{alkali}=100 mV)

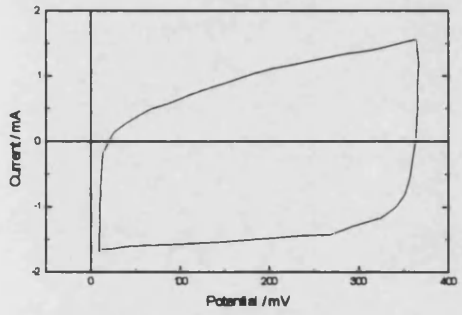

M43 (ΔV_{alkali}=230 mV)

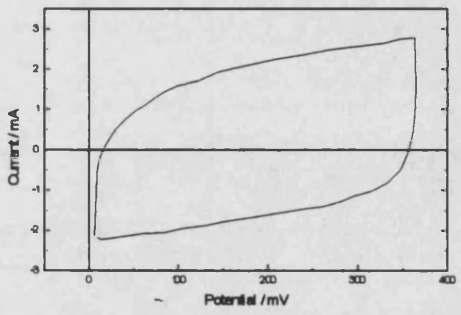

M45 (ΔV_{alkali}=340 mV)

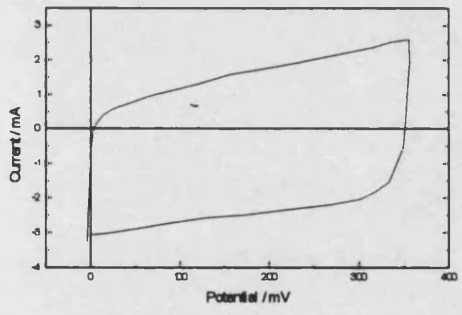

M44 (ΔV_{alkali}=360 mV)

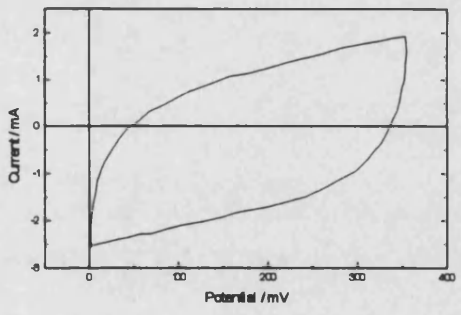

M46 (ΔV_{alkali}=370 mV)

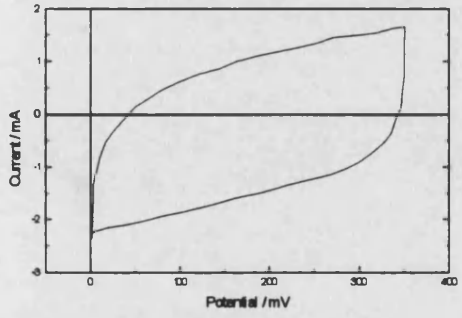

M47 (ΔV_{alkali}=1470 mV)

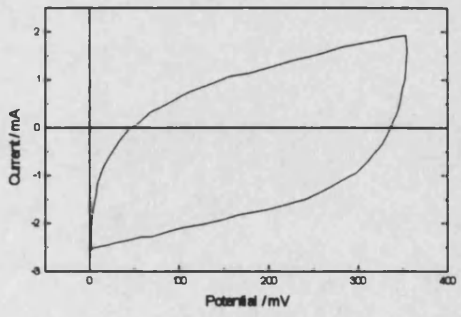

M48 (ΔV_{alkali}=2090 mV)

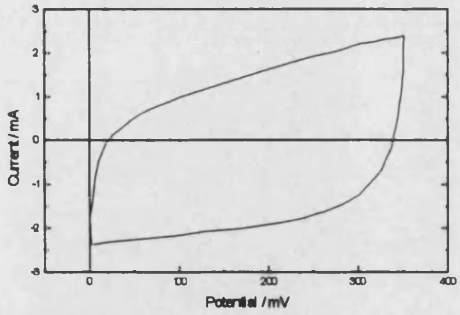

M51 (ΔV_{alkali}=0 mV)

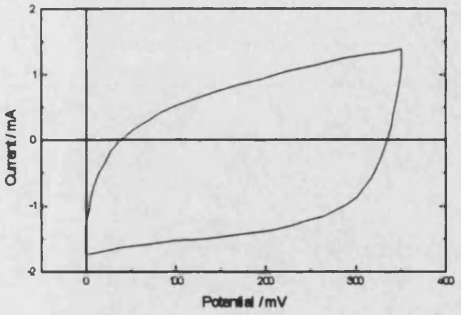

M52 (ΔV_{alkali}=100 mV)

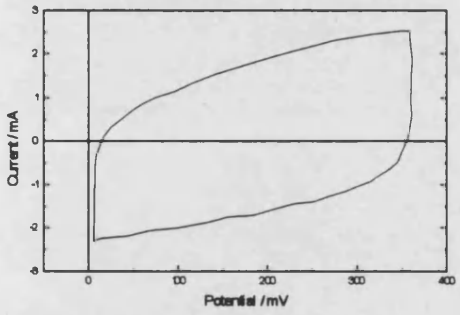

M53 (ΔV_{alkali}=600 mV)

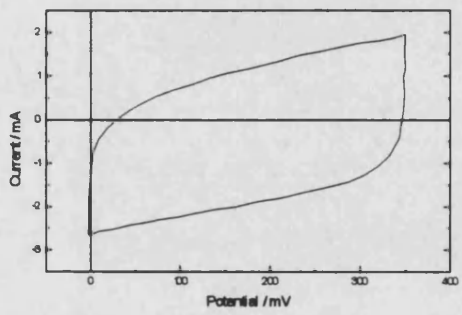

M55 (ΔV_{alkali}=930 mV)

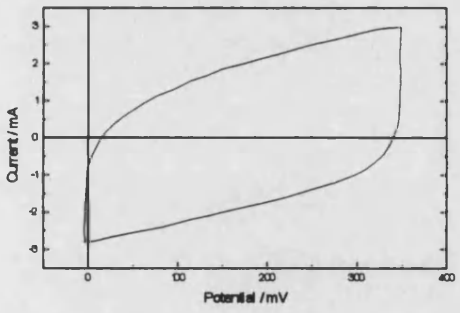

M54 (ΔV_{alkali}=1000 mV)

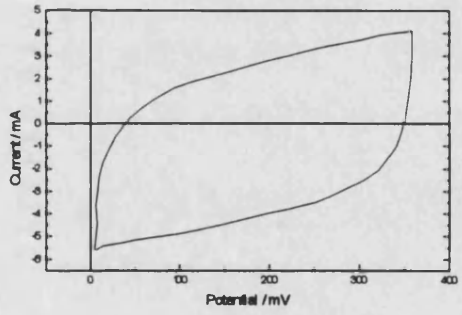

M56 (ΔV_{alkali}=1800 mV)

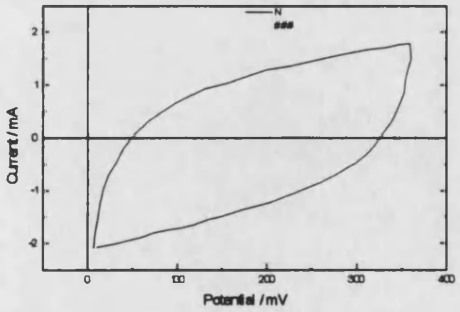

M57 (ΔV_{alkali}=2460 mV)

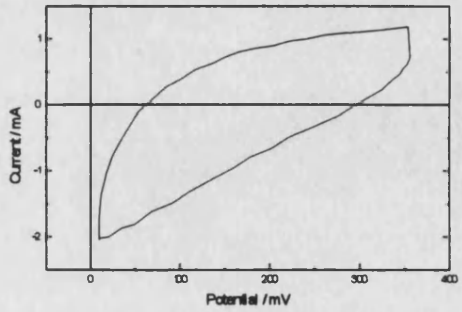

M58 (ΔV_{alkali}=4492 mV)

1 A. J. Bard, L. R. Faulkner, *Electrochemical methods*, Wiley, New York, 1980

2 Southampton Electrochemistry Group, *Instrumental methods in electrochemistry*, Wiley, New York, 1985

3 L.M. Peter, M. Kalaji, Personal communications with ICI

4 S. Trasatti, C. Angelinetta, L.D. Atanasoska, Z.S. Minevski, *Mat. Chem. And Phys.*, 22, 1989, 231-247

5 S. Trasatti, S. Ardizzone, M. Falciola, *J. Electrochem. Soc.*, 136(5), 1989, 1545-1550

6 S. Trasatti, S. Ardizzone, G. Fregonara, *Electrochimica Acta*, 35(1), 1990, 263-267

H. Vogt, *Electrochimica Acta*, 39(13), 1994, 1981-1983

S. Trasatti, D. Baronetto, N. Krstalic, *Electrochimica Acta*, 39(16), 1994, 2359-2362

7 S. Trasatti et al, *Electrochimica Acta*, 37(13), 1992, 2511-2518

8 Independent research carried by ICI

9 B.E. Conway, Gu Ping, *J.Chem. Faraday Trans.*, 87(17), 2705-2714, 1991

10 B.E. Conway, L. Bai, L. Gao, *J. Chem. Faraday Trans.*, 89(2), 235-242, 1993

11 B.E. Conway, L. Bai, L. Gao, *J. Chem. Faraday Trans.*, 89(2), 243-249, 1993

12 J.R. Macdonald, *Impedance spectroscopy*, ed J.R. Macdonald, Wiley, New York, 1987

13 J.E.R. Randles, *Disc. Faraday Soc.*, 1, 1947, 11

14 B.E. Conway, G. Ping, *J. Chem. Faraday Trans.*, 86(6), 923-930, 1990

15 B.E. Conway, G. Ping, *J. Chem. Faraday Trans.*, 87(17), 2705-2714, 1991

16 B.E. Conway, L. Bai, *J. Electrochem. Soc.*, 138(10), 2897-2907, 1991

17 P.W. Atkins, *Physical Chemistry 3rd ed.*, Oxford Univ. Press, 1986, 777

18 D. Pletcher, F.C. Walsh, *Industrial Electrochemistry-2nd ed.*, Blackie A & P, 1993, chapter 1

19 D.A. Harrington, B.E. Comway, J. Electroanal.Chem., 221, 1987, 1-21

20 B.E. Conway, V. Birss, R. Myeyrs, H. Angerstein-Kozlowska, *J. Electrochem. Soc.*, 131(7), 1502-1510, 1984

21 S. Trasatti, I.M. Kodintsev, M. Rubel, A. Wieckowski, N. Kaufher, *Langmuir*, 8, 1992, 283-290

22 S. Daolio, B. Facchin, C. Pagura, A. De Battisti, A. Barbieri, J. Kristof, *J. Mater. Chem.*, 4(8), 1994, 1255-1258

23 S. Trasatti, *Electrochimica Acta*, 36(2), 1991, 225-241

24 J. Jacquelin, *Electrochimica Acta*, 39(18), 2673-2684, 1994

25 A.S. Viner, P.S. Fedkiw, *J. Electrochem. Soc.*, 137(5), 1435-1444, 1990

26 R. De Levie, *Advances in Electrochemistry and Electrochemical Engineering*, ed. P. Delahay, Interscience, New York, 1964, vol. 6

27 D.A. Harington, B.E. Conway, *Electrochim. Acta*, 1987, 32,1703

28 R. De Levie, *J. Electroanal. Chem.*, 1989, 261,1

CHAPTER FIVE

Chapter Five

Steady state techniques

This chapter covers results obtained from total cell current-voltage and anode/reference electrode voltage-time experiments under steady state conditions and under galvanostatic control.

5.1 Current-Voltage measurements

The purpose of carrying out these experiments was three fold. The first objective was to look for significant increases in the total cell voltage as a function of electrode degradation. Secondly, the total cell voltage was analysed in order to determine the source of the potential increase. Finally, steady state measurements were carried out over the whole current range in an attempt to analyse the influence of the chlorine bubble layer on the total cell voltage.

5.1.1 Theory

When studying chlorine evolution in an electrochemical cell as a function of electrode lifetime, one usually starts by carrying out steady state current-voltage measurements. This is because the total amount of energy required to produce chlorine is the factor that generally determines commercial viability.

Consider a typical membrane cell where the total voltage is the sum[1] of individual voltages associated with the anode, cathode, electrolyte and membrane. The total cell voltage, E_{cell}, can be written as

$$E_{cell} = E^{\phi}_{cell} + \sum|\eta| + \sum iR \qquad (5.1)$$

where E^{ϕ}_{cell} depends on the anode/cathode processes, $\sum|\eta|$ is the sum of the anode and cathode overpotentials and $\sum iR$ is the sum of all ohmic components ($\sum iR$ includes the solution, the electrode, the membrane and the bubble layer resistance).

The question of the bubble layer resistance is a very complex issue as it depends on factors such as the geometry of the cell, the mass transport properties and bubble release. As for the electrode resistance, this includes changes in electrode contacts and other effects such as changes in electrode conductivity as a result of the growth of an insulating layer.

The electrochemical setup used in this project was simpler than the commercial cell and was designed so that the following assumptions could be made :

1. The solution was chlorine saturated. This was achieved by bubbling chlorine from a gas cylinder during the length of experiments and putting a lid on top of the cell so that the head space was filled by chlorine and that gas could only escape via a bubbler.
2. The cathode reaction was chlorine reduction, at least at low current densities.

Two reactions can take place at the cathode :

$Cl_2 \rightarrow 2\ Cl^-$ i.e. chlorine reduction (5.2)

or

$2\ H^+ + 2\ e^- \rightarrow H_2$ i.e. hydrogen evolution (5.3)

4 strips of RuO_2/TiO_2 were connected together as a cathode in order to ensure that chlorine reduction took place at the cathode in the current range used for experiments. The total cathode area was of approximately 46 cm^2 and was equivalent to a cathode/anode area ratio of 60:1. It was believed that such a ratio would ensure that chlorine reduction occurred at the cathode over the *entire* current range.

No membrane was used and the electrolyte was always discarded after each experiment. This was to remove the possibility of changes in cell voltage as a result of possible membrane degradation and changes in solution properties such as pH variations and changes in electrolyte concentration.

5.1.2 Results and discussion

Steady state measurements were initially carried out as separate experiments on the M3x series but were finally incorporated into a 'master' experiment including measurement of the total cell voltage, anode/reference electrode potential difference

before and after current interruption as well as frequency of bubble generation analysis. Unfortunately, OCPD experiments on the M4x and M5x series were only carried out from 500 to 1100 mA cm^{-2} and, as a result, total cell steady state current-voltage measurements over the *whole* current range were only obtained for the M3x series.

The next 4 plots show the results obtained for samples M31, M32, M35 and M37 :

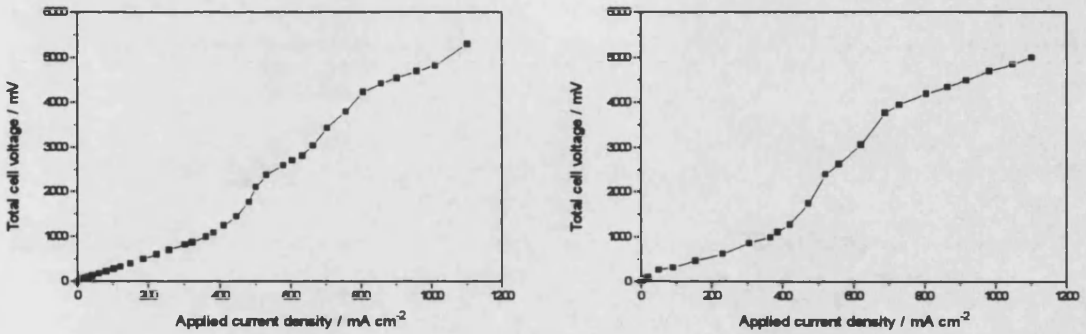

Figure 5.1 : total cell voltage-current density for sample A) M31 and B) M32.

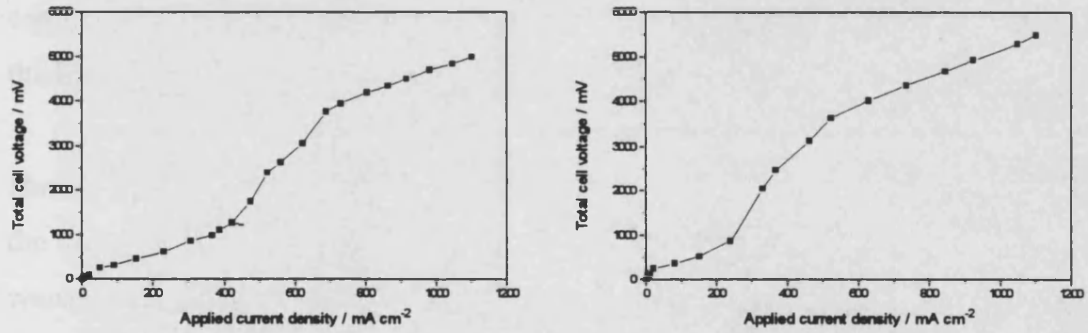

Figure 5.2 : total cell voltage-current density for sample A) M35 and B) M37.

Figures 5.1 and 5.2 show that the total cell voltage is not a linear function of applied d.c. current and that the current-voltage behaviour is divided into three regions. This was the case for all electrodes studied in this project but was particularly significant in the case of samples M32, M35 and M37, as shown above.

The first region corresponds to current densities ranging up to 300 mA cm^{-2}. In this region, the current-voltage behaviour obeys Ohm's law and the slope of the current-voltage behaviour can be considered as the total cell resistance, R_{cell}. Linear regression calculations reveal that R_{cell}=2.5 Ω. This value is consistent with the

anode/reference electrode solution resistance of 0.9 Ω as measured by impedance spectroscopy.

The second region corresponds to a current density range where both chlorine reduction and hydrogen evolution must be taking place at the cathode. It is clearly a region of mixed potential as the cell voltage is increasing by a value close to the HER potential. This is confirmed by the fact the cathode starts to evolve gas. This also means that the diffusion limited current for chlorine reduction at the cathode, j_{lim}, has been reached. An approximate value of the diffusion layer thickness can therefore be obtained by using the linear Nernst diffusion layer model.

If the concentration of chlorine at the cathode is considered to be equal to 0, it follows that

$$j_{lim} = \frac{nFD_o[Cl_2]}{\delta_o} \qquad (5.4)$$

where n is the number of electrons involved in the reaction, D_0 is the diffusion coefficient, $[Cl_2]$ is the bulk concentration of chlorine and δ_o is the diffusion layer thickness.

Assuming that $D_o = 10^{-5}$ cm^2 s^{-1} and $[Cl_2] = 0.08$ mol l^{-1} then $\delta_o = 0.23$ mm. However, the key feature is that the diffusion limited current for chlorine reduction at the cathode, i.e. 6.5 mA cm^{-2}, is very low and means that a much larger cathode area would have been required to ensure that the HER did not take place at the cathode. For chlorine reduction to take place at the cathode when the applied current density was 1000 mA cm^{-2}, the cathode area would have had to be 200 cm^2, i.e. 4 times bigger than the cathode area used in this project.

Although the fact that the cathode switched to the HER was a disappointing conclusion, this analysis enabled the hydrodynamics of the cathode to be clearly established.

The third region shows that the cathode must have switched to producing hydrogen only. Furthermore, The fact that the potential increase between region 1 and 3 is 2.5 V approximately and that the difference between the chlorine reduction and hydrogen evolution reaction potentials is 1.38 V means that the cathode overpotential is substantial, i.e. the HER is very sluggish of the RuO_2/TiO_2 coating.

Figure 5.3 shows the current-voltage behaviour for the total cell voltage as well as the reference electrode/anode voltage for samples M37 and M38 :

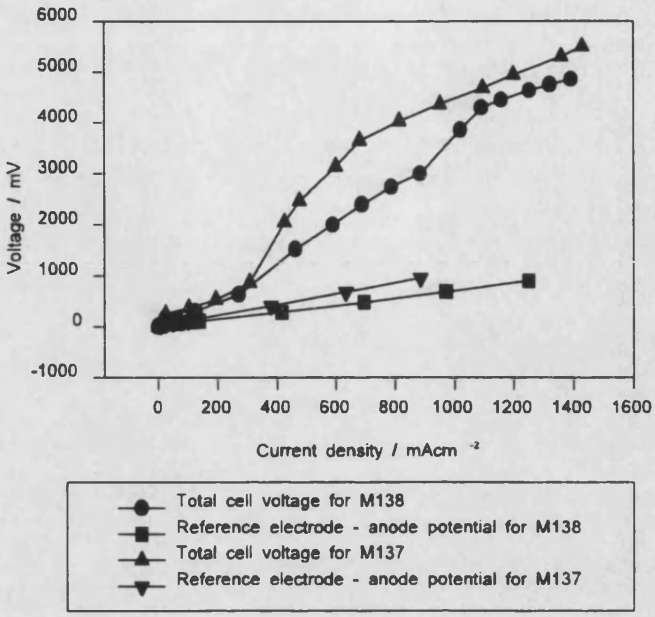

Figure 5.3 : plot of total cell and anode/reference electrode voltage as a function of current density for samples M37 and M38.

Figure 5.3 shows that the current-voltage response between the reference electrode and the anode is linear over the *whole* current range. This is also the case for all other samples studied throughout this project. A linear fit of the reference electrode/anode current-voltage plot resulted in a resistance value of 0.69 Ω and is consistent with the value obtained for the solution resistance from impedance spectroscopy. This was expected since all experiments were carried out in the same cell.

Since the reference electrode is placed just in front of the anode, this implies that the bubble layer resistance is negligible *under all conditions*. This is an important conclusion as it rules out the possibility that changes in the bubble layer properties could be responsible for the increase in total cell voltage and, more importantly, that the bubble layer resistance can be neglected under the experimental conditions used in this project.

The next table shows the cell voltage of undegraded sample M51 and degraded samples M56 and M58 at different current densities.

Voltage at	0 mA cm^{-2}	500 mA cm^{-2}	800 mA cm^{-2}	1000 mA cm^{-2}
M51 / mV	0	427	717	979
M57 / mV	0	686	1160	1875
M58 / mV	0	1392	1870	2168

Table 5.1 : anode/reference electrode current voltage behaviour for undegraded sample M51 and degraded samples M57 and M58.

Results from table 5.1 are illustrated in figure 5.4 below :

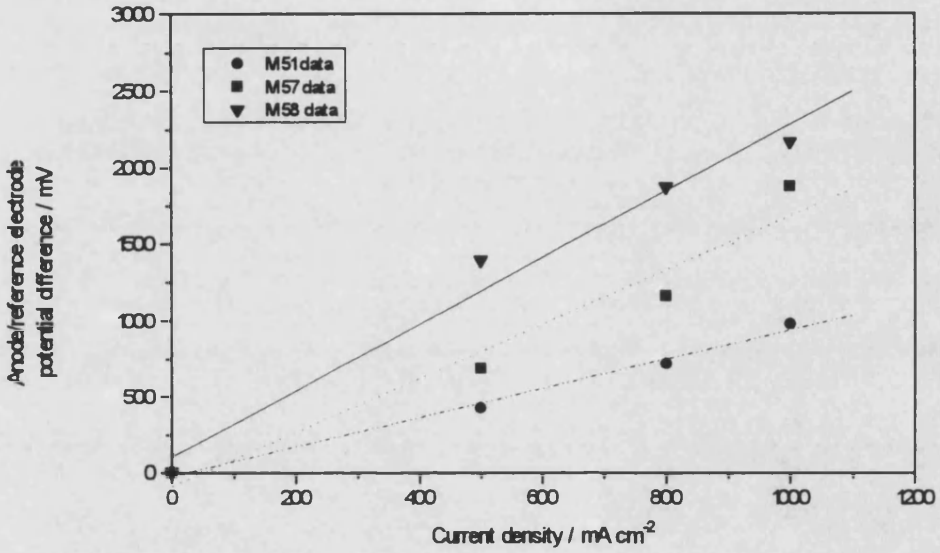

Figure 5.4 : anode/reference electrode current-voltage behaviour for samples M51, M57 and M58 as well as linear regression fits.

Table 5.1 reveals a significant increase in voltage. The fact that figure 5.4 shows that the current-voltage behaviour obeys Ohm's law suggests that the increase in voltage is due to an increase in ohmic contribution.

Having ruled out bubble layer effects and changes in solution properties, this strongly suggests that the electrode resistance must have increased. If this was the case then the increase in electrode resistance could either be caused by an increase in electrode porosity or the build-up of an resistive layer within the electrode. These models will be discussed in chapter 8. It must also be noted that had it been change in kinetics that was responsible for the voltage increase, the current-voltage behaviour would have not been a straight line.

Table 5.2 shows the values of the anode/reference electrode resistances as well as the equivalent increase in ohmic contributions resulting from degradation in the alkali wear pot.

Sample	$R_{anode/reference\ electrode}$ / Ω	$\Delta R_{anode/reference\ electrode}$ / Ω	ΔR_{alkali} / Ω
M51	0.96	0	0
M57	1.77	0.81	1.23
M58	2.19	1.23	2.25

Table 5.2 : values of the anode/reference electrode resistance and increases in ohmic contribution resulting in degradation in the alkali wear pot.

Table 5.2 shows that the increase in ohmic contribution measured from the anode/reference current-voltage behaviour, $\Delta R_{anode/reference\ electrode}$, is consistent with the increase in ohmic contribution resulting from degradation in the alkali wear pot, ΔR_{alkali}. Since the increase in cell voltage is of the same order as the increase in alkali wear pot running potential and since oxygen evolution is taking at the cathode in the alkali wear pot, this strongly suggests that the increase in total cell voltage is due to a significant increase in electrode resistance rather than an increase of the anode overpotential. The fact the alkali wear pot electrolyte conductivity is different that of the one used for chlorine evolution (brine) also tends to suggest that an increase in electrode resistance is responsible for the increase in cell voltage.

5.1.3 Conclusions

Steady state current-voltage results have shown that the apparent increases in ohmic contribution are consistent with the increases in alkali wear pot running potential. This strongly suggests that the source of the total cell voltage increase is an increase in electrode resistance. Two models have been suggested and will be discussed in greater detail in chapter 8.

It is clear that a more sophisticated method is needed to distinguish whether the increase in cell voltage is due to ohmic or kinetic effects. The use of interrupt techniques such as OCPD experiments should be conclusive as to the main effect of degradation and increase in total cell voltage as they will yield specific information about the change of reaction kinetics as a function of degradation.

Finally, steady state measurements have also shown that there is no detectable ohmic contribution resulting from the bubble layer. This is an important conclusion as it means that the bubble layer is not a factor that influences the total cell voltage in our experimental setup.

5.2 Potential-time measurements

This section covers results obtained from measuring the reference/working electrode potential difference as a function of time under steady state and under galvanostatic control. The purpose of these experiments was to study the frequencies of chlorine bubble detachment as a function of current density and electrode wear.

5.2.1 Theory

A Fast Fourier Transform (FFT) program was required to deconvolute the potential-time spectrum into a frequency spectrum[2]. This section describes the basic theory and relevant aspects of such a mathematical tool for the purpose of this project.

Consider a signal y(t) composed of a sinusoidal wave of amplitude A and frequency ω superimposed to a d.c. value B. y(t) can be written as follows :

$$y(t) = B + A*\sin(\omega t)$$

The potential-time dependence of such a signal is shown below :

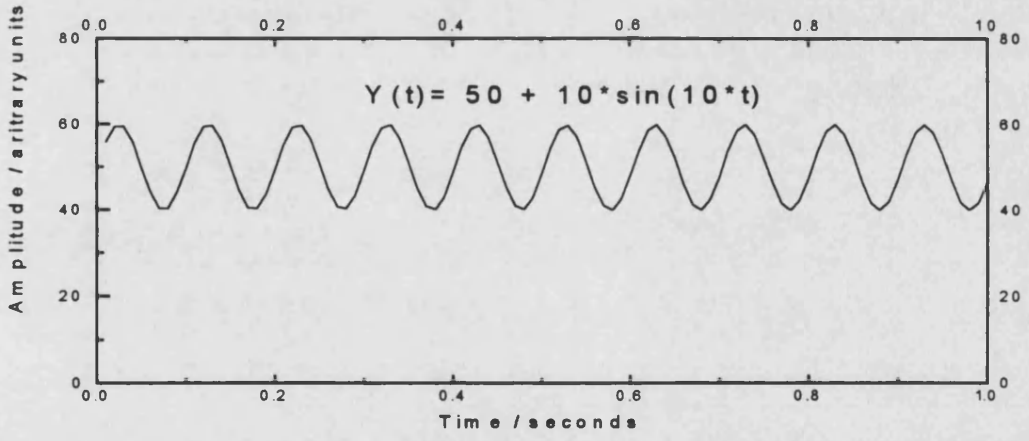

Figure 5.5 : Plot of a sinusoidal potential signal as a function of time

The potential-time dependence can be transformed into a frequency spectrum by performing what is called a Fourier transformation[2]. Let Y(f) be the Fourier transform of y(t). It is defined as follows :

$$Y(f) = \int_{-\infty}^{+\infty} y(t) e^{-j2\pi ft}\, dt \quad (\text{where } j^2 = -1)$$

This is a reversible operation and, hence, a potential-time plot can be derived from a frequency spectrum. In this case (and for the purpose of this project) interest only lies in the real part of the Fourier integral as it represents the frequency amplitude information.

The frequency spectrum obtained from operating a Fourier transform on y(t) looks as follows.

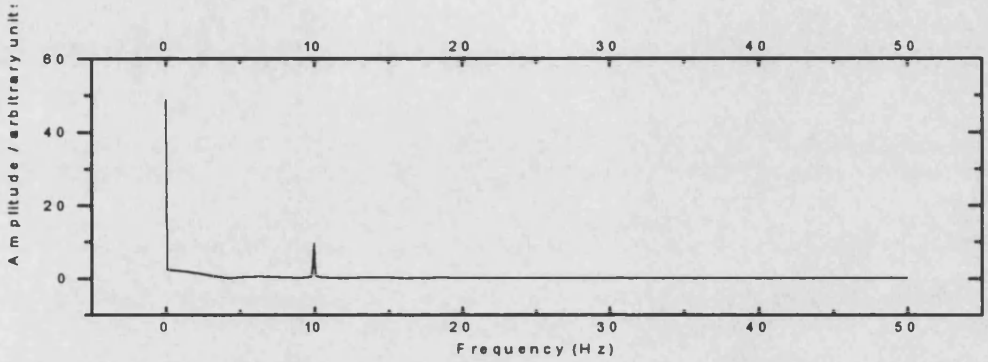

Figure 5.6 : Fast Fourier transform plot of figure 5.10

The frequency spectrum shows two peaks, one at 10 Hertz and the other at 0 Hertz. The latter is an artefact of the mathematical transformation : it corresponds to the fact that the d.c. value is considered as an oscillating signal of infinite period (and therefore 0 Hz frequency). This peak can be suppressed by subtracting the mean value of the y(t) potential signal before performing the Fourier transform. Such a transformation would only leave the frequency at 10 Hertz that corresponds to the oscillating contribution of y(t).

An important fact in Fourier transformations is that the magnitude of the peak in the frequency domain is a function of the magnitude of the oscillating signal in the potential-time domain. In the previous example, the dc component of y(t) was 50 and the magnitude of the oscillating component was of 10. The resulting frequency spectrum shows the corresponding peaks with magnitudes of 50 and 10 respectively. This is important since it means that a frequency will only be detected if the signal-to noise (STN) ratio is significant.

When performing real measurements there are always some random frequencies that cause interferences. This is called electrical noise and constitutes what is called the background. In some instances the electrical noise can be so significant that its minimisation is necessary in order to detect desired experimental frequencies coming

from experiments. One way to reduce electrical noise is to add filters that cut off frequencies above (or below) a certain frequency[3]. This, however, means that any information placed beyond the cut-off point is lost. Another way is to average the frequency spectrum a number of times. Averaging has the effect of minimising random noise and maximising fixed frequencies, i.e. random noise cancels itself out. The disadvantage is that measurement time is significantly increased and great care must be taken in maintaining constant experimental conditions.

5.2.2 Results and discussion

Figure 5.7 shows the background frequency spectra for the electrochemical setup used for these measurements.

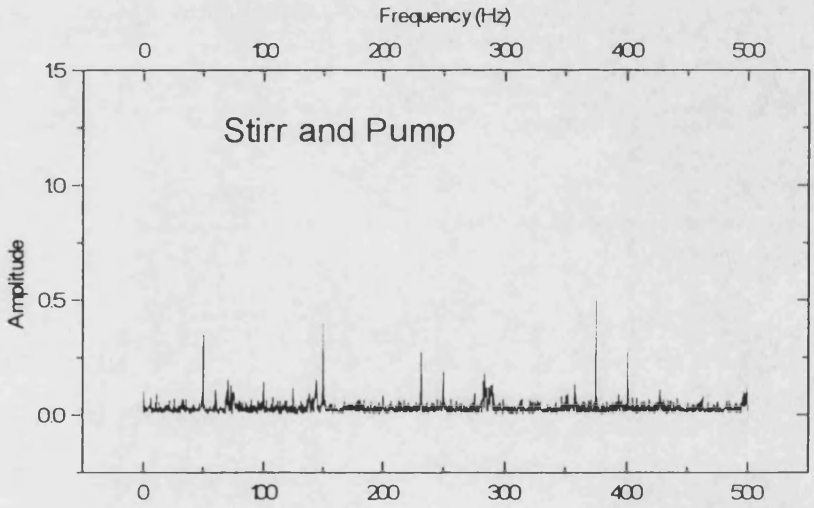

Figure 5.7 : background interference frequencies when stirrer and pump are switched on.

Figure 5.7 shows that the only significant frequencies detected were those associated with the mains frequency and its harmonics. Importantly, no interference peaks were found below 50 Hz. This is important as personal communications with ICI suggested the frequency of bubble generation would not be greater than 50-100 Hz.

Experiments were carried out on samples M33 to M38 at various current densities ranging from 5 to 900 mA cm^{-2} approximately. The next 4 plots show the frequency spectra for sample M33 from 5 to 900 mA cm^{-2} obtained from a Fourier transform of a single potential-time scan (90 Hz sampling frequency).

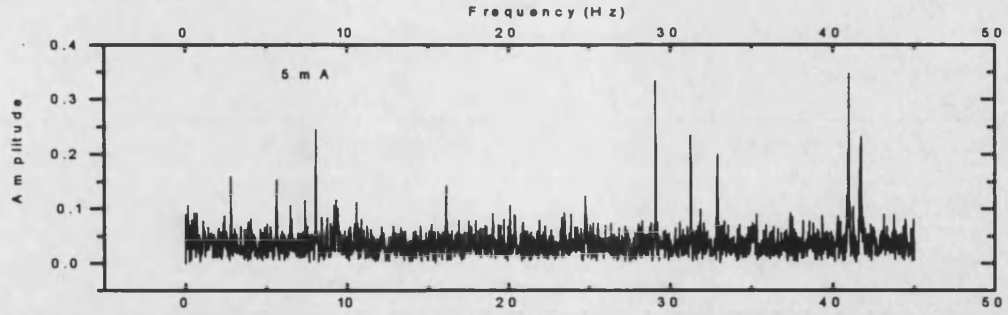

Figure 5.8 :FFT frequency plot for sample M33 at 5 mA applied d.c. current

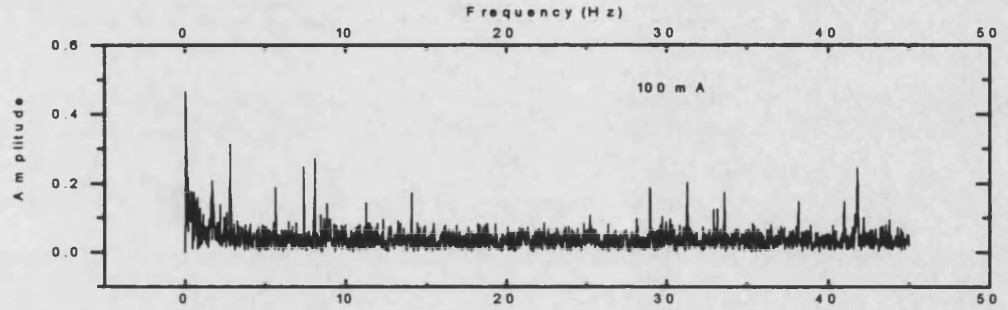

Figure 5.9 : FFT frequency plot for sample M33 at 100 mA applied d.c. current.

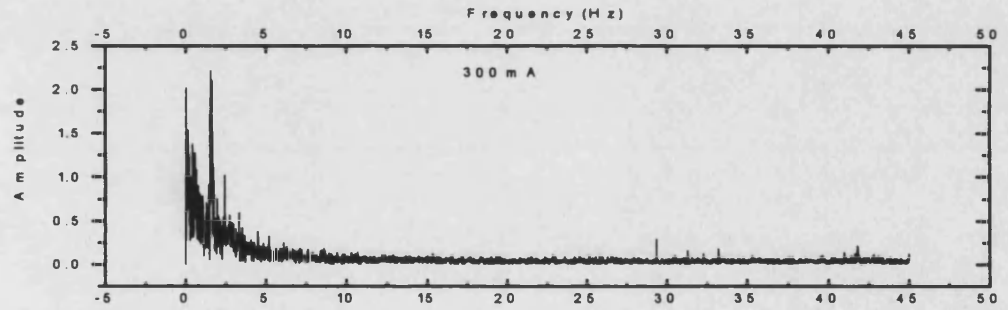

Figure 5.10 : FFT frequency plot for sample M33 at 300 mA applied d.c. current.

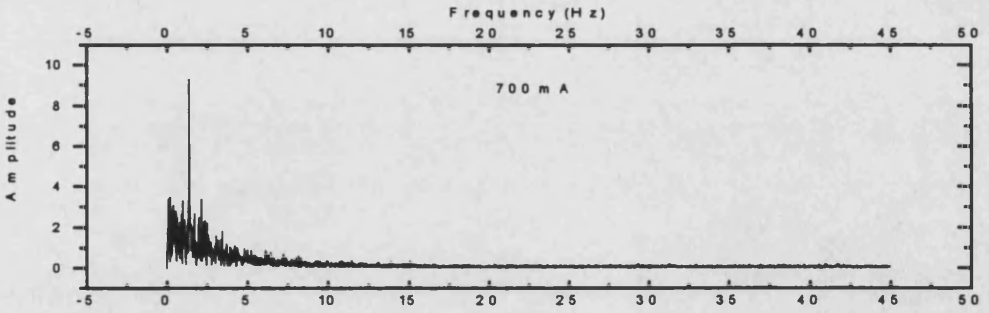

Figure 5.11 : FFT frequency plot for sample M33 at 700 mA applied d.c. current.

Analysis of figures 5.8 to 5.11 reveals a significant increase in frequency magnitude in the 0-5 Hz frequency region as a function of current density. This suggests that this region represents the bubble detachment frequency band of chlorine

gas molecules on the RuO_2/TiO_2 coating. Whereas the magnitude of the background noise level remains constant around 0.05, the magnitude of the distribution of frequencies in the 0-5 Hz region increases as a function of current density from 0.05 at 5 mA cm^{-2} to around a maximum of 3 at 900 mA cm^{-2}.

It also appears that there is a broadening effect as a function of current density : as the current density is increased from 300 to 900 mA cm^{-2}, the width of the bubble detachment frequency band increases from 0-5 Hz up to 0-15 Hz (approx.). Each of the frequency spectrum (i.e. 300, 700 and 900 mA) was fitted to an exponential decay in order to show the broadening and increase in magnitude of the band as a function of current density. This is shown in figure 5.12 below :

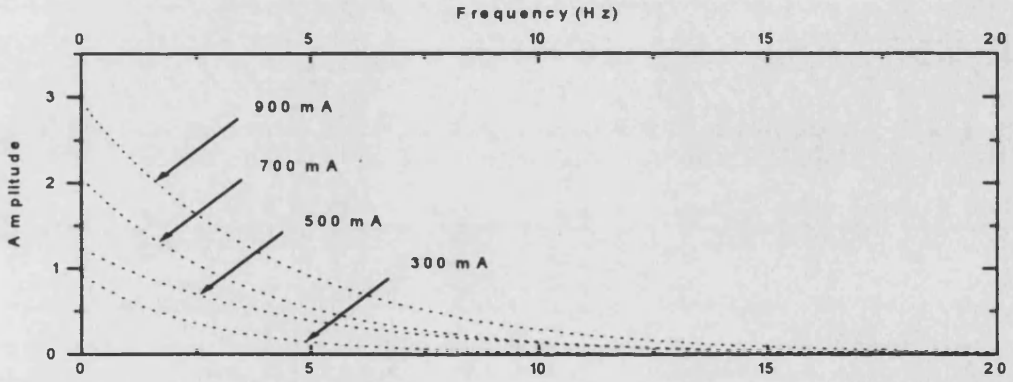

Figure 5.12 : broadening of frequency of bubble generation band of sample M33

The broadening of the frequency band suggests that the number of active bubble nucleation sites is increasing as a function of current density. Had it been a situation where there was a fixed number of sites then a shift in frequency towards higher values would have been observed.

As mentioned in the theory section, electrode wear may affect surface topography and therefore nucleation sites. Samples M33 to M38 were analysed to look for changes in the frequency spectra. The most degraded sample was M37. The following plots show the frequency spectra obtained at 300, 500 and 700 mA for this M37.

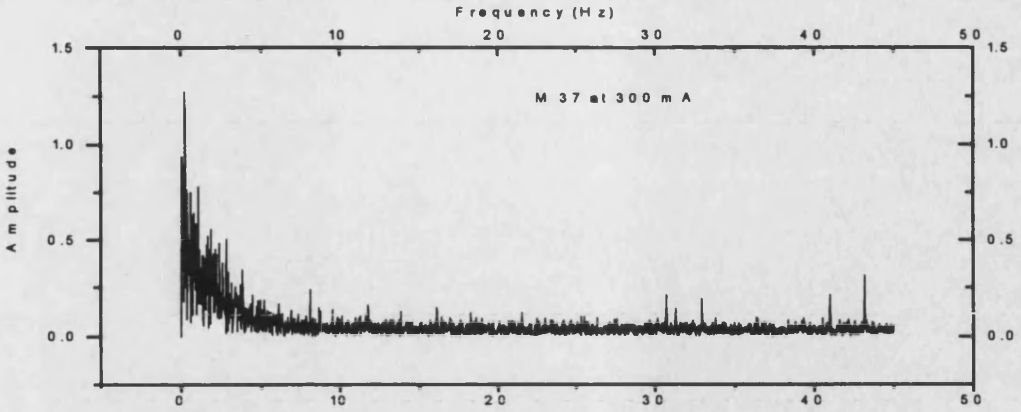

Figure 5.13 : FFT frequency plot of sample M37 after degradation at 300 mA.

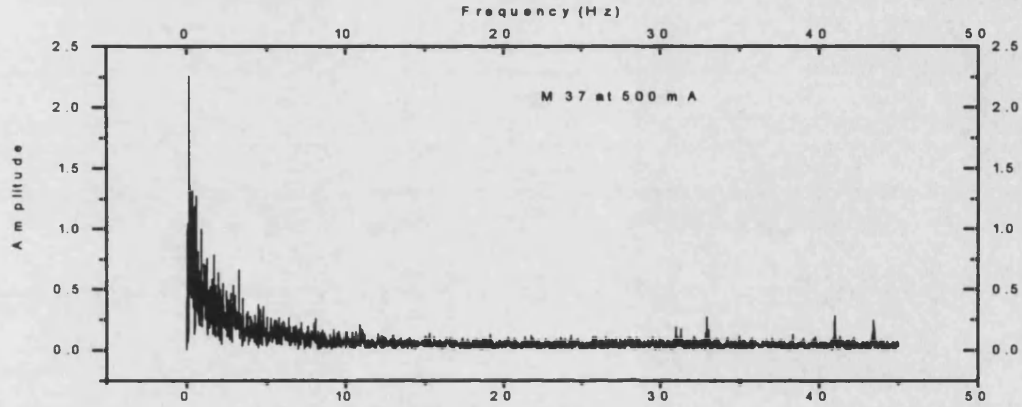

Figure 5.14 : FFT frequency plot of sample M37 after degradation at 500 mA.

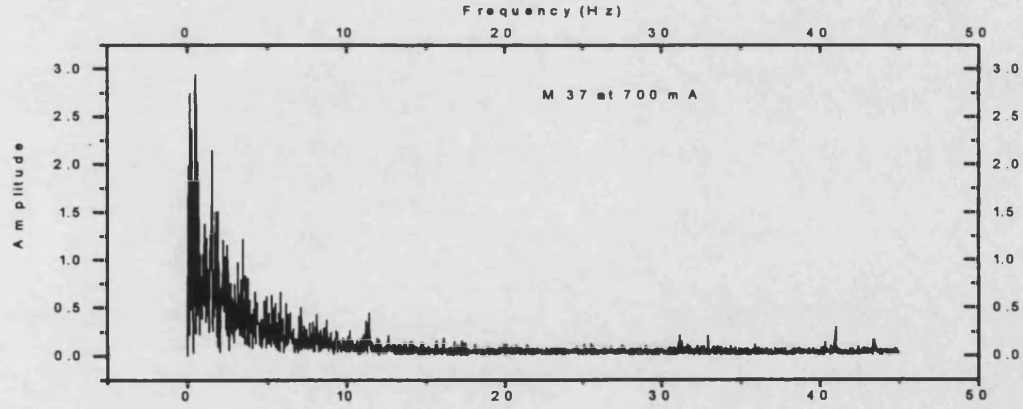

Figure 5.15 : FFT frequency plot of sample M37 after degradation at 700 mA.

Analysis of the frequency spectra in terms of bubble detachment frequency band broadening shows no detectable changes with electrode wear. There are no significant differences between the frequency spectra of sample M37 and M33 nor is there with any other sample.

5.2.3 Conclusions

Potential-time measurements were carried out because of the apparent simplicity of the experimental procedure and, especially, because of the high amount of information they could potentially yield in terms of surface topography and influence of degradation on reaction kinetics.

This has not been the case in our project and results from this technique are, unfortunately, not very conclusive. They seem to suggest that there is very no significant change in the frequency of bubble generation as a function of degradation.

Although this conclusion is consistent with results from other techniques, questions still remain about the effectiveness of this technique. In particular, since the smallest measurable potential difference was of 2.54 mV, it could be possible that a greater sensitivity was required to detect changes due to bubble detachment.

---

1 D. Pletcher, F.C. Walsh, *Industrial Electrochemistry*- 2nd ed, chap. 2, Blackie A&P, New York, 1993

2 R. Bracewell, *The Fourier Transform and its applications*, McGraw-Hill, New York 1965.

3 R.J. Smith, *Electronics - Circuits and Devices*, chap. 10, Wiley, New York, 1987

CHAPTER SIX

Chapter Six

Current Interrupt Methods

This chapter covers results obtained from interrupt techniques such as Tafel plot measurements and Open Circuit Potential Decay (OCPD) experiments. The purpose of using such techniques was to investigate the kinetics and change of reaction kinetics as a function of accelerated electrode wear for the chlorine evolution reaction on commercial RuO_2/TiO_2 electrodes.

6.1 Tafel plots measurements

Tafel plots measurements have traditionally played a very important role in the process of characterising a reaction mechanism at an electrode/electrolyte interface, and they are still very extensively used in industry in the field of electrocatalysis. The purpose of using Tafel plots in this project was two-fold. The first reason was to try and obtain *quantitative* information about the kinetics of the chlorine reaction at RuO_2/TiO_2 surfaces. Secondly, Tafel plot measurements were used to try and relate the change in reaction kinetics to accelerated electrode wear.

6.1.1 Theory

Consider the following reaction taking place at an electrode interface :

$$O + n\,e^- \rightleftharpoons R \qquad (6.1)$$

where C_o and C_R are the bulk concentrations of species O and R. Equilibrium is described by the Nernst equation :

$$E_{eq} = E^{\phi} + \frac{RT}{nF}\ln\frac{C_o^*}{C_R^*} \qquad (6.2)$$

where E^{ϕ} is the standard potential of the reaction and E_{eq} is the equilibrium potential. The total current density (j_{total}) will be the sum of the current for the forward ($j_{forward}$) and reverse current ($j_{reverse}$), i.e. reduction and oxidation currents respectively :

$$j_{total} = j_{forward} + j_{reverse} \qquad (6.3)$$

In this case $j_{forward}$ and $j_{reverse}$ are defined as follows :

$$j_{forward} = j_0\left(\frac{C_o(0,t)}{C_O^*}\right)\exp\left[-\alpha nf\left(E - E_{eq}\right)\right] \qquad (6.4)$$

$$j_{backward} = j_0\left(\frac{C_R(0,t)}{C_R^*}\right)\exp\left[(1-\alpha)nf\left(E - E_{eq}\right)\right] \qquad (6.5)$$

where $C_O(0,t)$ and $C_R(0,t)$ are the concentrations of O and R at the electrode surface (i.e. x = 0) and at time t; f = F/RT, α is the cathodic transfer coefficient and j_o is the exchange current density defined as $j_o = nFAk^oC_o^{*(1-\alpha)}C_R^{*\alpha}$ where n is the number of electrons involved in the reaction, A the working area, k^o the standard rate constant.

Combining equations 6.3, 6.4 and 6.5 allows the current-voltage equation to be derived :

$$j_{total} = j_0\left\{\left(\frac{C_0(0,t)}{C_O^*}\right)\exp(-\alpha nf\eta) - \left(\frac{C_R(0,t)}{C_R^*}\right)\exp\left[(1-\alpha)nf\eta\right]\right\} \qquad (6.6)$$

where $\eta = E - E_{eq}$ is the reaction overpotential. If there are no mass transfer effects and the concentrations of O and R at the surface are the same than at the bulk equation 6.6 then becomes as follows:

$$j_{total} = j_o\left[\exp(-\alpha nf\eta) - \exp\left[(1-\alpha)nf\eta\right]\right] \qquad (6.7)$$

This equation is most commonly known as the Butler-Volmer equation and is the starting point for the so-called 'Tafel plot' measurements.

When considering the Butler-Volmer equation, two approximations can be made depending on the value of the overpotential. They are as follows :

At small values of the overpotential η : $e^{\eta} \approx 1+\eta$. The Butler-Volmer equation can then be linearised as

$$j = j_o(-nf\eta) \qquad (6.8)$$

The current is linearly related to the overpotential in a narrow potential range near E_{eq}. The ratio $-\eta/i$ then has dimensions of resistance and is often referred to as the charge transfer resistance, R_{ct}, which is defined as follows :

$$R_{ct} = \frac{RT}{nFi_o} \qquad (6.9)$$

At large values of η either of the exponential terms becomes negligible and can therefore be neglected. For instance, at large negative values of overpotential

$\exp(-\alpha n f\eta) >> \exp[(1-\alpha) n f\eta]$. The Butler-Volmer equation then becomes the Tafel equation :

$$j = j_0 \exp(-\alpha n f \eta) \tag{6.10}$$

which can be rewritten in the form

$$\eta = \left(\frac{RT}{\alpha n F}\right) \ln j_o - \left(\frac{RT}{\alpha n F}\right) \ln j \tag{6.11}$$

The Tafel plot which is defined as the plot of $\log_{10}(\eta)$ vs. j (in the strictest sense) should therefore be linear at large values of η. The slope of the straight line, the Tafel slope, determines the value of the transfer coefficient α. The intercept on the j-axis allows the determination of the exchange current density, j_o.

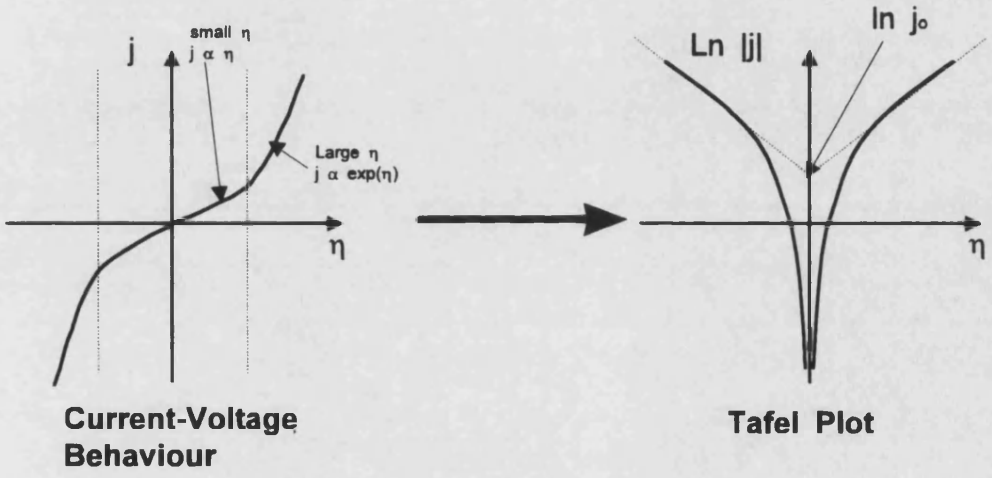

Figure 6.1 : Typical current-voltage behaviour and resulting Tafel plot for a simple 1 step reaction not involving adsorption.

At very large values of η, the reaction can become mass transfer controlled and the current reaches a limiting value if the mass transfer coefficient is also constant (at a rotating disc electrode for example). The resulting Tafel plot shows that the current-voltage behaviour deviates from linearity towards a constant limiting current, as illustrated in figure 6.2 :

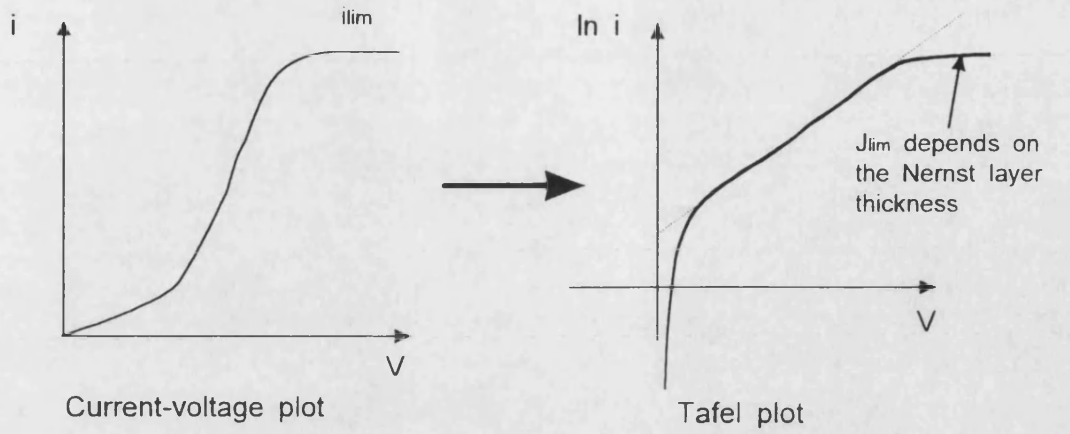

Figure 6.2 : Effect of mass transport on current-voltage and Tafel plot.

It must be emphasised that the present model does not consider adsorption processes. In the case of the chlorine reaction at a solid interface, it is generally accepted that the reaction mechanism involves more than one step. Conway and Trasatti have studied this reaction extensively and have proposed the following mechanism[1,2]:

step 1) $Cl^- + M \rightleftharpoons Cl_{ads}\text{-}M + e^-$

followed by step 2) $Cl_{ads}\text{-}M + Cl^- \rightleftharpoons Cl_2 + e^- + M$

or

step 3) $Cl_{ads}\text{-}M + Cl_{ads}\text{-}M \rightleftharpoons Cl_2 + 2\,e^- + 2\,M$

where M is a ruthenium activation site at the liquid/solid interface.

The total current will be the sum of the currents for each reaction step (i.e. $j_{total} = j_{tot1}+j_{tot2}+j_{tot3}$). Since this is a multistep reaction mechanism that also involves adsorption, it is therefore very unlikely that simple Tafel behaviour will apply to such a system. For instance, Conway et al. have treated the case for recombination and, assuming a Langmuir isotherm, derived[2] the following equation for the current-voltage equation :

$$j\left(\frac{1+\theta_0\exp(h\eta)}{1+\theta_0}\right)^2 = j_o\left[\exp(2h\eta)-1\right] \qquad (6.12)$$

where $\theta_o = \theta_{rev}/1\text{-}\theta_{rev}$ and θ_{rev} is the coverage at equilibrium.

It is clear that the current-voltage behaviour is not described in terms of the Butler-Volmer equation and that the experimental Tafel plot is not linear at large

overpotential values. However, there are instances where Tafel behaviour is observed even though the reaction mechanism is complex[3].

The reason why Tafel plots are used extensively in the field of electrocatalysis is because they can yield the value of the exchange current density and Tafel slope by measuring the overpotential of the reaction as a function of applied current. An increase in overpotential for a particular current density is used to characterise loss of electrocatalytic activity and can, therefore, be used as a measure of electrode wear. The exchange current density is also an important value as it reflects the electrocatalytic performance : the higher the value of the exchange current density, the better, in principle, the electrode performance.

Finally, Tafel plots have also been used to study the effect of pH[4], electrolyte concentration[5], convection[5,6,7] and temperature[8] on the electrocatalytic performance of RuO_2/TiO_2 electrodes. Although these parameters have been extensively studied, such characterisation was repeated on commercial electrodes as the non-ideality due to composition heterogeneity and surface roughness can affect the outcome of such a study. Furthermore, it appears that a proper characterisation has not been carried out under industrial operating conditions.

6.1.2 Results

The following section summarises the results obtained by Tafel plot measurements on undegraded and degraded electrodes as well as the influence of parameters such as convection and temperature on the reaction overpotential of chlorine evolution at RuO_2/TiO_2 electrodes.

Tafel measurements were carried out in the various flow cells (cf. chapter 3) and in the classical three arm electrochemical cell. Although it transpired that work in the flow cell gave incorrect values of overpotential because of reference electrode problems, the reproducibility of results meant that the effect of convection could be investigated. Tafel plot measurements were performed at flow rates of 3.3, 6.6 and 10 L sec^{-1} in a channel flow cell. Importantly, the flow rate was found to have no influence on the overpotential. These results are consistent with work carried out on rotating ring disk electrodes[9] which showed no influence of convection up to rates of 6400 rpm.

The effect of temperature was also studied. Measurements were carried out at 22, 40 and 60°C. Although the effects were not as marked as those described by Conway[10,11], it was found that the overpotential decreased as a function of temperature. The sensitivity of overpotential as a function of temperature was a factor that needed to be precisely studied in order to rule out the possibility that changes in overpotential could be the result of minor variations in experimental temperature.

In view of the conclusions reached about Tafel plot measurements later in this chapter it is important to recall a few points about the acquisition procedure for measuring the overpotential. A fast ADC was used in conjunction with a mercury wetted relay in order to interrupt the current and measure the overpotential of the reaction just after interruption. Although this may seem a trivial matter, work on studying the variation of the reference/working electrode potential before and just after interruption revealed significant problems associated with establishing the so-called instantaneous overpotential immediately after interruption (i.e. at 'time t = 0').

Tafel plots are usually obtained by measuring the potential value from an oscilloscope. This method is generally rather inaccurate. Closer analysis of the potential decay just after interruption has shown that the potential decreases very sharply just after the iR drop and that the measurement of the overpotential therefore depended on the horizontal time sensitivity of the oscilloscope. Although the apparent overpotential after interruption was reproducibly measurable, its value increased when the oscilloscope timescale was expanded. Differences in apparent overpotential of up 0 - 40 millivolts were found. Considering that overpotentials are reported to be in the range of 0 to 180 mV for current density ranges of 0 to 1500 mA cm^{-2}, this represents a substantial degree of uncertainty in this method of recording the overpotential. This was all the more important since it was anticipated that electrode wear would yield subtle changes in reaction overpotential for short periods of degradation time.

Since measuring the overpotential using an oscilloscope was found to be inaccurate, it was decided to program the Archimedes computer to perform the calculation of the overpotential just after interruption. Analysis of the potential variation in the first 300 microseconds after interruption revealed that, for *undegraded* electrodes, the potential could be approximated as a linear function of time in the 150-300 microsecond range. It was therefore decided to develop a curve fitting technique

that would determine the overpotential after interruption by performing a linear regression of the potential-time data and extrapolating back to the moment of interruption to obtain the overpotential at t = 0.

In order to increase the accuracy of this procedure, each value of the overpotential that was recorded to disk was the average of 30 current interruptions and curve fit calculations at the same current density. Furthermore, this allowed a standard deviation to be calculated for each overpotential recorded which was then used as a measure of reproducibility. Depending on this value, the software program either saved the overpotential to disk or repeated the measurement.

In the case of *undegraded* samples, measurement of the overpotential was found to be reproducible and analysis of successive measurements at the same current densities indicated that measured values deviated by a maximum of 5 % from each other. Comparison with values obtained from reading the potential values from an oscilloscope revealed that the computer measured values had a great degree of accuracy. It was therefore decided that Tafel plots carried out this way could be used to study the effect of degradation and allow trends to be established. The next figure illustrates the curve fitting process in order to determine the overpotential at time t=0 :

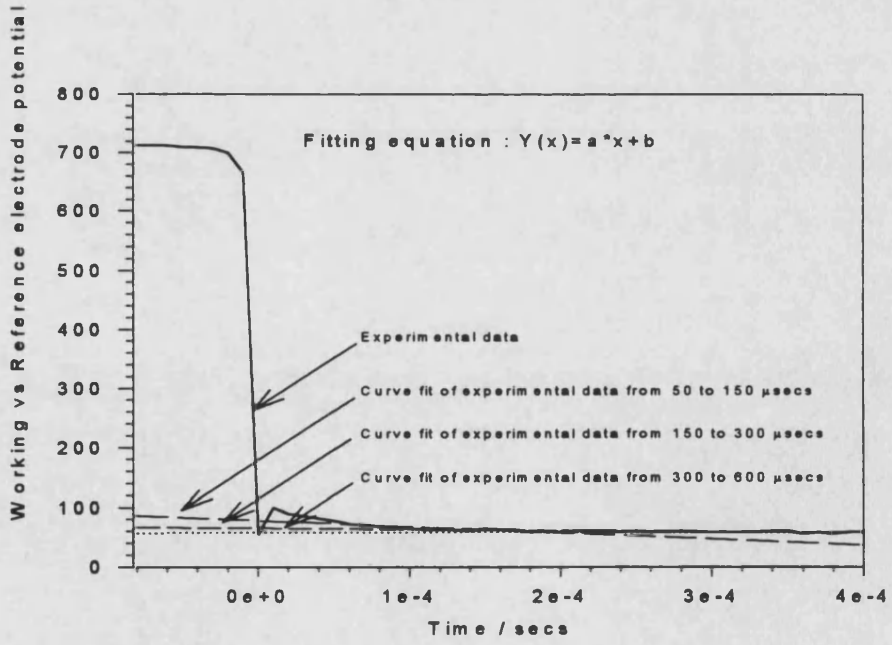

Figure 6.3 : Effect of fitting time range on the determination of overpotential at time t = 0.

Figure 6.3 clearly shows why the determination of the overpotential immediately after interruption is dependent on the time range chosen for the curve fit. This is equivalent to changing the time sensitivity on an oscilloscope. Since there is no reason why this effect should be restricted to the present instrumental system, absolute Tafel measurement values of overpotential quoted elsewhere should be treated with some caution. The key feature is that as long as the *same* procedure is used, the Tafel slope, exchange current density and reaction overpotential as a function of electrode wear can be used to study the loss of electrocatalytic performance.

Tafel plot measurements were carried out on undegraded samples for the M3x series according to this procedure in order to check whether all electrodes cut from the same strip behaved identically. This characterisation was considered very important in view of the analysis of overpotential increase as a function of electrode wear. The idea was that if all electrodes from the a series (i.e. same strip) behaved identically then it would not be necessary to carry out Tafel plots measurements for each of them *before* and *after* degradation. This was especially important in view of the electrode masking problems (see chapter 3) and in view of the significant amount of time taken to develop operational instrumentation.

This analysis revealed that it was impossible to calculate a value of the Tafel slope since the current-overpotential plot was continuously curved and that the resulting Tafel plot was, therefore, not linear. This also meant that no value for the exchange current density could be found. Since it has been established that the process is not mass transfer controlled, the curvature must be attributed to the fact that chlorine evolution is a multistep electrode process involving adsorbed intermediates. Conway[4] believes that the degree of curvature of the current-overpotential relation depends on the surface state of the RuO_2/TiO_2 coating, on its composition and its degree of surface roughness. This is why there is no unique polarisation behaviour for the RuO_2/TiO_2 catalytic material according to him. Experiments carried out on oxidised and reduced platinum electrode surfaces were also used to confirm this hypothesis.

In the case of the RuO_2/TiO_2 commercial samples used in this project, the polarisation behaviour depended on the amount of time chlorine was evolved, i.e. the measured overpotential after interruption before and after performing OCPD

measurements was not the same. No trend was identified but the differences were such that a change in the electrode behaviour must have been responsible for this. Personal communications with ICI suggested that electrodes need to be run for a short period of time before carrying out experiments as it was noticed that the reaction overpotential dropped after several minutes of flowing current through the electrodes. This was believed to be due to removal of contamination from the surface. In order to standardise the experimental procedures, a current of 300-500 mA cm^{-2} was used to generate chlorine at the surface of the electrode for a minimum period of 15 minutes before carrying out an experiment. Although this improved reproducibility, problems still remained.

In the case of degraded samples, it was found that the shape of the potential decay after interruption was not always the same. It was first thought that degradation was responsible, but it was subsequently discovered that this problem could either be due to the mercury wetted relay not operating properly or saturation of the OP amp just after interruption. (This will be explained in greater detail in section 6.3.2) The following figure illustrates the problem in accurately determining the overpotential just after interruption:

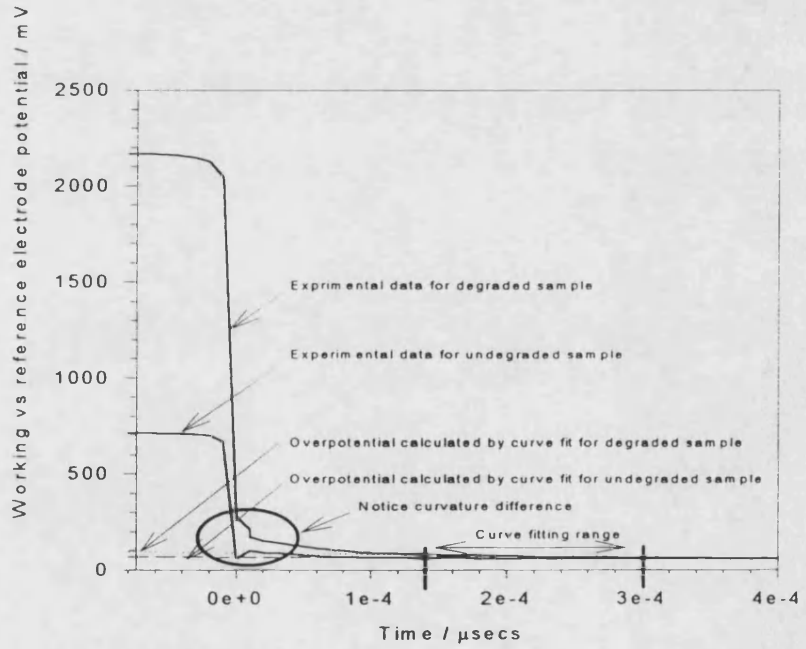

Figure 6.4 : difference in between potential decay shape of undegraded and degraded sample and resulting effect of curve fitting procedure (current density was 1100 mA cm^{-2} for all measurements).

At very short times, figure 6.4 shows that both traces show signs of irregularity which must be attributed to the performance of the mercury wetted relay and the oscillations due to stray lead inductance and capacitance. It also shows that the computer calculated overpotential after interruption is significantly different to the observed value after the iR drop in the case of the degraded electrode. The 'apparent' overpotential estimated from the trace for the degraded electrode is much higher than the value obtained by the computer extrapolation procedure. The very rapid decay observed between 0 and 200 μsec is thought to be associated with the inhomogeneous current distribution which could lead to lateral current flow across the electrode surface after interruption of the external current. If this is the case then the definition of the true overpotential becomes impossible as the decay reflects the redistribution of charge.

Since the method of measuring the overpotential using the oscilloscope was found to be unacceptable and since the method of determining the overpotential value just after interruption using a computer was open to question, it was concluded that Tafel plot measurements could not be used to characterise degraded electrodes under industrial conditions reliably. Tafel plots for undegraded electrodes were non-linear over the entire range and this meant no kinetic information was obtained.

6.1.3 Conclusions

A meticulous analysis of instrumentation and experimental procedure has revealed that it is not possible to use the Tafel plot measurement technique in order to obtain reproducible, accurate and meaningful polarisation curves for the RuO_2/TiO_2 anode coatings under industrially relevant operating conditions. This conclusion casts doubts on the validity of this technique in other electrochemical systems since part of the problem associated with the technique originate from the instrumentation. The Tafel plots for all electrodes are all continuously curved and since this is not a mass transfer effect, it must be due to the reaction involving potential dependent adsorbed intermediates.

6.2 Open Potential Circuit Decays (OCPD)

The OCPD technique was used for 2 reasons. Since analysis of OCPD traces allowed kinetic information to be derived, decay experiments were carried out to monitor changes in electrocatalytic activity as a function of electrode wear. The second purpose was to determine the reaction mechanism of chlorine evolution on commercial chlorine anodes under industrially relevant conditions.

In general, OCPD experiments last about 1-3 seconds. This is one the major advantages of the OCPD technique. To obtain the same information from impedance spectroscopy can take hours. The cost of instrumentation for OCPD experiments is also low compared with impedance spectroscopy which requires the use of a frequency response analyser.

6.2.1 Kinetic approach

Although the OCPD technique was first used in 1928[12], it has not been used widely as an investigative technique. In principle, the uncompensated ohmic potential drop, the double layer capacitance and kinetic information such as the exchange current density, Tafel slope and rates of individual reaction steps can be derived from the shape and curve fitting of the OCPD. It is also the best way to establish whether there is a pseudo-capacitive behaviour associated with adsorption.

The generally accepted reaction steps that are possible for the chlorine reaction at a catalyst surface are the starting point for this theory section, i.e.

step 1) $M + Cl^- \rightleftarrows M\text{-}Cl_{ads} + e^-$ (electrochemical adsorption)

step 2) $M\text{-}Cl_{ads} + Cl^- \leftrightarrows M + Cl_2 + e^-$ (electrochemical desorption)

step 3) $2\ M\text{-}Cl_{ads} \rightleftarrows 2\ M + Cl_2$ (chemical desorption)

The following assumptions were made :

- No mass transfer control.
- A Langmuir isotherm which neglects lateral interactions in between adjacent adsorbates and allows a maximum coverage of a monolayer is assumed. Although this choice is possibly a rather simplistic approximation to the real

situation, it does not affect the qualitative conclusions obtained from the derivations that will follow.

- Surface concentrations of Cl_2 and Cl^- are assumed to be constant and equal to bulk values. For convenience, they are included in the rate constants. The net rates of the individual steps (v_1, v_2, v_3 /mol cm^{-2}) are therefore dependent only on the overpotential, η, and the fractional coverage, θ, of the adsorbed intermediate, M-Cl_{ads}.
- the rate constants are assumed to have Tafelian potential dependence and α is taken as 0.5

It follows that the rates of steps 1-3 are defined by the following equations :

$$v_1 = k_1(1-\theta)\exp\left(\frac{F}{2RT}\eta\right) - k_{-1}\theta\exp\left(-\frac{F}{2RT}\eta\right) \qquad (6.13)$$

$$v_2 = k_2\theta\exp\left(\frac{F}{2RT}\eta\right) - k_{-2}(1-\theta)\exp\left(-\frac{F}{2RT}\eta\right) \qquad (6.14)$$

$$v_3 = k_3\theta^2 - k_{-3}(1-\theta)^2 \qquad (6.15)$$

where k_1, k_{-1}, k_2, k_{-2}, k_3 and k_3 are the rate constants for the forward and reverse steps 1-3 respectively.

The faradaic current density is proportional to the rate of electron production, r_0, which is equal to the sum of v_1 and v_2 :

$$\frac{j_f}{F} = r_0(\theta,\eta) = v_1 + v_2 \qquad (6.16)$$

In the same way, $d\theta/dt$ is proportional to r_1, the rate of production of M-Cl_{ads} :

$$\left(\frac{Q_{mono}}{F}\right)\left(\frac{d\theta}{dt}\right) = r_1(\theta,\eta) = v_1 - v_2 - 2v_3 \qquad (6.17)$$

Q_{mono} is defined as the charge required per cm^2 for monolayer coverage by the intermediate. v_3 is defined as the rate of chlorine production, which is half the rate of adsorbed M-Cl_{ads} consumption (this explain why the coefficient of two appears).

The double layer capacitance is assumed to be ideal (i.e. a well defined frequency independent quantity). The electrode is considered as perfectly homogeneous (i.e. all sites are equivalent). This is another simplistic approximation since the anodes used in this project have a heterogeneous composition and

significant surface roughness. However, results from impedance spectroscopy have shown that it is still possible to obtain useful results by considering the anodes as flat and homogeneous.

When the external current is interrupted, the charge stored in the double layer capacitance can only be changed by charge transfer. Overpotential decay therefore occurs as electrons are transferred in steps 1) and 3). It follows that

$$j_f = -\frac{d\sigma}{dt} = \left(\frac{-d\sigma}{dV_{dl}}\right)\left(\frac{dV_{dl}}{dt}\right) = -C_{dl}\left(\frac{d\eta}{dt}\right) \qquad (6.18)$$

where σ is the charge stored in the double layer capacitance. It is important to remember that this model does *not* take into account the possibility that the metal-solution potential difference can be changed by altering the distribution of charges in the double layer. The possibility of partial charge transfer and the effect of a partially charged adsorbed intermediate on the double layer is not considered either. These simplifications are equivalent to the assumption made in impedance spectroscopy that the charging and faradaic currents are separable. Another important simplification is the electrode is considered to have uniform potential and current density distributions. Although the electrodes used in this project are geometrically flat, the combination of their high surface roughness, possible porosity, and high degree of compositional heterogeneity means that lateral currents can occur and that current and potential distributions are non-uniform.

By combining equations 6.16 and 6.18, an expression of $d\eta/dt$ in terms of the reaction kinetics can be derived :

$$-\left(\frac{C_{dl}}{F}\right)\left(\frac{d\eta}{dt}\right) = r_0(\theta,\eta) = \nu_1 + \nu_2 \qquad (6.19)$$

Equations 6.17 and 6.19 can then be used as a set of simultaneous differential equations to determine the variation of η and θ as a function of time during the potential decay.

In order to use this kinetic model to obtain quantitative information, the value of the steady state coverage, θ_{ss} and initial overpotential, $\eta(0)$ must be known. $\eta(0)$ can be determined from the experimental data and θ_{ss} can be evaluated by inserting $\eta(0)$ in equation 6.13, setting it equal to zero and solving for θ_{ss}. As it will be seen

later, a FORTRAN program was written to simulate OCPDs in order to evaluate the effect of various kinetic parameters on the shape of the potential decay.

Finally, it is important to note that the rate constants are not all independent but, on the contrary, constrained by the equilibrium condition for the net reaction according to the following equation, i.e.

$$\frac{k_1 k_2}{k_{-1} k_{-2}} = \frac{k_1^2 k_3}{k_{-1}^2 k_{-3}} = 1 \qquad (6.20)$$

A) OCPD simulations

As mentioned previously, a FORTRAN program was written on the basis of equations 6.17 and 6.19 to simulate theoretical OCPDs (refer to appendix for a listing of it). This section summarises the conclusions obtained from the study of the influence of various kinetic parameters on the shape of OCPDs. As it will be seen later, this investigation shows that the OCPD technique is a powerful fingerprinting tool when it comes to determining the reaction mechanism of chlorine evolution at the surface of RuO_2/TiO_2 anodes.

Before going any further, it is important to define clearly the parameters that will be varied in these simulations. They are as follows :

- Temperature
- α_1, α_2 and α_3 cathodic transfer coefficients for steps 1), 2) and 3)
- Q_{mono} the surface charge density for monolayer coverage
- C_{dl} the double layer capacitance
- $\eta(0)$ the overpotential at t = 0, i.e. just after interruption
- $j_f(0)$ the faradaic current density at t = 0
- k_1 to k_{-3} the forward and reverse rate constants associated with steps 1) - 3)
- Kx ratio of k_x/k_{-x}, i.e. K1, K2 and K3
- X defined as K1/K2= $\frac{k_1 k_{-2}}{k_{-1} k_2}$

In order to gain understanding of the influence of steps 2) and 3) on the shape of the OCPD, simulations were first carried out assuming that step 2) was the *only* reaction responsible for chlorine formation. This meant that the simulation was mainly dependent upon the influence of the rate constants k_1, k_{-1}, k_2 and k_{-2}. In order to reduce

the number of rates constants required for the simulations, equation 6.20 and X (defined above) were combined to derive the values of k_{-1} and k_{-2} in terms of k_1, k_2 and X. This reduced the number of unknown parameters from 4 to 3 and allowed a better understanding of the influence of the rates of backward reaction for steps 1) and 2) (the utility of such a transformation will become more evident when studying the influence of these parameters). By combining equation 6.20 and X, the values of k_1, k_{-1}, k_2 and k_{-2} are obtained as

$$k_1 = k_1 \tag{6.21}$$

$$k_{-1} = \frac{k_1}{X} \tag{6.22}$$

$$k_2 = k_2 \tag{6.23}$$

$$k_{-2} = X * k_2 \tag{6.24}$$

The following section shows the contents of a typical file used to set the initial values of parameters for the FORTRAN OCPD simulation program :

5

0.5 0.5 333 3.3e-1 4.0e-4 1.0e-5 1.8e-7 4.5e0 .27 'A.DAT'

0.5 0.5 333 5.0e0 4.0e-4 7.0e-5 1.8e-7 30.0e0 .27 'B.DAT'

0.5 0.5 333 5.0e-2 4.0e-4 1.0e-6 1.8e-7 4.3e-1 .27 'C.DAT'

0.5 0.5 333 2.0e-1 4.0e-4 5.0e-6 1.9e-7 2.0e0 .27 'D.DAT'

0.5 0.5 333 1.0e-1 4.0e-4 2.0e-6 1.9e-7 8.0e-1 .27 'E.DAT'

Figure 6.5 : example of input file for FORTRAN simulation program.

The first digit represents the number of simulations to be performed by the program. The next five lines respectively contain the values of α_1, α_2 , temperature (K), surface charge for monolayer coverage (C cm^{-2}), double layer capacitance (F cm^{-2}), k_1, k_2 (mol cm^{-2} s^{-1}), X (i.e. K1/K2), $\eta(0)$ and the output filename for each of the simulations.

The next diagrams show 2 simulated OCPDs and corresponding variations of the surface coverage in the case where step 3 is *not* significant. The values used for the first OCPD are consistent with the case of the hydrogen reaction on platinum and values for the second one are consistent for the case of chlorine reaction on a commercial RuO_2/TiO_2 electrode.

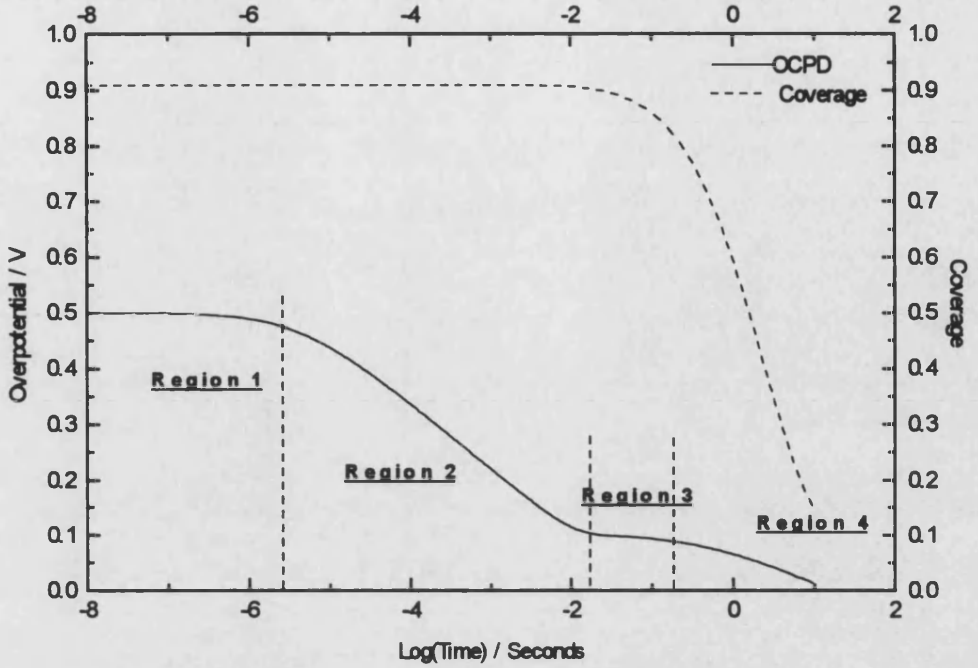

Figure 6.6 : OCPD for the case of hydrogen evolution on Pt for $k_1 = 10^{-9}$ mol cm^{-2}, $k_{-1} = 10^{-8}$ mol cm^{-2} s^{-1}, $k_2 = 10^{-10}$ mol cm^{-2} s^{-1}, $k_{-2} = 10^{-11}$ mol cm^{-2} s^{-1}, $k_3 = k_{-3} = 0$ mol cm^{-2} s^{-1}, $Q_{mono} = 210$ μC cm^{-2}, $C_{dl} = 25$ μF cm^{-2} and $\eta(0) = 0.5$ V.

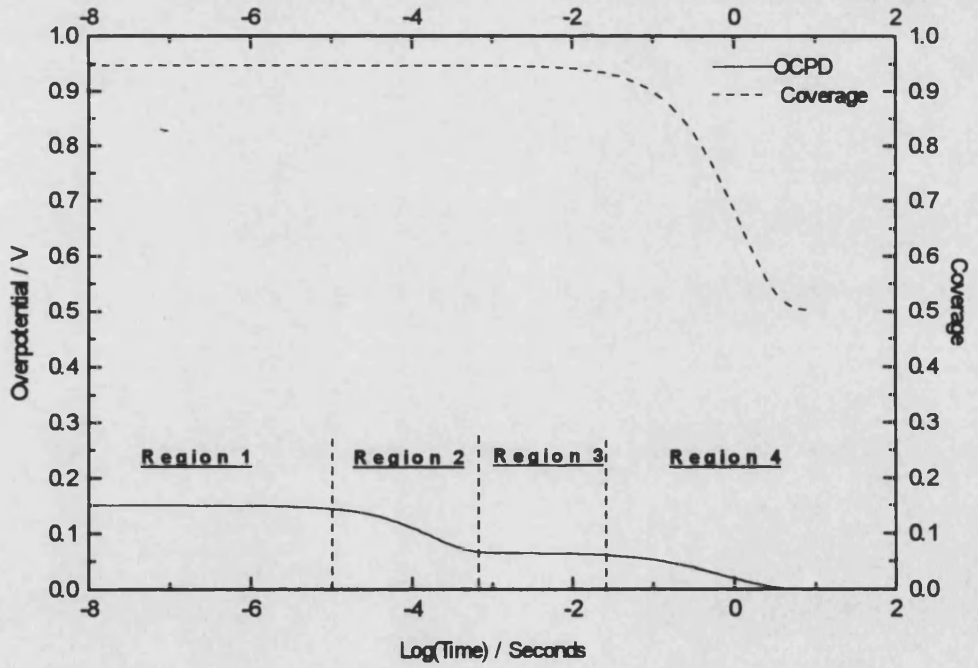

Figure 6.7 : OCPD for the case of chlorine evolution at ICI commercial RuO_2/TiO_2 anode measured at 1300 mA cm^{-2} approx., 60°C and fitted using simulation program.

Figures 6.6 and 6.7 show that the shape of the OCPD on a logarithmic time scale exhibits several characteristic features. They also show that the main difference between the two plots is the overall time scale for the decays : in both cases, one can identify 4 distinct potential-time regions that can be described for the case of chlorine evolution as follows :

In regions 1 and 2, the surface coverage of the adsorbed intermediate remains practically constant. The overpotential can be described in terms of the approximation to the Butler-Volmer equation :

$$j_f = j_{ss} = j_0 \exp\left(\frac{\alpha F}{RT}\eta\right) \tag{6.25}$$

which leads to

$$\eta(t) = \left(\frac{RT}{\alpha F}\right)\left\{\ln\left(\frac{\alpha F i_0}{CRT}\right) - \ln(t+\tau)\right\} \tag{6.26}$$

where $\tau = \frac{RTC}{\alpha F j_0}\exp\left(\frac{\alpha F}{RT}\eta(0)\right)$, j_f and j_{ss} are the faradaic and steady state current densities and C is the capacitance.

In region 1, $t \ll \tau$ so the overpotential is approximately constant. The total current density is proportional to the sum of the overall reaction rate for step 1) and step 2), and is equal to zero when the external current has been interrupted. In other words, since $j_{total} = j_{charging} + j_{faradaic}$, after interruption $j_{total} = 0$ and since the faradaic current density is not necessarily 0, $j_{faradaic} = -j_{charging}$.

In region 2, $t \gg \tau$ so that the overpotential falls linearly with ln(t) and the slope $d\eta/d\ln(t)$ is equal to the Tafel slope, i.e. $-RT/\alpha F$. The faradaic current then starts to decay to 0 until the double layer has been discharged. According to the kinetic analysis, this means that the quantity represented by equation 6.16 is far greater than that of equation 6.17 and, as a result, equation 6.16 controls the early part of the overpotential decay : the coverage is equal to that of steady state and remains constant in the early stage of the decay. The exchange current density cannot be calculated from the Butler-Volmer equation because the steady state coverage is significant.

Mathematically, for high overpotentials ($\theta = \theta_{ss} \approx 1$), only the positive exponentials need be retained, i.e. the rate of reaction for the back reaction in step 1) is negligible. As a result, the right hand side (RHS) of equation 6.13 is similar to equation

6.25 where j_o needs to be replaced by $F[k_1(1-\theta_{ss})]$. As a result, only if θ_{ss} is known to be small can the exchange current density be calculated this way. It is also clear that the capacitance identified in equation 6.26 should be identified with the double layer capacitance. The assumption that the transient faradaic current is only valid because equation 6.19 controls the rates and the backward rates are negligible. The faradaic current changes principally because of changes in the activation energies of the mechanism. This occurs in a way consistent with the relationship which governs the discharge of the double layer capacitance (equation 6.26) : the double layer capacitance is relaxing by virtue of the potential dependence of the rate constants. In region 1&2, the reaction mechanism is therefore as follows :

step 1) $Cl^- + M \rightleftharpoons M\text{-}Cl_{ads} + e^-$

step 2) $M\text{-}Cl_{ads} + Cl^- \rightleftharpoons Cl_2 + M + e^-$

Overall $2\,Cl^- \rightleftharpoons Cl_2 + 2\,e^-$

In region 3, the overpotential has dropped significantly but the coverage has remained practically unchanged. At this point, the overpotential reaches a plateau. Equation 6.16 still controls the main reaction. Equation 6.16 is still unimportant as the surface coverage has changed very little. Although both equations overlap in time, it is convenient to conceptually separate them. As the overpotential is changing slowly this means that the discharge of the double layer capacitance is almost negligible and that the faradaic current must be close to zero, i.e. $v_1 \approx -v_2$. According to equation 6.17 and 6.18 : v_1 changes more rapidly than v_2 because the back reaction of step 1) depends on θ whereas the back reaction for step 2) depends on $1-\theta$. Eventually v_1 becomes negative and step 1) is proceeds in reverse while step 2) still proceeds in the forward direction. Step 2) always proceeds in the forward direction because $k_{-2}(1-\theta)\exp[-F\eta/2RT] < k_2\theta\exp[F\eta/2RT]$ under all conditions. Under these conditions, the intermediate $M\text{-}Cl_{ads}$ is being removed by mixed anodic/cathodic mechanism without significant current flow across the interface, as described below :

step 1 $M\text{-}Cl_{ads} + e^- \rightleftharpoons Cl^- + M$

step 2 $M\text{-}Cl_{ads} + Cl^- \rightleftharpoons Cl_2 + M + e^-$

Overall $2\,M\text{-}Cl_{ads} \rightleftharpoons Cl_2 + 2\,M$

The next plot shows the variation of v_1 and v_2 throughout the entire decay for the case of chlorine evolution.

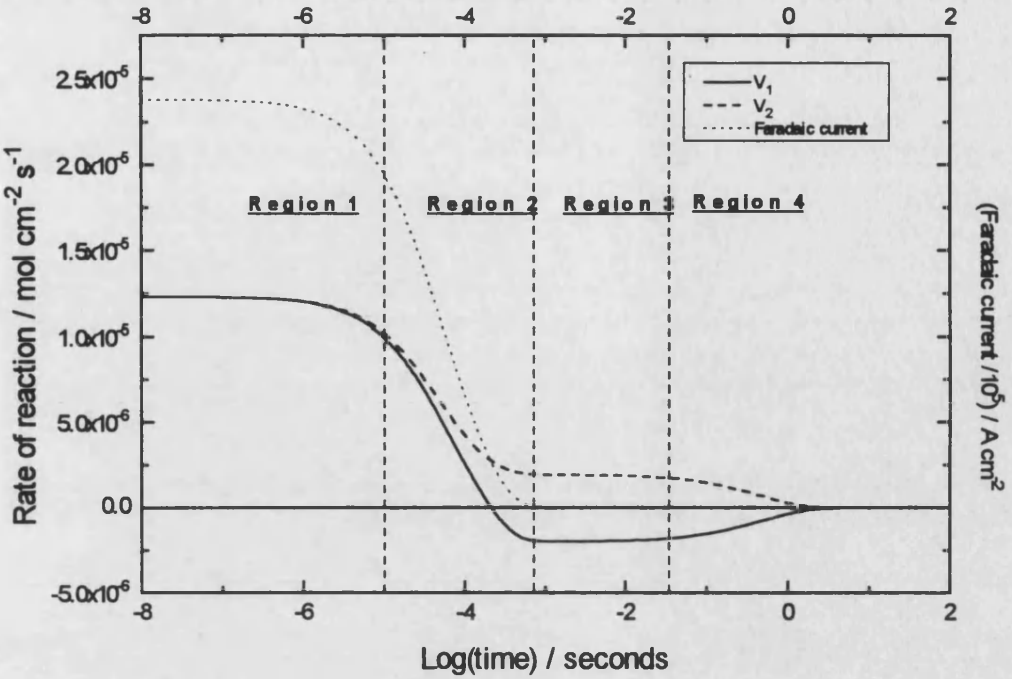

Figure 6.8 : variation of reactions rates v_1 and v_2 for steps 1 and 2 during OCPD for $k_1 = 10^{-6}$ mol cm^{-2} s^{-1}, $k_2 = 10^{-7}$ mol cm^{-2} s^{-1}, X = 10, $Q_{mono} = 2\ 10^{-1}$ C cm^{-2}, C_{dl} = 25 mF cm^{-2}, T = 333 K and $\eta(0) = 0.15$ V.

Figure 6.8 confirms that the faradaic current decays to zero as a result of the potential dependence of the reaction rates in region three.

Once θ is decreased by mixed anodic/cathodic mechanism, the assumption that θ is constant is no longer true (region 4). The plateau region is therefore expected to be short as equation 6.17 is no longer negligible. In region 4, equations 6.16 and 6.17 then control the behaviour of the transient and the potential begins to fall more rapidly to its equilibrium value.

An interesting feature of the OCPD simulation is that the equilibrium coverage is not equal to zero (cf. figure 6.6). This can be explained as follows :

At equilibrium, both reactions, i.e. steps 1) and 2) must be in equilibrium (microscopic reversibility). It follows that

$$E_1 = E_2 = E \qquad (6.27)$$

where E_1, E_2 and E are the equilibrium potentials of step 1), step 2) and the overall reaction. This leads to

$$E_1^{\phi} + \frac{RT}{F}\ln\left(\frac{a_{Cl^-}^2}{a_{Cl_2}}\right) = E_2^{\phi} + \frac{RT}{F}\ln\left(\frac{a_{Cl_2}}{a_{Cl_{ads}} * a_{Cl^-}}\right) \qquad (6.28)$$

which leads to

$$E_2^{\phi} - E_1^{\phi} = \frac{2RT}{F}\ln\left(a_{Cl^-}\right) - \frac{RT}{F}\ln\left(p_{Cl_2}\right) \qquad (6.29)$$

It follows that

$$E_2^{\phi} - E_1^{\phi} = \frac{RT}{F}\ln\left(\frac{a_{Cl_2}^2}{p_{Cl_2}}\right) \qquad (6.30)$$

For the Langmuir adsorption we define

$$a = \frac{\theta}{1-\theta} \qquad (6.31)$$

where the standard state is $\theta = 0.5$, i.e. $a = 1$.

1. If $E_2^{\phi} - E_1^{\phi} = -59$ mV then equation 6.30 means that $\frac{a_{Cl^-}^2}{p_{Cl_2}} = 0.1$. If we assume that $p_{Cl_2} = 1$ atm then $a_{Cl^-} = 0.316$ and $\theta_{eq} = 0.09$.

2. If $E_2^{\phi} - E_1^{\phi} = 59$ mV then equation 6.30 means that $\frac{a_{Cl^-}^2}{p_{Cl_2}} = 10$. Likewise, if $p_{Cl_2} = 1$ atm then $a_{Cl^-} = 3.16$ and $\theta_{eq} = 0.91$.

B) the influence of various parameters on the shape of OCPDs

The description of the overpotential decay in terms of the various regions has highlighted the three types of plots that will be used to detect the effect of kinetic parameters. They are as follows :

1) $\eta(t)$ vs. log(time) or OCPD plot

2) Coverage vs. log(time)

3) rates of reaction 1 & 2 vs. log(time)

Just as previously, the case where step 3 is not significant will be considered first. As it will be seen in the next sections, the best way to investigate the effect of various parameters on OCPD plots is to display results in a graphical format. For each of the parameters investigated, a minimum of 3 values is chosen so that any trend can clearly be identified. In each case, only one parameter is varied at a time. The factors

investigated are temperature, monolayer coverage surface charge, double layer capacitance, k_2, k_1, X and $\eta(0)$.

Effect of varying temperature on the shape of OCPD plot

Before investigating the effect of temperature on OCPDs it is important to remember that all rate constants will change exponentially as a function of 1/T via the Arrhenius equation, i.e. $k = A^*\exp(-E_a/RT)$. The temperature dependence of rate constants is generally much more important than the RT/F effect. Experimental temperature dependence should therefore be dominated by the kinetics. The next plot shows the effect of increasing the temperature from 0°C to 60°C on the shape of OCPD plots.

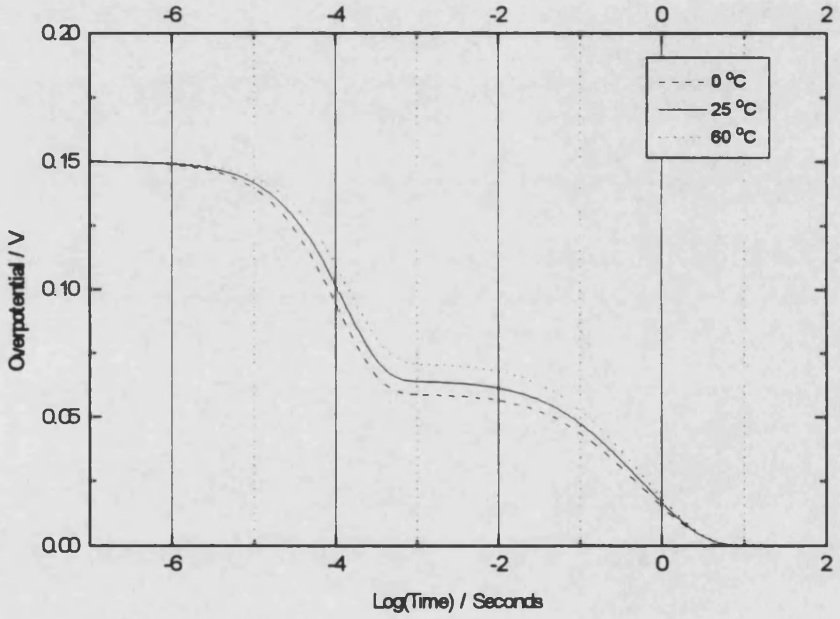

Figure 6.9 : Effect of increasing temperature on the shape of OCPD plots. α = 0.5; $\eta(0)$= 0.15 V; $Q_{mono} = 3\ 10^{-1}$ C cm^{-2}; $C_{dl} = 3\ 10^{-3}$ F cm^{-2}; $k_1 = 1\ 10^{-5}$ mol cm^{-2} s^{-1}; $k_2 = 2\ 10^{-7}$ mol cm^{-2} s^{-1}; X = 5.

Increasing the temperature increases the length of region 1 where the overpotential remains practically constant. Although it also causes an increase in the overpotential value of the plateau arrest, it does not affect the length or shape of regions 2 to 4. The slope of $d\eta(t)/d\log(t)$ will also increase since the theory predicts that the slope $d\eta(t)/d\log(t)$ to be equal to the Tafel slope, $b = RT/\alpha F$.

Lets assume that the OCPD slope in region 2 had a magnitude of s_0 at 60°C and that the temperature could vary by $\pm \Delta T$ °C. The error margin is therefore $\Delta s = \pm R\Delta T/\alpha F$. If ΔT is equal to $\pm$ 5°C then $\Delta s = \pm$ 0.9 mV. This would not be detectable within the experimental accuracy and, as a result, any major change in the calculated value of the slope could not be attributed to a temperature variation.

Effect of varying the double layer capacitance on the shape of OCPD plots

The next plot shows the effect of increasing the value of the double layer capacitance from 0.1 mF cm^{-2} to 5 mF cm^{-2} :

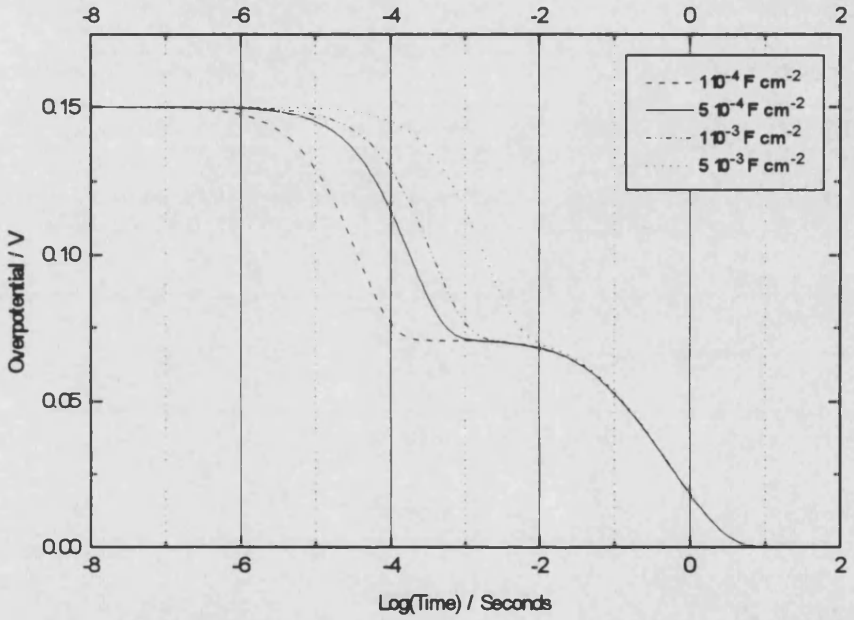

Figure 6.10 : Effect of increasing the double layer capacitance on the shape of OCPD plots. α = 0.5; T = 333 K; $\eta(0)$ = 0.15 V; $Q_{mono} = 310^{-3}$ C cm^{-2}; $k_1 = 110^{-5}$ mol cm^{-2} s^{-1}; $k_2 = 210^{-7}$ mol cm^{-2} s^{-1}; X = 5.

Increasing the double layer capacitance increases the length of region 1. This shifts both region 1 & 2 towards longer times. Whereas in the case of increasing the temperature, the overall shape remained the same, increasing the double layer capacitance results in decreasing the length of region 3.

Influence of monolayer coverage surface charge on the shape of OCPD plots

The next plot shows the influence of the monolayer coverage surface charge on the shape of the OCPD plots :

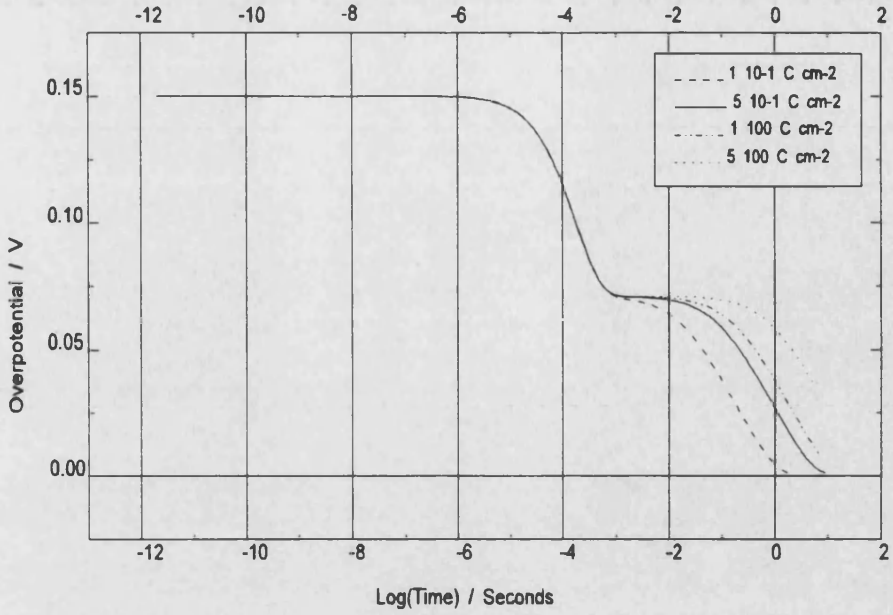

Figure 6.11 : Effect of monolayer coverage surface charge on the OCPD plot shape. $\alpha = 0.5$; T= 333 K; $\eta(0) = 0.15$ V; $C_{dl} = 310^{-3}$ F cm^{-2}; $k_1 = 110^{-5}$ mol cm^{-2} s^{-1}; $k_2 = 210\text{-}7$ mol cm^{-2} s^{-1}; X = 5.

The range of values chosen for the monolayer coverage surface charge for the OCPD simulations is questionable. This is because no measurements were carried out to estimate this value for the chlorine reaction on RuO_2/TiO_2. The case of hydrogen on platinum[1] where Q_{mono} is equal to 210 mC cm^{-2} approximately was chosen as a starting point for the approximation of Q_{mono} on RuO_2/TiO_2 : it was assumed that the only difference between H_2 on Pt and Cl_2 on RuO_2/TiO_2 was the surface roughness. Taking the surface roughness factor, R, to be 100, this would mean that Q_{mono} for Cl_2 on RuO_2/TiO_2 would be 25 mC cm^{-2}. If R was equal to 1000 then Q_{mono} would be equal to 250 mC cm^{-2}. Independent research carried out by ICI has suggested that R is in the range of 300 to 1000. Although some of the values used in the simulations are consistent with such R values, the purpose of using such a broad range of Q_{mono} values in the simulations was to *illustrate* the effect of varying Q_{mono} on the length of the plateau arrest and surface coverage.

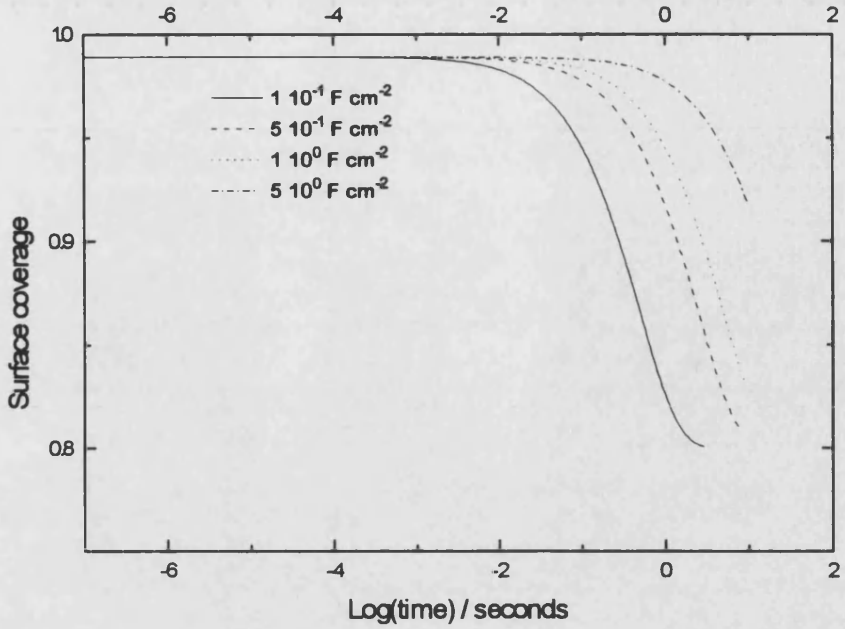

Figure 6.12 : Effect of the monolayer coverage surface charge on the decay of surface coverage. $\alpha = 0.5$; T = 333 K; $\eta(0) = 0.15$; $C_{dl} = 310^{-3}$ F cm^{-2}; $k_1 = 110^{-5}$ mol cm^{-2} s^{-1}; $k_2 = 210^{-7}$ mol cm^{-2} s^{-1} ; X = 5.

Increasing Q_{mono} means that more M-Cl_{ads} intermediates can be adsorbed at the electrode surface. As a result, it will take more time to desorb M-Cl_{ads} and, hence, region 3 and 4 will increase in duration, causing the overall decay to reach equilibrium slower. Region 1 and 2 are not expected to be affected as they correspond to the discharge of the double layer capacitance and this confirmed by 6.11.

Effect of varying k_2 on the shape of OCPD plots

The next plot shows the effect of varying k_2 on the shape of OCPD plots.

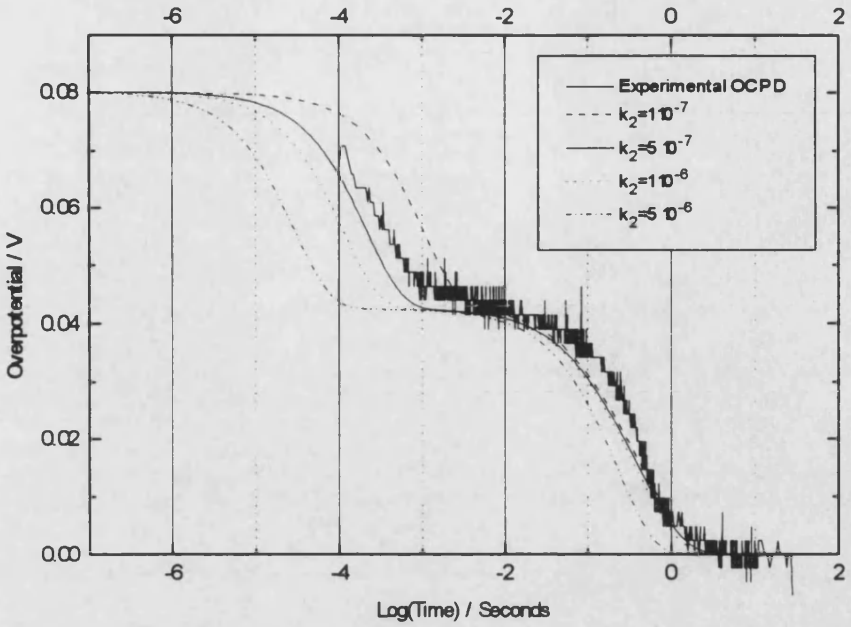

Figure 6.13 : Effect of varying k_2 on the OCPD plot shape. k_2 has units of mol cm^{-2} s^{-1}. α = 0.5; T = 333 K; Q_{mono} = 0.5 C cm^{-2}; $\eta(0)$ = 0.08 V; C_{dl} = 3.5 10^{-3} F cm^{-2}; k_2 = 1 10^{-7} mol cm^{-2} s^{-1}; X = 5.

This plot shows that the time scale of the initial decay due to double layer discharge via faradaic current is extremely sensitive to the value of k_2.. This because of the θ factor in the rate of the forward reaction of step 2). The greater the value of k_2, the greater the faradaic current becomes and, therefore, the faster the double layer capacitance discharges. In this case, the value of X (equation XX) was adjusted in order to maintain the same overpotential value of the plateau arrest.

Effect of varying k_1 on the shape of OCPD plots

The next plot reveals the influence of varying k_1 on the shape of OCPD plots.

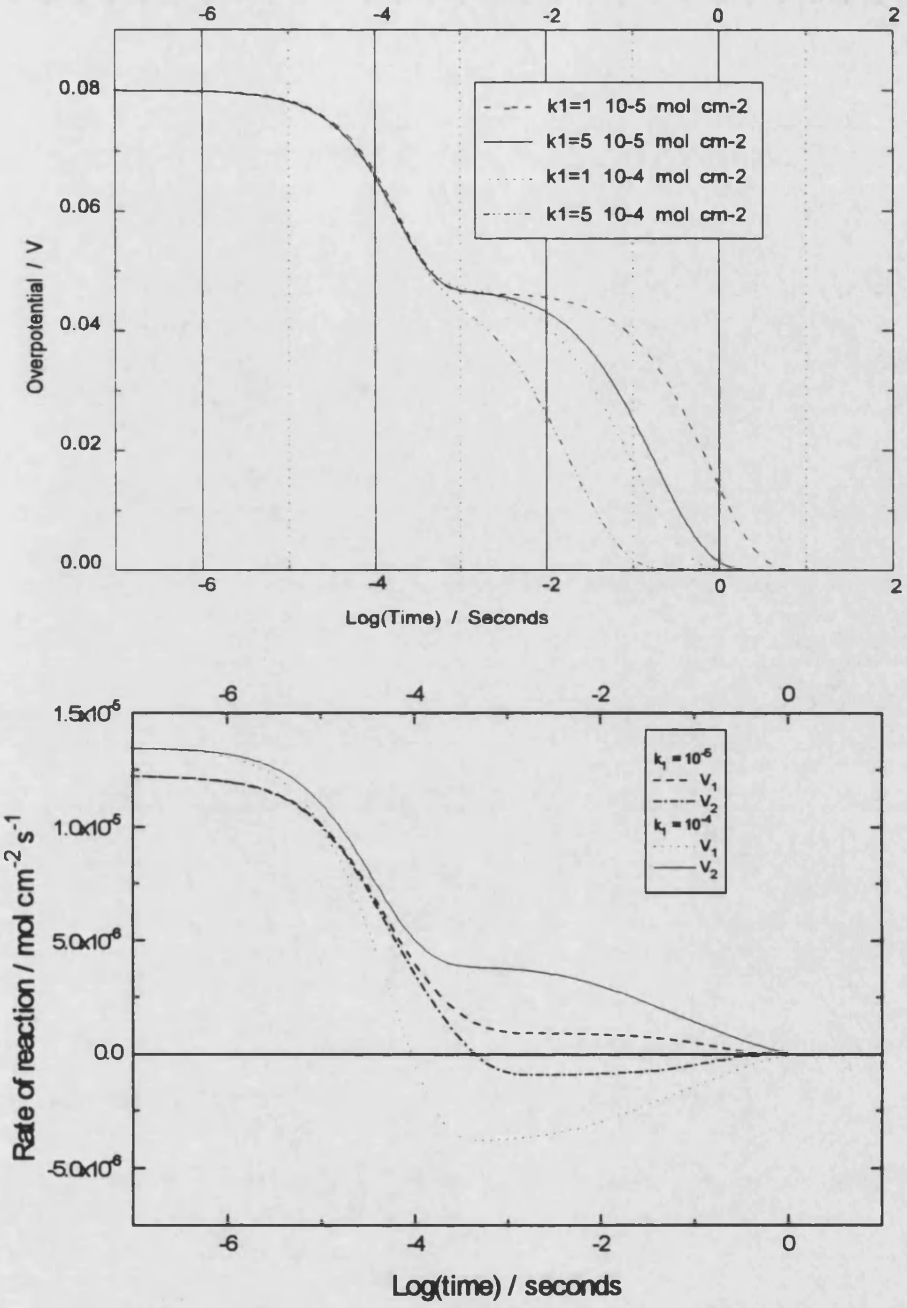

Figure 6.14 : Effect of varying k_1 on the OCPD plot shape as well as v_1 and v_2. α = 0.5; T = 333K, $\eta(0)$ = 0.08 V; $Q_{mono} = 2\ 10^{-1}$ C cm^{-2}; $C_{dl} = 4\ 10^{-3}$ F cm^{-2}; $k_2 = 1\ 10^{-6}$ mol cm^{-2} s^{-1}; X = 10.

Increasing k_1 results in shortening the length of region 3 and, as result, the overall length of the decay. Since regions 3 and 4 correspond to M-Cl_{ads} desorption, the smaller θ_{ss} becomes, the less M-Cl_{ads} there is to desorb from the surface and the faster the overpotential decay. An in-depth analysis shows that the closer k_1 becomes

to k_2, the more pronounced the plateau arrest will be. This is because v_1 will remain constant and opposite to v_2 for a longer period.

Effect of varying X on the shape of OCPD plot

The next plot shows the influence of X = K1/K2 on the shape of the OCPD.

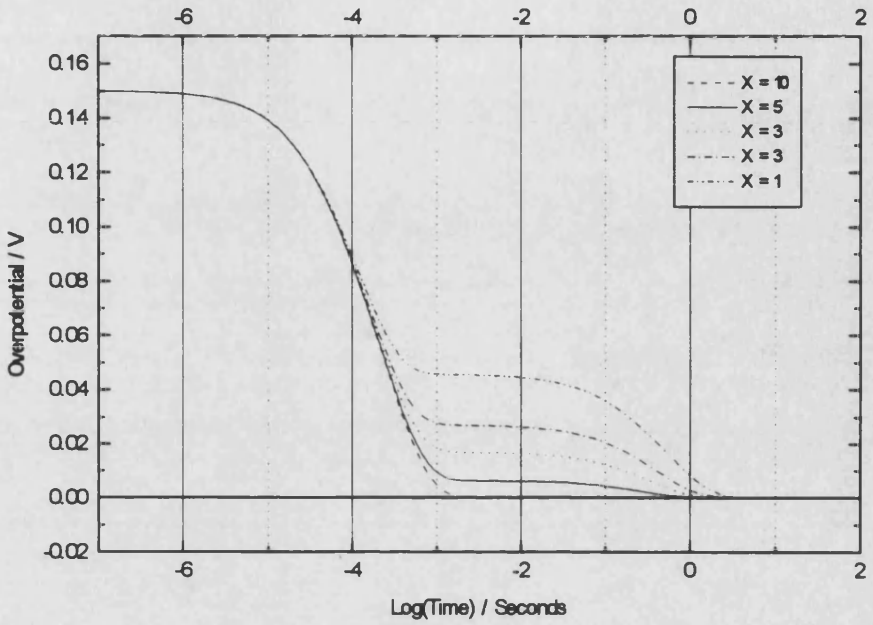

Figure 6.15 Effect of varying X = K1/K2 = $k_1k_{-2}/k_{-1}k_2$ on the shape of OCPD plots. $\alpha = 0.5$; T = 333 K; $Q_{mono} = 3\ 10^{-1}$ C cm^{-2}; $C_{dl} = 3\ 10^{-3}$ F cm^{-2}; $k_1 = 1\ 10^{-6}$ mol cm^{-2} s^{-1}; $k_2 = 1\ 10^{-7}$ mol cm^{-2} s^{-1}.

Increasing the value of X causes the overpotential value of the plateau arrest to increase and delays the time where region 3 appears. Since k_1 and k_2 are kept unchanged in the simulation, increasing X corresponds to decreasing k_{-1}, i.e. the back reaction of step 1 becomes significant at longer times.

Effect of varying η(0) on the shape of OCPD plots

The last parameter to investigate is the effect of increasing initial overpotential (labelled as V(0)) in the following plot.

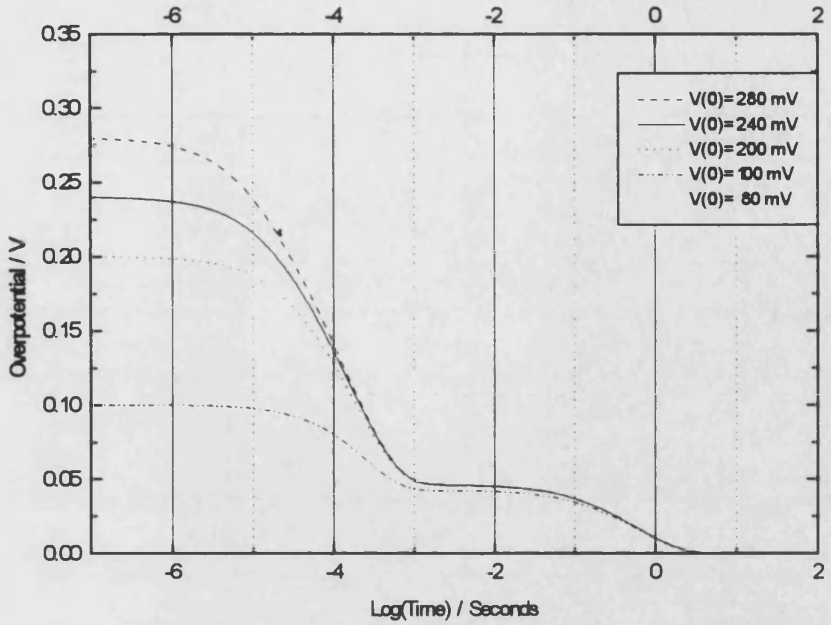

Figure 6.16 : Effect of the initial overpotential (labelled V(0) in this plot) on the OCPD plot shape. $\alpha = 0.5$; T = 333 K; $Q_{mono} = 5\ 10^{-1}$ C cm^{-2}; $C_{dl} = 3\ 10^{-3}$ F cm^{-2}; $k_1 = 1\ 10^{-6}$ mol cm^{-2} s^{-1}; $k_2 = 510^{-7}$ mol cm^{-2} s^{-1}; X =10.

Provided that $\eta(0)$ is greater than the potential value for the plateau arrest and the steady state coverage is independent of initial current density (i.e. at maximum surface coverage), increasing $\eta(0)$ increases the length of regions 2 and 3. Figure 6.17 shows that all curves meet in regions 2,3 and 4 if $\eta(0) > \eta p$. For values of $\eta(0)$ where the coverage is not at saturation level, the OCPD plots no longer meet in region 2 but the overall shape still remains the same, i.e. the total decay time is the same and the overpotential value of the plateau arrest does not differ much. Siince the shape of the OCPD in regions 2,3 and 4 is independent of $\eta(0)$ if $\eta(0) > \eta_p$ this means that only one OCPD for each electrode needs to be fitted in order to determine the values of the kinetic parameters that would fit the experimental data.

Influence of step 3) on the OCPD shape

The following section illustrates the influence of step 3) on the shape of the OCPD :

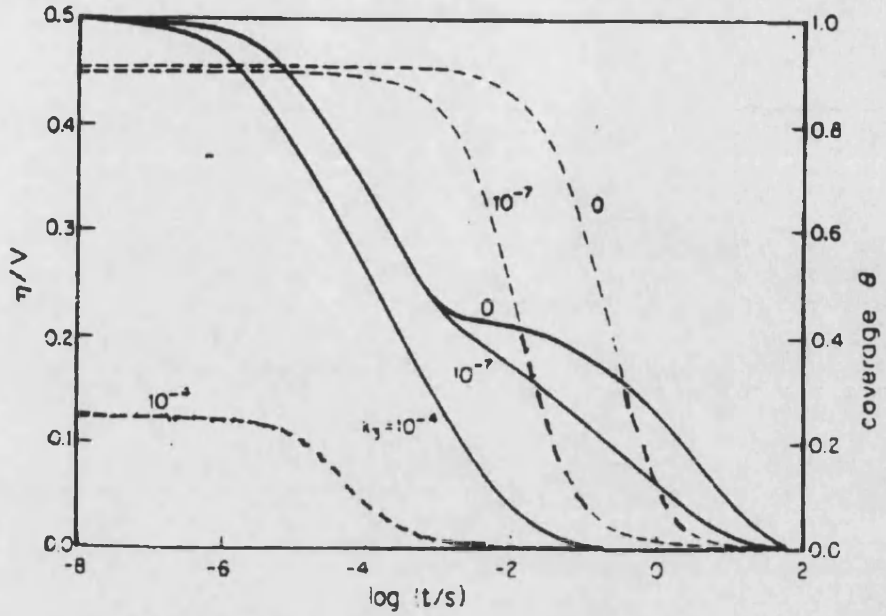

Figure 6.17 : effect of increasing the rate of recombination on the shape of OCPDs. a = 0.5; T= 298 K; Q_{mono} = 210 10^{-6} C cm^{-2}; C_{dl} = 30 10^{-6} F cm^{-2}; k_1 = 10^{-9} mol cm^{-2} s^{-1}; k_2 = 1 10^{-10} mol cm^{-2} s^{-1}.

Figure 6.17 shows that the shape of the OCPD plot is significantly affected if step 3) contributes to the overall reaction. Desorption of M-Cl_{ads} becomes even more rapid and this explains why the plateau arrest is no longer observed when step3) starts to contribute. The reason for this is that step 3) offers an extra path for M-Cl_{ads} desorption on top of step 2. As the surface coverage decreases more rapidly, region 3 nearly disappears.

The key feature is that the overall process is *very* sensitive to the contribution of step 3). Figure 6.17 shows that even a small contribution changes the shape of the OCPD plot drastically.

Although the effect looks similar to that of increasing k_1, especially when the plateau arrest has disappeared, an in-depth analysis of the OCPD curves reveals that there is no point of inflection in the case where step 3) is responsible for the disappearing of the plateau arrest. The combination of these two factors implies that it is possible, in theory, to distinguish between a reaction taking place only via step 1)-2), via 1)-2)-3) and via 1)-3).

C) *Summary of influence of parameters on the OCPD shape*

The theoretical study of the influence of various parameters on the shape of the OCPD plots shows that this technique is not only sensitive to changes in reaction kinetics but also to changes in surface properties such as the double layer capacitance or monolayer coverage surface charge. Since the shape of OCPD plots is also sensitive to the influence of reaction steps, this should allow the determination of the reaction mechanism of chlorine evolution on RuO_2/TiO_2 to be established under industrially relevant conditions.

6.2.2 The equivalent Circuit approach

Another approach was taken to obtain *quantitative* information from OCPDs. Instead of relying on the reaction mechanism to determine kinetic parameters that would fit the experimental data, OCPDs were considered in terms of an equivalent circuit discharge. Just as in impedance spectroscopy, the electrochemical system was modelled using an equivalent circuit (see chapter 4).

The basis of this approach is that OCPDs can be divided into two regions : at short times, the double layer capacitance is discharged (region 1&2) and is followed by the pseudocapacitance discharge.

Using this model, experimental data can be fitted to a polynomial function plus a log term[13] :

$$V(t) = a_0 + a_1 t + a_2 t^2 + a_3 t^3 + a_4 \log(t + a_5) \qquad (6.32)$$

The log term is introduced as it has basic significance in treatments of the course of the decay of potential with time (see equation 6.11).

The purpose of using this function is to accurately determine V(t = 0) and $(dV/dt)_{t=0}$. As it was highlighted in section 6.1, the determination of the overpotential just after interruption is not trivial. At t = 0, equation 6.32 can be written as follows :

$$V(t)_{t=0} = a_0 + a_4 \log(a_5) \qquad (6.33)$$

The iR drop, $\Delta V = V(j) - V(t = 0, j = 0)$ where V(j) is the potential prior interruption can be determined.. This allows the calculation of the solution resistance, R_{sol} :

$$R_{sol} = \frac{[V(j) - V(t = 0, j = 0)]}{j(V)} \qquad (6.34)$$

In this case, j(V) is the steady state current. The derivative of equation 6.32 with respect to time is:

$$\left(\frac{dV}{dt}\right)_t = a_1 + 2a_2 t + 3a_3 t^2 + \frac{a_4}{2.3(t+a_5)} \qquad (6.35)$$

At t = 0, equation 6.35 can be rewritten as follows :

$$\left(\frac{dV}{dt}\right)_{t=0} = a_1 + \frac{a_4}{2.3a_5} \qquad (6.36)$$

From the curve fit of the experimental data at short times, the values of a_0 to a_5 can be determined and the value of the double layer capacitance can be calculated from equation 6.32 and 6.35 :

$$C_{dl} = \frac{j(V)}{\left(-\frac{dV}{dt}\right)_{t=0}} \qquad (6.37)$$

It must be noted that the values of a_0 to a_5 have no physical significance as this approach was only used to accurately determine V(t = 0) and $(dV/dt)_{t=0}$. However, if the order of the polynomial fitting function was 0 then equation 6.32 would be equal to

$$V(t) = a_0 + a_4 \log(t + a_5) \qquad (6.38)$$

This is the basic equation for potential decay derived from the Butler-Volmer equation

$$-\left(c_{dl} + c_{\phi}\right)\left(\frac{dV}{dt}\right) = j(V,t) = j_0 \exp\left[\frac{\alpha F V}{RT}\right] \qquad (6.39)$$

In this case, the parameters have physical meanings:

$a_0 = -b\log\left[\frac{2.3 j_0}{bC}\right]$; $a_4 = \frac{2.3RT}{\alpha F}$, the Tafel slope and $a_5 = \frac{bC}{2.3 j(t=0)}$ where C is the total capacitance and j_0 the exchange current density.

This curve fitting procedure has some distinctive advantages in the sense that :

1. no assumptions are made about the reaction mechanism and change of capacitance as a function of time.
2. the only variables required are the steady state current value prior interruption and the potential decay as a function of time.
3. no arbitrary assumptions are made about the fitting parameters since they are obtained by a computational procedure.

Once the value of the double layer capacitance has been determined, the next step is to evaluate the value of the pseudo-capacitance, C_Φ, which is defined as the product of the charge density for monolayer coverage and derivative of coverage with respect to potential, i.e. $C_\Phi = Q_{mono} d\theta/dt$.

There has been discussion as to the definition of $d\theta/dt$[14,15,16] : it depends on the type of experiment used to determine θ as a function of η. Most authors tacitly assume that C_ϕ always refer to a derivative of the *steady-state* θ-η relation

$$C_{\Phi,ss} = Q_{mono}\left(d\theta_{ss} / d\eta_{ss}\right) \qquad (6.40)$$

However, $\theta(\eta)$ will not be equal to $\theta_{ss}(\eta)$ in general. A *transient pseudocapacitance* must therefore be defined i.e.

$$C_{\Phi,t} = Q_{mono}\left(d\eta / dt\right)\left(d\eta / dt\right) \qquad (6.41)$$

An *operational* definition of the pseudocapacitance has also been used by Conway based :

$$C = C_\phi + C_{dl} * C_{\phi,b} \qquad (6.42)$$

where $C_{\phi,b} = -j_{ss} / \left(d\eta / dt\right) - C_{dl}$.

Although it is not the purpose of this project to discuss the differences between these various definitions of the pseudocapacitance, it was important to mention that defining the pseudocapacitance is not a trivial matter and that some controversy remains on this point.

Equation 6.39 can be rewritten to express the total capacitance as a function of overpotential. Now, the total capacitance is no longer considered as constant as the case where the pseudocapacitance becomes significant is being considered. It will therefore be labelled as $C_{tot}(t)$. Rearranging equation 6.39 gives the following expression for $C_{tot}(t)$ as a function of $(d\eta(t)/dt)$ and the overpotential $\eta(t)$:

$$C_{tot} = -\frac{j_0}{\left(\frac{d\eta}{dt}\right)} \exp\left[\frac{\eta(t)}{b}\right] \qquad \text{where b is the Tafel slope} \qquad (6.43)$$

Once the whole curve has been curve fitted, it is then possible to numerically differentiate the OCPD. Combining that information to equation 6.43 then gives a complete picture of the variation of the total capacitance as a function of time after interruption.

6.3 Results

This section summarises results obtained from the treatment of OCPD data on new and degraded electrodes. As the aim of this project was to determine the reaction mechanism of chlorine evolution on commercial RuO_2/TiO_2 anodes as well as the mechanism of electrocatalytic performance loss, results from undegraded electrodes will be reported first. This will provide the basis for the study of the variation of reaction mechanism and electrocatalytic performance as a function of ruthenium loss.

6.3.1 New and undegraded electrodes

The next two plots show a typical OCPD plot, first as function of time then in its most usual format, on a logarithmic timescale.

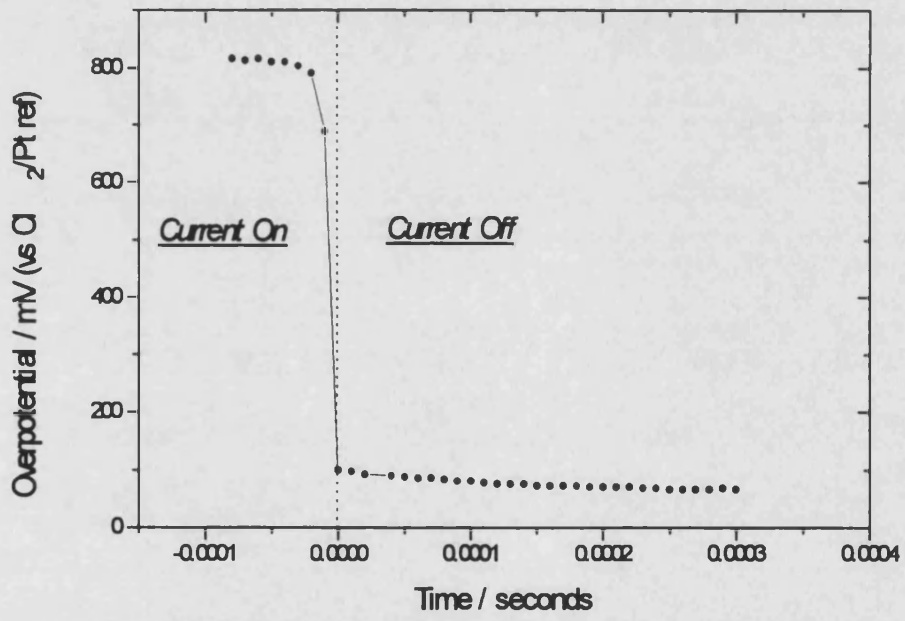

Figure 6.18 : potential vs. time before and after current interruption for M51 RuO_2/TiO_2 electrode at 1300 mA cm^{-2} and 60 °C.

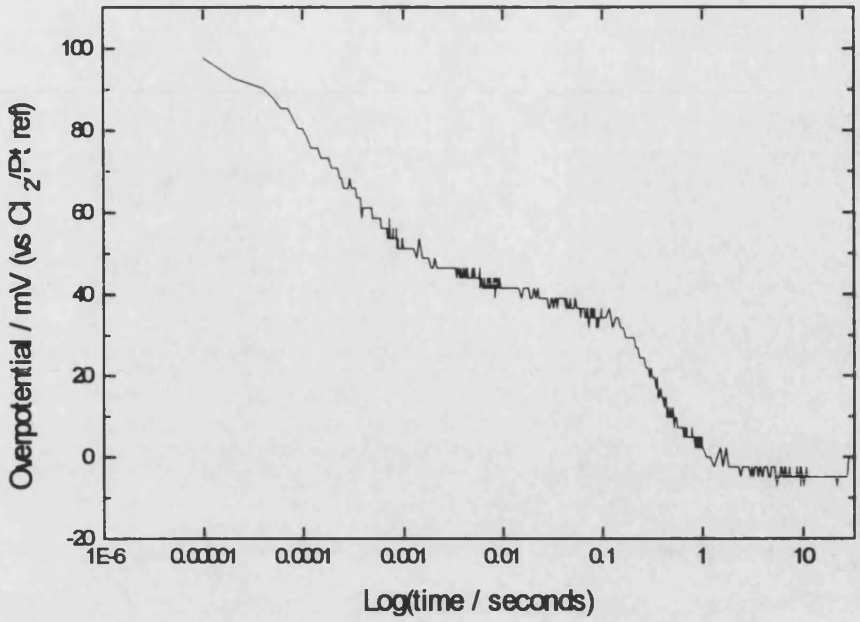

Figure 6.19 : potential vs. log(time) or OCPD plot corresponding to figure 6.19.

The first observation is that these plots are of extremely good quality, especially when compared to simulated data and, more importantly, to OCPDs obtained from idealised systems[4-6,8,10], i.e. Pt and Ti coated wires. One can see the 4 regions of overpotential-log(time) described in the section on simulated OCPDs very clearly.

Considering the previous analysis of the influence of various parameters on the shape of the OCPD plot and its sensitivity towards the contribution of step 3) as part of the reaction mechanism, the shape of the OCPD plot of undegraded electrodes reveals that the reaction mechanism involves *only* step 1) & 2) : the presence of such a pronounced plateau arrest in the decay of overpotential on a logarithmic time scale categorically rules out that step 3) has any significant contribution.

The similarity between real and simulated OCPDs according to an isotherm that considers a maximum of one monolayer suggests that the chlorine reaction on RuO_2/TiO_2 does not require adjacent ruthenium sites.

Since there is no doubt as to the reaction mechanism on new electrodes this means that the variation of reaction mechanism as a function of ruthenium loss will be easier to follow. Had the OCPD of new electrodes showed that it was not possible to rule out step 3) it would have been far more difficult to observe changes in the reaction

mechanism. In particular, it would have been difficult to detect changes in the relative contributions of step 2) and 3). The presence of the plateau arrest provides an excellent means of detecting a change in the reaction mechanism as simulations have shown that its presence is very sensitive to the contribution of step 3). Furthermore, this would suggest that loss of ruthenium will not affect the reaction mechanism, i.e. production of a chlorine molecule seems to take place on a single ruthenium active site and not involve Ru-Ru pairs.

The next plot shows a family of OCPD plots obtained on the same electrode at different current densities. It also shows the fitted simulated OCPD for each experimental OCPD using the FORTRAN program.

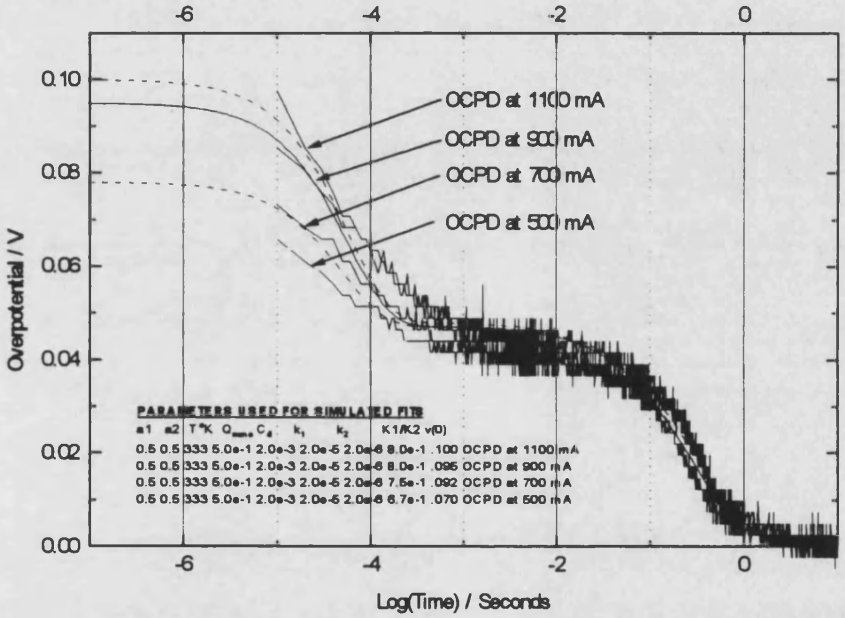

Figure 6.20 : Typical family of OCPD plots obtained from an ICI commercial RuO_2/TiO_2 sample. The only parameter changed in the simulation program was the initial overpotential value $\eta(0)$.

The procedure used to fit these OCPDs was the same for all fitting of experimental data and is as follows : a polynomial fit of 5th degree without the addition of a log term was used instead of the one used by Conway (see equation 6.32) in order to calculate the double layer capacitance over region 1 & 2 of the OCPD plot. It was found that Conway's polynomial fit was not as good as a simple polynomial and, since the purpose was only to determine C_{dl} reliably, omitting the log term had no

consequence. The next step was determine the value of k_2 as OCPD simulationsrevelead this was the most sensitive parameter. This allowed regions 1 & 2 to be fitted. A value of k_1 was then chosen and X=K1/K2 was varied in order to fit the overpotential and time value of the plateau arrest. Finally, the value of Q_{mono}, was adjusted to fit region 4, i.e. the length of the plateau arrest and decay to equilibrium.

At this point, it is important to make a few remarks about this procedure. As mentioned above, the determination of k_2 is straightforward as the OCPD model is very sensitive to it. This is not the case for k_1. An in-depth study showed that a very broad range of k_1 values could be used to fit the experimental data. The main reason for this is that the effect of k_1 on the plateau arrest can be compensated by varying Q_{mono} and X. This is also the reason why the fits give a broad range of steady state surface coverage values as its magnitude depends upon k_2, X and k_1. The problem is that no independent way of calculating k_1 or Q_{mono} was found.

There are two ways of determining the value of θ_{ss}. The first one is by inserting $\eta(0)$ into equation 6.17, setting it equal to 0 and solving for θ_{ss}.

$$\theta_{ss} = \frac{k_1 \exp(\Psi) + Xk_2 \exp(-\Psi)}{\left(k_1 + \frac{k_1}{X}\right)\exp(\Psi) + \left(k_2 + Xk_2\right)\exp(-\Psi)} \tag{6.44}$$

where $\Psi = \frac{\alpha RT}{F}\eta(0)$. If η_p and T_p are the overpotential and log(time) value of the real OCPD plateau arrest then η_p and T_p are defined as follows[8]:

$$\eta_p = \left(\frac{RT}{F}\right)\ln\left(\frac{j_-}{j_+}\right) \tag{6.45}$$

$$T_p = \frac{2C_{dl}RT}{F(j_- j_+)^{\frac{1}{2}}} \tag{6.46}$$

where $j_+ = F\left[k_1(1-\theta_{ss}) + k_2\theta_{ss}\right]$, $j_- = F\left[k_{-1}\theta_{ss} + k_{-2}(1-\theta_{ss})\right]$

By combining equation 6.45 and 6.46 one can determine θ_{ss} as a function of η_p, T_p and k_1

$$\theta_{ss} = \frac{1}{(k_2 - Fk_1)}\left\{\left(\frac{2C_{dl}RT}{FT_p}\right)\exp\left(\frac{F\eta_p}{RT}\right)^{-\frac{1}{2}} - Fk_1\right\} \tag{6.47}$$

In this case θ_{ss} is only dependent upon k_1.

A mathematical analysis was carried out to restrict the range of k_1 values based on the conditions governing θ_{ss}, i.e. $0 < \theta_{ss} < 1$. This illustrated below in table 6.1.

value of k_1	$-\infty$		k_2/F		A/F		$+\infty$
sign of (k_2-Fk_1)		+	0	−			−
sign of $(A-Fk_1)$		+		+	0		−
sign of θ_{ss}		+	] [	−	0		+
variation of θ_{ss}	**1**	↗	$+\infty$] [$-\infty$	↗	**0**	↗	**1**

Table 6.1 : variation of θ_{ss} as a function of the value of k_1.

$$\text{where } A = \frac{1}{(k_2 - Fk_1)}\left[\left(\frac{2C_{dl}RT}{FT_p}\right)\exp\left(\frac{Fn_p}{RT}\right)^{-\frac{1}{2}} - Fk_1\right]$$

Table 6.1 shows that for $0 < \theta_{ss} < 1$ to be true, $k_1 \geq A/F$ and $k_2 \leq A$.

The range of k_1 values can be narrowed even further by considering that $0 < \theta_{eq} < \theta_{ss}$. Results of the mathematical analysis are summarised in table 6.2 below :

value of k_1	$-\infty$	$-Xk_2$	0	Xk_2	$+\infty$
sign of $(k_1 - Xk_2)$	−		−	0	+
sign of $(k_1 + Xk_2)$	−	0	+		+
sign of $(\theta_{ss} - \theta_{eq})$	+	0	−	0	+

Table 6.2 : sign of $(\theta_{ss} - \theta_{eq})$ as a function k_1

In summary, the general conditions required to satisfy that $0 < \theta_{eq} < \theta_{ss}$ are the following :

$k_1 > A/F$ and $X < k_1/k_2$

Without additional information, it is not possible to determine a specific value of k_1 for the fitting of OCPD experimental data. As a result, it is not possible to determine the value of θ_{ss} accurately.

The next three tables show the variation of the initial overpotential for OCPDs obtained at 900 mA cm^{-2} (approx.) as a function of increase in alkali wear test running potential.

Sample Reference number	M31	M32	M33	M34	M35	M38	***M36***	***M37***
Increase in alkali wear test running potential / mV	0	100	250	400	580	900	***950***	***1500***
Overpotential at t = 0 / mV	150	70	77	56	80	80	***160***	***250***

Table 6.3 : variations of the initial overpotential as a function of increase in alkali wear test running potential for the M3x series.

Sample Reference number	***M42***	M41	M43	M45	M44	M46	***M47***	***M48***
Increase in alkali wear test running potential / mV	***0***	110	230	340	360	370	***1470***	***2090***
Overpotential at t = 0 / mV	***200***	77	50	100	85	80	***180***	***250***

Table 6.4 : variations of the initial overpotential as a function of increase in alkali wear test running potential for the M4x series.

Sample Reference number	M51	M52	M53	***M55***	M54	M56	M57	***M58***
Increase in alkali wear test running potential / mV	0	100	600	***930***	1000	1800	2460	***4500***
Overpotential at t = 0 / mV	100	?	80	***450***	77	110	320	***210***

Table 6.5 : variations of the initial overpotential as a function of increase in alkali wear test running potential for the M5x series.

Note : columns in bold italic font mean that the sample displayed an usual OCPD shape at short times and that initial overpotential values should be treated with suspicion. This will be explained later.

Tables 6.3 to 6.5 show that the initial overpotential for undegraded electrodes is always significantly higher than at the equivalent current density one for mildly degraded samples. Once the increase in alkali wear test running potential increased above 900 mV approximately, the initial overpotential of degraded electrodes finally becomes higher than that of the new electrodes.

Two explanations have been suggested : the first is that the surface is contaminated and that chlorine evolution cleans the surface, possibly by oxidising organic impurities. However, this explanation would mean that the surface is only partially contaminated as chlorine evolution takes place as soon as the external circuit is closed to allow current flow. Had the surface been totally contaminated then the layer of contamination would act as an insulating layer and no current would have flown through the anodes.

The second explanation is that running current through the anodes causes an initial surface reorganisation which increases the surface area and density of active sites exposed to solution.

It must noted that this trend is similar to the trend observed in cyclic voltammetry and impedance spectroscopy, i.e. running the electrodes in the alkali wear pot for 1 hour seems to change the properties of the RuO_2/TiO_2 coating.

6.3.2 Degraded electrodes

The following plot shows the potential vs. time potential trace measured at 1100 mA cm^{-2} (approx.) for all electrodes of series M5x before and just after current interruption. For each curve, the value of the alkali wear test running potential increase is given.

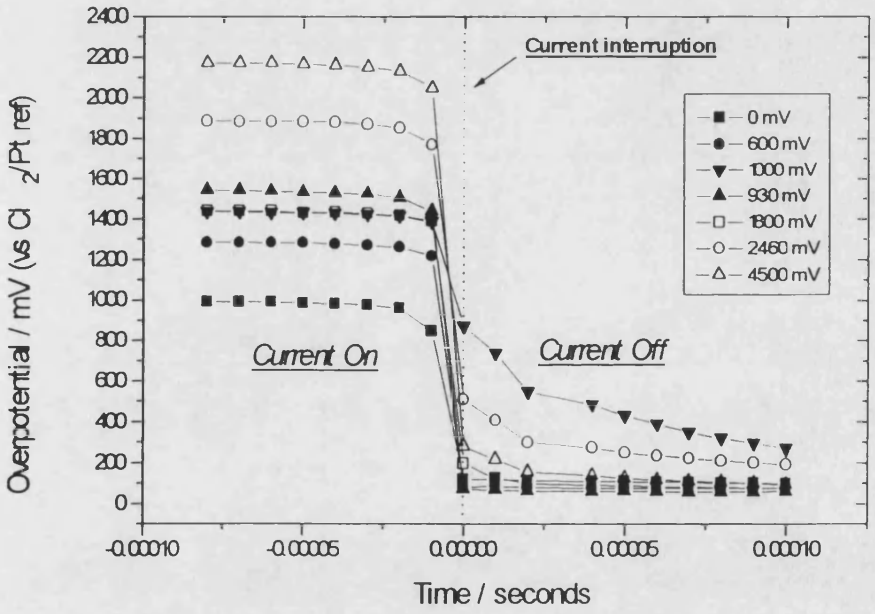

Figure 6.21 : Plot of Potential vs. Time before and after current interruption for the M5x series at 1100 mA cm^{-2}.

Figure 6.21 is very useful in determining the source of the potential increase as a function of degradation. It shows that the increase in potential *during* current flow is greater than the increase of the overpotential just after interruption. The fact that the overpotential varied only by a maximum of 150 mV as a result of degradation and the alkali wear pot running potential increased by 4V means that the increase in

cell voltage *must* come from an increase in ohmic contribution. This indicates that the effect of degradation seems to be the build-up of a resistive layer. Since an increase in electrode porosity cannot account for such a substantial increase in ohmic contribution, figure 6.21 suggests that the increase in ohmic contribution *must* come from build-up of an insulating layer of TiO_2 between the RuO_2/TiO_2 coating and titanium substrate. Further analysis of such a model will be carried out in chapter 8.

Before going any further, it is necessary to consider what might be happening at the surface of the electrode during current flow and just after interruption. The question of lateral currents is an important point. As mentioned before, comparison of the potential traces before and after opening the circuit imply that chlorine evolution is taking place deeper and deeper inside the RuO_2/TiO_2 coating and that the resistive Ru-depleted layer is extending further and further into the RuO_2/TiO_2 coating.

Using a simple model, this means that the surface becomes mainly composed of insulating TiO_2. While the current is flowing, the double layer capacitance at the surface will be more charged than that at the bottom of a pore since $Q_{surface}=C_{dl}*V_{surface}$ and $Q_{pore}=C_{dl}*(V_{surface}-R_{pore}*current)$. Although the electrode is at equipotential, there will be an uneven distribution of charge stored at the surface once the current is interrupted. Since this is an untenable situation, there will have to be a redistribution of charge from the surface into the pores of the anode coating, i.e. lateral currents will flow 'inside' the electrode. The present model for OCPD simulations has neglected the inherent current distribution due to effects mentioned above. This is a problem that has been treated in detail by Newman[17]. However, the purpose of this section is to show that it is likely that lateral currents will flow in RuO_2/TiO_2 electrode after opening the circuit. Figures 6.22 to 6.64 show a simple model for a porous electrode system and the plots of current vs. time after interruption. This analysis was carried out using the software package *Micro Cap IV.*

```
.DEFINE Ext PULSE 1.1 0 5E-8 1E-8 1E-8 20 21

.DEFINE Rsol 5
.DEFINE Rfar 5.1E4

.DEFINE Rpore 574     .DEFINE Rctp 4.6E6
.DEFINE Rpore1 574    .DEFINE Rctp1 4.6E6
.DEFINE Rpore2 574    .DEFINE Rctp2 4.6E6
.DEFINE Rpore3 574    .DEFINE Rctp3 4.6E6
.DEFINE Rpore4 574    .DEFINE Rctp4 4.6E6
.DEFINE Rpore5 574    .DEFINE Rctp5 4.6E6
.DEFINE Rpore6 574    .DEFINE Rctp6 4.6E6
.DEFINE Rpore7 574    .DEFINE Rctp7 4.6E6
.DEFINE Rpore8 574    .DEFINE Rctp8 4.6E6
.DEFINE Rpore9 574    .DEFINE Rctp9 4.6E6

.DEFINE Cdl 9.62E-7
.DEFINE Cdlp 1.067E-8
.DEFINE Cdlp1 1.067E-8
.DEFINE Cdlp2 1.067E-8
.DEFINE Cdlp3 1.067E-8
.DEFINE Cdlp4 1.067E-8
.DEFINE Cdlp5 1.067E-8
.DEFINE Cdlp6 1.067E-8
.DEFINE Cdlp7 1.067E-8
.DEFINE Cdlp8 1.067E-8
.DEFINE Cdlp9 1.067E-8
```

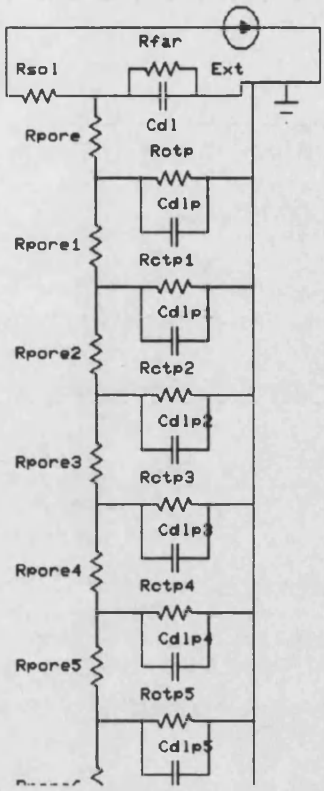

Figure 6.22 : circuit diagram for a porous electrode. Only the 6 first 'portions' of the pore are shown.

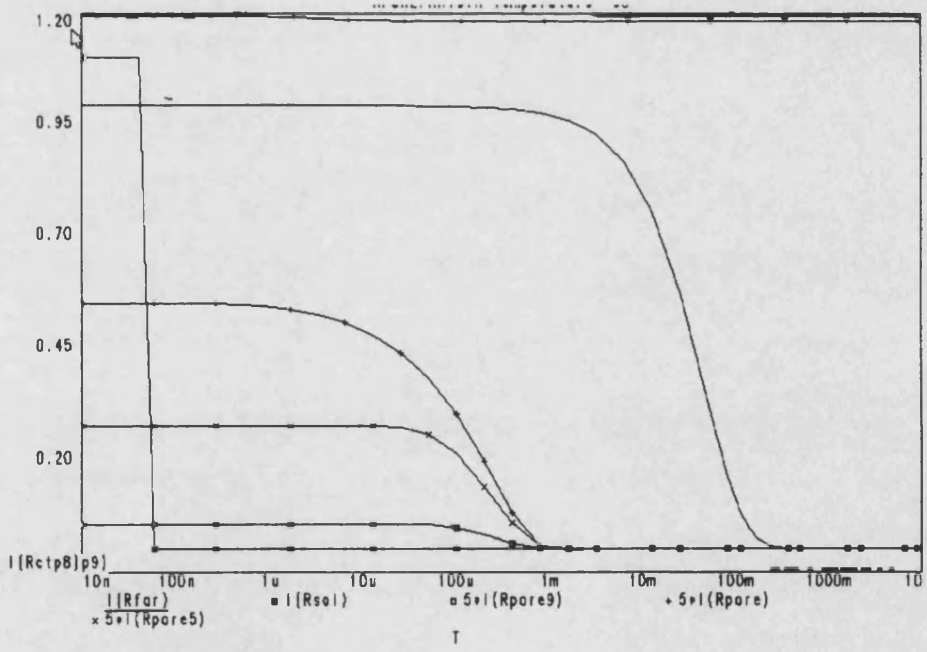

Figure 6.23 : transient currents flowing through some of the components of the circuit shown in figure 6.22 after interrupting the current flow in the external circuit.

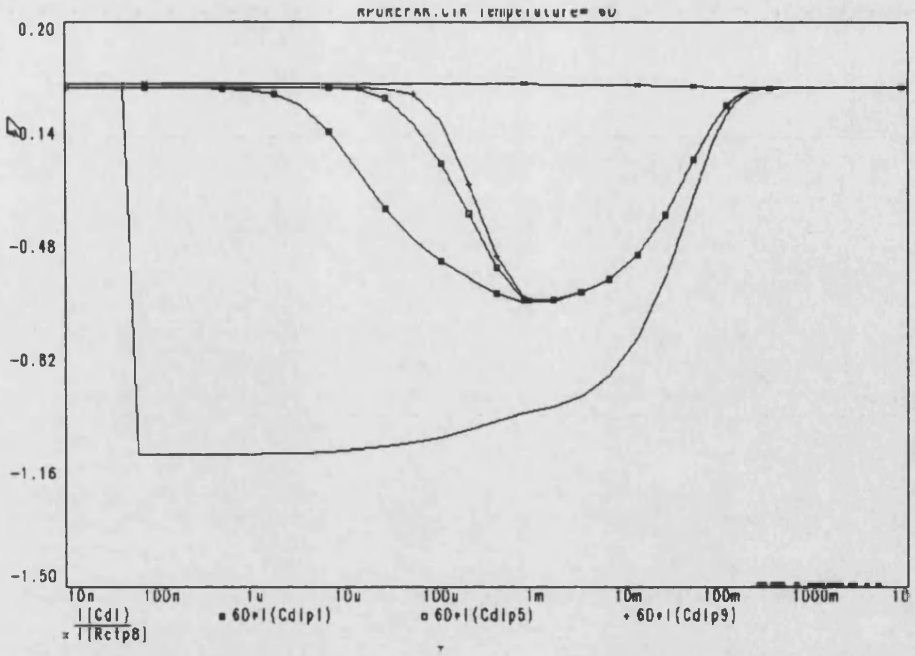

Figure 6.24 : transient currents flowing through some of the double layer capacitances in the pore of the circuit shown in figure 6.22.

Figure 6.23 and 6.24 show that lateral currents are flowing in the circuit used to model a porous electrode after interruption of the flow in the external. A closer analysis reveals that currents are flowing from the surface into the pore. In view of the microporosity of the RuO_2/TiO_2 electrodes it is therefore very likely that lateral currents will also flow 'inside' the electrode after interruption of the external current flow. Figure 6.23 shows that lateral currents flow down the pore up to 1 ms after interruption of the external current, and one can therefore expect that this will have some influence on the shape of OCPDs.

The next 4 plots show the OCPD plots of electrodes from the M5x series that have been increasingly degraded.

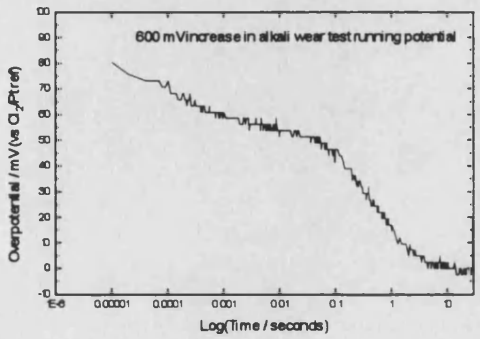

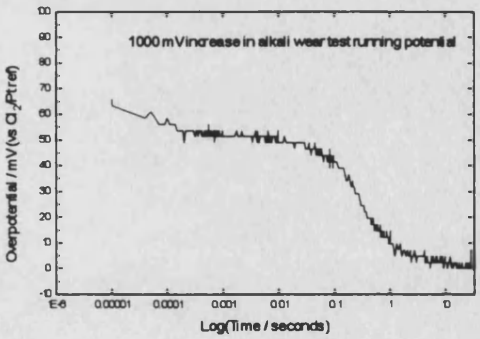

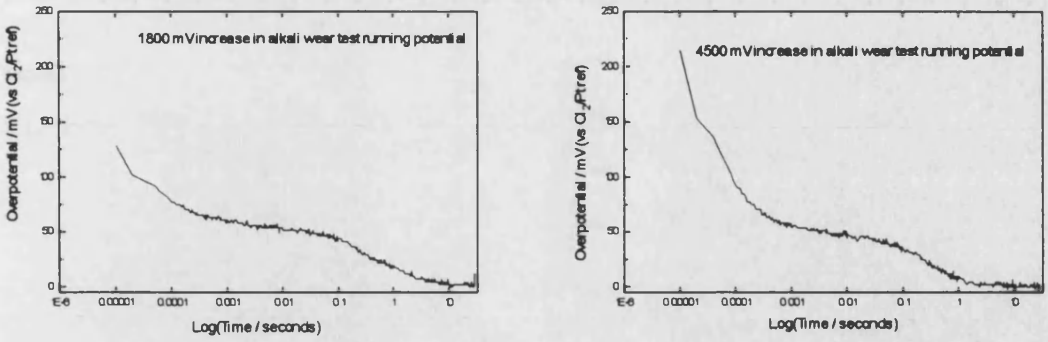

Figure 6.25 : Effect of degradation on the shape of experimental OCPDs

Figure 6.25 shows that degradation only affects the initial part of the OCPD plots. It also shows that η has only varied by 150 mV when the alkali wear pot running potential has increased by 4 V. The increase in η only affects region 1&2, regions 3&4 remain unchanged, i.e. the potential and time value of the plateau arrest remains the same, the timescale of regions 3 and 4 is unchanged and the overall decay time remains constant.

The next three tables summarise the results of curve fitting of real OCPDs for all electrodes studied by OCPD in this project. They also show the variations of C_{dl}, k_2, T_p and the value of the OCPD slope in region 2 where η(t) vs. log(t) is linear.

Sample	*M58-0900*	M57-0900	M56-0900	*M55-0900*	M54-0900	M53-0900	M52-0900	M51-0900
DVrunning	*4492*	2460	1800	*930*	1000	600	1 HOUR	0
Np	*58*	58	56	*58*	52	60		51
Tp	*-2.896*	-2.453	-2.986	*-3.212*	-3.192	-2.646		-2.721
Slope(real)	*-0.121*	-0.12	-0.0262	*-0.235*	-0.0116	-0.013		-0.0287
Slope(fit)	*-0.1*	-0.111	-0.0405	*-0.122*	-0.0171	-0.0184		-0.0381
k2	*1.80E-07*	5.00E-08	1.00E-06	*8.00E-08*	1.50E-06	9.00E-07		9.00E-07
k1(MIN)	*1.00E-06*	2.00E-07	2.00E-06	*2.00E-07*	1.00E-05	5.00E-06		5.00E-06
K1/K2(MIN)	*4.30E-01*	3.30E-01	1.30E-01	*2.00E-01*	3.00E-01	2.00E-01		4.60E-01
Qmono(MIN)	*5.00E-02*	1.00E-02	2.00E-01	*1.00E-02*	6.00E-01	3.00E-01		2.00E-01
k1(MAX)	*7.00E-05*	1.00E-05	5.00E-05	*5.00E-05*	5.00E-04	5.00E-04		9.00E-05
K1/K2(MAX)	*30*	1.50E+01	3.2	*10.6*	15	22		7.7
Qmono(MAX)	*2.3*	1.80E-01	1.2	*3.00E-01*	8	20		3.5
Cdl	*4.00E-04*	4.00E-04	2.00E-03	*2.00E-04*	5.00E-03	6.00E-03		5.00E-03

Note: the columns in bold italic font mean that the OCPDs for the samples had an unusual shape at very short times. This will be explained at the end of the section.

Table 6.6 : summary of OCPD data fitting using the simulation program for the M5x series

In each case the numbering on the X-axis means that electrode 1 is the new electrode and increasing numbers correspond to the state of degradation, i.e. electrode 8 is the most degraded.

Sample	*M48-0900*	*M47-0900*	M46-0900	M45-0900	M44-0900	M43-0900	*M42-0900*	M41-0900
DVrunning	*2090*	*1470*	370	340	360	230	*0*	1 hour
Np	*55*	*61*	56	54	48	49	*54*	46
Tp	*-2.549*	*-2.866*	-3.2	-3.004	-2.69	-3.42	*-2.962*	-3.523
Slope(real)	*-0.1024*	*-0.0743*	-0.0127	-0.0225	-0.0282		*-0.126*	-0.0351
Slope(fit)	*-0.0817*	*-0.0802*	-0.0199	-0.0269	-0.0305		*-0.0759*	-0.0325
k2	*9.00E-07*	*2.00E-07*	1.00E-06	1.00E-06	1.00E-06		*6.00E-08*	2.30E-06
k1(MIN)	*5.00E-06*	*1.00E-06*	1.00E-05	1.00E-05	1.00E-05		*1.00E-05*	1.00E-05
K1/K2(MIN)	*4.60E-01*	*4.00E-01*	6.00E-01	7.00E-01	8.00E-01		*15*	3.80E-01
Qmono(MIN)	*3.60E-01*	*6.00E-02*	4.30E-01	4.00E-01	3.20E-01		*4.00E-01*	5.00E-01
k1(MAX)	*9.00E-05*	*9.00E-05*	5.00E-04	5.00E-04	5.00E-04		*same*	same
K1/K2(MAX)	*7.5*	*4.33E+01*	25	30	37		*same*	same
Qmono(MAX)	*4.5*	*4.5*	11	11	7		*same*	same
Cdl	*5.00E-03*	*7.00E-04*	5.00E-03	5.00E-03	8.00E-03		*2.00E-04*	2.00E-03

Table 6.7 : summary of OCPD data fitting using the simulation program for the M4x series

Sample	M38-0900	*M37-0900*	*M36-0900*	M35-0900	M34-0900	M33-0900	M32-0900	M31-0900
DVrunning	900	*1500*	*950*	580	400	250	1 hour	0
Np	46	*56*	*57*	48	42	51	49	51
Tp	-2.987	*-2.638*	*-3.393*	-3.045	-3.393	-3.031	-3.091	-2.129
Slope(real)	-0.0251	*-0.043*	*-0.0507*	-0.0219	-0.01	-0.0232	-0.0124	-0.0549
Slope(fit)	-0.0355	*-0.0465*	*-0.0433*	-0.0331	-0.0143	-0.0238	-0.0198	-0.0731
k2	1.50E-06	*2.00E-08*	*2.00E-07*	2.00E-06	4.00E-06	6.00E-06	2.00E-06	4.00E-07
k1(MIN)	9.00E-05	*7.00E-06*	*9.00E-06*	9.00E-06	3.00E-05	3.00E-06	1.00E-05	8.00E-06
K1/K2(MIN)	5	*24*	*3*	3.50E-01	6.00E-01	3.00E-02	3.00E-01	3
Qmono(MIN)	2.2	*3.00E-01*	*3.00E-01*	3.00E-01	9.00E-01	7.00E-01	4.00E-01	4.00E-01
k1(MAX)	?	*?*	*7.00E-05*	7.00E-05	5.00E-05	1.00E-05	?	9.00E-06
K1/K2(MAX)	?	*?*	*33*	3.3	7.00E-01	9.50E-02	?	2.5
Qmono(MAX)	?	*?*	*1.8*	1.8	1	9.00E-01	?	4.00E-01
Cdl	6.00E-03	*2.00E-04*	*5.00E-04*	2.00E-03	8.00E-03	6.00E-03	3.00E-03	3.00E-03

Table 6.8 : summary of OCPD data fitting using the simulation program for the M3x series

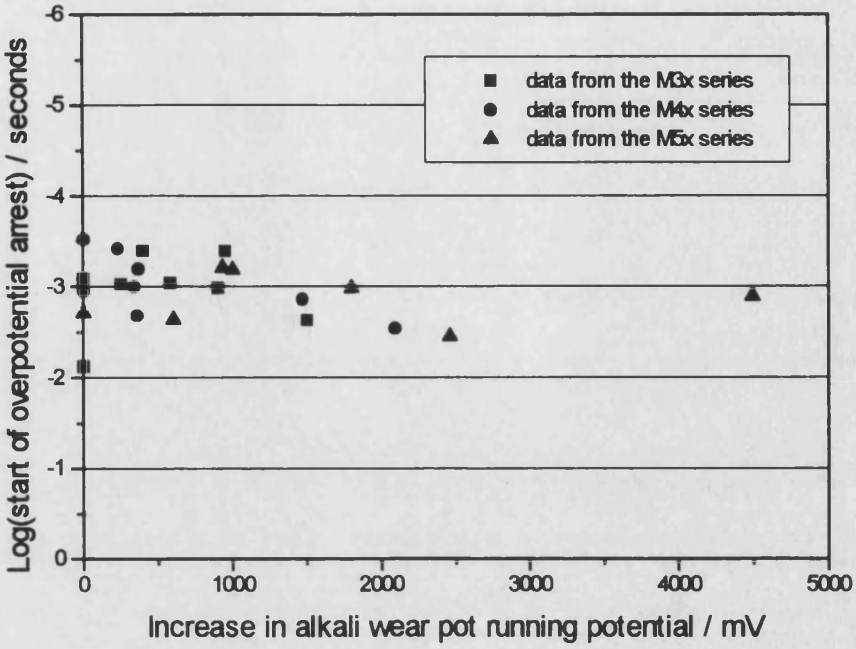

Figure 6.26 : variation of time at which the overpotential plateau arrest starts as a function electrode wear for all series.

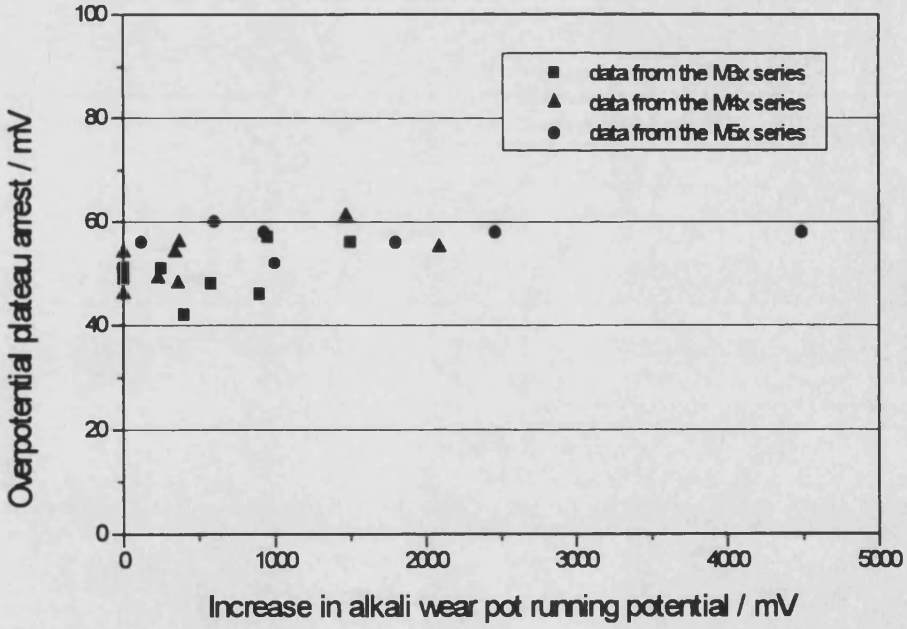

Figure 6.27 : variation of the height of the overpotential plateau arrest as a function of time for the M3x, M4x and M5x series.

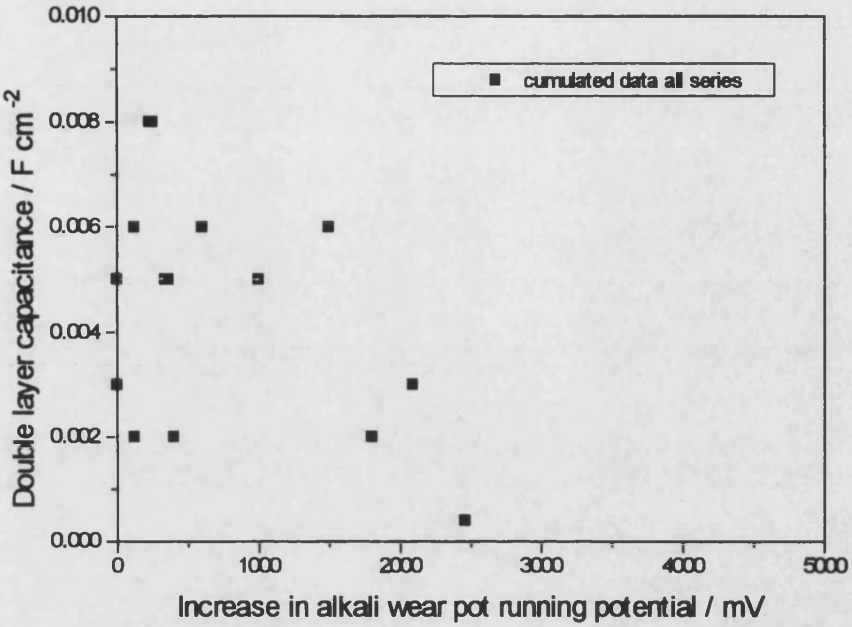

Figure 6.28 : variation of the double layer capacitance measured by OCPD as a function of degradation for all series.

Tables 6.6 to 6.8 show that the values of η_p and T_p do not change as a function of degradation. This is illustrated in figures 6.26 and 6.27. Although it is not as noticeable as from cyclic voltammetry and impedance spectroscopy measurements, figure 6.28 seems to show that C_{dl} goes through a maximum.

An interesting feature is that the scale of C_{dl} values measured from OCPD is significantly lower than that of cyclic voltammetry and impedance spectroscopy measurements. It is believed that the reason for this is the frequency dependence of the double layer capacitance. Determination of C_{dl} from OCPD corresponds to calculating the double layer capacitance at high frequencies whereas cyclic voltammetry and impedance spectroscopy C_{dl} values are obtained from a lower frequency range. Alternatively, OCPD could be measuring a different type of double layer capacitance. Further work needs to be carried out in order to explain this observation.

Qualitatively, since the shape of the OCPD does not change as a function of degradation, this leads to the conclusion that there is no loss of catalytic activity as a function time. This is further confirmed by the quantitative analysis of tables 6.4 to 6.6 which show that there is little change in the parameters used to fit experimental data as a function of degradation.

Some of the OCPD traces recorded were classified as 'anomalous', i.e. the overpotential at short times tends to infinity as opposed to a constant value as predicted by theory. About 15 % of the total number of acquired OCPDs fell into this category. A typical anomalous OCPD trace is shown in figure 6.29 :

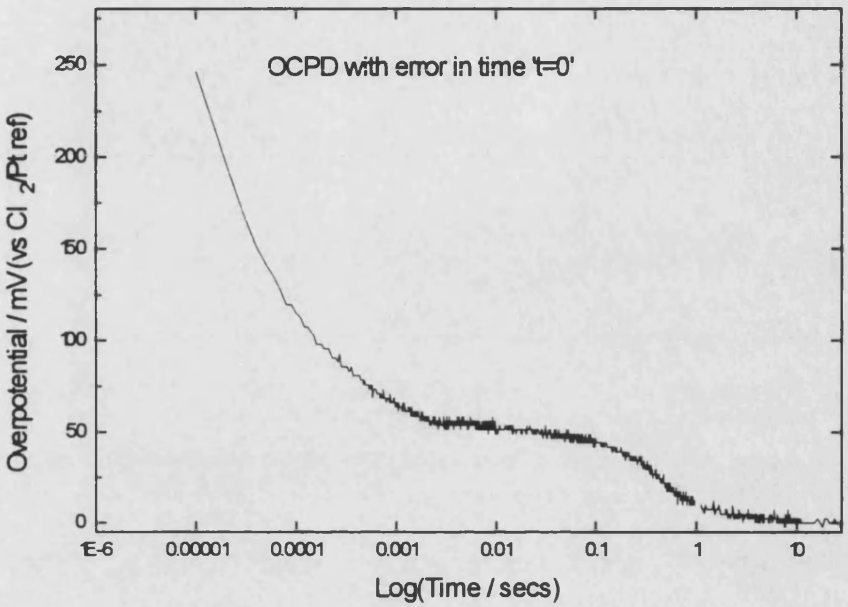

Figure 6.29 : OCPD plot displaying unusually high overpotential just after interruption.

Initially, it was believed that the reason for this was the re-equilibration of surface charge through lateral currents just after interruption. This type of effect would have been consistent with the effects describe by Newman[18]. However, this explanation was rejected and the two most plausible explanations were that it was either a result of the method used by the OCPD acquisition program to determine the point of current interruption or an electronic artefact caused by the mercury wetted relay not interrupting the current instantaneously.

If there was an error in the determination of the point of current interruption, its effect would be noticeable on a logarithmic time scale. The next plot shows the effect of a 5 μsecond error in determining the point of interruption.

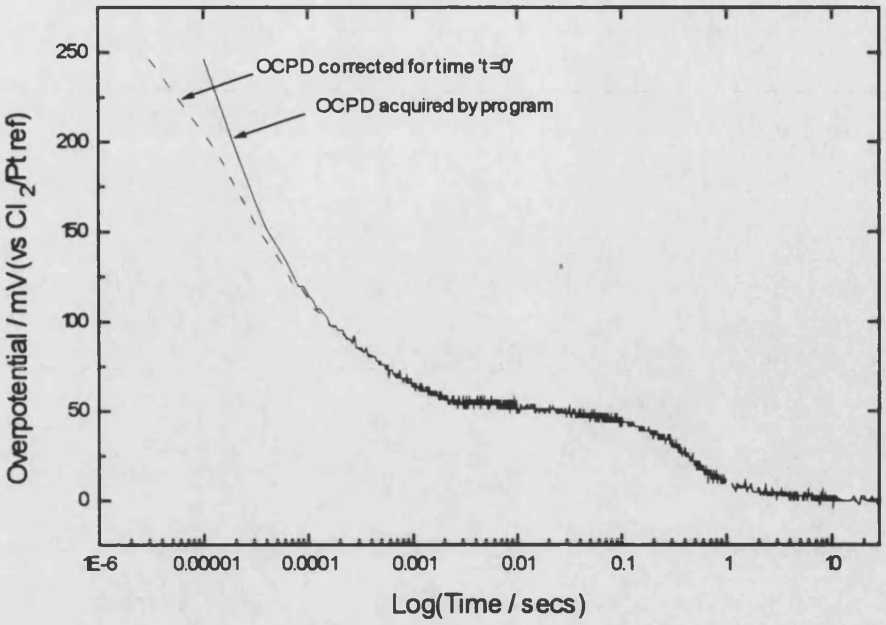

Figure 6.30 : OCPD corrected for a possible 5 μsecond error in the determination of current interruption.

Although the effect of such a correction makes the OCPD look more like a simulated one, it does not appear that this is what is responsible for the high overpotentials at short times : a close inspection of the corrected OCPD at short times shows that shifting the decay curve by 5 μs does not correct the overpotential value so that, at short times, η tends towards a constant value.

The second possibility is that the mercury wetted relay did not interrupt the current cleanly, so that a short current pulse flows after the switch was opened. This would increase the overpotential just after interruption.

In order to test for this possibility, the first points recorded were deleted and the time value was reset from the last point of deletion. The effect of such a correction on the OCPD is shown in fig 6.31.

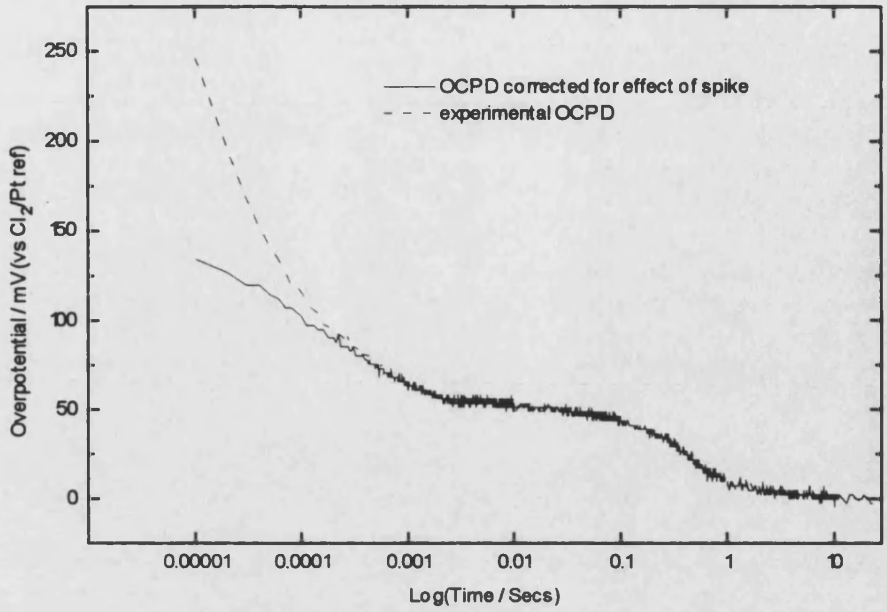

Figure 6.31 : OCPD corrected for a possible mercury wetted relay unclean interruption.

The effect of this correction is such that region 1 can be identified clearly and that the corrected OCPD resembles a simulated one. The main conclusion is that a 'classical' OCPD shape was restored by effectively altering the time that was chosen correspond to 'true' current interruption. This highlights the fact that although the circuitry for OCPD seems simple, great care must be taken in the choice of cables and electronic components to avoid artefacts.

Since the double layer capacitance is calculated as the current before interruption divided by the derivative at short times (equation 6.37), this means that the artefact-corrected derivative is substantially smaller, i.e the artefact results in apparent lower C_{dl} values..

Sample M36 exhibited an anomalous OCPD shape and the double layer capacitance calculated was found to be 0.5 mF cm^{-2}. After correction, the new value was of found to be 2 mF cm^{-2}, i.e. 4 times bigger. This example illustrates how significant the error in double layer capacitance can be.

Correction of all the OCPDs suspected of being affected by such a problem reinforced the conclusion that the double layer capacitance goes through a maximum

and that there is little change in the value of the initial overpotential compared to the increase in alkali wear pot running potential.

6.3.3 Conclusions

OCPD has revealed be a powerful *fingerprinting* technique both for the determination of the reaction mechanism and for the study of the effect of degradation on the electrocatalytic activity of RuO_2/TiO_2 coatings.

Analysis of OCPD data made it possible to establish a reaction mechanism for the production of chlorine under industrially relevant conditions on a RuO_2/TiO_2 coatings prepared by ICI. The extremely good resemblance of real OCPDs with simulated OCPDs only considering step 1) & 2) as the reaction mechanism has proven that this is the reaction mechanism that is taking place on the RuO_2/TiO_2 coating.

More importantly, it has also led to the conclusion that degradation must cause the build-up of a resistive layer that cannot be accounted for by an increase in porosity alone, i.e. OCPD suggests that an insulating layer of TiO_2 between the RuO_2/TiO_2 coating and titanium substrate is responsible for the apparent loss of performance.

[1] Conway, B. V. Tilak, *Electrochem. Acta*, 22, 1167-1178, 1977

[2] B. E. Conway. D.M. Novak, *J. Electroanal. Chem.*, 99, 133-156, 1979

[3] A. J. Bard, L.R. Faulkner, *Electrochemical methods*, Wiley, 111-112, 1980

[4] L. Bai, L. Gao, B.E. Conway, J. Chem. Soc. Faraday Trans., 89(2), 1993, 243-249

[5] B.E. Conway, D.M. Novak, *J.electroanal. chem.*, 99, 1979, 133-156

[6] S.H. Jordanov, B.E. Conway, *J. Electronal. Chem.*, 326, 1992, 177-195

[7] B.E. Conway, G. Ping, *J. Chem. Soc. Faraday Trans.*, 86(6), 1990, 923-930

[8] B. Tilak, B.E. Conway, *Electrochimica Acta*, 37(1), 1992, 51-61

[9] B. E. Conway, G. Ping, A. De Battisti, A. Barbieri, G. Battaglin, *J. Mater. Chem.*, 1(5), 725-734, 1991

[10] B. E. Conway, H. Jordanov, *Maced. Acad. Sci.*, 8(1), 19-31, 1987

[11] B. E. Conway, H. Jordanov, *J. Electroanal. Chem.*, 326, 177-195, 1992

[12] F.P. Bowen, E.K. Rideal, *Proc. R. Soc.*, 120, 59, 1928

[13] B.E. Conway, P. Gu, L. Bai, L. Gao, R. Brousseau, *Electrochim. Acta*, 37(12), 2145-2154, 1992

[14] D.A. Harrington, B.E. Conway, *J. Electroanal. Chem.*, 221, 1-21, 1987

[15] B.E. Conway, D.F. Tessier, *J. Electroanal. Chem.*, 161, 39, 1984

[16] E. Gileadi, B.E. Conway, *J. Chem. Phys.*, 39, 3420, 1963

[17] J.Newman, A.C. West, *J. Electrochem. Soc.*, 136(10), 2935-2939, 1989

[18] J. Newman, A. Hauser, *J. Electrochem. Soc.*, 136(11), 3319-3325, 1989

CHAPTER SEVEN

Chapter Seven

XPS and XRF measurements

This chapter covers results obtained from scanning electron microscope (SEM), X-ray fluorescence (XRF) and X-ray photoelectron spectroscopy (XPS) measurements. In total, 3 series of 8 electrodes each were degraded. In each of the series, one sample was kept as a standard, i.e. it was not degraded in the alkali wear pot.

In view of the commercial sensitivity regarding the nature of the RuO_2/TiO_2 coating, no information can be given about their preparation procedure. The composition of the RuO_2/TiO_2 strips was 75% titanium-25% ruthenium. Initially, 3 strips of the commercial coating were provided. Each of them was cut into 8 pieces of equivalent size using a guillotine. The same procedure was repeated for each strip. It was expected that samples coming from the same initial strip would be similar in composition and topography. One sample was kept undegraded and the remaining 7 samples from each strip were degraded at 2 A cm^{-2} for different lengths of time.

7.1 XRF results

The purpose of using XRF as a probing technique was to measure the *total* amount of ruthenium per unit area contained in the sample before and after degradation. Comparison of the results allowed the determination of total ruthenium loss during degradation. Fisher claims a ± 5 % error in the reproducibility of measurements. This has also been confirmed by independent analysis carried out by ICI using standard samples of known ruthenium content. The instrument used allowed a 3 dimensional ruthenium loading map of the whole sample to be obtained. It was anticipated that loss of ruthenium might be non-uniform, and that 'weaker' sites would preferentially lose ruthenium before others. This consideration is significant when

considering the size of industrial electrodes in terms of electrode efficiency and operating costs.

During current flow, the whole electrode is at the same potential. However, if the electrode is degraded then there might be significant differences in the values of local current densities, i.e. most of the current will flow to the area(s) of the electrode which are not degraded.

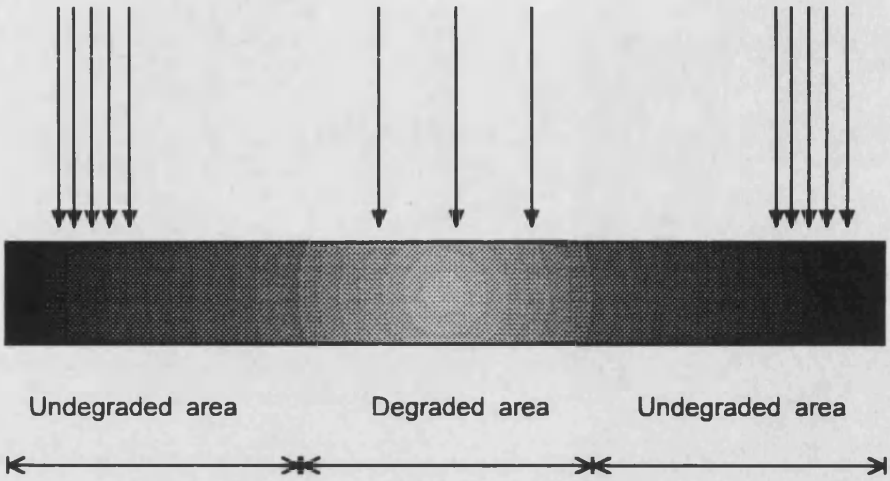

Figure 7.1 : current flow to a partly degrade electrode.

As a consequence, for a given current density, one needs a higher overpotential since, in effect, only part of the electrode is doing most of the work. The following figure shows the current-voltage plot for a homogeneous and partly degraded electrode.

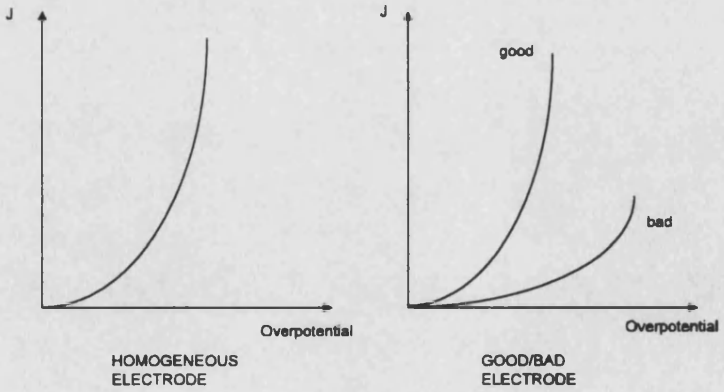

Figure 7.2 : current-voltage plot for a homogeneous electrode and partly degraded electrode.

For a partly degraded electrode, the total current density can be written as

$$j_{total} = f_{good} * j_{good} + \left(1 - f_{good}\right) j_{bad} \qquad (7.1)$$

at any particular overpotential.

In the limit where $j_{bad} << j_{good}$ then

$$j_{total} \rightarrow f_{good} * j_{good} \qquad (7.2)$$

For example, if 5 % of the electrode area is responsible for an increase of 2-3 % in the overall running potential, this could mean that the electrode needs replacing because of the extra energy cost required to run it. Should one know about the degradation properties of the electrode, it is then possible to work on making these 5 % of electrode area more resistant to wear. The saving in terms of material, energy and electrode lifetime are of significance at this level. One can clearly see that homogeneous degradation is a preferred option as it would have less of an impact on the running potential which is the determinant factor in industrial efficiency of chlorine electrocatalysis.

7.1.1 Theory

As mentioned above, each electrode was characterised using XRF according to the same procedure. Series M3x was the only one where all electrodes were characterised before degradation : since all electrodes were prepared the same way, it was concluded that results from one series should suffice to reach conclusions about the homogeneity of undegraded electrodes made from all strips.

At this point, it is necessary to consider the way XRF measurements were carried out. The electrode was either divided in five or seven XRF measurements along the width (or 'X' axis). The length ('Y' axis) was also divided in a similar way. This method allowed a grid structure of ruthenium loadings to be obtained for the whole electrode area. This is illustrated in figure 7.3 below.

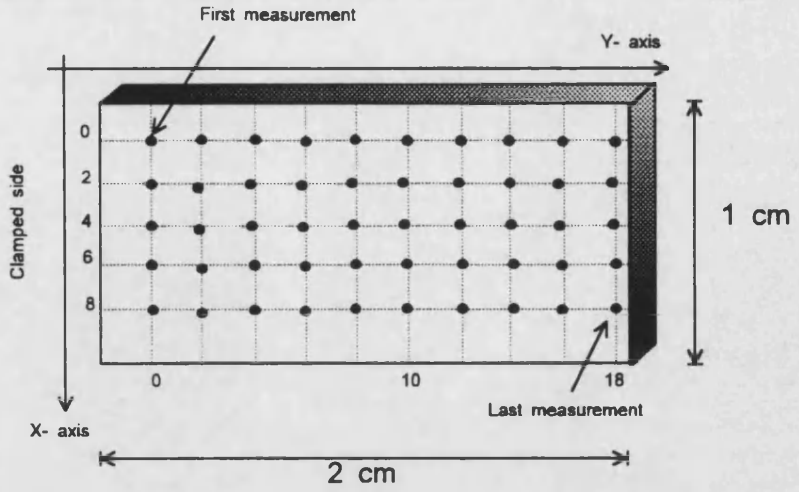

Figure 7.3 : mapping diagram of XRF measurements carried out on RuO_2/TiO_2 samples.

In order to obtain a representative ruthenium loading map of the whole electrode, a minimum of 5 x 14 = 70 XRF measurements were carried out. Results were plotted out as a 3D mesh for qualitative analysis. As for quantitative analysis, three average ruthenium quantities were defined and were as follows :

1. Total average ruthenium loading for the whole sample, $[Ru]_{TOTAL}$, i.e.

$$[Ru]_{TOTAL} = \frac{1}{n}\left(\sum_{i=1}^{i=last}[Ru]_{X_i,Y_i}\right) \qquad (7.3)$$

where $[Ru]_{X_i,Y_i}$ is the ruthenium loading at position (X_i,Y_i) and n is the total number of measurements.

2. Average ruthenium loading along the width of the anode at Y= i, $[Ru]_Y$, i.e.

$$[Ru]_Y = \frac{1}{5}\left(\sum_{i=1}^{i=5}[Ru]_{X_i}\right)_Y \qquad (7.4)$$

3. Average ruthenium loading along the length of the anode at X=i, $[Ru]_X$, i.e.

$$[Ru]_X = \frac{1}{14}\left(\sum_{i=1}^{i=14}[Ru]_{Y_i}\right)_X \qquad (7.5)$$

Furthermore, a standard deviation was calculated for each of the average quantities defined above. Its value allowed to the variation of local ruthenium loading to be analysed.

In summary, the total average ruthenium loading value for each electrode allowed the total amount of ruthenium lost to be calculated and, also, to investigate the dependence of the total average ruthenium loading on degradation time. The average ruthenium loading values at particular X and Y values enabled preferential loss of ruthenium to be investigated. Finally, values of the standard deviations were used to investigate preferential loss at particular areas of the anodes in greater details.

7.1.2 Characterisation of undegraded electrodes

The following table summarises the total average ruthenium for the M3x series prior degradation.

Sample	Initial total average Ru loading / g m^{-2}	Standard deviation
M31	6.62 ± 0.33	0.80
M32	7.56 ± 0.38	0.47
M33	7.36 ± 0.37	0.58
M34	7.12 ± 0.35	0.56
M35	2.38*	0.92
M36	7.39 ± 0.37	1.12
M37	6.97 ± 0.35	0.93
M38	7.12 ± 0.35	1.30

Table 7.1 : initial total average ruthenium loadings for the M3x series.

Table 7.1 reveals that all strips in the M3x series have a similar total average ruthenium loading of 7 g m^{-2}. The low total average value for sample M35 suggests that this measurement was carried out incorrectly. Unfortunately, degradation was carried out on this sample before receiving the XRF measurements and, as a result, it was not possible to repeat the measurement. Table 7.1 also shows that the standard deviation of total average ruthenium loading values for all samples is of 0.31 (M35 not

included). This indicates that all samples have similar composition and that there is little variation between samples coming from the same strip. As for the standard deviation of total average ruthenium loading for each sample, results confirm the ± 5 % error in the evaluation of the ruthenium loading claimed by Fischer. Since all series of electrodes were prepared the same way, it can be concluded that all electrodes will have the same total average ruthenium loading as the M3x series prior degradation. It can also be concluded that the preparation procedure yields samples that are homogeneous in composition and that degrading *many samples* to higher increases in the value of the alkali wear pot running potential can be considered as equivalent to artificially simulating the lifetime of *one electrode*.

The next table summarises average ruthenium loading values along the Y-axis before degradation, i.e. $[Ru]_Y$ (see equation 7.4).

Y / mm	M31	M32	M33	M34	M35	M36	M37	M38
0	5.84	7.58	7.40	7.37	3.20	7.52	7.14	6.93
1.82	6.12	7.63	7.48	7.50	2.37	7.51	7.16	6.91
3.63	6.40	7.71	7.36	7.48	2.32	7.50	6.92	6.91
5.46	6.63	7.77	7.48	7.38	2.28	7.61	6.88	6.83
7.28	6.93	7.85	7.55	7.20	2.31	7.59	6.95	6.70
9.10	7.08	7.75	7.51	7.10	2.31	7.50	6.89	6.63
10.92	7.11	7.63	7.54	7.09	2.34	7.42	6.65	6.67
12.74	7.32	7.58	7.57	7.06	2.29	7.39	6.58	7.15
14.56	7.41	7.42	6.96	6.84	2.20	6.71	6.77	7.21
16.38	7.08	7.14	6.71	6.79	2.24	6.40	6.82	7.95
18.20	6.62	7.56	7.36	7.12	2.38	7.39	6.97	7.12
Std Dev	**0.50**	**0.19**	**0.27**	**0.24**	**0.27**	**0.39**	**0.17**	**0.37**

Table 7.2 : average ruthenium loading values along the Y-axis for the M3x series

Table 7.2 shows that the average ruthenium loading values along the Y-axis are similar to each other along the whole *length* of the electrode and to that of the total average value for the whole electrode. Since the value of the standard deviation values of average ruthenium loading along the Y-axis are low, i.e. the local ruthenium loading

values vary by less than ± 8 % from the average value along each position on the Y-axis, this indicate that samples are homogeneous in composition along the *length* of the electrode.

The following table summarises ruthenium loading values along the X-axis for the M3x series.

X / mm	M31	M32	M33	M34	M35	M36	M37	M38
0	6.07	8.49	7.57	7.56	8.65	7.34	7.21	6.54
2	5.55	7.19	7.05	7.15	2.14	7.88	6.30	7.14
4	5.61	7.46	7.51	7.17	2.17	7.18	7.00	7.06
6	5.53	7.08	7.51	6.73	2.25	6.39	6.33	6.90
8	5.38	7.16	7.38	7.98	2.14	8.98	9.52	7.81
Std Dev	**0.26**	**0.58**	**0.21**	**0.47**	**2.89**	**0.96**	**1.32**	**0.46**

Table 7.3 : average ruthenium loading values along the x-axis for the M3x series.

Results from Table 7.3 yield similar conclusions as those from Table 7.2, i.e. samples from the M3x series are also homogeneous in composition along the *width* of the electrode.

In conclusion, table 7.1 showed that all electrodes made from the same strip had the same total average ruthenium loading. As for table 7.2 and 7.3, they led to the conclusion that there were no variations in composition along the *width* nor *length* of the electrodes. As a result, it can be concluded that coating the samples with a paint brush gave the same homogeneity in composition as the spraying method used to coat large industrial anodes. This conclusion is significant as it was believed that leaving the 20x1 cm strips to dry hanging downwards would cause differences in composition along the length and width of the strips.

7.1.3 Characterisation of degraded electrodes

This section covers results that were obtained from XRF measurements carried out on the M3x, M4x and M5x series after degradation.

The total average ruthenium loading for all samples in the M3x series was found to be identical and below 2 g m^{-2}. Since all electrodes were degraded to different increases in the value of the alkali wear pot running potential, this suggested that

measurements were carried out incorrectly. It is believed that an error in the programmation of the XRF instrument caused it not to carry out XRF measurements over the area of the electrode. As a result, measurements obtained from the degraded M3x series were not used for the analysis of the effect of degradation in the alkali wear pot on the electrocatalytic performance of the anodes.

In terms of the M4x series, sample M42 was kept as standard and, as a result, its total average ruthenium loading was considered to be the total average ruthenium loading value of all the sample for that series prior degradation. The reason for this approximation comes from the analysis of all samples of the M3x series prior degradation, i.e. section 7.1.2.

The following table summarises degradation length, increase in alkali wear pot running potential and total average ruthenium loading for the M4x series.

Sample	Degradation time / h	Potential increase / mV	Final Ru Loading / g m^{-2}	Standard Deviation
M42	0.00	0.00	7.35 ± 0.37	0.55
M41	1.06*	120	6.47 ± 0.32	0.55
M43	13.75	230	6.22 ± 0.31	0.85
M45	31.00	340	4.93 ± 0.25	1.13
M44	35.50	360	5.46 ± 0.27	1.04
M46	64.90	960	3.91 ± 0.19	1.00
M47	46.50	1470	3.54 ± 0.18	1.10
M48	69 < t < 77	2090	3.40 ± 0.17	0.69

* measurements were carried out for 1 hour in order to look for an 'activation' effect.

Table 7.4 : total average ruthenium loading for the M4x series after degradation.

Table 7.4 shows that the total average ruthenium loading decreases exponentially as a function of increase in alkali wear pot running potential and as a linear function of degradation time. Such plots are shown in Figure 7.4 below :

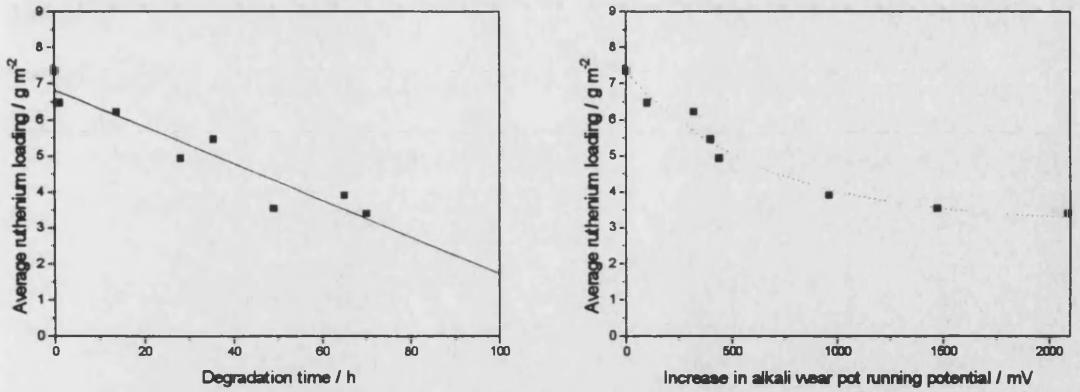

Figure 7.4 : plot of ruthenium loading as a function of degradation time and increase in alkali wear pot running potential for the M4x series.

The plot of total average ruthenium loading as a function of degradation time indicates that the amount of ruthenium left in an electrode falls linearly with degradation length, suggesting that the rate of ruthenium loss is constant. As for the plot of total average ruthenium loading as a function of increase in alkali wear pot running potential, it indicates that the average ruthenium loading decays towards a constant value close to 3 g m^{-2}. This seems to correspond to a 50 % loss in ruthenium per unit area once the alkali wear test running potential has increased by 2 V. It also seems to imply that the ruthenium content will not decrease below 3 g m^{-2} if the alkali wear pot running potential is increased further.

At this point, it is necessary to mention that independent research carried out by ICI has revealed that if the structure of the anodes has changed as a result of degradation then the background level can increase, i.e. some of the X-rays reflected have lost energy and contribute to a higher background level. The implication of such an effect is that the 3 g m^{-2} measured on highly degraded samples is correct if the degraded samples have the same structure as undegraded ones. Research carried by ICI suggest that this is not always the case and, as results, the fact that the total average ruthenium loading tends towards 3 g m^{-2} really means that a significant amount of ruthenium has been removed. In view of the commercial sensibility, the exact value of ruthenium loss cannot be given but it is fair to assume that the measured 3 g m^{-2} corresponds to loss of ruthenium in the range of 50-100 % loss.

Since the total average ruthenium loading varies linearly as a function of degradation time and exponentially as a function of increase in alkali wear pot running

potential, Table 7.4 therefore indicates that the increase in alkali wear pot running potential is not a linear function of degradation time. Such a plot is shown in Figure 7.5 below.

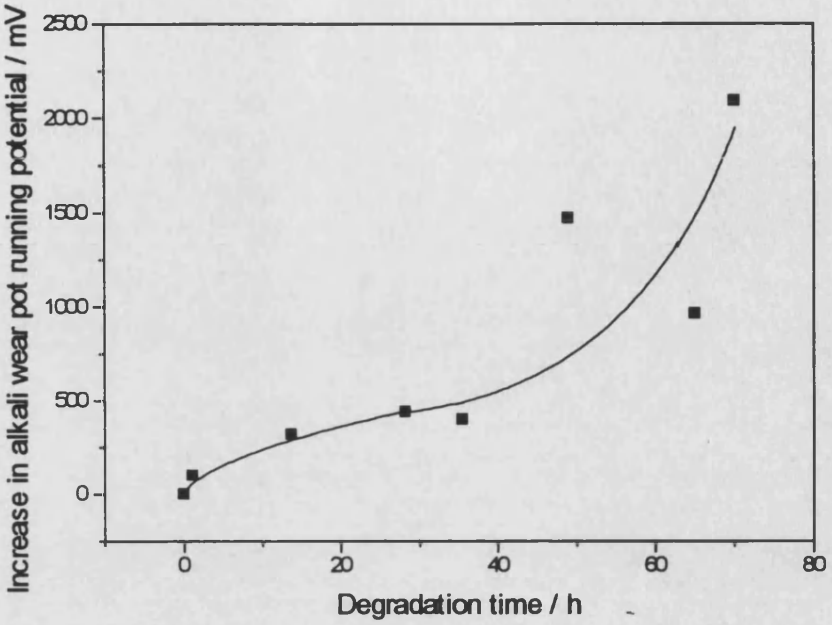

Figure 7.5 : increase of alkali wear pot running potential as a function of degradation time for the M4x series.

It shows that alkali wear pot running potential initially increases steadily as a function of degradation time up to approximately 45 hours and then exponentially beyond this amount of degradation time. This type of behaviour is characteristic of a catastrophic breakdown in electrocatalytic performance. Since the rate of ruthenium loss as a function of time is constant, this indicates that electrocatalytic performance breakdowns once the total average ruthenium loading has fallen below a critical value greater than 50 % loss.

Table 7.5 summarises information about the ruthenium loading distribution along the *length* of the electrodes for the M4x series.

Y / mm	M42	M41	M43	M44	M45	M46	M47	M48
0.00	7.32	5.93	6.52	5.52	4.66	3.63	3.75	3.30
1.42	7.31	5.99	6.62	5.56	4.78	3.84	3.91	3.44
2.86	7.22	6.03	6.69	5.51	5.07	3.96	4.07	3.52
4.28	7.23	6.24	6.77	5.52	5.02	3.96	4.03	3.56
5.68	7.37	6.36	6.65	5.55	5.07	4.12	4.03	3.55
7.12	7.19	6.37	6.63	5.49	5.07	4.16	3.99	3.49
8.54	7.36	6.56	6.66	5.53	4.91	4.19	3.90	3.40
9.96	7.41	6.66	6.69	5.60	5.00	4.20	3.74	3.42
11.38	7.35	6.73	6.67	5.48	5.10	4.13	3.57	3.43
12.80	7.41	6.71	6.66	5.33	4.96	4.01	3.32	3.31
14.22	7.40	6.68	6.59	5.37	5.04	3.92	3.00	3.12
15.64	7.45	6.65	6.51	5.37	4.95	3.76	2.67	3.09
17.06	7.45	6.78	6.63	5.35	4.75	3.45	2.64	3.22
18.48	7.33	6.77	6.38	5.25	4.64	3.46	2.85	3.56
Std Dev	**0.08**	**0.31**	**0.10**	**0.10**	**0.16**	**0.26**	**0.53**	**0.16**

Table 7.5 : average ruthenium loading value along the Y-axis for the M4x series.

The average ruthenium loading values along each Y-position for samples M41 to M45 are similar to the total average ruthenium loading value for the sample. Since the standard deviation values are also significantly low, this indicates that the degradation results in a homogeneous loss of ruthenium along the whole *length* of these electrode. However, this is not the case for samples M46 to M48. Analysis of the average ruthenium loading values shows that the edge of the sample closest to the cathode has a lower ruthenium loading than the rest of the sample. Since the electrodes were placed perpendicular to the nickel cathode in the alkali wear pot, it was thought that the loss of ruthenium might be greater at the end closer to the cathode. Although this could be due to the current flow distribution changing as a function of degradation time, it is most likely that this is because of the anode/cathode geometry resulting in a higher current density at the edge of the anode. This effect is illustrated in Figure 7.6 below.

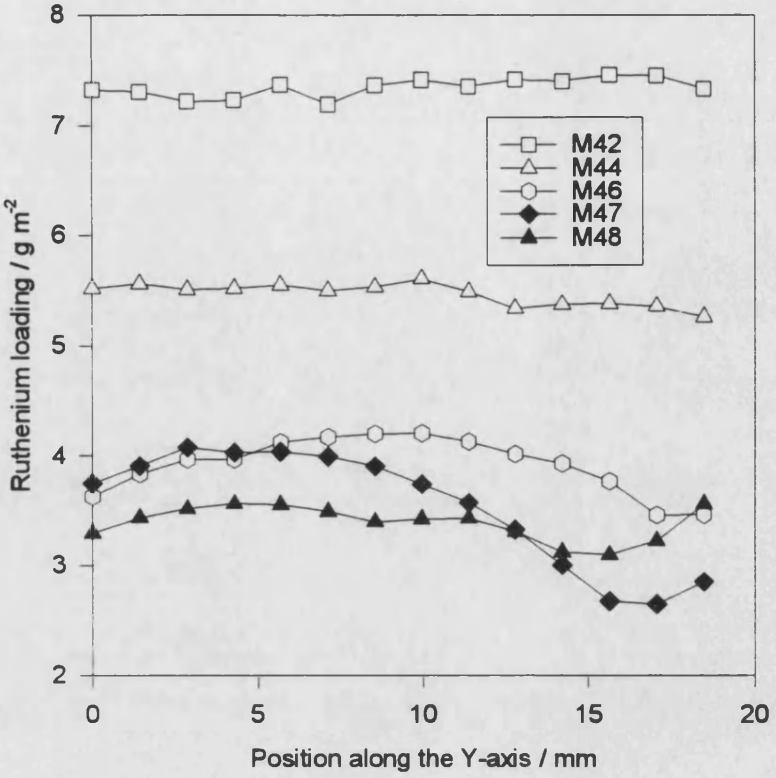

Figure 7.6 : variation of the ruthenium loading across the length of electrodes for the M4x series. The edge closest to the cathode corresponds to high values on the Y-axis.

The following table shows the average ruthenium loading values along the *width* of the electrodes of the M4x series.

X / mm	M42	M41	M43	M44	M45	M46	M47	M48
0	7.47	6.25	7.13	6.36	5.60	4.88	3.14	2.83
1.43	7.62	5.66	6.87	6.83	5.19	4.64	4.53	2.81
2.86	7.82	6.33	6.72	5.89	5.62	4.73	5.74	4.19
4.29	7.74	6.40	6.39	5.78	5.00	3.63	4.33	4.32
5.72	7.17	6.14	5.76	5.15	4.16	2.94	3.68	3.47
7.15	6.80	5.44	5.39	4.43	3.34	1.99	2.55	2.42
8.58	6.62	5.30	7.36	4.18	3.72	2.58	2.25	3.02
Std Dev	**0.47**	**0.45**	**0.72**	**0.98**	**0.92**	**1.16**	**1.22**	**0.73**

Table 7.6 : variation of the average ruthenium loading along the electrode width of the M4x series.

Table 7.6 reveals a trend in the variation of the average ruthenium loading along the X-axis as a function of increase in alkali wear pot running potential : results indicate that the ruthenium loading at the edges is lower than in the middle of the electrodes. Standard deviation values of average ruthenium loading across the X-axis reveal that this effect does not intensify as a function of degradation. On the contrary, it reaches a maximum for mildly degraded electrodes : the fact that the standard deviation values increase from 0.45 to 1.12 to finally decrease to 0.73 means that degradation initially results in preferential removal of ruthenium from the edges and then removal from the middle of the electrode. Since the local ruthenium loading at the edge of samples which have the greatest value of standard deviation is approximately 3 g m^{-2}, i.e. the loading that seems to be the lowest possible, this implies that ruthenium can no longer be removed from the edges and, as a result, must be removed from the middle . This can seen clearly in figure 7.7 and 7.8 below :

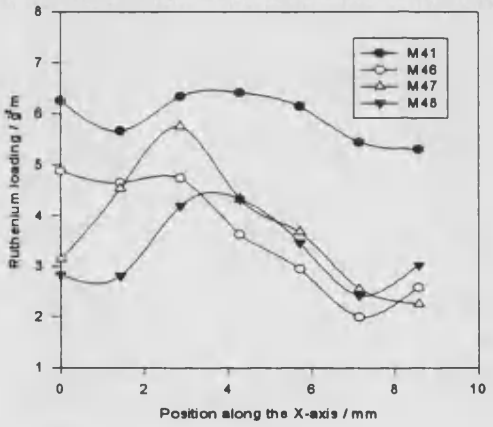

Figure 7.7 : variation of the average ruthenium loading along the electrode width for the M4x series.

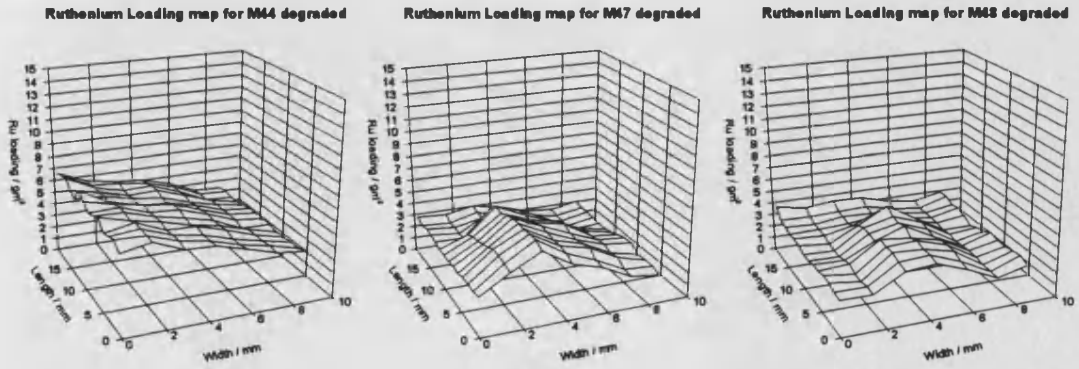

Figure 7.8 : 3D mesh ruthenium loading maps for samples M44, M47 and M48 after degradation.

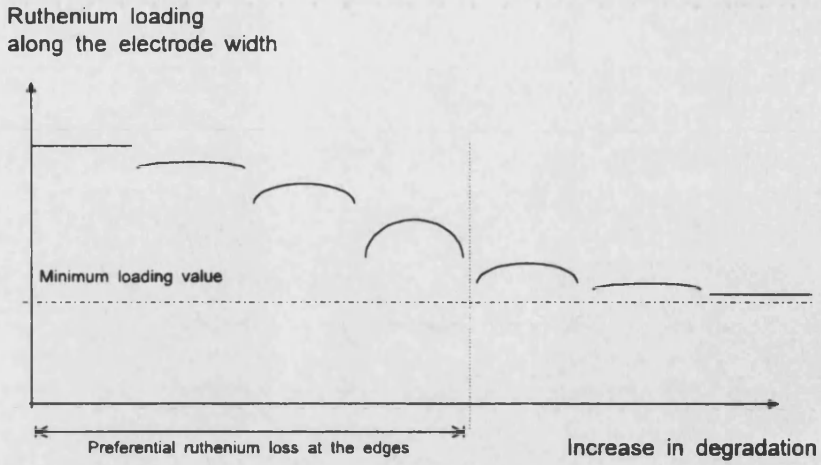

Figure 7.9 : variation of the ruthenium loading along the electrode width as a function of degradation

The same analysis was carried out for the M5x. Table 7.7 summarises the total average ruthenium loading values for the M5x series..

Sample	Degradation time / h	Potential increase / mV	Final Ru loading g m^{-2}	Standard deviation
M51	0.00	0	6.36	0.54
M52	1.00	120	6.53	0.59
M53	43.50	600	5.25	0.98
M55	49.50	930	5.01	1.42
M54	101.00	1000	4.06	0.90
M56	79.50	1800	4.36	1.17
M57	73.50	2460	3.82	0.67
M58	75.00	4492	3.20	0.54

Table 7.7 : total average ruthenium loading values for the M5x series after degradation.

Table 7.7 confirm the previous findings that the alkali wear test is effective in decreasing the total amount of ruthenium in the samples. However, standard deviation values of the total average ruthenium loading suggest that the degradation is not as homogeneous over the whole sample as it was for the M4x series.

Table 7.8 presents results from analysis of average ruthenium loadings along the Y-axis. Just as in the case of the M4x series, the edge closest to the cathode has lost more ruthenium than the rest of the electrode. Analysis of sample M52 shows that the average ruthenium loading along the length of the electrode is approximately 3 g m^{-2}. Since M52 was to degraded to an increase in alkali wear pot running potential of 4500 mV approximately, this suggests that this value is the lowest ruthenium content per unit area for this RuO_2/TiO_2 coating and, since it is not equal to zero, that the structure of the electrode has changed. This is confirmed by the fact that there is little difference in ruthenium loading between the edge furthest away from the cathode and the one closest to it. The larger range in increases of alkali wear pot running potential reveals a trend in the standard deviation of average ruthenium loading along the Y-axis as a function of degradation. The fact the standard deviation values increases up to a maximum for M56 indicate that ruthenium is preferentially removed from the edge closest to the cathode until it has reached the limiting ruthenium loading of 3 g m^{-2}. After that, ruthenium is removed from the rest of the sample but still according to the same principle, i.e. ruthenium is removed preferentially from the area of the electrode closets to the cathode. This is illustrated in Figure 7.10 below.

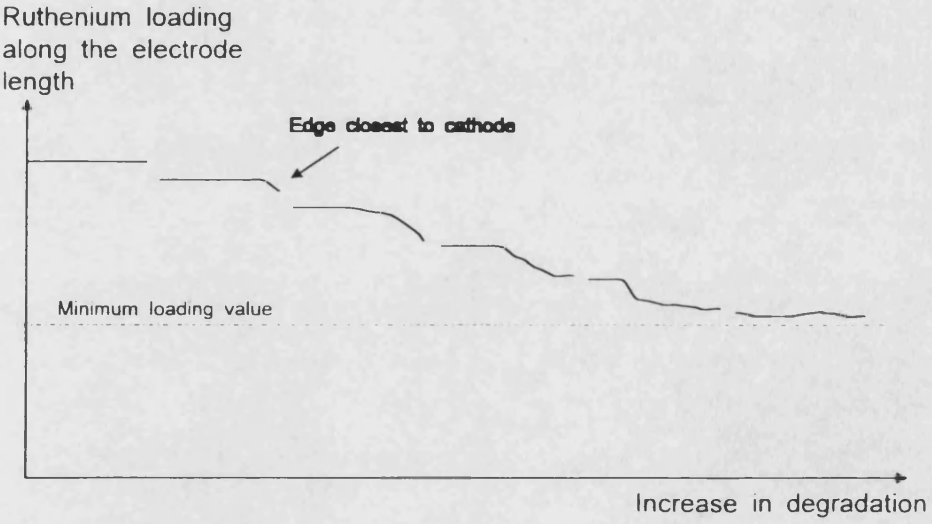

Figure 7.10 : variation of the average ruthenium loading along the electrode length as a function of degradation.

Y / mm	M51	M52	M53	M54	M55	M56	M57	M58
0.00	6.02	6.38	5.94	4.13	6.84	6.20	3.99	3.03
1.42	6.07	6.33	5.26	3.87	4.58	4.07	3.93	2.98
2.86	6.06	6.41	5.18	4.02	4.44	4.06	4.14	3.06
4.28	6.01	6.66	5.21	4.03	4.63	4.12	4.04	3.20
5.68	5.99	6.51	5.27	4.17	4.89	4.49	4.00	3.36
7.12	6.15	6.66	5.37	4.26	5.07	4.82	3.96	3.29
8.54	6.27	6.67	5.39	4.28	5.17	4.71	4.02	3.27
9.96	6.38	6.58	5.37	4.31	5.09	4.57	3.95	3.30
11.38	6.43	6.56	5.36	4.29	5.04	4.39	3.95	3.32
12.80	6.54	6.67	5.32	4.09	5.14	4.24	3.82	3.16
14.22	6.75	6.63	5.32	3.98	5.10	4.07	3.67	3.07
15.64	6.96	6.42	5.21	3.91	4.98	3.76	3.26	2.97
17.06	6.74	6.48	4.83	3.78	4.66	3.57	3.33	3.22
18.48	6.70	6.54	4.29	3.57	4.33	3.81	3.28	3.45
Std Dev	**0.33**	**0.12**	**0.36**	**0.21**	**0.60**	**0.64**	**0.30**	**0.15**

Table 7.8 : variation of the average ruthenium loading along the electrode length for the M5x series.

The next table summarises the analysis of ruthenium loading along the X-axis for the M5x series.

X / mm	M51	M52	M53	M54	M55	M56	M57	M58
0	7.21	6.64	5.22	2.92	5.37	2.94	2.83	2.64
1.43	5.74	5.71	4.67	2.58	5.41	3.92	2.97	2.63
2.86	5.64	5.92	5.72	4.27	6.54	6.17	4.23	2.82
4.29	5.71	6.25	6.76	5.27	8.18	7.43	4.59	3.86
5.72	5.85	7.07	6.59	4.82	7.69	7.47	4.59	3.17
7.15	5.79	6.67	6.17	4.42	7.48	7.64	4.63	3.00
8.58	6.21	6.37	6.46	4.62	7.20	7.83	4.06	3.10
Std Dev	**0.55**	**0.47**	**0.77**	**1.00**	**1.11**	**1.99**	**0.77**	**0.42**

Table 7.9 : average ruthenium loadings along electrode width for the M5x series.

Just as in the case of the M4x series an increase to a limiting value of the standard deviation followed by a decrease is observed (i.e. Figure 7.11 below).

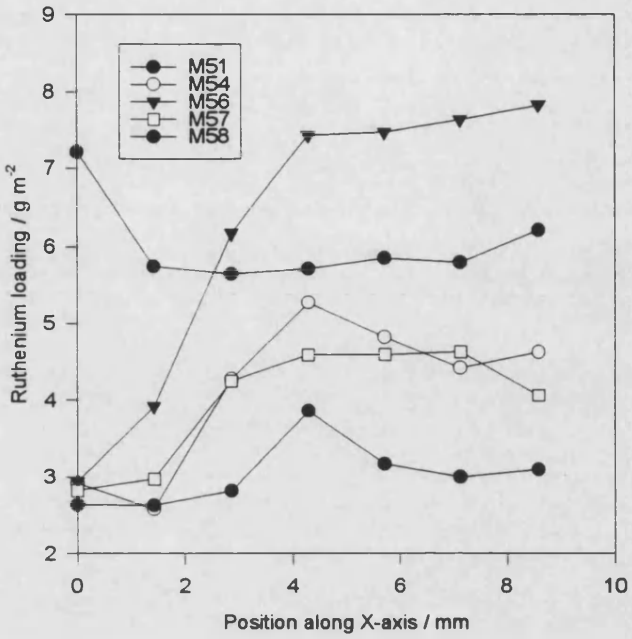

Figure 7.11 : variation of the average ruthenium loading along the electrode width for the M5x series.

Inspection of the 3D maps reveals preferential degradation on the edges just as in the case of the M4x series. This is illustrated below in the case of M54, M57 and M58.

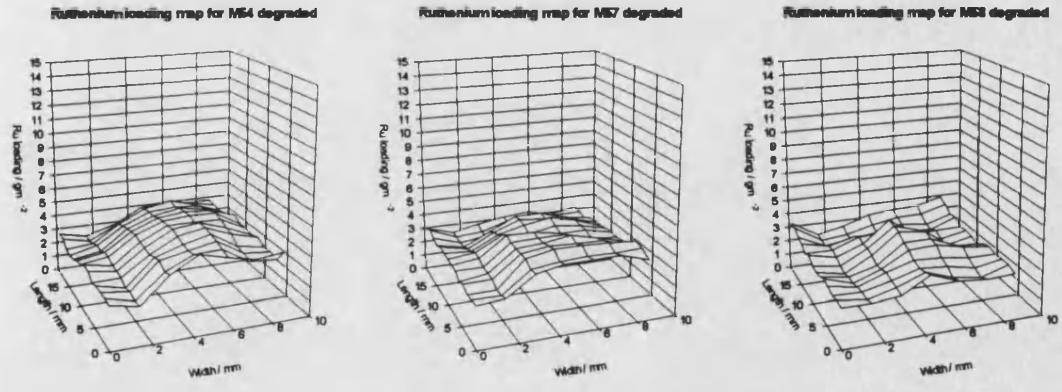

Figure 7.12 : 3D mesh plots of samples M54, M57 and M58 after degradation.

The next two plots represent the ruthenium loading value for series M5x vs. the degradation length and increase in running potential respectively.

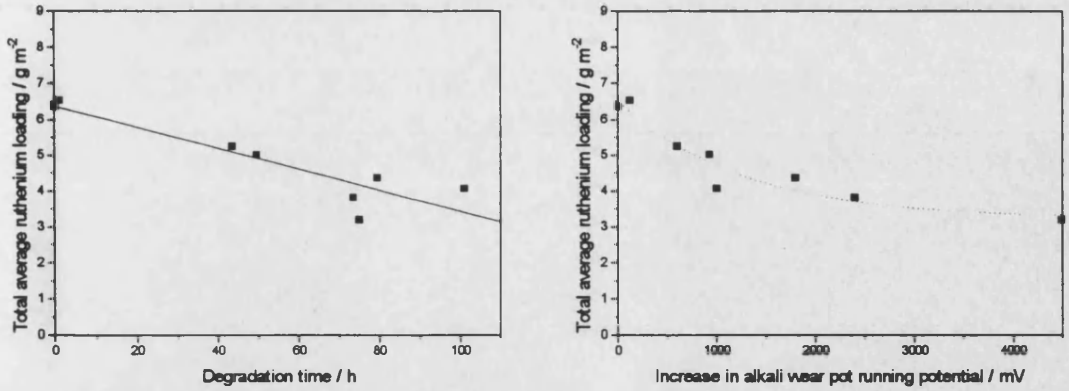

Figure 7.13 : variation of the total average ruthenium loading as function of degradation time and increase in alkali wear pot running potential for the M5x series.

These plots show that the M5x series exhibits the same behaviour as the M4x series. The slope of the linear fits of the total average ruthenium loading vs. degradation time plots for the M4x was of 0.0294 and 0.0511 g m^{-2} h^{-1} for the M5x, i.e. the rate of ruthenium loss for the M4x series is 56 % smaller than for the M5x series. In view of the fact the interelectrode gap between cathode and anode in the alkali wear pot was not adjusted to always be the same such a difference means that the rate of ruthenium loss in *our* alkali wear pot was of the order of 40 mg m^{-2} h^{-1} for the RuO_2/TiO_2 coating. It must be emphasised that this value will vary according to the experimental degradation conditions.

Finally, just as for the M4x series, the increase in alkali wear pot running potential increases exponentially as a function of degradation time above 45 hours of degradation.

7.1.4 Conclusions from XRF measurements

The use of the XRF technique has resulted in the following conclusions :

1. Electrodes were initially homogeneous in composition over the whole electrode area. The total average ruthenium value prior degradation was 7 g m^{-2} approximately.

2. The amount ruthenium measured falls linearly with degradation time at a rate of loss of the order of 40 mg m^{-2} h^{-1}.

3. The ruthenium loading measured after degradation decays exponentially as a function of increase in alkali wear pot running potential towards a constant value of 3 g m^{-2} approximately. In view of the possibility that degraded samples do not have the same structure as the undegraded samples used for calibration, this means the value of 3 g m^{-2} could, in fact, mean that the ruthenium loading of samples highly degraded was negligibly small. This also means that degradation of RuO_2/TiO_2 samples was studied up to amounts of ruthenium loss of the order of 50-100 %. As mentioned earlier, it is not possible to give a precise value in view of the commercial sensitivity regarding this project.

4. The geometrical arrangement of the anode/cathode in the wear pot results in a preferential loss of ruthenium at the edge closest to the anode. As it will be later, no evidence was found that this affected the electrochemical analysis of the RuO_2/TiO_2 samples. It must be remembered that only a small part of the anode was exposed to solution during electrochemical characterisation.

5. Degradation results in preferential removal of ruthenium from the edges and this is a true effect, i.e. it is not due to the anode/cathode geometry. This confirms expectations that the coating does not bind to the edges as strongly as on the face of the electrodes.

7.2 XPS measurements

The following section covers results obtained from XPS measurements carried out at ICI's research centre at The Heath. Initially, the purpose of using this technique was to study the variation of surface composition as a function of electrode wear. However, results from XPS experiments were also used to determine the proportion of ruthenium lost at the surface with respect to total loss of ruthenium (measured by XRF). Finally, the study of the Ti/Ru ratio as a function of electrode wear was used to determine the effect of degradation on the surface morphology of anodes.

7.2.1 Theory

Since the purpose of using XPS measurements in this project was to study trends resulting from electrode wear, this section will only deal briefly with the description of XPS measurements and concentrate more on the possible interpretation of data.

When performing XPS measurements, the resulting information is a count (or peak intensity) vs. binding energy spectrum. Each of the peaks in the plot must be attributed to a particular species contained in the material studied. In this project, only one type of commercial anode coating was used. It was a RuO_2/TiO_2 anode coating deposited onto an etched titanium substrate. Each element (i.e. Ru, Ti and O) has a set of peaks that correspond to the binding energies of its various electron energy orbitals. The first step is to attribute each peak or group of peaks to the electron orbital energies of an element. This process is achieved by comparing the binding energies of the peaks to known binding energies of standard materials. The table below displays the binding energy values for the $3d_{5/2}$ orbitals for ruthenium in various states of oxidation :

Ruthenium material	Ruthenium oxidation state	$3d_{5/2}$ orbital binding energy / eV
Ru	0	279.94
Ru	0	280.20
$RuCl_3$	3	281.80
RuO_2	4	280.90
RuO_3	6	282.50
$BaRuO_4$	7	284.20
RuO_4	8	283.30

Table 7.10 : binding energies of the 3d orbitals for ruthenium in various oxidation states.

In the present case, attribution of peaks was made much easier since the elemental composition of the anode was already known. The next step was to curve fit all the peaks in order to determine the atomic surface ratios of oxygen, ruthenium and titanium. Although this method seemed straightforward many problems associated with

such a technique were encountered. Amongst one of them was surface contamination. In order to obtain an accurate atomic ratio of elements, the sample should ideally be very clean. Surface contamination by atmospheric species, carbon in particular, can be very significant even when under vacuum. The problem is that the carbon 1s orbital binding energy is similar to that of the ruthenium $3d_{5/2}$ orbital binding energy. Other problems arise from the fact that this is also the case for the oxygen 1s orbital binding energy. This means that instead of having well defined and separated peaks, most of the relevant peaks are superimposed. This is shown in the case of sample M52 below:

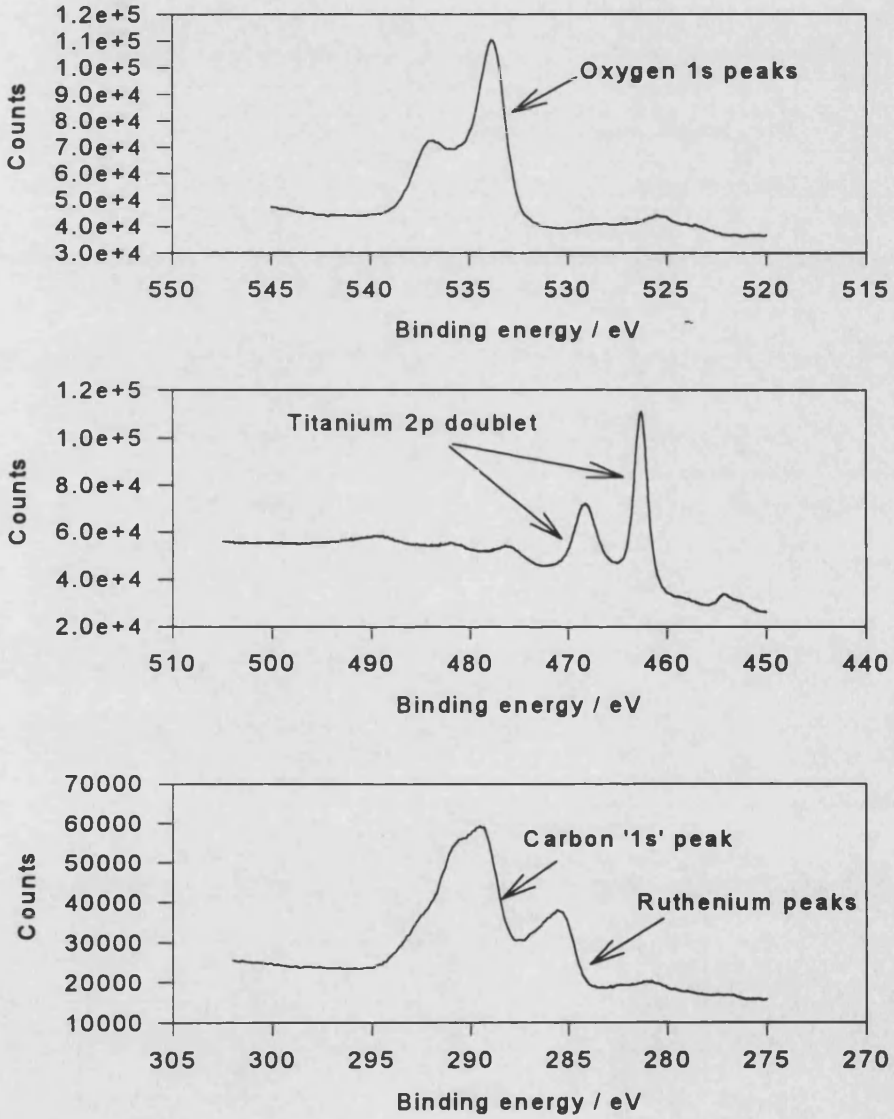

Figure 7.14 : XPS spectra for sample M52 showing the effects of carbon 1s contamination on the ruthenium 3d orbital peaks.

The process of curve fitting then becomes more arbitrary as assumptions have to be made about the width and/or the height of the contributing peaks To this date, there is still a degree of controversy as to the curve fitting procedure for the RuO_2/TiO_2 mixed oxide electrodes. This is reinforced by the fact that little work has been carried out on standard mixed oxide ruthenium materials and that it is not known how many peaks must be used to curve fit the so-called 'Ru 3d' peaks. In this project, the way XPS data was curve fitted was always the same so that useful information could be obtained from the analysis of trends. It must be said that although the absolute atomic ratios may have a certain degree of uncertainty, this is not the case for the relative atomic ratios of one element to the other. (For example, there is greater degree in uncertainty when saying that there is 3 % of ruthenium than when saying that the ration of titanium to ruthenium is 3:1)

The most useful information obtained from XPS measurements was the variation of the Ti/Ru ratio as a function of electrode wear. As mentioned before, the purpose of putting the electrode through the alkali wear pot was to remove ruthenium in order to simulate electrode wear. The total loss of ruthenium was measured with XRF. However, these measurements could not tell whether titanium was also being lost during degradation experiments in the alkali wear pot. This was made possible with the XPS technique. Basically, there are two possible effects of degradation on surface composition. The first is that ruthenium and titanium are removed simultaneously during degradation. If that were the case then the analysis of the Ti/Ru ratio as a function of electrode wear would be expected to reveal little or no change. The second possibility is that degradation causes preferential loss of either ruthenium or titanium. Such a process could be driven either by kinetic of thermodynamic effects. This preferential loss should be reflected in the changes of the Ti/Ru ratio.

7.2.2 Determination of the Ti/Ru atomic ratio prior degradation

This section summarises results obtained from the curve fitting of XPS measurements carried out on undegraded samples. The following table shows the atomic percentages for each of the elements present on the surface of the electrode as well as the resulting Ti/Ru ratio:

Sample	Element				Ti/Ru ratio
	Ti 2p / %	Ru 3d / %	O 1s / %	C 1s / %	
M31	19.51	2.02	49.67	28.80	9.65
M33	21.09	2.10	52.82	23.99	10.04
M35	21.28	2.54	54.67	21.52	8.38
M38	22.10	2.53	55.61	19.75	8.73
M42	15.17	1.90	50.41	32.53	7.98
M51	16.22	1.44	47.06	35.27	11.26

Table 7.11 : atomic percentages of titanium, oxygen ruthenium and carbon with the surface of various samples from the M3x, M4x and M5x series.

Table 7.11 shows that the average Ti/Ru ratio of undegraded samples presented in this table is of 10:1 ± 1.5. Analysis of all other samples shows this is also the case and, as a result, it can be concluded that the surface Ti/Ru ratio of undegraded electrode is of 10:1 ± 1.5. Table 7.11 also reveals that carbon contamination is significant with a C/Ru ratio in the order of 14:1 ± 2. Since the composition of the liquid RuO_2/TiO_2 coating material is of 75 % titanium, 25 % ruthenium, i.e. a Ti/Ru ratio of 3:1, this implies that a phase separation occurs when the samples are dried and heat treated. This also means that the surface of samples is richer in ruthenium than the underlying bulk.

7.2.3 Effect of degradation on the Ti/Ru ratio

The next tables summarise results obtained from XPS experiments carried out after degradation in the alkali wear pot on the M3x, M4x and M5x series. Sometimes, the ruthenium 3d peaks were so negligible that it was impossible to determine the Ti/Ru ratio. This was either because the amount of ruthenium at the surface was so negligible that XPS did not detect it or because there was too much carbon surface contamination.

Sample	Increase in alkali wear test running potential / mV	Ti 2p / %	Ru 3d / %	O 1s / %	C 1s / %	Ti/Ru ratio
M31	0	7.69	0.72	36.23	55.36	10.68
M35	580	12.86	0.89	45.69	40.56	14.45
M36	950	1.96	-	20.24	77.80	-
M37	1500	2.14	-	20.59	77.27	-

Table 7.12 : atomic percentages and Ti/Ru ratios for various samples of the M3x series after degradation.

M41	1 hour	11.67	1.45	50.16	36.73	8.05
M42	0	15.17	1.90	50.41	32.53	7.98
M46	370	16.01	0.91	58.53	24.56	17.59
M47	1470	14.60	0.63	57.67	27.09	23.17
M48	2090	3.95	0.28	56.59	39.19	14.11

Table 7.13: atomic percentages and Ti/Ru ratios for various samples of the M4x series after degradation.

M51	0	16.22	1.44	47.06	35.27	12.26
M52	1 hour	13.11	1.52	48.81	36.56	8.62
M53	600	8.03	0.40	49.87	41.71	20.07
M56	1800	15.04	0.57	50.94	33.45	27.85
M57	2460	14.63	0.63	52.88	31.87	23.22
M58	4492	14.90	0.71	52.65	31.74	20.96

Table 7.14: atomic percentages and Ti/Ru ratios for various samples of the M5x series after degradation.

Tables 7.12 to 7.14 results show two interesting features. The first one is that the surface Ti/Ru ratio increases as a function of degradation. This indicates that degradation in the alkali wear pot results in preferential loss of ruthenium at the surface. The second feature is that the Ti/Ru ratio reaches a maximum value and then begins to decrease. Examination of the variation of the Ti/Ru ratio as a function of alkali wear pot running potential increase reveals that the Ti/Ru ratio increases until the

increase alkali wear pot running potential exceeds a value of 1500-1800 mV and then falls. This is shown in the diagram below :

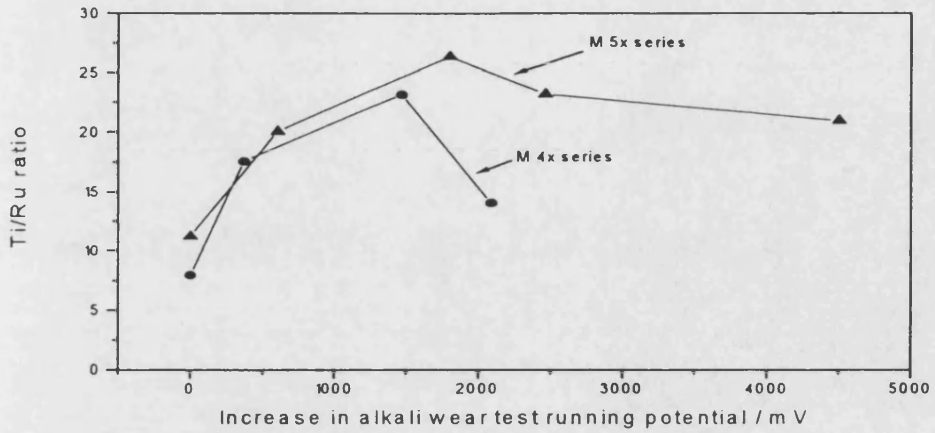

Figure 7.15 : variation of the Ti/Ru ratio as a function of increase in alkali wear pot running potential for the M4x and M5x series.

Since XRF measurements indicate that ruthenium is always being lost from the bulk, this implies that titanium starts to dissolve above this critical potential range. This reduction in the Ti/Ru ratio can be explained when comparing the increases in alkali wear pot running potential with the simplified Pourbaix diagrams for titanium and ruthenium shown below:

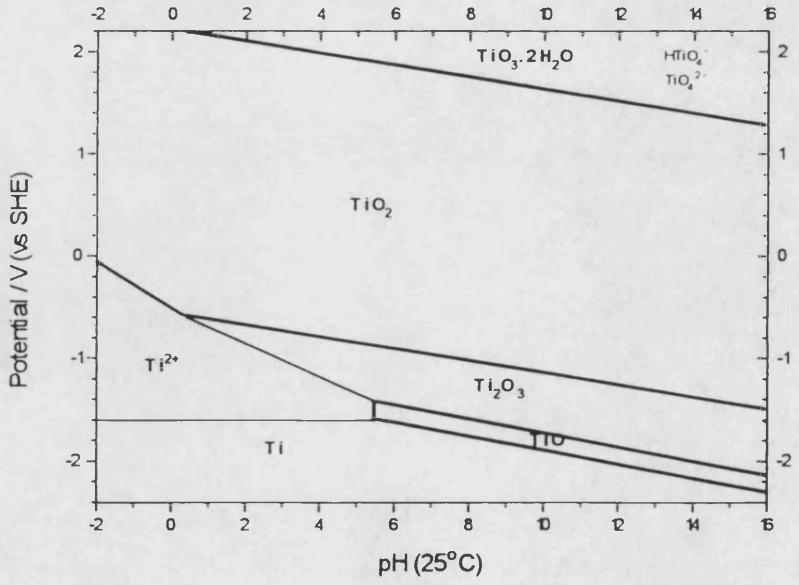

Figure 7.16 : Pourbaix diagram for titanium at 25°C.

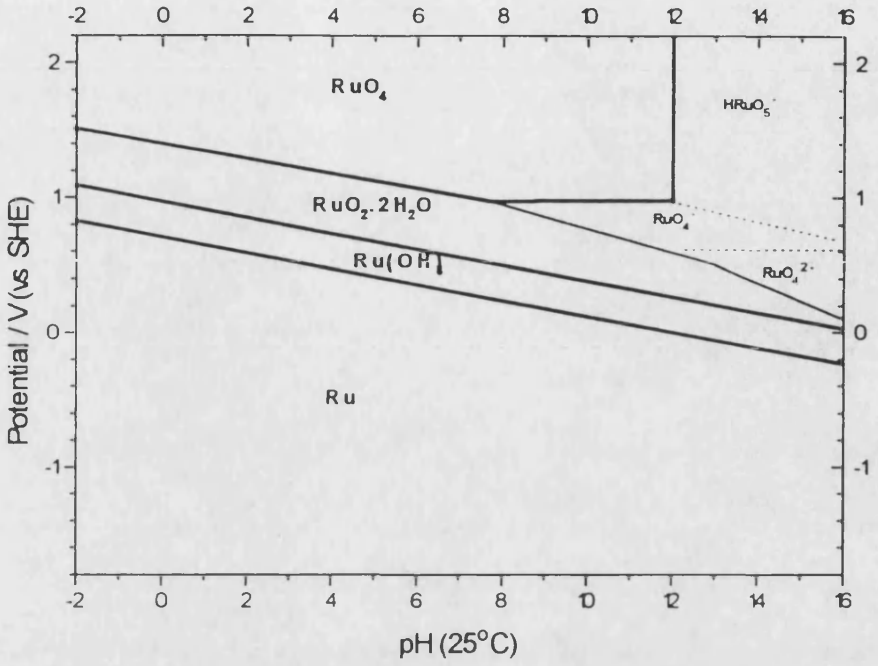

Figure 7.17 : Pourbaix diagram for ruthenium at 25°C.

The titanium Pourbaix diagram shows that, at constant pH, TiO_2 becomes less and less thermodynamically stable as the potential is increased. At pH=11, TiO_2 begins to turn into $TiO_3.2H_2O$ and then dissolve into other ionic species ($HTiO_4^-$ and TiO_4^{2-}) when the potential is greater than 1.6 volts.

At this point, it must be emphasised that TiO_3 is never seen on bulk titanium. It must be remembered that Pourbaix diagrams are theoretical thermodynamic predictions.

At pH=14, the Pourbaix diagram shows that the potential for TiO_2 dissolution has dropped to 1.4 volts: the greater the pH the lower the critical potential for TiO_2 into ionic species becomes. As for ruthenium, its Pourbaix diagram shows that RuO_2 starts to dissolve into ionic species at much lower potentials for the same pHs. (At pH=14 it only takes a potential of 0.3 volts for RuO_2 to dissolve into RuO_4^-). According to the Pourbaix diagram, as the pH of the alkali wear pot is kept constant and its running potential is increased then RuO_2 starts to dissolve from the anode coating into solution until the potential value for TiO_2 dissolution is reached and surpassed. At pH=14, the potential difference between RuO_2 and TiO_2 dissolution potentials is of 1.1 volts. This significant potential difference would result in

preferential loss of ruthenium and cause the Ti/Ru ratio to increase initially until TiO_2 starts to dissolve once the alkali wear pot running potential has increased above the transition potential for TiO_2 dissolution. Beyond that critical potential the Ti/Ru ratio would then start to decrease as both RuO_2 and TiO_2 are being removed from the anode coating.

This qualitative thermodynamic description is consistent with the observed trend resulting from the analysis of XPS data from the M4x and M5x series and corresponding increases in alkali wear pot running potential.

Analysis of XPS data from the M3x series after degradation revealed the presence of tin peaks. Furthermore, no ruthenium peaks were detected for samples M36 and M37. However, their analysis prior degradation revealed no presence of tin. It looks most likely that these samples were subjected to a high level of surface contamination. This is reinforced by the fact that no ruthenium peaks were detected: this series of samples was only mildly degraded compared to the M4x and M5x series and both series showed the presence of ruthenium even at the highest degree of degradation. It is therefore not possible that all ruthenium was removed from the surface of the degraded M3x series. It is more likely that surface contamination by tin and carbon covered the surface of the anode and that the XPS only detected their presence. After all, XPS is a very surface sensitive technique that only probed 5-10 nm of the anode coating depth. The next two plots show the XPS spectra for sample M41 without tin contamination and sample M35 with tin contamination.

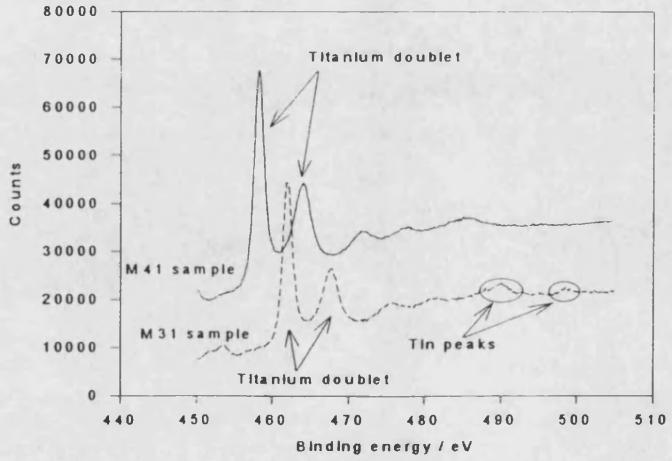

Figure 7.18 : XPS spectra of the titanium region of a sample contaminated with tin and one without contamination.

Finally, another interesting feature shown in table 7.13 and 7.14 is that the Ti/Ru ratio for samples degraded for one only hour does not reveal any particular trend. This experiment was carried out because it was experimentally observed that the chlorine reaction overpotential was lower after a period of producing chlorine at the anode. It was thought the reason for this could be either a surface contamination effect or a surface morphology or composition modification. Had it been the latter then there would be a trend in the Ti/Ru ration variation. This was not the case. This means that the observed improvement in the chlorine reaction overpotential probably resulted from the removal of surface contamination by chlorine evolution.

7.2.4 Conclusions

The use of XPS to probe the surface composition of undegraded and degraded RuO_2/TiO_2 samples has revealed several key features which are as follows :

1. The Ti/Ru surface ratio varies from 10:1 when the electrodes are undegraded and goes through a maximum ratio of 26:1 before decreasing back towards its initial value when the electrodes are highly degraded. The preferential loss of ruthenium can be explained by the differences in stability of RuO_2 and TiO_2 according to the Pourbaix diagrams. There does, however, remains some doubt as Pourbaix diagrams only relate to thermodynamic considerations.

2. Comparison of elemental composition of the RuO_2/TiO_2 coating composition with the surface Ti/Ru ratio reveals that there is a phase separation between the surface of the coating and the bulk which has a higher ruthenium content per unit area. This might help explain why electrodes have to evolve chlorine for a while in order for them to be 'activated' when they are used for the first time, i.e. time must be given for the electrolyte to reach the ruthenium rich layer beneath the surface of the coating.

3. The preferential degradation of ruthenium must be causing the electrode to become increasingly porous. Since all electrodes studied still evolved chlorine and the surface Ti/Ru ratio increased by nearly 300 % this means that the chlorine reaction

must have taken place deeper inside the anode coating. This also implies that degradation would increase the total ohmic contribution of the operating cell.

7.3 SEM Characterisation

This section reports on the results obtained from SEM characterisation of all RuO_2/TiO_2 samples before and after degradation.

Inspection of SEM photos reveals that the RuO_2/TiO_2 anodes have a mud-crack type of structure on the macroscopic scale. This is probably because the samples were left to dry without controlling the temperature decrease. Closer analysis of the photos shows that the width of the crevasses is of the order of 0.5 to 0.9 μm. However, the fact that the roughness factor as measured BET is in the range of 300-1000 means that the anodes must also be microporous. This was not seen using SEM and would probably require a technique such as TEM.

The SEM photos taken on degraded samples showed no difference in morphology compared to undegraded samples. Although XRF reveals that at least 50% ruthenium is removed by degradation, SEM photos show no signs of increase in the macroporous nature of the coatings. Furthermore, SEM photos taken at a 45° angle did not show any sign of coating removal nor thinning of the RuO_2/TiO_2 coating. This observation is consistent with XPS results which indicate preferential loss of ruthenium and implies that ruthenium must be leached out of the coating. This also implies that the anodes must be becoming increasingly porous.

Figures 7.19 to 7.22 show SEM photos of undegraded sample M51 and degraded sample M58 at two different magnifications.

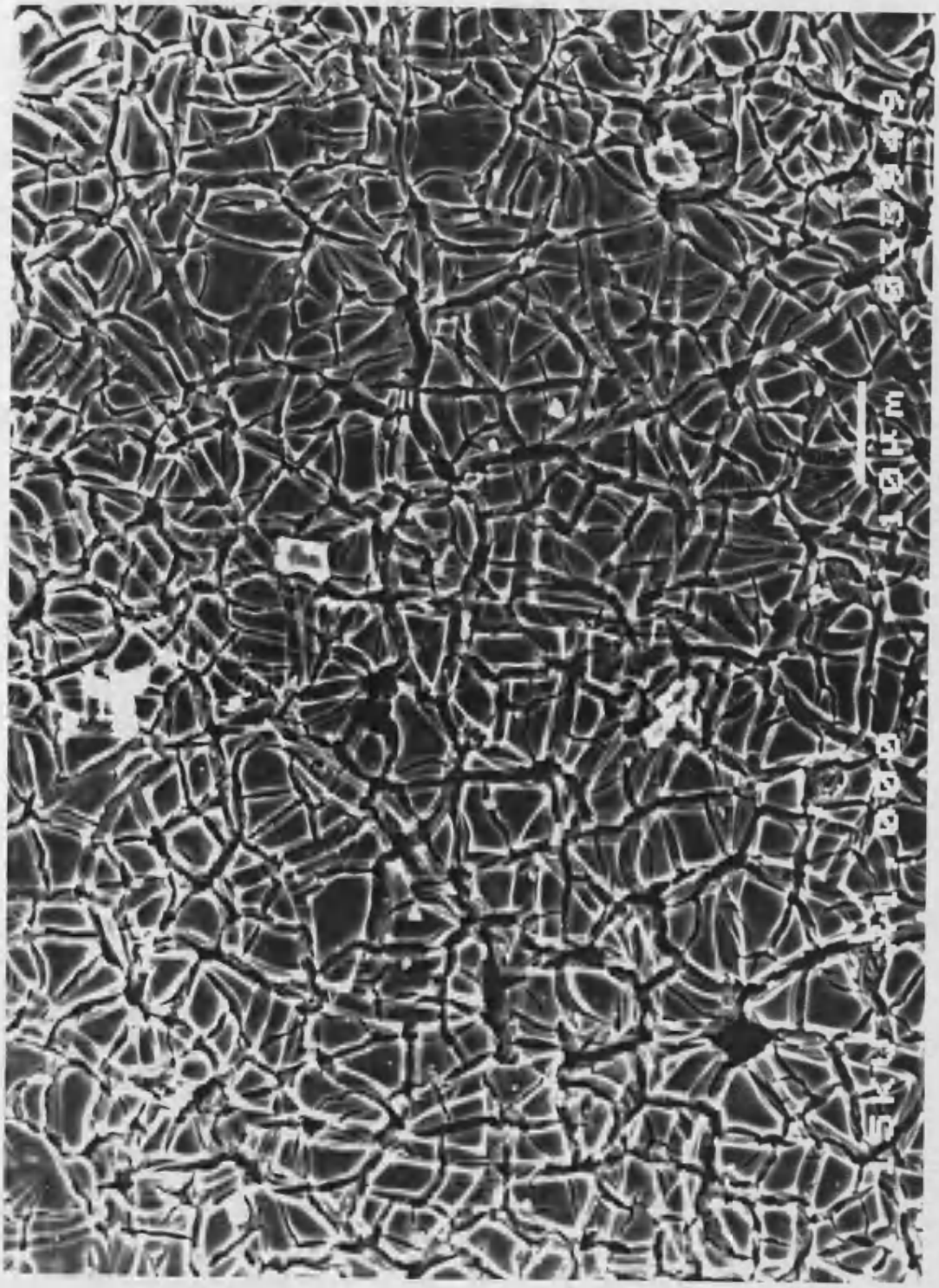

Figure 7.19 : SEM photo of undegraded sample M51 at magnification of 1000

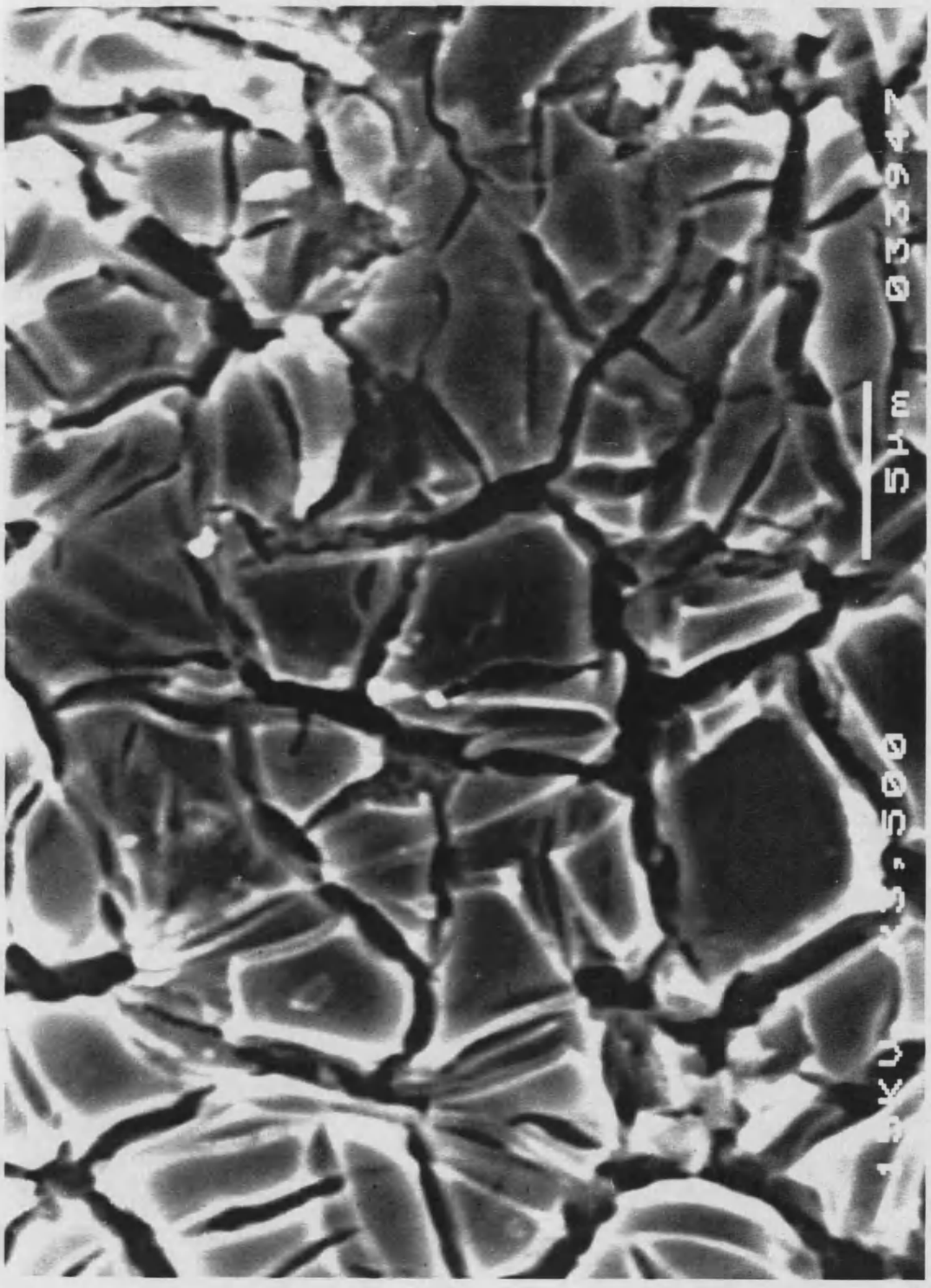

Figure 7.20 : SEM photo of degraded sample M51 at magnification of 3500

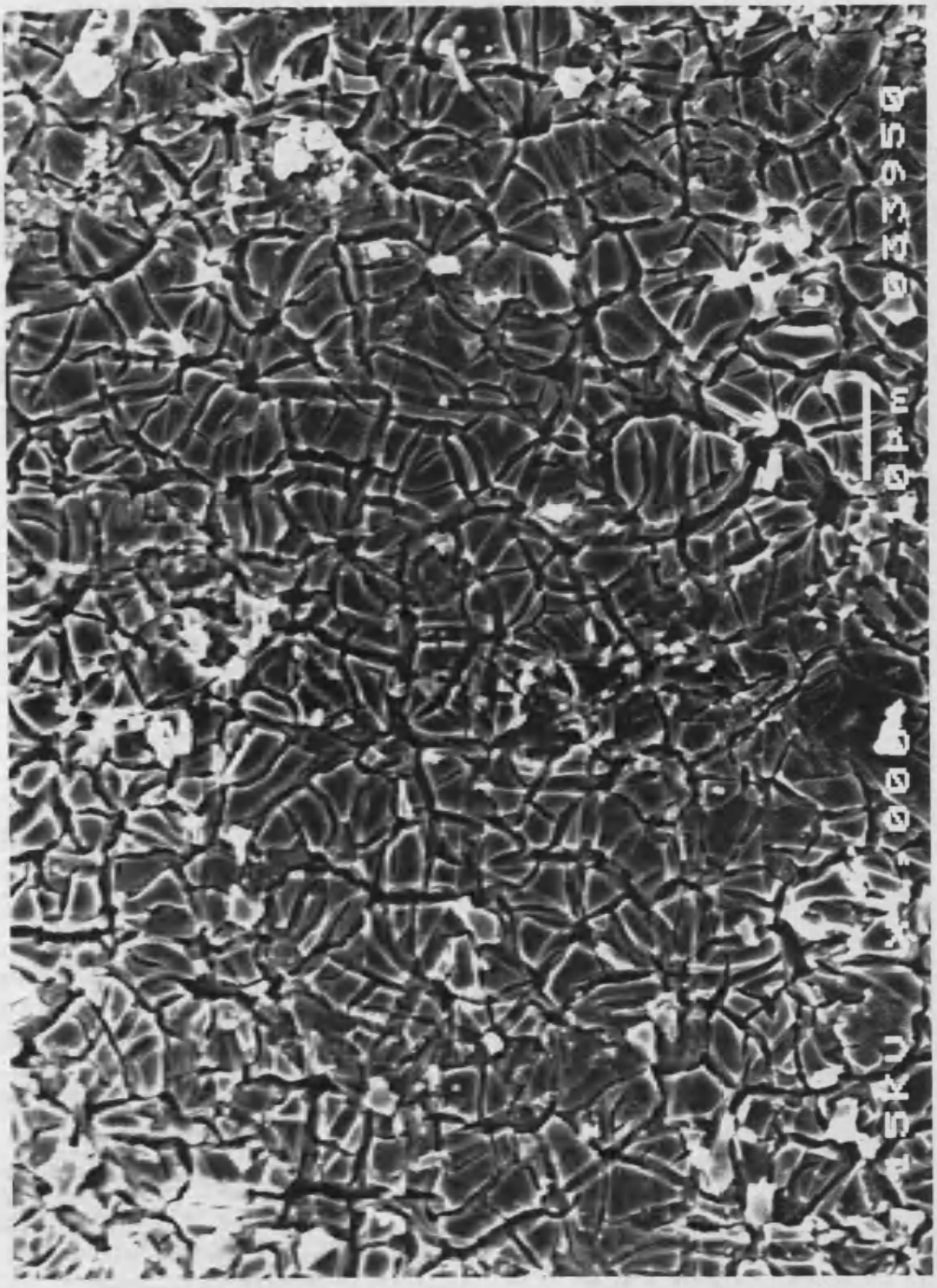

Figure 7.21 : SEM photo of degraded sample M58 at magnification of 1000

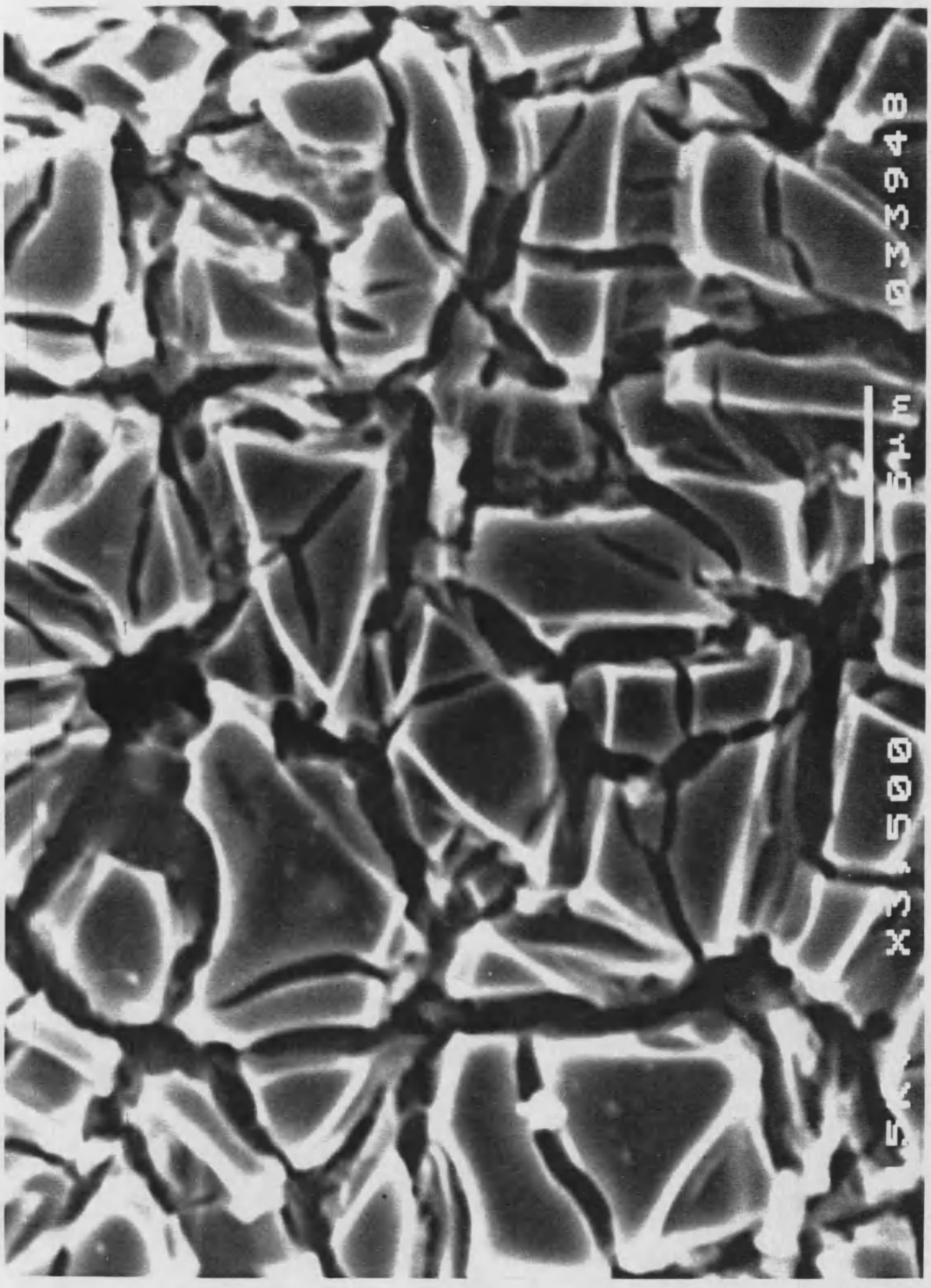

Figure 7.22 : SEM photo of degraded sample M58 at magnification of 3500

CHAPTER EIGHT

Chapter Eight

Correlation of Physical and Electrochemical techniques

8.1 The reaction mechanism

The use of the OCPD technique has established that the reaction mechanism of chlorine evolution on commercial RuO_2/TiO_2 anodes under industrially relevant conditions is as follows

$$Cl^- + M \rightleftharpoons Cl_{ads}\text{-}M + e^-$$

followed by

$$Cl_{ads}\text{-}M + Cl^- \rightleftharpoons Cl_2 + M + e^-$$

Furthermore, study of degraded electrodes has shown that the reaction mechanism is independent of degradation.

8.2 Loss of electrocatalytic performance

This section summarises results from the physical and electrochemical techniques in order to get a complete picture of the electrocatalysis of chlorine evolution on commercial RuO_2/TiO_2 anodes under industrially relevant conditions as well as their change of electrocatalytic performance following accelerated wear. The main conclusions from all the techniques are as follows :

1. XPS and XRF have shown that ruthenium is preferentially lost as a result of degradation in the alkali wear pot. Measurements have shown that up to 50% ruthenium, at least, is removed from the RuO_2/TiO_2 coating. Since there is no indication of titanium loss, this means that the electrode is becoming increasingly porous.
2. SEM showed no change in the macroscopic mud-crack type of morphology nor loss of any coating. In view of the amount of ruthenium lost and since no changes are seen even at 3500 magnification, this means that either the

crevasses are becoming deeper or that the size of the micropores must be extremely small, i.e. less than 0.2 μm diameter.

3. The roughness factor as measured by BET is in the range of 300-1000 and it is, therefore, most unlikely than the muck-crack structure is responsible for the very high capacitance values, i.e. anodes must be microporous on a scale that cannot be seen using SEM.
4. Cyclic voltammetry, impedance spectroscopy and OCPD revealed no significant change in the value of the double layer capacitance as a function of degradation. Prior degradation, its value was of 20 mF cm^{-2} and after an increase of the alkali wear pot running potential of 4V, its value was still 16 mF cm^{-2}. It is therefore concluded that the double layer capacitance does not reflect any signs of electrocatalytic loss of performance of the RuO_2/TiO_2 coating.
5. Impedance spectroscopy has shown no change in the value of the charge transfer resistance as a function of degradation time and confirms that the RuO_2/TiO_2 coating maintain electrocatalytic activity in spite of ruthenium loss.
6. Steady state measurements have revealed that the increase in cell resistance is of the same order than the equivalent increase in ohmic contribution from the alkali wear pot and that the bubble layer resistance is negligible under the experimental conditions used in this project.
7. Quantitative and qualitative analysis of OCPD data as a function degradation has shown no change in reaction kinetics as a function degradation. It has also shown that the reaction overpotential only increases by 150 mV when the alkali wear pot running potential increased by 4V, confirming that the increase in cell voltage is dominated by an increase in ohmic contribution rather than a significant change in reaction kinetics, i.e. an overpotential increase.

Conclusions 1 to 7 lead to the overall conclusion that the so-called loss of electrocatalytic activity of commercial RuO_2/TiO_2 anodes is in fact due to an increase in the electrode resistance, i.e. it is an ohmic effect and not a kinetic effect. This

analysis has shown that although the electrodes have lost at least 50 % ruthenium, there is no change in catalytic activity of the RuO_2/TiO_2 coating. This is a remarkable conclusion which suggests that the so-called loss of electrocatalytic performance is not dominated by loss of the RuO_2/TiO_2 properties..

8.3 Suggested models

Results from the alkali wear test and steady measurements revealed that a 1Ω increase in ohmic contribution would suffice to produce the increases in cell voltages that were observed.

8.3.1 Model 1 : Increase in electrode porosity

This models assumes that the increase in cell voltage is due to an increase in electrode porosity which would lead to an increase in solution resistance. This would be consistent with the fact chlorine evolution is taking place deeper and deeper inside the electrode as suggested by the XPS data and the fact that the electrocatalytic activity is not significantly affected by ruthenium loss.

If this was the case then it follows that

$$R_{increase}=R_{electrolyte}*F_v \qquad (8.1)$$

where $R_{increase}$ is the increase in ohmic contribution, $R_{electrolyte}$ is the electrolyte resistance and F_v is the volume fraction of the electrode that is porous.

If we consider that the pores are cylindrical then equation 8.1 can be rewritten as

$$R_{increase} = \frac{h}{\lambda \pi r^2} * F_v \qquad (8.2)$$

where h is the height of the pore, r is the radius of pore and λ is the conductivity of brine (650 S cm^2 mol^{-1}).

Analysis of the SEM photos revealed no sign of microporosity at the 3500 magnification factor. This means that the radius of the pores is no greater than 0.5μm. Furthermore, lets assume that the height is 10 times bigger than the diameter of the pore, i.e. h=5 μm. It follows that

$$F_v = \frac{R_{increase}\lambda \pi r^2}{h} \qquad (8.3)$$

$\therefore F_v = 1.02\ 10^{-2}$

If this model is true, this means that an increase in 1 % of the porosity would be responsible for the 1 Ω increase. This is clearly too small a value and suggests that the increase in cell voltage is not dominated by an increase in electrode porosity.

8.3.2 Model 2 : build-up of a resistive layer

In this model, it is assumed that the increase in cell voltage is due to the build-up of a resistive layer between the RuO_2/TiO_2 coating and the titanium substrate. This would occur if electrolyte reached the titanium substrate and allowed an insulating layer of TiO_{2-x} to build-up on top of the titanium. The result of such a layer would be to gradually decrease the area where current can flow through the anode and, hence, causing an increase in cell voltage. This is best illustrated in figure 8.1 below :

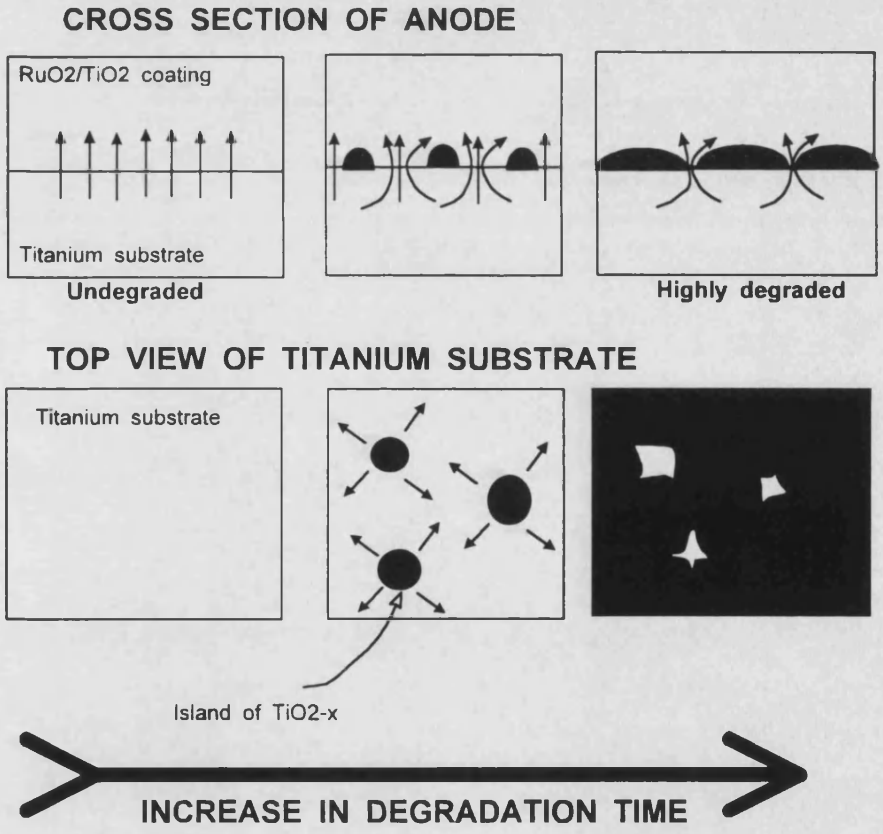

Figure 8.1 : increase in electrode resistance due to growth of an insulating layer of TiO_{2-x} on the titanium substrate. (arrows in cross section view represent current flow).

Peter[1,2,3] et al. have shown that TiO_{2-x} can grow at the surface of titanium as Magnelli phases where x can vary from 0 to 1. Although no quantitative analysis can be made to see if this the case for the titanium substrates used in this project, there is evidence from the alkali wear pot running potential vs. time data which suggests that such a process is occurring at the anode : if the current is interrupted and the alkali wear pot switched on a few minutes later then the alkali wear pot running potential does not immediately return to the value it had prior interruption. Instead, it takes a finite time to return to it. This is characteristic of the presence of a TiO_{2-x} layer which relaxes once the current is interrupted and gradually increases as the current is switched on.

It is therefore concluded that the increase in cell voltage of RuO_2/TiO_2 anodes is due to the growth of an insulating layer of TiO_{2-x} which causes the electrode to be more resistive. Although the TiO_{2-x} layer does relax, this is an irreversible process, i.e. the layer will grow until all the titanium substrate is covered and will then become thicker and thicker.

---

1 D.J. Blackwood, L.M.Peter, H.E. Bishop, P.R. Chalker, D.E. Williams, *Electrochimica Acta*, 34(8), 1989, 1401-1403

2 D.J. Blackwood, R. Greef, L.M. Peter, *Electrochimica Acta*, 34(6), 1989, 875-880

3 D.J. Blackwood, L.M. Peter, *Electrochimica Acta*,34(11), 1989, 1505-1511

CONCLUSIONS

Chapter Nine

CONCLUSION

AND FUTURE WORK

9.1 Conclusions

The use of physical and electrochemical techniques has allowed the determination of the reaction mechanism for the electrocatalysis of chlorine on a commercial RuO_2/TiO_2 anode under industrially relevant conditions. It has been shown that the OCPD technique is a very powerful fingerprinting technique that can be used qualitatively as well as semi-quantitatively to study the kinetics of this reaction. The extremely good similarity between OCPD simulations and the experimental data means there is no doubt as to the reaction mechanism on this type of electrode. This is major achievement in view of the obstacles that were encountered and the previous failure to carry out such an investigation.

By performing a complete characterisation of the electrocatalysis of chlorine on RuO_2/TiO_2 anodes as a function of accelerated wear, it has been possible to explain the mechanism which is responsible for the increase in total cell voltage. It has been found that the performance of the anodes is not critically dependent on the amount of ruthenium in the coating as was previously believed. On the contrary, all the evidence indicates that the increase in total cell voltage depends on the fact that electrolyte can reach the titanium substrate and cause the growth on an insulating layer of TiO_{2-x}/TiO_2, causing an increase in the electrode resistance. Although this is not a major surprise, the fact that a full analysis has ruled out changes in reaction kinetics as the possible cause for the total voltage increase means that there is no longer any doubt as to the main factor responsible for the loss of catalytic performance.

9.2 Future work

Further work needs to be carried out to detect the presence of this insulating layer between the titanium substrate and RuO_2/TiO_2 coating. In terms of the OCPD technique and the fitting of experimental data, a Langmuir isotherm was used to describe the adsorption of the chlorine intermediate in this project. Work needs to be carried out using different isotherms in order to see study the outcome of the semi-quantitative results on the choice of isotherm used to describe the adsorption of the chlorine intermediate.

The collaboration with ICI has continued and the new project is now focused on a more microscopic scale. In view of the complexity of the commercial anodes, it was not possible to investigate the chemistry taking place on the atomic scale, i.e. the mechanism of chlorine adsorption and formation of chlorine at the atomic level. The aim of this project is to gain a theoretical understanding of the specific roles of ruthenium and titanium in the electrocatalysis of chlorine and also to find out the nature of the chlorine intermediate as this is still an area of controversy.

APPENDIX

```
S::Harold - SIMPLE_OCP   13:29:52 19-Sep-1994   Page 1

10REM #title OCPD 1.00
30REM ------------------------------------------------------------
50REM     ANTHONY SHINGLETON 6/2/1994
70REM     USING GAIN 1 OR 10 !!!
90REM     OPEN POTENTIAL DECAY RELAXATION STORAGE PROGRAM
10REM ------------------------------------------------------------
30 PRINT''' " This program was made by Anthony SHINGLETON  3/1/94 "
50 PRINT' " Its purpose is to record Open Potential Decay Relaxation trans
ents (OPDR)"
70 PRINT'' "  It  will also calculate the derivative of overpotential w.r.
time "
10 REM ------------------------------------------------------------
30 REM                      INITIAL SETTINGS
50 REM ------------------------------------------------------------
60 SOUND ON
70 DIM stack% 411400:REM              RESERVE MEMORY SPACE 102850PTS FOR ADC
90 DIM data(102849):REM               RESERVE SPACE TO STORE 102850PTS
10 DIM potential(4657):REM            RESERVE SPACE FOR 4658 OVERPOTENTIALS
30 DIM time(4657):REM                 RESERVE ARRAY FOR TIME 4658PTS
70 SYS"WVAIO_Channel",1:REM ---------------SELECT CHANNEL 1 FOR RECORDING
90 SYS"WVAIO_ViaWrite",2,255:REM ----------MAKE ALL PBX LINES OUTPUTS
10 SYS"WVAIO_ViaWrite",0,2:REM ------------SELECT PB1 AS SWITCH TRIGGER
20 PRINT' " See diagram for circuit connections "
30 data()=0:potential()=0
50 INPUT'''' "HOW MANY DECAYS TO YOU WANT TO AVERAGE ";totaldecay%
70 *FX 15,1
72 INPUT' " Please input an estimate of the solution resistance ";sol
90 INPUT' "  PLEASE GIVE FILENAME ";filename$
10 channel=OPENOUT ("ADFS::Harold.$.Anthony.DATA.OPDR."+filename$)
30 INPUT' "WHAT CURRENT DENSITY DO YOU WANT TO MEASURE (in mA) ";cur%
50 REM ------------------------------------------------------------
70 REM                          SIGNAL ACQUISITION
90 REM ------------------------------------------------------------
10 numdecay%=0
30 CLS:FOR A%=0 TO 4000000:NEXT A%
90 D%=stack%:Z%=stack%+404000:Y%=stack%+407600
10 PRINT' " FILE NAME IS ---------------> ";filename$
30 PRINT " DECAYS PER MEASUREMENT -----> ";totaldecay%
50 PRINT " DECAYS STORED SO FAR -------> ";numdecay%
70 PRINT' " CURRENT DENSITY IS (in mA) -> ";cur%
90 IF (totaldecay%-numdecay%)>=2 THEN
10 PRINT''' "     POTENTIAL DECAYS LEFT TO BE RECORDED ";(totaldecay%-num
cay%)
30 ELSE
50 PRINT''' "      LAST DECAY TO BE RECORDED"
70 ENDIF
80 SOUND 1,-15,-229,5
90 SYS"WVAIO_Clock",100000
10 SYS"WVAIO_ViaWrite",0,0:SYS"WVAIO_ADC",101000,1,D%,1:SYS"WVAIO_Clock",1
:SYS"WVAIO_ADC",900,1,Z%,1:SYS"WVAIO_Clock",50:SYS"WVAIO_ADC",950,1,Y%,1
30 SYS"WVAIO_ViaWrite",0,2
50 PRINT' "      TRANSLATING FIRST 1000 POINTS INTO VOLTS  "
70 SYS"WVAIO_Display",200,1,20,D%
90 FOR A%=0 TO 999
10 valeur=((((stack%!(A%*4))*10)/4096)-5)
30 data(A%)=-valeur
50 NEXT A%
70 REM - - - - - - - - - - - - - - - - - - - - - - - - - - - - - - - - -
```

```
::Harold - SIMPLE_OCP   13:29:52 19-Sep-1994   Page 3

50 FOR A%=(1000+ref%) TO (9999+ref%) STEP 10
70 valeur=((((stack%!(A%*4))*10)/4096)-5)
90 data(A%)=-valeur
0 potential(counter%)=(potential(counter%)+data(A%))
0 counter%=counter%+1
30 NEXT A%
0 FOR A%=(10000+ref%) TO (100799+ref%) STEP 100
20 valeur=((((stack%!(A%*4))*10)/4096)-5)
0 data(A%)=-valeur
0 potential(counter%)=(potential(counter%)+data(A%))
0 counter%=counter%+1
0 NEXT A%
40 FOR A%=101000 TO 102849
0 valeur=((((stack%!(A%*4))*10)/4096)-5)
0 data(A%)=-valeur
60 potential(counter%)=(potential(counter%)+data(A%))
0 counter%=counter%+1
0 NEXT A%
0 IF numdecay%<totaldecay% THEN GOTO 630
0 REM ------------------------------------------------------------------
0 REM                    END OF ACQUISITION
0 REM ------------------------------------------------------------------
0 CLS
0 IF totaldecay%=1 THEN
0 GOTO 2810
0 ELSE
0 PRINT' "     AVERAGING ! "
0 FOR A%=0 TO 4657
0 potential(A%)=potential(A%)/totaldecay%
0 NEXT A%
30 CLS
0 ENDIF
0 CLS
0 PRINT' "     SAVING INFORMATION ON HARD DISK !"
0 @%=&01010408
0 time(0)=1.001E-5
0 FOR A%=1 TO 999:time(A%)=time(A%-1)+9.996E-6:NEXT A%
0 FOR A%=1000 TO 1899:time(A%)=time(A%-1)+9.996E-5:NEXT A%
0 FOR A%=1900 TO 2807:time(A%)=time(A%-1)+9.996E-4:NEXT A%
0 time(2808)=time(2807)+0.00299
0 FOR A%=2809 TO 3707:time(A%)=time(A%-1)+0.01:NEXT A%
0 time(3708)=time(3707)+0.0215
0 FOR A%=3709 TO 4657:time(A%)=time(A%-1)+.02:NEXT A%
0 REM
0 REM
0 REM
0 FOR A%= 0 TO 4657
0 FOR D%= 1 TO LEN(STR$(time(A%)))
0 BPUT#channel,ASC(MID$(STR$(time(A%)),D%,1))
0 NEXT D%
0 BPUT#channel,ASC(",")
0 FOR D%= 1 TO LEN(STR$(potential(A%)))
0 BPUT#channel,ASC(MID$(STR$(potential(A%)),D%,1))
0 NEXT D%
0 BPUT#channel,ASC(","):BPUT#channel,CHR$(13)
0 NEXT A%
0 @%=&0000090A
0 CLOSE#channel
```

```
::Harold - SIMPLE_OCP   13:29:52 19-Sep-1994   Page 2

0 REM FIND MINIMUM POTENTIAL AND DECIDE IF IT IS THE OVERPOTENTIAL AT t=0
0 REM - - - - - - - - - - - - - - - - - - - - - - - - - - - - - - - - -
0 ref%=0
0 iRdrop=(0.0007*sol*cur%)
0 REPEAT
0 IF ref%>=300 THEN GOTO 630
0 ref%=ref%+1
0 small=data(ref%)
0 UNTIL (data(ref%)-data(ref%-1))<= -iRdrop AND ref%>=70
0 IF (data(ref%+1)-data(ref%))>= 0 THEN
0 ref%=ref%+1
0 small=data(ref%)
0 GOTO 1250
0 ELSE
0 ENDIF
0 IF (data(ref%+1)-data(ref%))<= -iRdrop THEN
0 ref%=ref%+1
0 GOTO 1370
0 ELSE
0 ENDIF
2 IF (data(ref%)<0) OR (data(ref%)>0.6) OR (ref%<=70) OR (data(ref%)-data
f%-1)>= 0.04) THEN
4 SOUND 1,-14,239,5
6 GOTO 630
8 ELSE
0 ENDIF
0 mean=0
0 FOR A%=ref% TO (ref%+3):mean=mean+data(A%):NEXT A%
0 mean=(mean/4)
0 IF (data(ref%)/mean)>= 1.15 OR (mean/data(ref%))>= 1.1 THEN
0 ref%=ref%+1
0 GOTO 1470
0 ELSE
0 ENDIF
0 small=data(ref%)
0 PRINT '' "                          Overpotential is ";(1000*small);
0 PRINT "  Index : ";ref%
0 PRINT '"                          Previous voltage ";(1000*data(ref%-2))
2 PRINT "                          Previous voltage ";(1000*data(ref%-1))
0 PRINT' "                          Next voltage     ";(1000*data(ref%+1))
0 PRINT "                          Next voltage     ";(1000*data(ref%+2))
0 PRINT' "                          Mean voltage     ";(1000*mean)
0 overpot=small
0 CLS:FOR A%=0 TO 4000000:NEXT A%
0 *FX 15,1
0 PRINT' "     STORING DECAY TO FINAL ARRAY "
0 numdecay%=numdecay%+1
0 counter%=0
0 FOR A%=ref% TO 999
0 potential(counter%)= (potential(counter%)+data(A%))
0 counter%=counter%+1
0 NEXT A%
0 FOR A%= 1000 TO (1000+ref%-1)
0 valeur=(((stack%!(A%*4))*10)/4096)-5)
0 data(A%)=-valeur
0 potential(counter%)=(potential(counter%)+data(A%))
0 counter%=counter%+1
0 NEXT A%
```

```
3370 CLS
3380 SOUND 1,-15,89,100
3390 *FX 15,1
3430 PRINT' "FILE NAME WAS "; filename$
3490 PRINT' "ANOTHER MEASUREMENT "
3510 reponse%=GET
3530 IF reponse%=ASC("Y") OR reponse%=ASC("y") THEN
3350 GOTO 430
3570 ELSE
3590 GOTO 3630
3630 END
```

```
* FORTRAN 77 PROGRAM FOR OCPD SIMULATIONS
* OCPD simulations by Dr. A. Fisher and A. Shingleton (Bath University)
* Chlorine evolution reaction
* model for abs/des kinetics
* 13/6/95
      Real*4 k1,km1,k2,km2,opt,opt1,tlog,K1_K2
      Real*4 thetat,v1,v2,thetat1,time,finale,alpha1,alpha2
      Real*4 DT(8),T(8)
      Real*4 R,F,Temp,qmono,qini,Const,fcurr,X,Z,Cphi
      character* 25 filen, filena

      PRINT *, 'This program was created by :'
      PRINT *, '  Dr. Adrian Fisher '
      PRINT *, '       and'
      PRINT *, '  Anthony Shingleton'
      PRINT *, ' '
      PRINT *, 'September 1995'
      PRINT *, ' '
      PRINT *, 'It simulates Open Potential Circuit Decays'
      PRINT *, 'The time range is from 10 nanofarads to 80 seconds '
      PRINT *, ' '

*     Input variables

      PRINT *, 'enter initial conditions data file name : '
      READ 111, FILEN
      OPEN (18, file = filen, status = 'old')
      read (18,*) NI

  111 FORMAT (A25)

* Set Initial Values

      Do 5 I = 1,NI

      read (18,*) alpha,Temp,qmono,cap,k1,k2,K1_K2,opt,filena
      write (6,*) filena,(NI-I),' files left'
      OPEN (19, file = filena, status ='unknown')

      R = 8.314
      F = 96485.0
      Const = (F*alpha)/(R*Temp)
      Time = 0.
      DT(1)=1.e-9
      DT(2)=1.e-8
      DT(3)=1.e-7
      DT(4)=1.e-6
      DT(5)=1.e-5
      DT(6)=1.e-4
```

```
      DT(7)=1.e-3
      DT(8)=1.e-3
      T(1)=9000
      T(2)=9000
      T(3)=9000
      T(4)=9000
      T(5)=9000
      T(6)=9000
      T(7)=9000
      T(8)=90000
      km1=(k1/K1_K2)
      km2=(k2*K1_K2)
      X = exp(Const*opt)
      Z = exp(-1.0*Const*opt)
      thetat = ((k1*X+km2*Z)/((k1+k2)*X+(km1+km2)*Z))

* Evaluate initial charge

      qini = thetat*qmono
      tlogt = log10(DT(1))

      Do 13 J= 1,8

      if (J.le.8.) then
       write(6,*) 'loop',J,'/8'
      else
      goto 13
      endif

      DO 20 O = 1,T(J)

      if (opt.le.1.e-7) then
       O = T(J)
       J = 8
       finale = (exp(tlogt)/10)
       write(6,*) 'Overpotential less than 1e-6 V at',finale,' seconds'
       write(6,*) ' '
       goto 13
      endif

* Evaluate Rates v1,v2 and v3

      v1 = k1*(1.0-thetat)*exp(Const*opt)
      v1 = v1 - km1*thetat*exp(-1.0*Const*opt)
      v2 = k2*thetat*exp(Const*opt)
      v2 = v2 - km2*(1.0-thetat)*exp(-1.0*Const*opt)
      Cphi= ((qmono*F)/(R*Temp))*((1-thetat)/(1+thetat*(1-thetat)))

* Evaluate Faradaic Current, Coverage and Overpotential
```

```
      fcurr = (v1 + v2)*F
      thetat1 = thetat + ((F*DT(J)/qmono)*(v1-v2))
      opt1 = opt + (((F*DT(J))/Cap)*(v1 + v2)*(-1.0))
      tlog = log10(O*DT(J)+time)

      if (abs(tlogt) - abs(tlog).gt.0.02) then
       write (19,999) tlog,thetat1,opt1,v1,v2,fcurr
       tlogt=tlog
      endif

      if (abs(tlog) - abs(tlogt).gt.0.02) then
       write (19,999) tlog,thetat1,opt1,v1,v2,fcurr
       tlogt=tlog
      endif

*  Update new theta, DT and overpotentals

      opt = opt1
      thetat = thetat1

 20   CONTINUE

      Time=Time+(T(J)*DT(J))

 13   CONTINUE

      write(6,*) ' '

 999  FORMAT(1X,E12.4,E12.4,E12.4,E12.4,E12.4,E12.4,E12.4)

      CLOSE (19)

 5    CONTINUE
      write(6,*) 'Program finished ! '
      STOP
      END
```

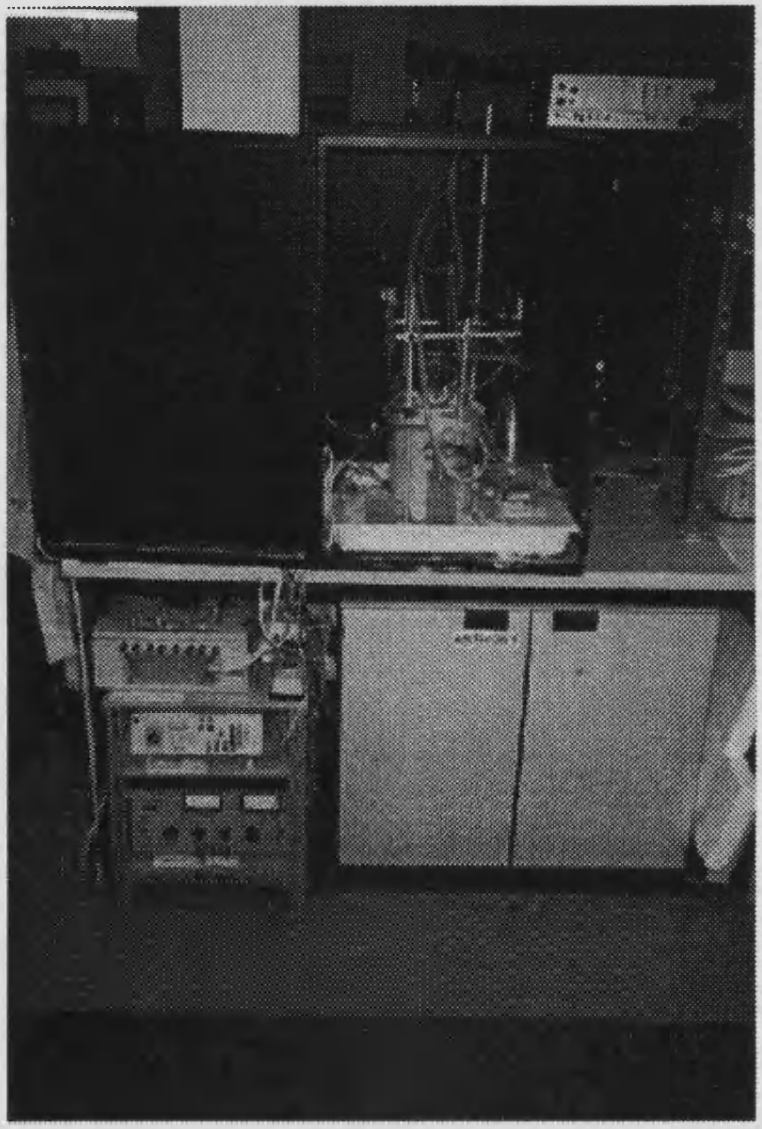

Figure 1 : photo of the alkali wear test setup used in this project. Bottom unit is the power supply, middle unit is the control unit and top unit is the current divider.

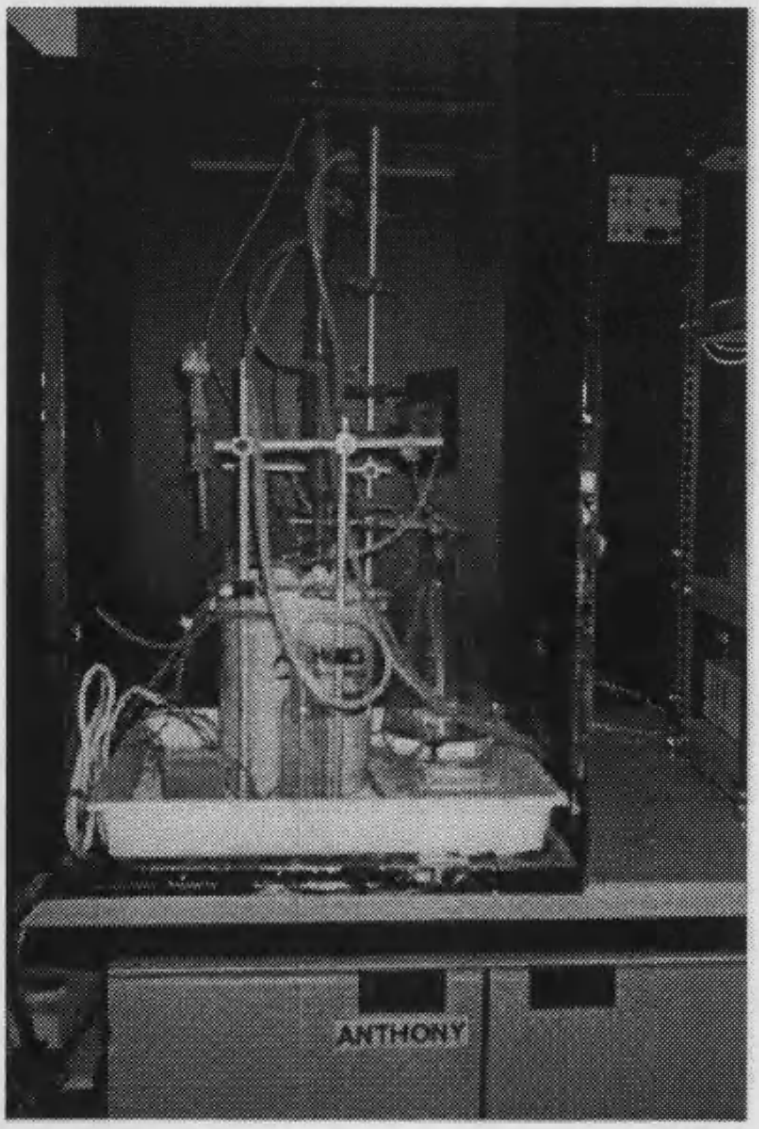

Figure 2 : close-up photo of the degradation pot.

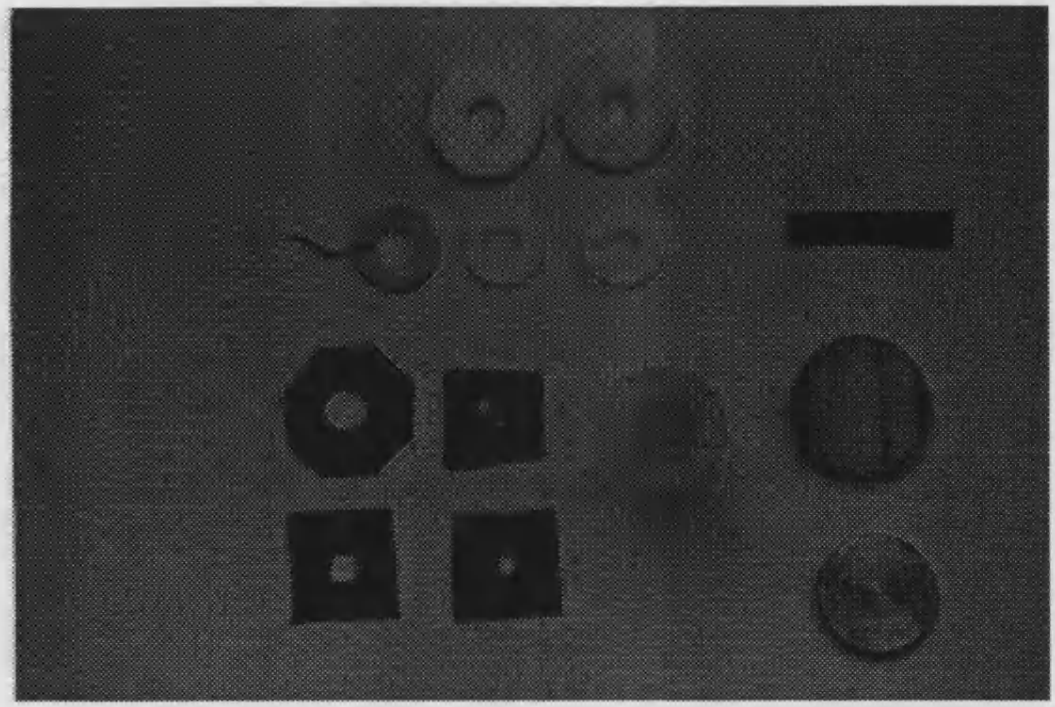

Figure 3 : photo of various PTFE rings and Viton® sheets used to determine anode working area for cell 2.

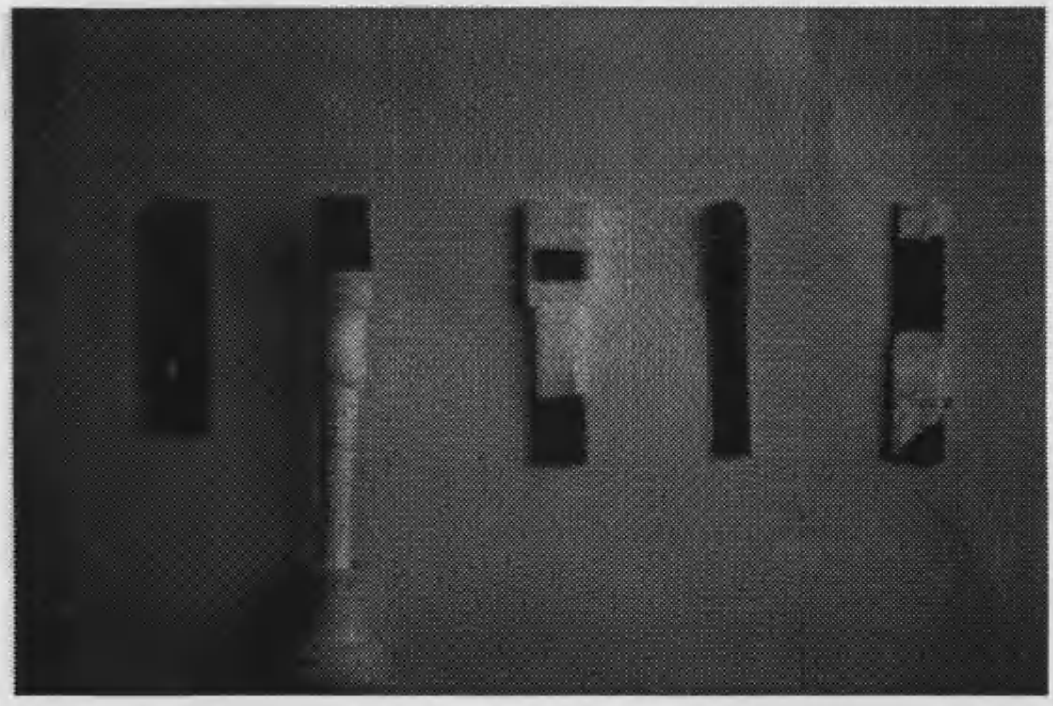

Figure 4 : photo of the various types of masking agents tried out in this project.

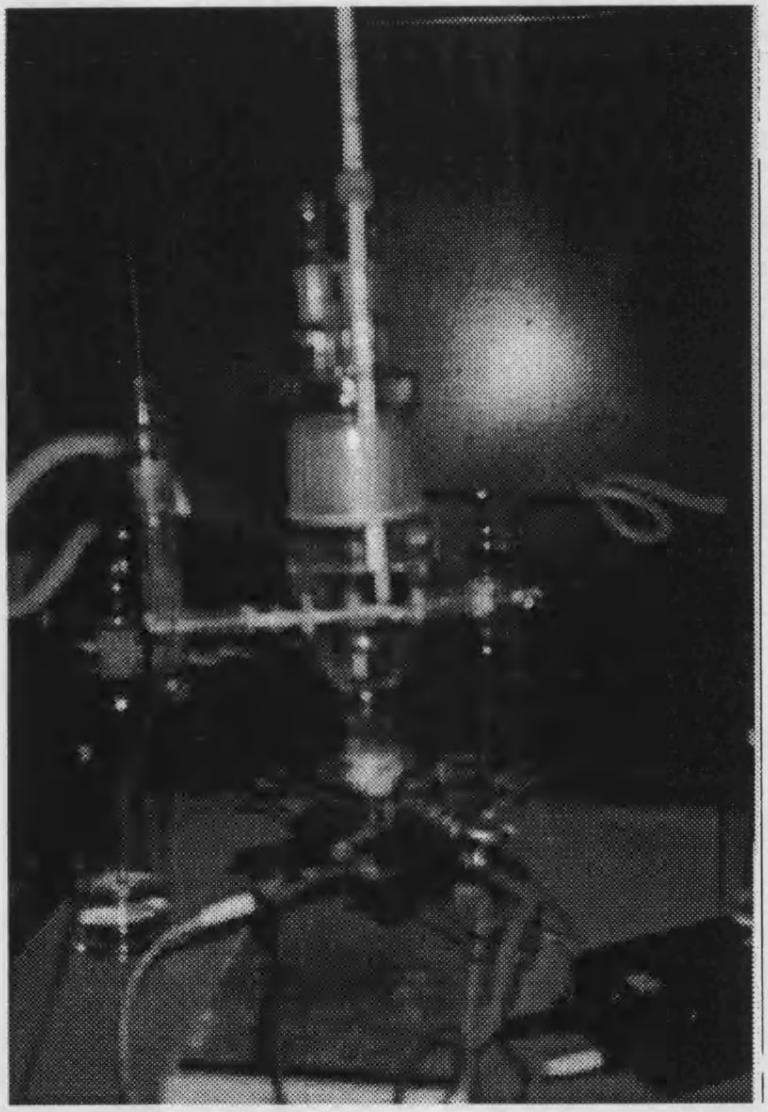

Figure 5 : photo of Cell 2.

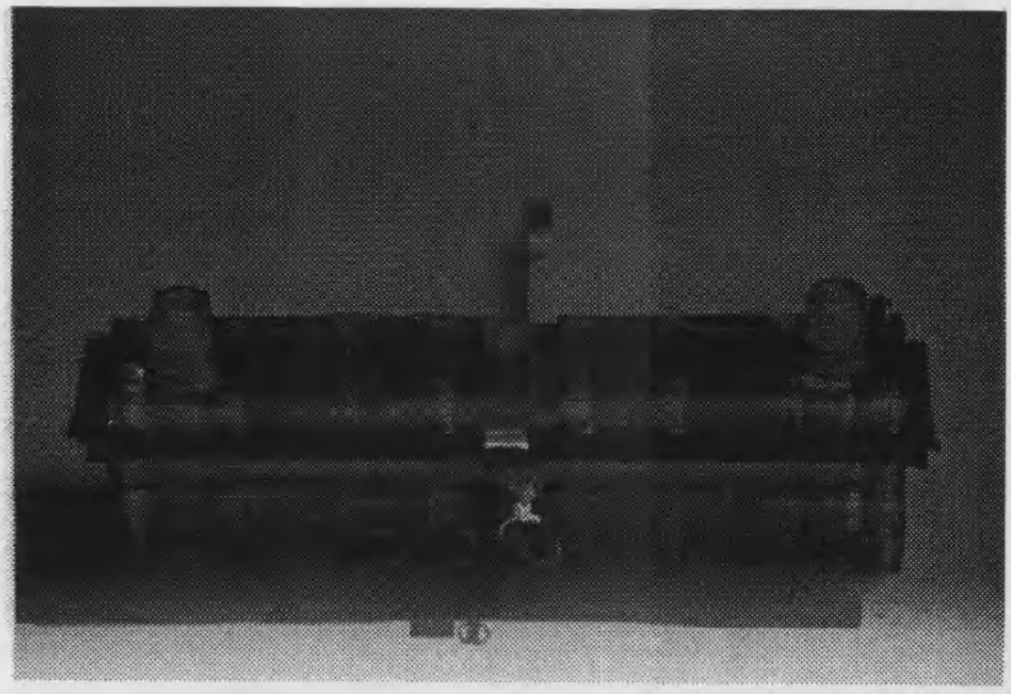

Figure 6 : photo of Cell 3 assembled.

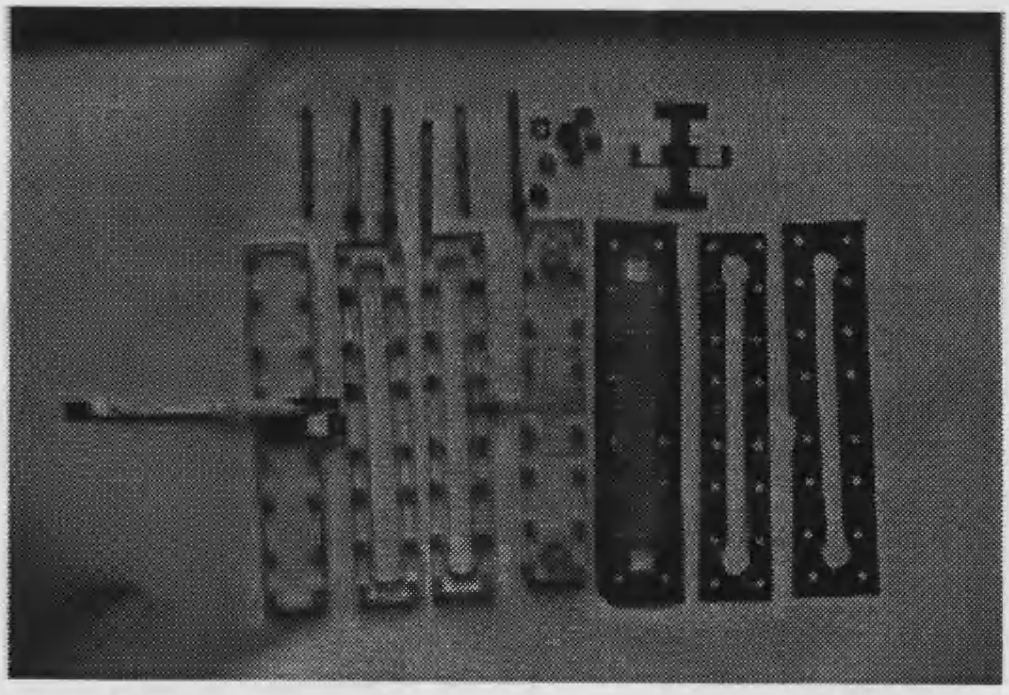

Figure 7 : photo of Cell 3 dissassmbled.

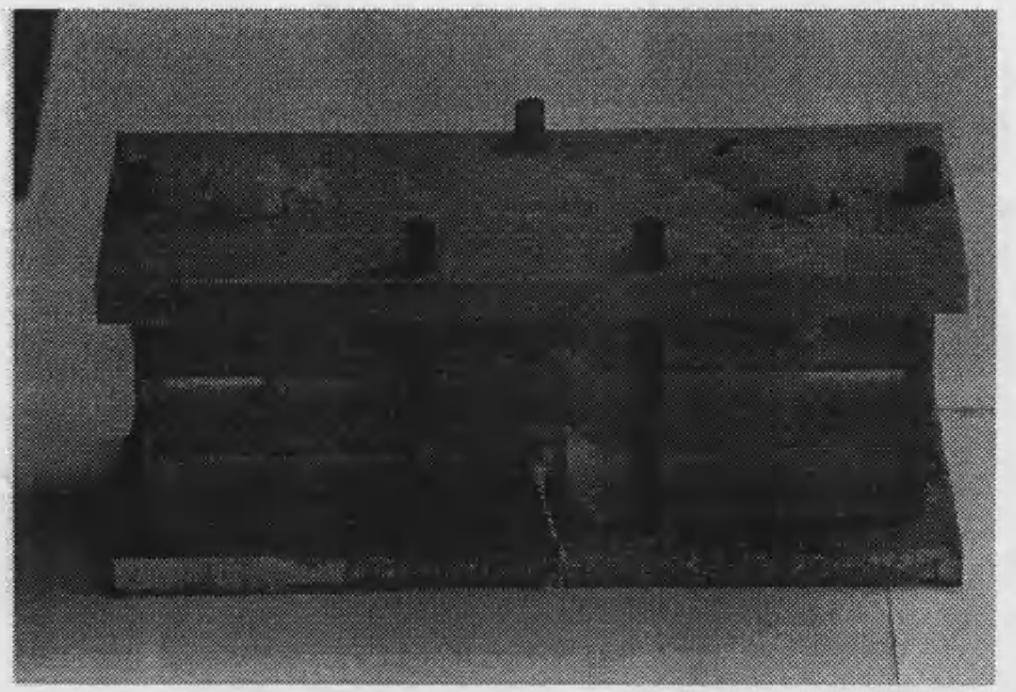

Figure 8 : photo of Cell 4 assembled.

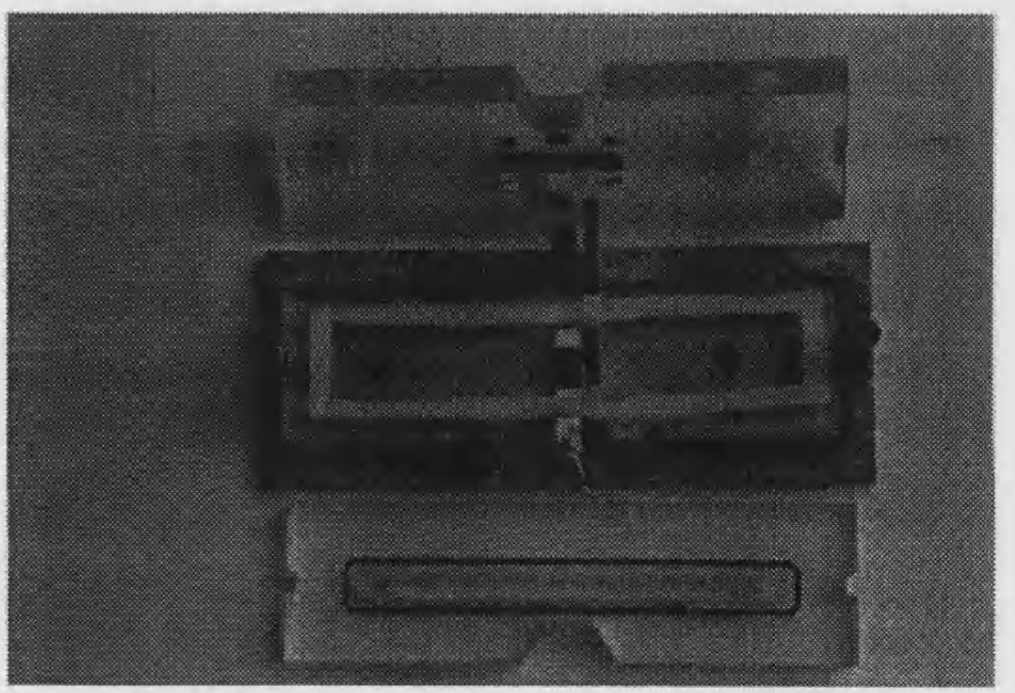

Figure 9 : photo of Cell 4 disassembled.

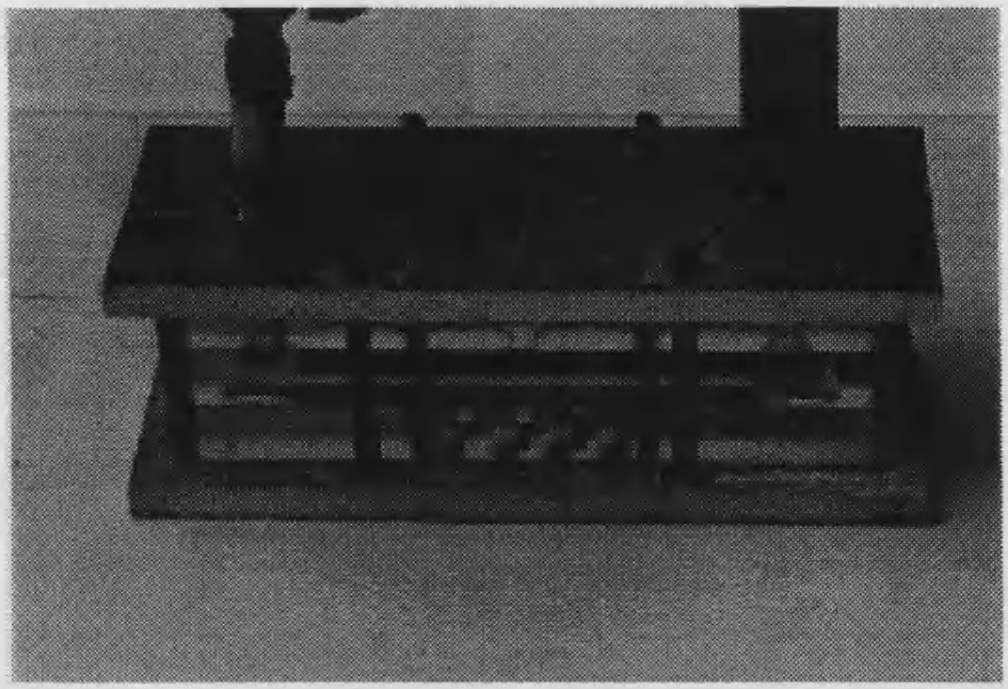

Figure 10 : photo of cell 5 assembled.

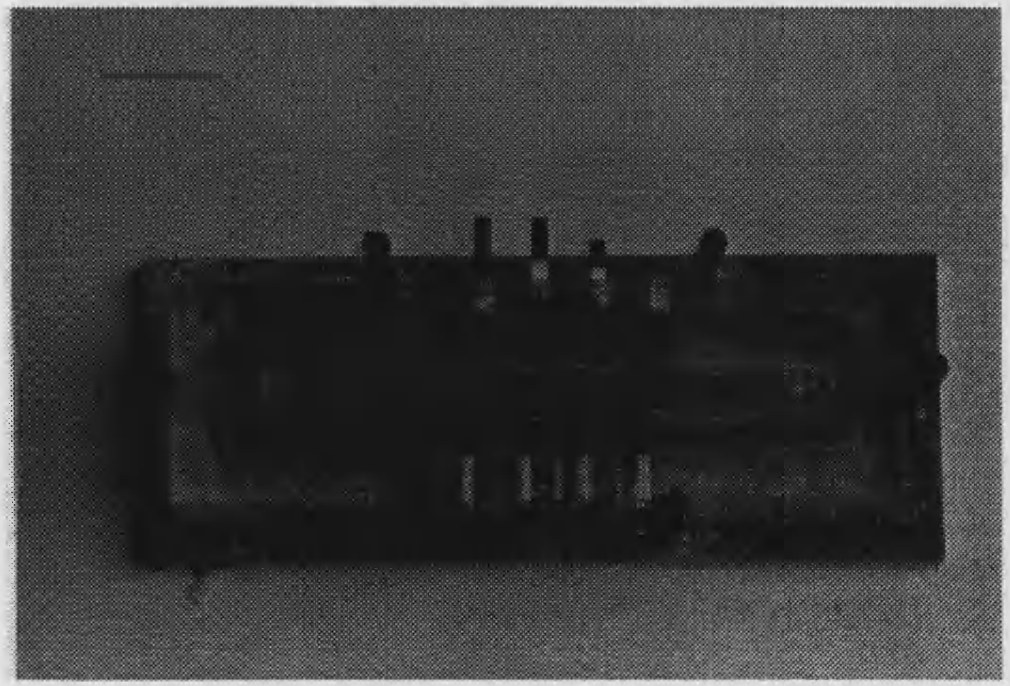

Figure 11 : photo of cell 5 disassembled (top view)

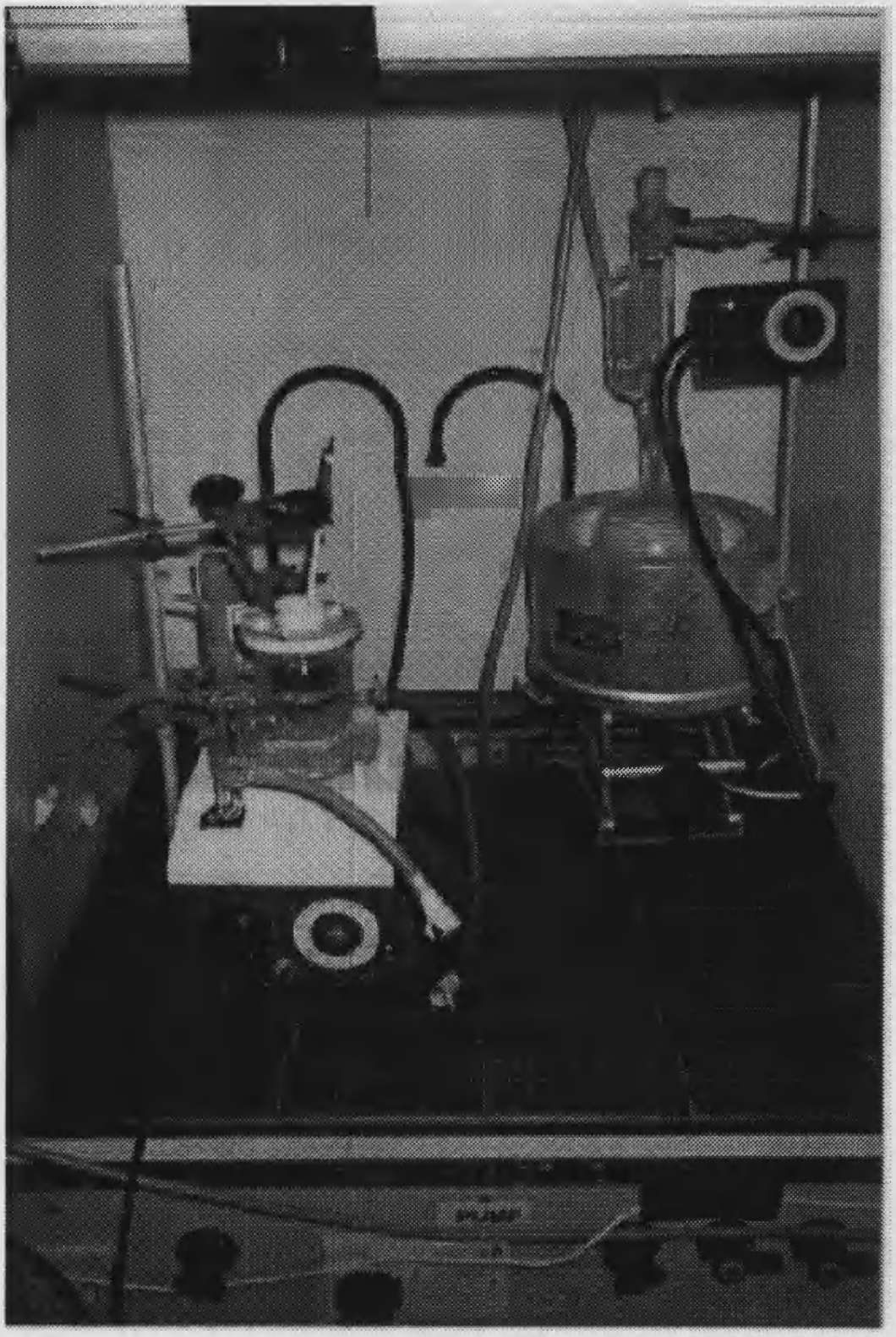

Figure 12 : photo of experimental setup for cell 6b.

Figure 13 : photo of experimental rig used for electrochemical measurements, i.e. cyclic voltammetry, steady state measurements, Tafel plots, impedance spectroscopy and OCPD.